Spin in Low Dimensional GaAs Hole Systems

LaReine A. Yeoh

A thesis submitted in fulfilment of the degree of

Doctor of Philosophy

The University of New South Wales

School of Physics

July 2015

PLEASE TYPE

THE UNIVERSITY OF NEW SOUTH WALES
Thesis/Dissertation Sheet

Surname or Family name: YEOH

First name: LAREINE Other name/s: A. YEOH

Abbreviation for degree as given in the University calendar: PhD

School: PHYSICS Faculty: SCIENCE

Title: Spin in Low Dimensional GaAs Hole Systems

Abstract 350 words maximum: (PLEASE TYPE)

There has been recent interest in quantum confined holes in GaAs semiconductors as they have potential applications in electrical spin manipulation via the spin-orbit interaction, for the development of spintronic devices. As this is a developing area of research, further theoretical and experimental investigation is needed to form a complete understanding of hole spin behaviour in low-dimensional structures. In this thesis we conduct experimental studies in two different types of low-dimensional hole systems, fabricated on GaAs/AlGaAs heterostructures: two-dimensional Hall bars and zero-dimensional quantum dots.

We begin by investigating an unusual, non-collinear spin response of a 2D hole system, grown on a low symmetry (311)A crystal plane, where applying an in-plane magnetic field generates a spin polarization perpendicular to the applied field. We probe this effect by performing tilted field transport measurements and demonstrate that this phenomenon only occurs along a low symmetry crystal axis, and is caused by the presence of an off-diagonal g^*_{xz} contribution to the g tensor. Next we turn our attention from the static properties of 2D hole systems, and explore the dynamic, non-adiabatic spin evolution of 2D holes in tilted fields. We show that the phase evolution of the Shubnikov-de Haas oscillations is very different between a high symmetry crystal axis and a low symmetry crystal axis. We model the experimental data using two paradigms (the abelian Berry and the non-abelian gauge field) and demonstrate that our dataset can only be explained by the presence of a non-abelian gauge field.

Finally we fabricate and characterize induced, lateral, gated quantum dots to isolate single spin states, including one electron quantum dot and one hole quantum dot. We perform 3D simulations to visualize the effect of the depletion region down at the 2D gas layer and optimized the quantum dot design to achieve a few-hole quantum dot. We tune the quantum dot down to the last hole and verify this independently with an integrated, quantum point contact charge detector.

Declaration relating to disposition of project thesis/dissertation

I hereby grant to the University of New South Wales or its agents the right to archive and to make available my thesis or dissertation in whole or in part in the University libraries in all forms of media, now or here after known, subject to the provisions of the Copyright Act 1968. I retain all property rights, such as patent rights. I also retain the right to use in future works (such as articles or books) all or part of this thesis or dissertation.

I also authorise University Microfilms to use the 350 word abstract of my thesis in Dissertation Abstracts International (this is applicable to doctoral theses only).

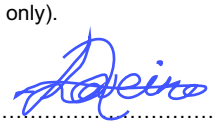

..... Signature

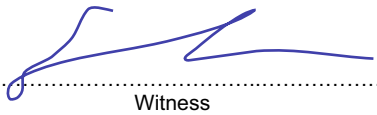

..... Witness

13/03/2014

..... Date

The University recognises that there may be exceptional circumstances requiring restrictions on copying or conditions on use. Requests for restriction for a period of up to 2 years must be made in writing. Requests for a longer period of restriction may be considered in exceptional circumstances and require the approval of the Dean of Graduate Research.

FOR OFFICE USE ONLY Date of completion of requirements for Award:

THIS SHEET IS TO BE GLUED TO THE INSIDE FRONT COVER OF THE THESIS

ORIGINALITY STATEMENT

'I hereby declare that this submission is my own work and to the best of my knowledge it contains no materials previously published or written by another person, or substantial proportions of material which have been accepted for the award of any other degree or diploma at UNSW or any other educational institution, except where due acknowledgement is made in the thesis. Any contribution made to the research by others, with whom I have worked at UNSW or elsewhere, is explicitly acknowledged in the thesis. I also declare that the intellectual content of this thesis is the product of my own work, except to the extent that assistance from others in the project's design and conception or in style, presentation and linguistic expression is acknowledged.'

Signed ……

Date ……13/03/2015……

'Not everything that can be counted counts,
and not everything that counts can be counted.'

- Cameron, 1963.

Acknowledgements

Firstly I would like to thank my supervisor Alex Hamilton to whom I am deeply grateful for the opportunity to undertake this PhD with the QED group at UNSW. His very 'hands on approach', support and enthusiasm, many ideas and suggestions (even late into the night), have taught me a lot of things about semiconductor physics, the scientific method and what it means to be a good researcher. Also, my co-supervisor Adam Micolich, whose efficiency, encouragement and advice with paper writing has been invaluable during the PhD.

I am also indebt to our postdocs Oleh Klochan and Andrew See. Oleh's extensive practical knowledge of device measurements, operation and maintenance of the dilution fridges has been crucial to my PhD. He also introduced me to cleanroom processing during a short trip to Cambridge with Ashwin Srinivasan, and the time he has spent providing me with advice and troubleshooting in the lab, on top of the enjoyable short coffee breaks, has been of immense help. Andrew's generous support and encouragement on the quantum dot project later in my PhD, and the time he has sacrificed to help me with fabrication, measurement and running of the Helium liquefier is invaluable.

A special thanks goes to my collaborators, Roland Winkler and Ulrich Zülicke whose theoretical expertise have provided many insights into interpreting the measurement results - thank you for the many wonderful discussions, encouragement and infectious enthusiasm and excitement. Special thanks also goes to Tommy Li and Oleg Sushkov for putting a new 'spin' on the interpretation of our experimental results, which has greatly increased my understanding and appreciation of the subtleties of 2D spin dynamics by drawing connections from different areas to form a much broader picture.

I would also like to thank the other members of the QED group, both past and present, for the wonderful times shared during my term: Ted Martin, Lasse Taskinen, Ashwin Srinivasan, Roy Li, Sarah MacLeod (who introduced me to the group), Daisy Wang, Laphang Ho, Jason Chen and Karina Hudson.

In particular Ashwin Srinivasan with whom I've worked closely with on our ex-

periments during the first year, including a string of non-stop fridge measurements - thanks for the great company during this whole time! Also Jack Cochrane's technical expertise of the lab infrastructure and his support with the design work I've done for the group was invaluable, as were the many enjoyable coffees! I would also like to thank Yaroslav Kharkov for kindly taking the trouble to help review the theoretical segments of my thesis, in depth - I've learnt a lot during the process as well!

I am very thankful to the staff members of the Australian National Nanofabrication Facility for the use of their cleanroom facilities as well as to Dave Ritchie and Alex Hamilton for making the arrangement for me to train in the Cavendish Laboratory cleanroom. Special thanks to Andrew Croxall, Francois Sfgakis and Luke Smith for showing me around the Cavendish cleanrooms and the sights and sounds of Cambridge.

Finally to my family and to my friends - thank you for your unconditional love and support, I would not have been able go through this journey without you.

Publications List

Publications arising from this work include:

1. L. A. Yeoh, A. Srinivasan, O. Klochan, A. P. Micolich, R. Winkler, U. Zülicke, M. Y. Simmons, D. A. Ritchie, M. Pepper and A. R. Hamilton, *Noncollinear Paramagnetism of a GaAs Two-Dimensional Hole System*, Phys. Rev. Lett. **113**, 236401 (2014).

2. L. A. Yeoh, A. Srinivasan, T. P. Martin, O. Klochan, A. P. Micolich and A. R. Hamilton, *Piezoelectric rotator for studying quantum effects in semiconductor nanostructures at high magnetic fields and low temperatures*, Rev. Sci. Instr., **81**, 113905 (2010).

3. A. Srinivasan, L. A. Yeoh, O. Klochan, T. P. Martin, J. C. H. Chen, A. P. Micolich, A. R. Hamilton, D. Reuter and A. D. Wieck, *Using a Tunable Quantum Wire To Measure the Large out-of-Plane Spin Splitting of Quasi Two-Dimensional Holes in a GaAs Nanostructure*, Nano Lett., **13**, 148-152 (2013).

4. G. Scappucci, W. M. Klesse, L. A. Yeoh, D. J. Carter, O. Warschkow, N. A. Marks, D. L. Jaeger, G. Capellini, M. Y. Simmons and A. R. Hamilton, *Bottom-up assembly of metallic germanium*, [Accepted for publication in Scientific Reports, 2015].

Manuscripts currently under review:

1. T. Li, L. A. Yeoh, A. Srinavasan, O. Klochan, D. A. Ritchie, M. Y. Simmons, O. P. Sushkov and A. R. Hamilton, *Observation of a non-abelian gauge field in a p-type semiconductor system*, [Submitted to Nature Physics].

Conference presentations:

1. L. A. Yeoh, A. Srinivasan, O. Klochan, A. P. Micolich, R. Winkler, M. Y. Simmons, D. A. Ritchie, M. Pepper, A. R. Hamilton, "Direct observation of an out-of-plane spin polarisation caused by an in-plane field magnetic field in a GaAs

2D hole system", Oral presentation, March Meeting of the American Physical Society, Denver, USA, 3-7 March 2014.

2. L. A. Yeoh, A. M. See, O. Klochan, I. Farrer, D. A. Ritchie, A. R. Hamilton, "Induced few-electron/hole GaAs Quantum Dots", Oral presentation, Wagga Wagga 38th Condensed Matter and Materials Meeting, Waiheke Island Resort, Auckland, NZ, 47 February 2014.

3. T. Li, L. A. Yeoh, A. Srinavasan, O. Klochan, D. A. Ritchie, M. Y. Simmons, O. P. Sushkov and A. R. Hamilton, "Mapping spin precession in the presence of strong spin-orbit interaction", Oral presentation (joint presentation with T. Li), Gordon Godfrey Workshop on Spins and Strong Electron Correlations, Sydney, Australia, 25-29 November 2013.

4. L. A. Yeoh, A. Srinivasan, O. Klochan, R. Winkler, U. Zülicke, M. Y. Simmons, D. A. Ritchie, M. Pepper and A. R. Hamilton, "Unusual generation of a spin polarisation at right angles to the applied magnetic field in a two dimensional hole system", Oral presentation, EP2DS-21, Sendai, Japan, 27-31 July 2015.

Contents

Chapter 1

Overview

1.1 Introduction

The field of spintronics ("spin-based electronics") uses the intrinsic spin of charged particles in a semiconductor nanostructure to carry information, treating it as an additional degree of freedom which can potentially enhance the functionality of conventional electronics [288, 309]. Low dimensional quantum structures such as spin-based transistors, wires and dots may become the basic building blocks of future quantum storage, computation and information processing technologies [18, 100].

One intriguing property of such systems is the inherent coupling between the spin of a charged particle and its orbital motion, which can be used as a mechanism to control the spin properties of a particle using electric fields from metallic gates built into the device, rather than external magnetic fields [194]. In comparison to electrons, spin-3/2 holes arising from the valence band possess strong spin-orbit interaction, due to their non-zero angular momentum and exhibit a rich variety of spin-based physical phenomena, much of which still remains unknown. There have been comparatively fewer studies into GaAs holes compared electron systems, as it was only after the discovery of modulation doping, that high mobility hole transistors could be created [56, 275], and stable, low dimensional nanostructures fabricated. More recently, hole devices based upon the dopant-free "induced" style of architecture have been developed [130]. These devices possess even higher mobilities than their doped couter-

parts, as the main source of scattering of charge carriers, off the ionized impurities is eliminated [104]. Recent theoretical work has also resulted in some exotic and seemingly counter-intuitive predictions unique to hole-based systems, such as: anisotropy in the Landé g factor [284], anomalous out-of-plane spin-polarisation due to crystal symmetry [284], negative-differential Rashba effect [97] and longer-lived, coherent spin-states in quantum dots [30, 33]. A number of these results are still incomplete or inconclusive, and further research is necessary in order to develop a complete theoretical framework and improve our understanding of the complex behaviour of spin-3/2 systems.

This body of work aims to contribute to the field by perform transport measurements on two main types of low-dimensional devices with a focus on p-GaAs semiconductors. The first involves a rare demonstration of the anomalous out-of-plane spin-polarisation in a low-symmetry, high-mobiilty two-dimensional (2D) hole system, due to the presence of off-diagonal elements in the anisotropic g tensor. In the same 2D system we also observe for the first time, the presence of the non-abelian gauge field in a semiconductor system, as a modulation to the phase of the magneto-oscillations in longitudinal resistivity and demonstrate that these results cannot be reconciled with the paradigm of abelian Berry phases alone. In the second half of this thesis, we move onto studying isolated charge and spin transport properties of zero-dimensional (0D) quantum dots. Here we fabricate and characterize quantum dots in the few-electron (hole) regime, using an induced-style of architecture, which employs a one-dimensional (1D) quantum point contact as a charge sensor to confirm the last hole has been reached.

1.2 Context and Scope

In this thesis we present studies in two main types of in quantum confined p-type GaAs/AlGaAs semiconductor systems, with the goal of understanding the behaviour of spin-3/2 phenomena in low-dimensional systems and the development of new devices to enable such studies. The thesis content is structured as follows:

The background chapter first introduces the theory behind low-dimensional structures with a specific focus upon charge and spin transport relevant to the thesis.

Beginning with a 2D heterostructure and the response of charge carriers to a magnetic field, followed by conductance quantization in 1D devices and the tunneling of single charge carriers through a 0D system. Next we briefly introduce the band structure of GaAs, the material system upon which devices in this thesis are based, with an emphasis on the valence band. We outline the different spin-orbit mechanisms of holes and the effect of the crystal lattice symmetry upon the spins of such carriers.

Chapter 3 the fabrication of such 2D heterostructures, briefly comparing the benefits of the induced architecture to doped architectures. An outline of the process-flow used to fabricate our induced devices is also provided.

Chapter 4 introduces the need for a g tensor treatment of holes in a low-symmetry GaAs structure and the origin of the anomalous out-of-plane spin polarisation. We describe the concept behind our tilted field measurement setup to detect this non-collinear spin polarisation followed by results from our transport measurements which demonstrate its presence only along the low-symmetry crystal axis. The results are explained in terms of the interplay between the symmetric and off-diagonal elements of the anisotropic g tensor followed by details of the subtle complexities of the electronic band structure of such systems in tilted magnetic fields.

Chapter 5 further investigates the subtleties of spin dynamics in a 2D hole system. We begin with a brief introduction to Berry phase and its extension into non-abelian gauge fields and how this general theory can be applied to semiconductor hole systems. Our transport measurements demonstrate a strong modulation in the phase of the longitudinal magnetoresistivity, which is indicative of the matrix-valued phase of a non-abelian gauge field. Furthermore we show that only the non-abelian Berry model is able to reproduce the coincidence angles of our dataset along 3 different crystal directions, whilst the abelian Berry model falls short and thus constitutes the first demonstration of a non-abelian gauge field in a 2D semiconductor system.

To bypass the complexities of a 2D system, Chapter 6 focuses upon isolating a single spin states by fabricating quantum dots using an induced architecture using 2 designs. The chapter begins by introducing quantum dots as artificial atoms, highlighting the challenges faced in creating robust, reproducible quantum dots and how a QPC charge

sensor can be used to independently determine dot occupancy in the few-N regime. We fabricate and show preliminary characterization results of a small electron quantum dot, followed by some modelling in Nextnano++ which was used to optimize the quantum dot and charge sensor design for the hole quantum dot. We implement the new, optimized design in a hole quantum dot and characterize the dot down to the last hole with charge sensing. We demonstrate the presence of excited states in both the dot and charge sensor conductances and some preliminary measurements of the shell filling of this structure.

The thesis concludes with a summary of the results stemming from this body of work and address possibilities for future research to be taken.

Chapter 2

Background

2.1 Introduction to low dimensional systems

This chapter briefly introduces the physics of low dimensional systems with a focus towards the influence of different length scales upon the spin and charge transport properties of such systems. This is followed by a brief introduction to the GaAs material system, central to this thesis, with an emphasis on the role of spin-orbit coupling in hole-based systems.

2.1.1 Dimensionality

The classical picture of transport through a bulk semiconductor treats charges as a 'gas' as they are free to travel in all directions and transport is independent of the sample size. However as the size is reduced, the electronic properties of the semiconductor become increasingly affected by the shape and size of the sample. The dimensionality of a system is defined by the number of spatial dimensions in which a particle's eigenstates are free to evolve and hence transport charge. Considering the wave-like nature of an electron with boundary conditions on the wavefunctions, the single particle energy level spacings are governed by sample's dimensions L, W, D (where $L>W>D$) in the x-, y- and z-directions respectively.

For large samples, the energy levels are closely spaced, appearing as a continuum, but if the dimensions are made sufficiently small the energy level spacings become

significant, drastically altering the properties of the sample. If D is reduced so that the level spacings become greater than the level broadening and k_BT, electrons are no longer free to travel in the z-direction. Instead they form a series of discrete standing waves in the z-component and the semiconductor system is now considered two-dimensional [22]. The thinner the 2D plane is, the larger the separation between energy levels. The exact value of D at which the system transitions from $3D \rightarrow 2D$, L_D, is system specific but is typically around the order of the Fermi wavelength λ_F. If both D and W are comparable to L_D the system becomes one-dimensional, like the quantum point contacts and wires and energy spectroscopic studies can be conducted which allow us to measure the energy levels of a 1D system directly [178]. If L is also comparable to L_D, the system becomes zero-dimensional, as in the case of quantum dots, where the only way for a particle to travel into and out of the dot is via quantum tunneling [22, 245].

This thesis covers all 3 lower-dimensional structures starting from spin dynamics in a 2D hall bar to using a 1D quantum point contact to detect the spin and charge states of 0D quantum dots. The sizes of 2D GaAs samples considered in this thesis are typically determined by the Hall bar, with L and W typically in the range of 10× - 100μm whilst D is around 10nm or less.

2.1.2 Length scales (scattering times)

In the Drude model the probability of an electron undergoing a collision which changes its momentum within time Δt is $\Delta t/\tau$. Thus the momentum relaxation length is $l = v_F\tau$, where v_F is the velocity of an electron at the Fermi energy. Scattering can be divided into two broad categories:

1. *Elastic scattering*: where energy and wavelength remain unaltered after the collision.

2. *Inelastic scattering*: where electron gains or loses energy during the collision.

Elastic scattering processes are predominantly due to Coulomb scattering from ionized impurities, whilst inelastic scattering processes stem from electron-electron or

electron-phonon interactions. The total scattering time τ_Σ can be expressed as

$$\frac{1}{\tau_\Sigma} = \frac{1}{\tau_e} + \frac{1}{\tau_{in}} \quad , \tag{2.1}$$

where τ_e and τ_{in} are the elastic and inelastic scattering times respectively.

In the 2DEG at low temperatures scattering is mostly elastic, i.e. $\tau_{in} \gg \tau_e$ and the length scales for elastic and inelastic scattering are:

$$\begin{aligned} l_e &= v_F \tau_e \\ l_{in} &= \sqrt{D\tau_{in}} \quad , \end{aligned} \tag{2.2}$$

where D is the diffusion constant. At low temperatures (T<10K) τ_e, is temperature independent and determined by the ionized impurity concentration. On the other hand as the temperature trends to zero, electron-electron and electron-phonon scattering rates also tend to zero i.e. $\tau_{in} \to \infty$. Thus $l = l_e$ and is temperature independent. Nominally obtaining τ from the measured mobility does *not* give the total scattering time $\tau_\sum$, rather it gives an upper limit, since τ is only affected by large angle scattering events which change the electron's momentum significantly. A more direct measure of $\tau_\sum$ comes from the Dingle time extracted from the rate at which the amplitude of Shubnikov-de Haas oscillations grow with magnetic field. This gives the quantum lifetime of an electron eigenstate in a Landau level [10, 49].

As an electron travels through a 2DEG, it may undergo several collisions and still retain sufficient phase memory that its coherence needs to be considered. The phase relaxation (coherence) length l_ϕ is the average distance an electron diffuses before its phase becomes uncorrelated with respect to its initial value. As phase is only randomized by inelastic collisions and for a 2DEG $\tau_{in} \gg \tau_e$, l_ϕ is related to the corresponding phase relaxation time τ_ϕ by $l_\phi = \sqrt{D\tau_\phi}$. Nominally in a 2DEG $l_\phi = l_{in}$ but sometimes l_ϕ may be larger than l_{in} as phase memory is not lost immediately after the collision if the change in energy is small.

These length scales can now be used to identify 3 main conduction regimes in metallic semiconductors of decreasing size L:

1. Diffusive regime ($L \gg l_\phi$): classical transport, similar to that of the free electron

gas model. Sometimes small corrections due to phase coherence within small regions of l_ϕ may be applied.

2. Quantum coherence regime ($l_\phi > L > l_\Sigma$): classical transport models break down due to quantum phase coherence and the device must be treated as a complex quantum mechanical system

3. Ballistic regime ($l_\Sigma > L$): the mean free path of an electron is longer than the sample length, so electrons move through the structure without scattering and can be modelled as a simpler quantum mechanical system. The coherence length can be simply written as $l_\phi = v_F \tau_\phi$.

If a magnetic field threads through the system, another length scale becomes important. This is shown by the effect of a perpendicular field upon the 2DEG, where in the classical picture, electrons (at the Fermi energy E_F) will tend to move in circular orbits of radius

$$r_c = \frac{m^* \nu_F}{eB_z} = \frac{\nu_F}{\omega_c} \ , \tag{2.3}$$

where $\omega_c = \frac{eB_z}{m^*}$ is the cyclotron frequency.

If the momentum relaxation length $l > r_c$ (i.e. $\omega_c \tau > 1 \equiv \mu B_z > 1$), the electron can complete one full cyclotron orbit without being scattered, thus entering the magnetic localization regime. A full quantum mechanical treatment results in an expression for the spatial extent of the electrons wavefunction in terms of the magnetic length

$$l_B = \sqrt{\frac{\hbar}{eB_z}} = \frac{25nm}{\sqrt{B(T)}} \ , \tag{2.4}$$

where a radius of l_B encloses one magnetic flux quantum h/e.

2.2 Electron transport in 2D

A 2D system sandwiched between a top-gate and a back-gate can be treated as a parallel plate capacitor, where applying a voltage to the gate electrode causes charges to spread over the entire gate layer, inducing an opposing charge across the other plate. This can be expressed as $Q = (n_{2D}e)A = C(V_g - V_T)$, where A is the surface

area of the 'plates', n_{2D} is the 2D electron density, e is the electronic charge and $V_g - V_T$ refers to the voltage difference between the gate and the 2DEG. $C = \frac{\epsilon_0 \epsilon_r}{d} A$ is the capacitance over the plate area, d is the distance between the gate and the well, $\epsilon_0 = 8.854 \times 10^{-12}\text{F.m}^{-1}$ is the permittivity of free space and $\epsilon_r = 13.2$ for GaAs. This voltage gradient can be controlled by the applied voltage to the gate electrode, where increasing the voltage causes the 2DEG well to become deeper and increases the number of bound states available for electrons to occupy.

2.2.1 2D density of states

The energy of a heterostructure is governed by the density of states (DOS) and the Fermi-Dirac distribution, where the density of states depends upon the number of dimensions in the system. The product of these gives the density of occupied states in the system, when summed across all available k states within a Fermi circle of radius k_F (i.e. the wave vector at the Fermi energy) [57]:

$$N = \int_{-\infty}^{\infty} N(E) f(E) dE \ . \tag{2.5}$$

The Fermi-Dirac distribution $f(E)$, determines the probability of an energy state being occupied at a given temperature. At $T = 0$K, the distribution is effectively a step function, where all energy states are populated between 0 and the Fermi Energy E_F (energy of the highest occupied state), such that $f(E) = 1$ within this region and zero elsewhere:

$$N(T = 0K) = \int_{-\infty}^{E_F} N(E) dE \ . \tag{2.6}$$

Since the 2D DOS is constant, i.e. it has the same number of available states for each energy level, so the density of states $n(E)$ per unit area A over the 2DEG, for an infinitesimal energy range dE can be written as [57]:

$$\frac{n(E)}{A} dE = \frac{m^*}{\pi \hbar^2} dE \ . \tag{2.7}$$

Where m^* is the effective mass and A corresponds to the surface area of the 2DEG. From this expression it can be seen that the number of states available remains constant with energy. To find the total density of charges at a given energy, we multiply the

DOS by the likelihood of occupation and sum over all available energies. For low temperatures close to 0K we can integrate the DOS up to the Fermi energy, to get the number of charges per unit area, and the expression for density becomes [57],

$$n_s = \frac{g_s m^*}{2\pi\hbar^2} E_F \tag{2.8}$$

where g_s refers to the spin degeneracy of the electron and at zero field $g_s = 2$.

The corresponding Fermi wavevector and wavelengths are given as

$$k_F = \frac{\sqrt{2m^* E_F}}{\hbar} = \sqrt{2\pi n_s} \tag{2.9}$$

$$\lambda_F = \frac{2\pi}{k_F} = \sqrt{\frac{2\pi}{n_s}} \tag{2.10}$$

Using the model of a parallel plate capacitance, we can infer that when we apply a voltage across a uniform gate to increase the electron density, the Fermi level in the 2D system will also increase linearly.

2.2.2 Transport in a magnetic field

We now turn our attention to the effects of a magnetic field upon the transport properties of electrons in a 2D system.

Zero field transport

From the Drude model we can express conductivity as $\sigma = n_s e\mu$. Relating conductivity to the properties of the sample using the Einstein relation in the degenerate limit, $\mu = \frac{eD}{n_s}\frac{\partial n_s}{\partial E}$, in a 2DEG the conductivity becomes

$$\sigma = e^2 D \frac{\partial n_s}{\partial E} = e^2 D N_{2D} \ . \tag{2.11}$$

The 2D diffusion constant D in terms of the Fermi velocity v_F and the mean free path l is given by

$$D = \frac{1}{2} v_F^2 \tau = \frac{1}{2} v_F l \ . \tag{2.12}$$

In 2D ballistic transport however, it is the conductance g (or resistivity ρ) rather than the conductivity σ (and resistance R) which plays a key role in transport, as sample resistance is independent of its shape and size. Resistance in units of Ω are

related to the sample's length L and width W via a dimensionless quantity $R = \rho\frac{L}{W}$. Hence the units of resistivity ($\Omega/\square$) are given in terms of the number of squares covered by the 2D region and conductance in terms of the conductance quantum $2e^2/h$.

Low field transport ($\mathbf{B} < 0.1\mathbf{T}$)

In the semi-classical picture at low fields, the Hall voltage cancels out the average Lorentz force on the electrons and longitudinal magnetoresistance is negligible. However, there are 2 corrections necessary to this picture:

- Electron-electron interactions: In the free electron model these tend to be ignored and if there is no disorder present, no corrections are required. However if a small disorder potential is present, this resulting correction is a small positive magnetoresistance [155].

- Weak localisation (quantum interference): If the phase coherence length is larger than the mean free path $l_\phi \gg l$ it is possible for the path of scattered electrons to form a phase coherent loop. A zero field enhancement of backscattering occurs due to constructive interference of the time reversed paths at the entry point of the loop. A magnetic field introduces a phase shift between the two paths around the loop, shifting the point of constructive interference around the loop. Averaging over many of these loops in low fields results in a reduced backscattering probability due to the presence of the field [4, 151].

In a typical 2DEG the dominant effect is weak localization, resulting in an overall negative magnetoresistance at low fields. However in some instances, such as parallel conducting planes or two hole bands with different effective masses within a 2DHG, a positive magnetoresistance may be observed [99, 190]. In this thesis, such low field effects can be used to help tune the operating point of our samples, which we discuss in Section 2.6.3.

Higher field transport (B>0.1T)

As mentioned briefly, the classical effect of a magnetic field applied perpendicular B_z to the plane of the 2DEG causes charge carriers to move in circles. At low fields, these charge carriers scatter before completing one cyclotron orbit, resulting in diffusive transport. In the case of higher B fields, the magnetic length is reduced and carriers are able to complete an orbit without scattering, changing the nature of their transport dramatically.

Effect of the magnetic field upon the density of states

The motion of both electron and hole states in the presence of a magnetic field perpendicular B_z to the 2DEG plane, differ for those of an in-plane field $B_{\|}$ - electrons move in curved trajectories within the plane, normal to B_z, induced by the Lorentz force. As mentioned earlier, the magnetic length scale becomes important. To understand the quantum mechanical behaviour of such a situation, we start with the Schrödinger equation with momentum,

$$\hat{\boldsymbol{p}} = -i\hbar\nabla - e\boldsymbol{A} \ . \tag{2.13}$$

To understand the quantum mechanical behaviour, we can represent the influence of the magnetic with the Hamiltonian (neglecting the Zeeman term)

$$\mathcal{H} = \frac{1}{2m^*}(\boldsymbol{p} - e\boldsymbol{A})^2 \ , \tag{2.14}$$

where $\boldsymbol{A}$ is the magnetic vector potential. For a perpendicular field $\boldsymbol{B} = \nabla \wedge A = (0, 0, B)$ there are 2 common gauge choices for $\boldsymbol{A}$: the symmetric gauge $2\boldsymbol{A} = B(-y, x, 0)$ and the Landau gauge $\boldsymbol{A} = (0, B_x, 0)$. Although the Schrödinger equation wavefunctions depend upon the gauge choice, the physical observables remain gauge invariant.

Using the Landau gauge, if we assume a plane wave moving in the y-direction, the Schrödinger equation is reduced to [57]:

$$\left[-\frac{\hbar^2}{2m^*}\frac{d^2}{dx^2} + \frac{1}{2}m^*\omega_c^2\left(x + \frac{\hbar k_y}{eB}\right)^2\right]\psi(x) = \varepsilon\psi(x) \ . \tag{2.15}$$

Where the plane wave cancels out on both sides leaving an equation in x only. This describes the motion of the particle inside a parabolic potential proportional

to cyclotron frequency squared, perpendicular to the direction of momentum y and centered around the point $x_0 = \frac{\hbar k_y}{eB}$. Since the Schrödinger equation is in the form of a 1D harmonic oscillator, its solution yields energies of the form:

$$E_n = (n + \frac{1}{2})\hbar\omega_c \ . \tag{2.16}$$

Only certain energy levels are allowed to exist for $n = (0, 1, 2, ...)$. representing these discrete cyclotron orbits and are called Landau levels. In the presence of a perpendicular field, each Landau level separates into its two spin components, corresponding to two peaks in the SdH oscillations which become more pronounced at larger fields. Each energy level can be described as follows, where n is the Landau level index and g^* the effective Landé g factor,

$$E_n = \hbar\omega_c(n + \frac{1}{2}) + \frac{g^*}{2}\mu_B B_z \sigma_z \ . \tag{2.17}$$

Here energy states of the solution are dependent upon n rather than k, meaning that states with the same n but different k are degenerate. This effectively collapses the 2D DOS to a series of delta functions at these energies, separated by an amount proportional to B as illustrated in Fig. 2.1b. In a non-ideal system, these delta functions broaden into peaks whose widths increase with temperature and the amount of scattering shown in Fig. 2.1c. Landau levels are best observed at low temperatures, $k_B T \ll \hbar\omega_c$. Moreover, the number of states within each level n, increases with increasing B, although the radius of these semi-classical cyclotron orbit decreases.

Fig. 2.2 plots energy over magnetic field, illustrating the effect of these Landau levels upon the Fermi energy. As the field is increased, the Landau levels spread out and successively cross through the Fermi energy E_F. In order to conserve charge, both the Fermi energy and the DOS oscillate with B_z. Each of the diagonal lines in E_F marks the region where a Landau level is being depopulated. E_F tracks the Landau level to minimize the total energy, until it is empty and becomes more energetically favourable to drop to the next lowest Landau level (indicated by a dashed vertical line). At higher fields, the levels are further spread apart in energy, hence the oscillation takes on a greater change in amplitude. In the case of electrons, the spread of Landau level

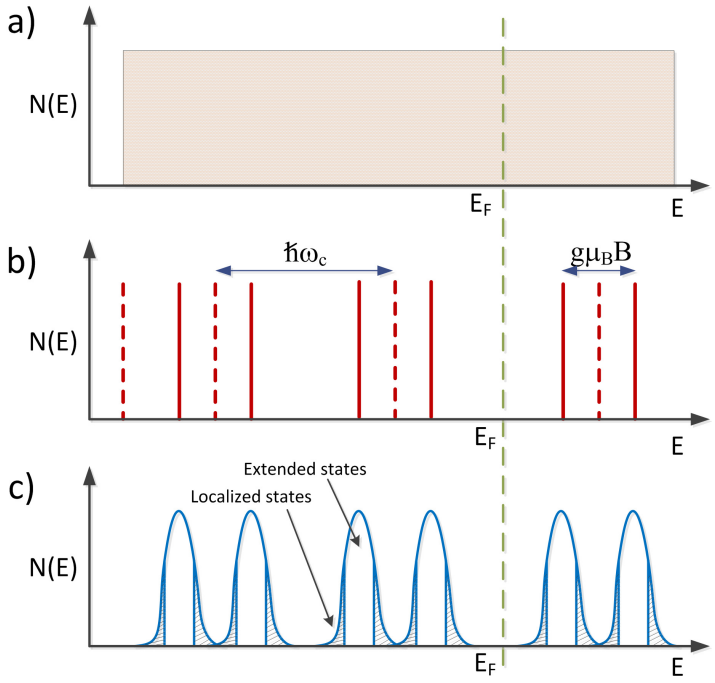

Figure 2.1: Schematic showing the effect of a magnetic field upon the 2D DOS. (a) At zero field, the DOS remainst constant. (b) In the presence of a perpendicular field, the DOS splits into a series of discrete Landau levels (assuming no disorder). The dashed lines mark the positions of these levels without spin splitting, separated by $\hbar\omega_c$. (c) In a real system disorder is present which broadens the levels and creates localized states along the band edges. Figures modified from Ref. [57].

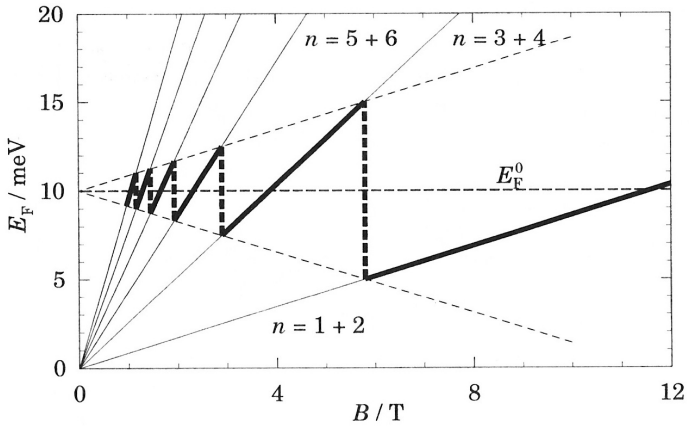

Figure 2.2: Changing Fermi energy level (thick black line) as a function of perpendicular magnetic foeld in a 2DEG. Initial value of $E_F = 10$meV at zero field. Thin fan of lines indicates the Landau levels. Reproduced from Ref. [57].

energies is linear in B and cross E_F periodically in $1/B$, where the number of occupied Landau levels below the Fermi level is given by the filling factor $\nu \approx \frac{E_F}{\hbar\omega_c}$.

These oscillations in the DOS set up Shubnikov-de Haas (SdH) oscillations in the longitudinal resistivity ρ_{xx} of a 2D system as a function of magnetic field. When the Fermi energy lies in between two Landau levels, the DOS at that point drops to zero, hence the conductance at E_F follows suit, dropping to zero. If the Fermi energy is aligned with one of the DOS peaks, the longitudinal conductivity will correspondingly reach a maxima. Since the Landau levels cross the Fermi energy periodically in $1/B$, the SdH oscillation period is also periodic in $1/B$, and increases linearly with density:

$$n_{2D} = \frac{2e}{h}\frac{\delta n}{\delta(1/B_n)} \ . \tag{2.18}$$

Here δn is the difference between two adjacent levels and $\delta(1/B_n)$ corresponds to the spacing in inverse B between the two peaks, n. Since this periodicity of the SdH oscillations in B is known, this relation allows us to calculate the density of a 2D system from the frequency of the SdH oscillations. Another method to calculate density is to take the Fourier transform of the SdH traces.

Just as the longitudinal resistance oscillates with the DOS, so does the transverse resistance R_{xy}. The classical Hall Effect works when charge carriers move through a conductor in the presence of a perpendicular magnetic field, they experience a force

perpendicular to both the direction of current and the magnetic field. The Lorentz forces cause the charges to curve and accumulate on one side, resulting in a voltage drop across the width of the conductor, known as the Hall Voltage V_H.

Classical theory predicts that $V_H = -\frac{IB}{ne}$ increases linearly with increasing field, whilst the longitudinal voltage $V_L = IR = \text{const.}$ remains constant. But in a confined 2D quantum device, both the Hall voltage and longitudinal voltage oscillate, in phenomena known as the integer quantum Hall effect and SdH respectively, the latter first predicted by Ando *et al.* [9].

From the integer quantum Hall effect, plateaus occur when the Fermi energy lies in between two Landau levels and the DOS at that point drops to zero, which also corresponds to a minima in the SdH. Similarly, the greatest slope in the Hall voltage is seen when the DOS peaks at each Landau level, as does the SdH. Hence another method to determine the density of the 2D system is by taking the slope of the Hall voltage trace and multiplying it by a quantum of conductance $\frac{e^2}{h}$, resulting in a density relation $n_{2D} = \frac{h}{e^2}\frac{1}{R_{xy}}$ From this it can be inferred that the number of occupied levels below E_F indicated by the filling factor is $\nu = \frac{hn_{2D}}{eB}$.

These concepts are crucial to this thesis. In subsequent chapters we shall perform magnetotransport studies in 2D samples, using the Hall effect to align and calibrate the sample as it is tilted in a magnetic field. Moreover 2D heterostructures provide a convenient platform from which lower-dimensional structures can be fabricated and studied.

2.3 Electron transport in 1D: QPCs and wires

A one-dimensional (1D) system can be formed within a 2DEG by lateral confinement to a narrow channel using a number of techniques. One example involves using electron beam lithography to etch a narrow channel into the surface of a $p+$ GaAs cap layer, which induces electrons at the 2DEG. The base 2D Hall bar structure shown in Fig. 2.3 is created by optical lithography [53] and aligned along the direction which corresponds to the highest mobility axis of the crystal structure. The 1D quantum point contact (QPC) is formed by dividing the $p+$ layer into 3 separate, independently biasable

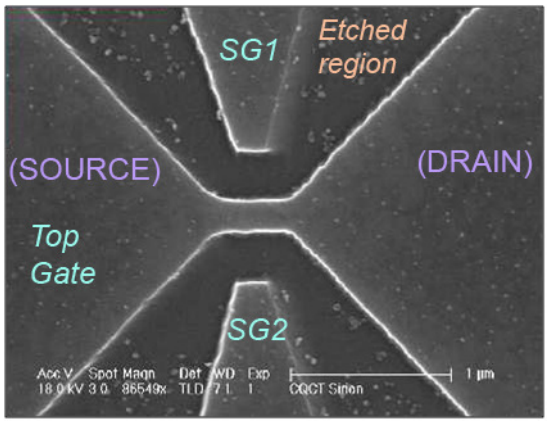

Figure 2.3: Microgram of a split gate design Reproduced from Ref. [53, 138]. Etched dark regions divide the cap into 3 gates; Top Gate, Side Gate 1 and Side Gate 2. The top gate narrows into a 1D channel in the middel region, on which either side are the source and drain areas of the 2DEG.

gates.

This standard 'split gate' configuration was first developed in GaAs by Thornton *et al.* [261], in a modulation doped heterostructure, to define a 1D channel in a 2D electron gas, where ohmic contact to the 2D regions allow them to act as a 'source' and a 'drain' on either end of the wire. The width of the 1D channel can be controlled electrostatically by applying a voltage over the two side gates [53, 138]. To reduce the amount of scattering experienced by charge carriers moving through the wire, the length of the split gates and the 1D channel L is reduced until it is smaller than the mean free path of the carriers and ballistic transport is achieved [142, 277].

If the junctions between the 1D and 2DEG regions are smooth enough, the electron eigenstates entering the channel will evolve adiabatically from $2D \rightarrow 1D$ as a travelling wave. For N occupied subbands in a 1D channel (assuming no scattering), the total conductance can be expressed as

$$G = \frac{I}{V_{SD}} = \frac{2e^2}{h} N \quad . \tag{2.19}$$

The phenomena of conductance quantization was first discovered by van Wees *et al.* [272] and Wharam *et al.* [277]. Assuming globally adiabatic transmission, the 1D confinement can be modelled as a saddle point potential [34, 179] and tuned using the side gates. In this model, transverse 1D subbands are generated in the 1D constriction

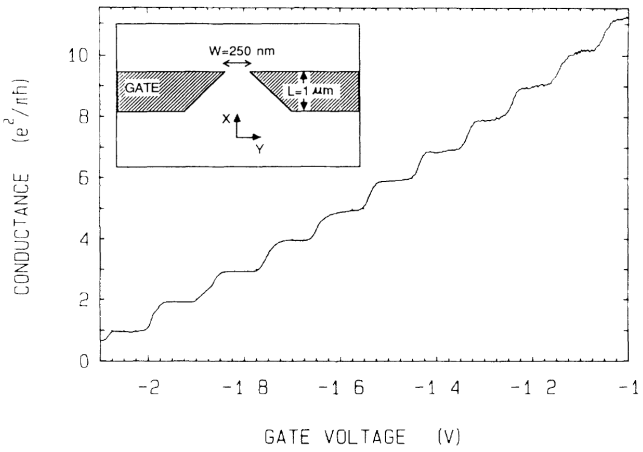

Figure 2.4: Plot of conductance through a quantum point contact (dimensions in insert) as a function of side gate voltage, exhibiting distinct steps in units of the conductance quantum. Reproduced from Ref. [272].

as current passes through the constriction. Increasing the bias between the split gates constricts the channel, squeezing the (parabolic) confining potential and raising the saddle point up in energy. This allows one to tune the 1D subbands through the Fermi energy of the 2D reservoir, until only the lowest subband $n = 1$ is occupied, at which the channel has reached the 1D limit. Increasing the split gate bias further raises the $n = 1$ subband above the 2D Fermi energy and the channel becomes completely depopulated, also known as the 'pinch-off' point. This results in a staircase-like trace shown in Fig. 2.4, where each additional subband sequentially contributes to the current.

The phenomena of conductance quantization has allowed experimentalists to perform spectroscopic transport measurements to study the behaviour of the individual energy levels and map out their g factors along different crystal axes [178, 192, 250]. More recently it has been shown that 1D channels also behave as ultra-sensitive charge detectors, and have been used to independently count the number of charges passing through a nearby low-dimensional structure such as a quantum dot [76]. In this thesis we shall use QPCs as charge sensors to study induced few-hole quantum dots.

2.4 Electron transport in 0D: Quantum dots

A quantum 'box' (or 'dot') is created within a 2DEG by laterally confining it in both x- and y-directions, so all edges of the box are smaller than L_D. If the size of the quantum dot is comparable to the Fermi wavelength of the electrons occupying it, the system exhibits discrete, bound eigenstates which are zero-dimensional (0D), similar to those seen in naturally occurring atoms. As a result quantum dots are sometimes referred to as "artificial atoms" [16, 133].

These small, confined islands of charge are capacitively coupled to one or more gates, which can be used to tune the electrostatic potential of the dot with respect to its reservoirs and hence change the number of electrons (occupancy) on the island, depicted in Fig. 2.5. Transport of charge between the dot and its source and drain reservoirs can only occur via tunnelling, where the entry and exit tunnel barriers can be formed and controlled by a pair of quantum point contacts [137, 175, 238].

2.4.1 The constant interaction model

Following from the generalization of charging theory for metallic systems in 0D [17, 20, 183], the constant interaction (CI) model provides a simple picture describing how electrons in a dot interact with each other and with their reservoirs. The model is based upon 2 assumptions: (1) Coulomb interactions amongst electrons and those in the surrounding environment can be parameterized by a single constant capacitance C_Σ, which is the sum of capacitances between the dot and the source C_S, drain C_D and gate C_G, i.e. $C_\Sigma = C_S + C_D + C_G$. (2) The single-particle energy (ΔE) level spectrum is independent of these Coulombic interactions and hence independent of the number of electrons on the dot. A schematic representation of a lateral quantum dot is given in Fig. 2.5a, and its equivalent circuit diagram in (b). For more details on the constant interaction model refer to reviews [101, 150].

Based upon the two main assumptions of the CI model, the total energy of a dot $U(N)$ possessing N electrons in the ground state can be expressed as

$$U(N) = \sum_{n=1}^{N} E_n + \frac{[-|e|(N - N_0) + C_S V_S + C_D V_D + \Sigma C_g V_g]^2}{2C} \,. \tag{2.20}$$

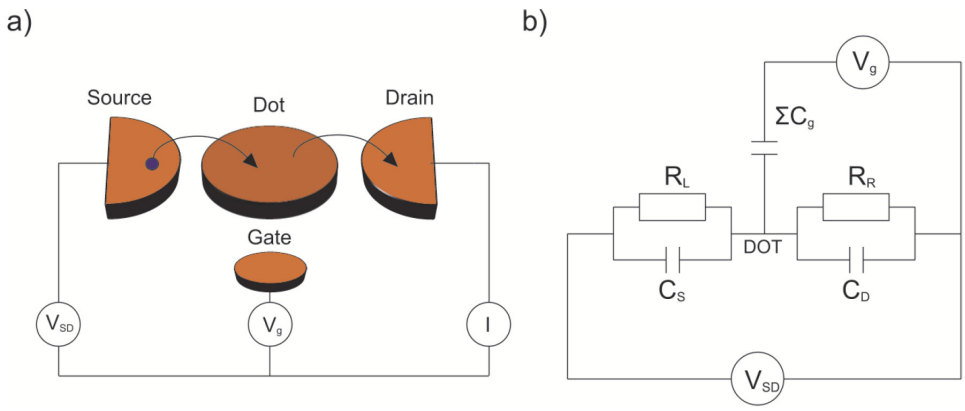

Figure 2.5: Schematic picture of a lateral quantum dot. (a) Depicts tunneling of a charge particle from the source reservoir onto the island and off into the drain reservoir. (b) Equivalent circuit diagram showing the capacitive coupling between the reservoirs and the dot as well as the metallic gates to the dot. Adapted from [101, 237].

The first term is a discrete sum over all occupied single-particle energy levels E_n. In the second term, e is the electronic charge, $N - N_0$ is the number of electrons, where N_0 corresponds to the dot's state at zero gate bias. The remaining terms $C_S V_S$, $C_D V_D$ and $C_g V_g$ can be continuously varied and represent an effective induced charge that changes the electrostatic potential defining the dot [101].

From this, we can derive the ground state electrochemical potential energy of the dot $\mu(N)$, i.e. the minimum energy needed to add the Nth electron to the dot as

$$\begin{aligned} \mu(N) &\equiv U(N) - U(N-1) \\ &= \left(N - N_0 - \frac{1}{2}\right) E_c - \frac{E_c}{|e|}(C_S V_S + C_D V_D + \Sigma C_g V_g) + E_n \ , \end{aligned} \tag{2.21}$$

where $E_c = e^2/C$ is the charging energy and the first 2 terms constitute the electrostatic part, whilst the last term is the 'chemical part' [101]. More specifically, $\mu(N)$ denotes the transition between the N-electron ground state $GS(N)$ and the $(N-1)$-electron ground state $GS(N-1)$. The electrochemical potential is linearly dependent upon the gate voltage, whilst energy has a quadratic dependence. This dependence is the same for all N, thus enabling the whole 'ladder' of electrochemical potentials to be shifted whilst keeping the distance between levels constant [101].

The difference in the electrochemical potentials of transitions between successive

ground states is referred to as the 'addition energy' E_{add}

$$\begin{aligned} E_{add} &\equiv \mu(N+1) - \mu(N) \\ &= U(N+1) - 2U(N) + U(N-1) \\ &= E_c + E_{N+1} - E_N \\ &= e^2/C + \Delta E \quad . \end{aligned} \tag{2.22}$$

The addition energy consists of a purely electrostatic part (the charging energy E_c) plus the single particle energy level spacing ΔE between two discrete quantum levels. The single particle level spacing can be approximated as

$$\Delta E \cong \frac{2\pi\hbar^2}{m^* A} \, , \tag{2.23}$$

where m^* is the effective mass, A the dot area. In the case of a large quantum dot, $\Delta E \to 0$ and so $E_{add} \cong e^2/C_\Sigma$.

2.4.2 Single electron transport and Coulomb blockade

Electron tunnelling relies upon the alignment of the dot's electrochemical potentials with respect to those of the source μ_S and the drain μ_D. By applying a bias voltage between the source and drain reservoirs $V_{SD} = V_S - V_D$, an energy window of $\mu_S - \mu_D = -|e|V_{SD}$ is opened, known as the 'bias window'. From the perspective inside the bias window, electron states in one reservoir μ_S appear full, whilst the other μ_D appears empty. So when an appropriate dot electrochemical potential level falls within this bias window $\mu_S \geqslant \mu(N) \geqslant \mu_D$, electrons can tunnel from one reservoir, onto the dot and off into the empty states of the other reservoir, as illustrated in Fig. 2.6b. If no electrochemical potential falls within the window, tunneling cannot occur and no current flows. This condition is known as Coulomb blockade and is depicted in Fig. 2.6a.

If the temperature is negligible compared to the energy-level spacing $\Delta E \gg k_B T$, the size of the bias window creates 2 different transport regimes; the low bias regime and the high bias regime.

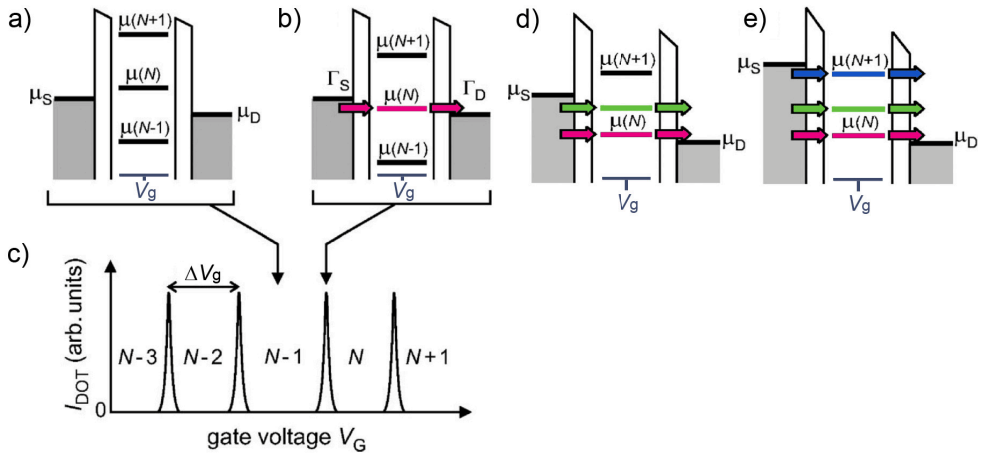

Figure 2.6: Schematic of electron transport in different quantum dot biasing regimes. (a,b) Show the low-bias regime - the bias window set by μ_S and μ_D is large enough to accommodate only a single dot level. In (a) no dot level falls within the source-drain bias window and transport is blockaded. The occupancy of the dot is fixed at $N-1$. In (b) one dot level $\mu(N)$ falls within the bias window, the occupancy of the dot alternates between N and $N+1$ and single-electron transport occurs. The magnitude of the current is dependent upon the tunnel rate between the dot and the source Γ_S as well as the dot and drain Γ_D. (c) Schematic plot of dot current as a function of gate voltage, showing the alignment of scenarios (a) and (b). Panels (d,e) illustrate the electrochemical potentials of the dot in the high-bias regime, where transport through an excited state is marked in green. In (d) $V_{SD} > \Delta E$ and electrons can tunnel through 2 dot levels. In (e) $V_{SD} > E_{add}$ for N electrons, and we enter the regime of double-electron tunneling. Figures reproduced from [101].

Low-bias regime ($-|e|V_{SD} < \Delta E, E_{add}$)

This regime is similar to the situation described previously, where only one dot level falls within the bias window at most. This results in single-electron tunneling, from the source to the dot (increasing the number of electrons on the dot from N to $N+1$) and out to the drain (after which another electron is free to tunnel onto the dot) as per Fig. 2.6b. In this transition the number of electrons on the dot oscillates between N and $N+1$ and the magnitude of the current is determined by the tunnelling rates through the source Γ_S and drain Γ_D, which are limited by the thickness of the barriers.

As gate voltage is swept, and current through the dot (I_{dot}) measured, a series of peaks are obtained known as Coulomb blockade oscillations, shown in Fig. 2.6c. At a peak position, a dot level corresponding to transport between 2 ground states falls within the bias window and single-electron tunneling current flows. In between peaks, the number of electrons on the dot remains fixed as current is blockaded. By tuning the gate voltage V_g, the occupancy of the dot can be precisely controlled. The capacitance ratio of the gate to the dot known as the 'leverarm' $\alpha = C_g/C_\Sigma$ can be extracted from the distance between adjacent Coulomb blockade peaks

$$\Delta V_g = \left(\frac{1}{e}\right)\frac{C_\Sigma}{C_g}\left\{\Delta E + \frac{e^2}{C_\Sigma}\right\} \quad . \tag{2.24}$$

There are 2 main conditions required to observe Coulomb blockade. Firstly the number of electrons in the dot must be well defined, implying that the energy uncertainty of an electron due to its dwell time on the dot should be smaller than the charging energy ($\Delta_{dot} \ll E_c$). Secondly, the thermal distribution of charges near the Fermi level in the leads must be much smaller than the charging energy (i.e. $k_B T \ll E_c$).

High-bias regime ($-|e|V_{SD} \geqslant \Delta E$ and/or E_{add})

Bias window is large enough to allow multiple dot levels to participate in electron tunneling. For example, if V_{SD} is increased so that an excited state (ES) transition falls within the bias window, there are two paths available for electrons to tunnel through the dot Fig. 2.6d. How the current changes depends upon the tunnel coupling of the 2 levels involved. Increasing V_{SD} even further such that the bias window is

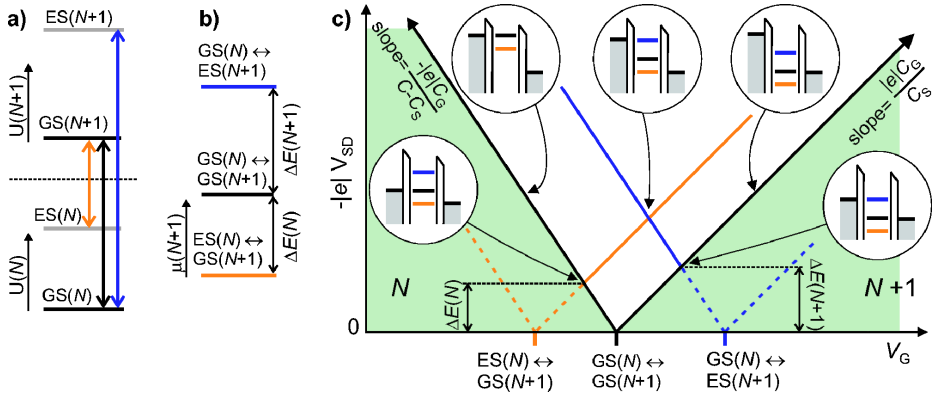

Figure 2.7: Schematic representation of a high-bias measurement. (a) Energy levels for N electrons $U(N)$ and N+1 electrons $U(N+1)$, where possible transitions of GS and ES are indicated using arrows. (b) Corresponding electrochemical potential ladder for the transitions given in (a). (c) Schematic map of differential conductance dI_{dot}/dV_{SD} over source drain bias versus gate voltage, for the transitions between occupancies $N \leftrightarrow (N+1)$. The alignment of the chemical potentials of the source, drain and dot levels for different configurations of V_{SD} and V_g are given. Figures adapted from [101].

larger than the addition energy, allows the occupancy of the dot to alternate between $N-1$, N and $N+1$, leading to a double-electron tunneling current shown in Fig. 2.6e.

Fig. 2.7a,b maps out the transitions between two successive ground states $GS(N)$ and $GS(N+1)$, and excited states $ES(N)$ and $ES(N+1)$ to energy, which are separated from the GSs by $\Delta E(N)$ and $\Delta E(N+1)$ respectively. These transitions include the ground state transitions $GS(N) \leftrightarrow GS(N+1)$, and 2 excited state transitions $GS(N) \leftrightarrow ES(N+1)$ and $GS(N+1) \leftrightarrow ES(N)$, where the transition between $ES(N) \leftrightarrow GS(N+1)$, is lower in energy than the transition between the 2 ground states. In this figure we leave out the excited state transitions for simplicity.

Such behaviour allows us to perform source-drain bias spectroscopy measurements to map out and study the individual energy levels of the quantum dot. A plot of differential conductance dI_{dot}/dV_{SD} as a function of V_{SD} and V_G, shows a splitting of the ground state for $V_{SD} \neq 0$ (solid black lines forming a 'V' shape), shown in Fig. 2.7c. If the drain is grounded i.e. $V_D = 0V$, as V_{SD} is varied, only the source potential changes and the two slopes can be described as $-eC_g/(C_\Sigma - C_S)$ and C_g/C_S. For the positive slope of the black line, μ_{dot} is fixed at the dot level corresponding to transition $GS(N) \leftrightarrow GS(N+1)$ is aligned with the drain electrochemical potential

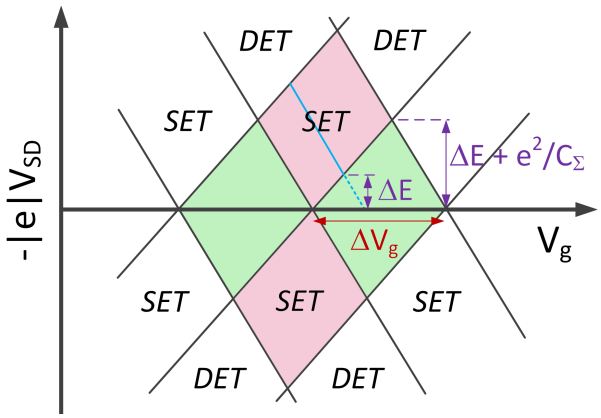

Figure 2.8: Source drain bias spectroscopy schematic showing Coulomb diamonds in green. The pink regions correspond to regions of single-electron tunneling (SET) and further out, regions of double-electron tunneling (DET) are also indicated. The addition energy $E_{add} = \Delta E + e^2/C_\Sigma$ can be extracted from half the diamond height, whilst the single particle level spacing ΔE comes from the distance between the V_g axis and the intersection of the ES line (blue) with the GS diamond edge.

μ_D lead as the source electrochemical potential μ_S increases in energy. Conversely, following the negative sloped black line, the same GS transition is aligned with the source lead and changes in energy together with the source lead.

The intersection between the blue ES and black GS lines marks point where the dot level $ES(N{+}1)$ aligns with the source lead allowing transition $ES(N{+}1) \leftrightarrow GS(N)$ to occur. Likewise, at the corresponding section between the orange and black line $ES(N)$ aligns with the drain lead and the transition between $ES(N) \leftrightarrow GS(N{+}1)$ is allowed.

In Fig. 2.8 the ground states which split as a 'V'-shape are extended to form a series of diamond-like fully blockaded regions in dI_{dot}/dV_{SD} in the V_{SD} vs V_g map. The orange regions indicate where single electron tunneling occur in the higher-bias regime. The addition energy $E_{add} = \Delta E + e^2/C_\Sigma$ can be extracted from half the diamond height and the single particle level spacing ΔE from the vertical separation between the V_g axis and the intersection of the ES line to the diamond GS edge. The gate coupling factor can also be calculated from $\alpha = E_{add}/V_g$.

Such transport measurements in the different bias regimes can be used to map out the energy spectra of a quantum dot. These techniques will be employed later in this

thesis to characterize induced quantum dots.

2.5 Electronic band structure of GaAs

We shall now turn our attention to the band structure of GaAs with a focus upon the unique, complex properties of holes in valence band. We shall highlight the effects of spin-orbit coupling in holes travelling through the lattice and briefly touch upon the role crystal symmetry plays in the spin response of these holes to the presence of an external magnetic field.

2.5.1 GaAs bulk 3D valence band structure

One way to understand the electronic band structure of bulk (3D) semiconductors, is to use the $\boldsymbol{k} \cdot \boldsymbol{p}$ method [131, 284] which can be derived from the Schrödinger equation for a Bloch function, with a periodic crystal lattice potential $V_0(\boldsymbol{r})$, to describe interactions of the charge carrier as it moves through the lattice. The Schrödinger equation for an electron in state n, with wave function $\psi_{n,k}$ can be expressed as

$$\left\{ \frac{p^2}{2m_0} + V_0(\boldsymbol{r}) \right\} \psi_{n,k} = E_n(\boldsymbol{k}) \psi_{n,k} \tag{2.25}$$

where the wave vector $\boldsymbol{k}$ lies within the first Brillouin zone such that $|k| \ll 2\pi/a$, where a is the lattice constant, $\boldsymbol{p} = -i\hbar\nabla$ the momentum operator and m_0 the free electron mass. In Bloch notation the wavefunction is

$$\psi_{n,k} = e^{i\boldsymbol{k}\cdot\boldsymbol{r}} u_{n,k}(\boldsymbol{r}) \tag{2.26}$$

such that $e^{i\boldsymbol{k}\cdot\boldsymbol{r}}$ is the plane wave and $u_{n,k}(\boldsymbol{r})$ has the periodicity of $V_0(\boldsymbol{r})$. Substituting this back into Eq. 2.25, we get the Schrödinger equation for the periodic function $u_{n,k}(\boldsymbol{r})$:

$$\left\{ \frac{p^2}{2m_0} + V_0(\boldsymbol{r}) + \frac{\hbar^2 k^2}{2m_0} + \frac{\hbar}{m_0} \boldsymbol{k} \cdot \boldsymbol{p} \right\} \psi_{n,k} = E_n(\boldsymbol{k}) \psi_{n,k} \tag{2.27}$$

A popular method to describe charge carriers travelling through a crystal lattice in the presence of electric and magnetic fields that vary slowly over the length scale of the lattice constant, is to generalize $\boldsymbol{k} \cdot \boldsymbol{p}$ theory in terms of the envelope function

approximation (EFA). These fields can be internal or externally applied via metallic gates or external magnets. To accommodate these, the Schrödinger equation [from Eq. 2.25] can be extended to

$$\left\{\frac{(-i\hbar\nabla + e\boldsymbol{A})^2}{2m_0} + V_0(\boldsymbol{r}) + V(\boldsymbol{r}) + \frac{g_0}{2}\mu_B\boldsymbol{\sigma}\cdot\boldsymbol{B}\right\}\psi_{n,k}(\boldsymbol{r}) = E_n(\boldsymbol{k})\psi_{n,k} \tag{2.28}$$

On top of the original crystal lattice potential $V_0(\boldsymbol{r})$, there is an additional slowly changing potential $V(\boldsymbol{r})$ plus a vector potential $\boldsymbol{A}$=$\boldsymbol{A(r)}$ which gives rise to a magnetic field $\boldsymbol{B} = \nabla\times\boldsymbol{A}$. $\mu_B = \frac{e\hbar}{2m_0}$ is the Bohr magneton and g_0 is the g factor for a free electron. In second-order Löwdin pertubation theory, using the simplest description of non-degenerate, isotopic, parabolic energy bands, gives rise to an effective-mass Hamiltonian (without SO interaction, but with spin) [284]:

$$\mathcal{H} = \frac{(-i\hbar\nabla + e\boldsymbol{A})^2}{2m_0} + V(\boldsymbol{r}) + \frac{g_0}{2}\mu_B\boldsymbol{\sigma}\cdot\boldsymbol{B} \tag{2.29}$$

Electrons in the nth energy band are treated like free particles possessing an effective mass m^* and an effective g factor g^*, moving within an external potential $V(\boldsymbol{r})$. However the simple effective-mass approximation (EMA) cannot account for the complexities of holes in the valence band.

For most applications of the $\boldsymbol{k}\cdot\boldsymbol{p}$ method, we are interested only in a few adjacent bands, where we want the $E_n(\boldsymbol{k})$ dispersion relations close to the vincinity of the $\boldsymbol{k} = \boldsymbol{k_0}$ expansion point, and all remote bands are considered via Löwdin pertubation theory. By using a matrix of eigenfunctions at the Γ point $\boldsymbol{k_0} = 0$, Kane extended the $\boldsymbol{k}\cdot\boldsymbol{p}$ method to solve the Schrödinger equation, where the accuracy of the calculations is limited by the number of energy bands considered. Models such as the 4×4 Luttinger Hamiltonian [173] provide an adequate description close to the $\boldsymbol{k} = 0$ band edge (which is adequate for most low temperature transport measurements). For a more accurate treatment at finite $\boldsymbol{k}$, the 'extended Kane model' can be employed, which uses higher order matrices for greater accuracy. The resulting dispersion curves for GaAs obtained by using a 24×24 matrix are depicted in Fig. 2.9.

Despite being at the Γ point, the valence (Γ_8, Γ_7) bands exhibit more complex behaviour than the conduction (Γ_6) bands. This is due to the phenomenon of spin-orbit (SO) coupling. Charge carriers in semiconductors possess an intrinsic spin angular

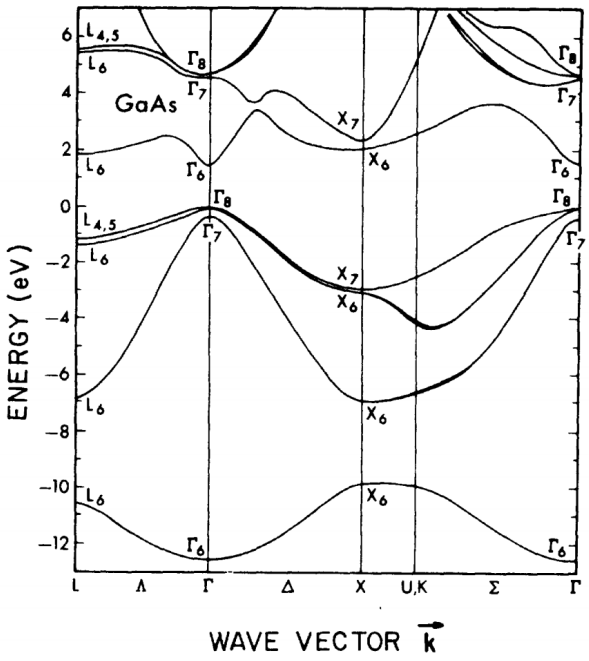

Figure 2.9: 24×24 $\boldsymbol{k} \cdot \boldsymbol{p}$ calculation of the GaAs dispersion relation, plotted as a function of wavevector where $\boldsymbol{k} = 0$ at the Γ point. Image reproduced from Ref. [37].

momentum, which interacts with the electrostatic potential from atoms in the crystal lattice. Spin-orbit can be introduced into the Hamiltonian via a nonrelativistic approximation to the Dirac equation [284], resulting in the Pauli SO term [131]

$$\mathcal{H}_{SO} = \frac{\hbar}{4m_0^2c^2} \left[\nabla V_0 \times \boldsymbol{p}\right] \cdot \boldsymbol{\sigma} \tag{2.30}$$

where $\hbar$ is Planck's constant, m_0 is the mass of a free electron, c is the speed of light, $\boldsymbol{p}$ is the momentum operator, V_0 is the Coulomb potential of the atomic cores and $\boldsymbol{\sigma} = (\sigma_x, \sigma_y, \sigma_z)$ is a vector of the Pauli spin matrices.

A schematic band diagram for bulk GaAs zinc blende semiconductor with a direct band gap of $E_g = 1.52$eV is illustrated in Fig. 2.10a, which assumes parabolic bands close to $\boldsymbol{k} = 0$ for simplicity. At the Γ point, the Bloch wavefunctions of the valence band edge (defined to be at $E = 0$), have the same symmetry properties under T_d group operations as $p-$like atomic orbitals, and are six-fold degenerate at $\boldsymbol{k} = 0$. On the other hand, the conduction band edge is $s-$like in nature with a two-fold degeneracy. When spin-orbit is introduced (in Fig. 2.10b), the conduction band states simply split into spin $s = \pm 1/2$. Since their orbital angular momentum $l = 0$, there

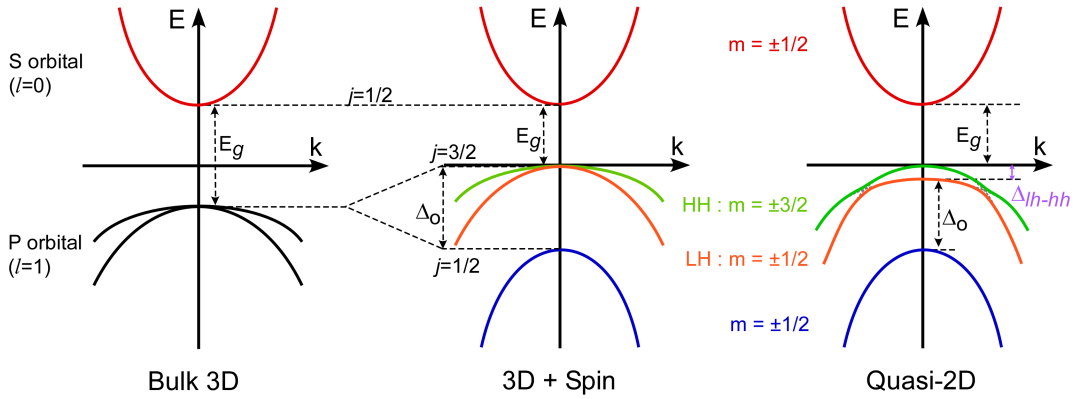

Figure 2.10: Schematic parabolic dispersions of GaAs showing the effect of reduced dimensionality for (a) Bulk 3D without spin, (b) 3D with spin-orbit interaction, (c) 2D with spin-orbit.

is no direct SO coupling to the spin states and SO interaction can only take place via the valence band [154]. This leads to a weak SO interaction for electrons in large band gap materials like Si, GaAs and stronger SO for narrow band gap materials like InGaAs [178]. However, since $l = 1$ in the valence band, the Γ point six-fold degeneracy is lifted into: (i) a four-fold degeneracy whose states are described by a total angular momentum $J = l + s = 3/2$ (Γ_8 in Fig. 2.9), (ii) a separate $J = 1/2$ doublet known as the 'split-off band' (Γ_7 in Fig. 2.9) which is generally ignored in transport measurements as a large SO gap $\Delta_o = 0.341$eV in GaAs, means the split-off band remains unoccupied at low temperatures. At larger non-zero values of $\boldsymbol{k}$, the four-fold degeneracy is lifted to form two distinct bands: heavy-holes (HH) with a $m_j = \pm 3/2$ (projection onto J) and light-hole (LH) with $m_j = \pm 1/2$. The terms 'heavy' and 'light' stem from the inverse relation between their effective masses and curvature of their energy bands $m^* = \frac{1}{\hbar^2} \cdot [\frac{\delta^2 E}{\delta k^2}]^{-1}$.

2.5.2 2D confinement

When a 3D system is spatially confined into two-dimensions (2D) such as in a quantum well, the energy bands become quantized into a series of discrete standing waves along the quantum well and the four-fold degeneracy of the uppermost valence band is lifted (Fig. 2.10c), resulting in a $\boldsymbol{k} = 0$ splitting between the heavy-hole and light-hole bands Δ_{lh-hh}, where only the lowest energy hole band (i.e. heavy-holes), are occupied at

low temperatures [284]. Moreover, the different m^* values of the light- and heavy-hole bands, introduces extra complexity to the spin behaviour, such as anticrossings at larger values of $\boldsymbol{k}$ [192].

This $\boldsymbol{k} = 0$ spin splitting defines a natural quantization axis of angular momentum $\hat{J}$ along the growth direction (z-axis), perpendicular to the 2D plane of the quantum well. Due to the non-zero orbital component of the heavy-hole states, the SO interaction results in the spin axis of the heavy-holes $\hat{J}$ being locked perpendicular to the 2D hole plane, leading to a spin projection of $m_z = \pm 3/2$ onto the z-axis. The amount of HH-LH splitting determines the degree of HH-LH mixing and other SO phenomena such as asymmetry induced $B = 0$ spin splitting, become higher order effects which compete with the HH-LH splitting [284] as discussed in the following sections.

2.6 Spin-orbit interactions: Inversion asymmetry and $B = 0$ spin splitting

Inversion symmetry results in a two-fold degeneracy, $E_+(\boldsymbol{k}) = E_-(\boldsymbol{k})$ [284]. However if charge carriers move within an inversion-asymmetric potential, the spin degeneracy is lifted even without a magnetic field, producing a B=0 spin splitting between two separate energy dispersion bands $E_+(\boldsymbol{k})$ and $E_-(\boldsymbol{k})$. In a quasi-2D system there are two main sources of inversion symmetry: bulk inversion asymmetry (BIA) of the underlying crystal lattice structure, and structural inversion asymmetry (SIA) in the confinement potential of the quantum well [284]. Both BIA and SIA vary depending upon the material, density and geometry of the sample and will be discussed in the following sections.

2.6.1 Bulk inversion asymmetry (Dresselhaus spin-orbit)

The zinc blende crystal structure of GaAs is non-centrosymmetric (i.e. lacks a center of inversion), resulting in the presence of BIA spin spitting, also referred to as Dresselhaus spin splitting [63]. BIA depends only upon the crystallographic orientation of the heterostructure (i.e. varies with $\boldsymbol{k}$), and is independent of any external fields.

In a bulk 3D zinc blende semiconductor, BIA spin splitting can be regarded as the result of an effective magnetic field upon the spin of an electron, where the electron precesses around this field with an effective momentum dependent Larmor vector $\mathbf{\Omega}$. In this framework BIA spin splitting (or the Dresselhaus term) for electrons can be expressed as [19, 63]

$$\mathbf{\Omega}_{BIA}^{3D}(\boldsymbol{k}) = \frac{\gamma}{\hbar}\left[k_x(k_y^2 - k_z^2), k_y(k_z^2 - k_x^2), k_z(k_x^2 - k_y^2)\right] \tag{2.31}$$

Here γ is the Dresselhaus coefficient and $\boldsymbol{k} = (k_x, k_y, k_z)$ is the electron wave vector in 3 spatial directions. For electrons in a 2D quantum well, where $\boldsymbol{k}$ along the growth axis z is quantized, the form of the Dresselhaus term depends upon the direction of the in-plane crystal axes. For example the effective field for the high symmetry (100) direction is

$$\mathbf{\Omega}_{BIA}(\boldsymbol{k}_{\parallel}) = \frac{\gamma}{\hbar}\langle k_z^2\rangle(-k_x, +k_y, 0) \tag{2.32}$$

where $\langle k_z^2\rangle$ is the averaged squared wave vector along the growth direction and $\boldsymbol{k}_{\parallel}$ is the in-plane wave vector. The corresponding Hamiltonian can be expressed as [284]:

$$\mathcal{H} = \frac{\gamma}{\hbar}\langle k_z^2\rangle(k_+\sigma_+ - k_-\sigma_-) \tag{2.33}$$

where $k_\pm = k_x \pm ik_y$, $\sigma_\pm = \frac{\sigma_x \pm i\sigma_y}{\sqrt{2}}$ and are the corresponding 2×2 Pauli spin matrices.

In the case of 2D holes in the valence band, grown along the high symmetry (100) direction, the 2×2 Pauli spin matrices are replaced with a 4×4 total angular momentum matrix $\boldsymbol{J}$. Due to the extra complexity of spin-3/2 holes, the BIA term becomes cubic in k [33] and the Hamiltonian becomes:

$$\mathcal{H} = \beta(k_-k_+k_-J_+ - k_+k_-k_+J_-) \tag{2.34}$$

where the coefficient $\beta = \frac{3\gamma_0\gamma}{\hbar}\left\langle \frac{k_z^2}{2m_0\eta\Delta_{lh-hh}} \right\rangle$ [33]. Here γ_0 is the Luttinger parameter [172], γ is the Dresselhaus coefficient, m_0 the free electron mass, $\eta = \Delta_0/(E_g + \Delta_0)$ where Δ_0 is the split-off gap (in Fig. 2.10) and Δ_{lh-hh} is the HH-LH splitting.

The BIA SO interaction can be controlled by selecting the crystal orientation along which the length and width of the heterostructure is fabricated and the amount of HH-LH splitting (admixture) can be controlled by the width of the quantum well. But

once the heterostructure is grown, the Dresselhaus effect remains fixed and cannot be tuned.

2.6.2 Structural inversion asymmetry (Rashba spin-orbit)

Another source of zero-field spin splitting comes from asymmetry in the confinement potential due to the presence of an electric field, known as structural inversion asymmetry (SIA) or the Rashba SO interaction [35]. This electric field ε can be either built into the sample during growth, (such as a layer of dopant atoms within the heterostructure) or later applied by an external electric field e.g. using metallic gates deposited onto the sample, which allows one to tune the SIA spin splitting, unlike BIA which is a fixed material property [168, 194, 204].

The general first order Rashba SO Hamiltonian for electrons in the conduction band is [284]:

$$\mathcal{H} = \alpha \boldsymbol{\sigma} \cdot (\boldsymbol{k} \times \boldsymbol{\varepsilon}) \tag{2.35}$$

where ε is the electric field vector characterizing the confining potential, k is the wave vector, $\boldsymbol{\sigma} = (\sigma_x, \sigma_y, \sigma_z)$ refers to the Pauli spin matrices and α is a material specific prefactor for GaAs. From the reference frame of an electron moving within an electric field, Rashba SO appears as an effective magnetic field which can interact with the spin of the electron. Hence Eq. 2.35 takes on a similar form to the Zeeman Hamiltonian when the effective magnetic field $k \times \boldsymbol{\varepsilon}$ is substituted with $\boldsymbol{B}$.

In a 2D system, where electrons are confined to move within a plane $\boldsymbol{k}_{\parallel} = (k_x, k_y, 0)$, only an electric field applied perpendicular to the growth direction can contribute to SIA spin splitting and the Rashba term becomes [283]

$$\mathcal{H} = \alpha \varepsilon_z i \left(k_- \sigma_+ - k_+ \sigma_-\right) \tag{2.36}$$

Where α is a material dependent prefactor and ε_z is the (effective) electric field. From the reference frame of an electron, this can be expressed in a Zeeman form [286]

$$\mathcal{H} = \frac{1}{2} \boldsymbol{B}(\boldsymbol{k}_{\parallel}) \cdot \boldsymbol{\sigma} \tag{2.37}$$

where $\boldsymbol{B}(\boldsymbol{k}_{\parallel}) = 2\alpha\varepsilon_z(k_y, -k_x, 0)$ is an effective magnetic field such that $\boldsymbol{B}$ orients the electron spin along the 2D plane. The corresponding energy dispersion relation

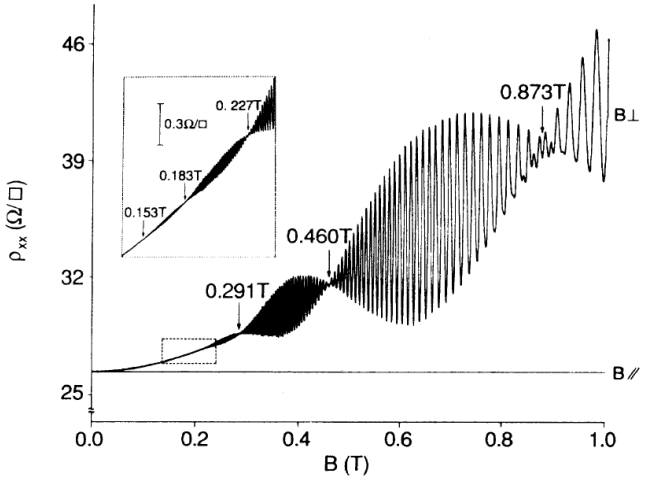

Figure 2.11: Beating pattern in the SdH oscillations due to the presence of two distinct spin subbands for 2D electrons in an InGaAs quantum well [55].

can be expressed as:

$$E_{\pm}(k_{\parallel}) = \frac{\hbar^2 k_{\parallel}^2}{2m} \pm \alpha \varepsilon_z k_{\parallel} \tag{2.38}$$

The Rashba SO yields an additional $k_{\parallel}$-linear term, resulting in the loss of spin degeneracy and a lateral shift between the two bands in k, rather than in energy. The Rashba spin splitting behaviour of spin$-1/2$ electrons, is weak in wider band gap materials such as GaAs [154] but stronger in narrow gap semiconductors such as InGaAs.

The end result is two unequal spin populations $N_{\pm}$ for the 2 spin subbands at zero magnetic field where $N_{tot} = N_{+} + N_{-}$ is the total carrier population [68, 252]. This effect has been observed in transport measurements as a pronounced beating pattern in the Shubnikov-de Haas (SdH) oscillations in electron systems with strong SOI, due to the superposition of two frequencies $f_{\pm}$ close to each other, where $N_{\pm} = \frac{e}{2\pi\hbar} f_{\pm}$. This beating was first studied by Das et. al. [55] in an InGaAs/InAlAs heterostructure at low fields, shown in Fig. 2.11.

For the case of 2D hole systems the Rashba spin splitting is more complex and the Pauli spin matrices $\boldsymbol{\sigma}$ need to be replaced by the 4×4 total angular momentum matrix $\boldsymbol{J} = (J_x, J_y, J_z)$. The general Hamiltonian for a perpendicular electric field

yields [283, 286]

$$\mathcal{H} = \beta\varepsilon_z i \left(k_-^3 J_+ - k_+^3 J_-\right) \tag{2.39}$$

where $J_\pm = \frac{J_x \pm iJ_y}{\sqrt{2}}$. To lowest order, the spin splitting dispersion now becomes [284]

$$E_\pm(k_\parallel) \propto \pm\beta\varepsilon_z k_\parallel^3 \quad . \tag{2.40}$$

The orbital component in hole spins results in a SIA spin splitting proportional to $k_\parallel^3$ which is qualitatively different to the $k_\parallel$-linear case of electrons [286]. Moreover the prefactor β is dependent upon the HH-LH splitting, which in turn depends upon the geometry of the 2D quantum well. Using third-order pertubation theory, the following expression for the prefactor of the first heavy-hole subband can be obtained [97],

$$\beta_1^{HH} = \frac{e\hbar^4}{m_0^2} a\gamma_3(\gamma_2 + \gamma_3)\left[\frac{1}{\Delta_{11}^{hl}}\left(\frac{1}{\Delta_{12}^{hl}} - \frac{1}{\Delta_{12}^{hh}}\right) + \frac{1}{\Delta_{12}^{hl}\Delta_{12}^{hh}}\right] \quad , \tag{2.41}$$

where $a = 64/9\pi^2$ for an infinitely deep rectangular quantum well and Δ^{hl} is the HH-LH splitting.

The definition for the effective magnetic field $\boldsymbol{B}$ given in Eq. 2.37 remains valid for holes, and its tendency is to orient the holes in-plane. But due to the presence of HH-LH splitting (since the spin axis of the HHs are locked perpendicular to the 2D plane whilst the spin-1/2 LHs maintain a $k_\parallel$-linear relation like electrons), the Rashba zero-field spin splitting becomes a higher order effect [286].

2.6.3 Tuning Rashba spin-orbit interaction

The tunability of the magnitude of the Rashba SO interaction, provides an important experimental handle in the study of spin dynamics. It provides the capability to change the shape of the confining potential and in some circumstances, even allows for the compensation of the nominally fixed Dresselhaus SO interaction, enabling other subtle spin-orbit physics to be highlighted. We shall use a similar technique in our study of a 2D hole system later in this thesis.

Zero-field spin splitting due to the lifting of Kramer's degeneracy in the absence of inversion symmetry in a GaAs single heterojunction interface (which yields a roughly triangular confining potential) was first observed by Stormer *et al.* [252], as a beating in

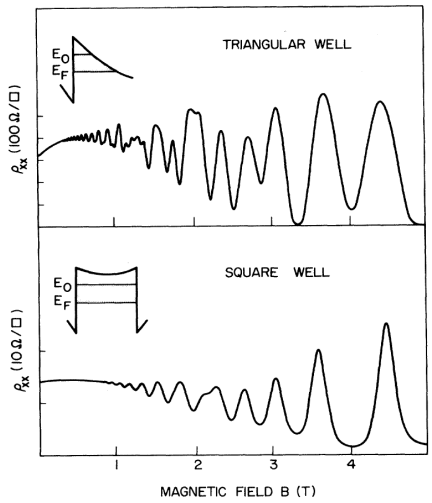

Figure 2.12: Top panel shows the SdH trace for a triangular confining potential made from a single heterojunction interface, exhibiting a distinctive beating pattern due to the presence of inversion asymmetry. The bottom panel shows a corresponding SdH trace for a symmetric quantum well, where only a single frequency is resolvable [68].

the Shubnikov-de Haas oscillations. This was attributed to the presence of two carrier species with two different effective masses, resulting in two distinct Fermi surfaces contributing to the 2D transport at two separate frequencies.

This was followed shortly after with a study by Eisenstein *et al.* comparing the effect of a single heterojunction to a symmetric square well made by joining two equal but opposite interfaces together [68]. Fig. 2.12 shows the results for the two scenarios in a perpendicular field at similar carrier densities ($4.7 - 4.8{\times}10^{11}\mathrm{cm}^{-2}$). The SdH oscillations for the triangular well exhibit a distinct beating pattern, indicative of two frequencies, whilst there is no resolvable beating in the case of the symmetric square well. The frequencies of the oscillations at low field were extracted, 2.4 for the triangular well, and 0.98 for the square well, suggesting near zero splitting for the latter [68]. Moreover the relative spin populations were found to be independent of the magnetic field, implying the presence of spin splitting at $B = 0$T right from the beginning.

The ability to tune Rashba spin splitting via an electric field across the 2D system, was first demonstrated by Wieck *et al.* [278] in a $p-$channel Silicon metal-oxide-semiconductor structure, followed shortly by Lu *et al.* in a GaAs hole system [168].

This study was taken further by Papadakis *et al.* [204], whose device featured metal gates deposited on both the top and back of the sample, allowing the electric field across the quantum well to be varied, whilst keeping the density constant. SdH oscillations were then measured over a series of different front/back gate voltage combinations, whilst the electric field was adjusted from positive to negative. The SdH oscillations for each setting of the electric field are shown in Fig. 2.13a [204]. Panel (b) gives the Fourier transform of the corresponding magnetoresistance trace, highlighting the presence of two spin species as two distinct frequencies. Panel (c) roughly illustrates the corresponding confining potential shape over the quantum well. When the electric field across the well is positive, a clear beating in the SdH and two spin subbands are seen (top datasets) and likewise for a negative electric field (bottom datasets). When the front/back gate bias voltages are adjusted such that there is a net zero electric field across the quantum well, no beating observed is observed and there is only a single spin degenerate heavy-hole band (middle traces).

2.7 Zeeman spin splitting

The Zeeman effect was discovered in 1987 [301], and describes the splitting of a degenerate spin state in the presence of a magnetic field. For electrons in bulk GaAs, the Zeeman Hamiltonian is:

$$\mathcal{H} = \frac{g^*}{2}\mu_B \boldsymbol{B} \cdot \boldsymbol{\sigma} \tag{2.42}$$

where the isotropic bulk effective Landé g factor is $g^* = -0.44$ for electrons, μ_B is the Bohr magneton and $\boldsymbol{\sigma} = (\sigma_x, \sigma_y, \sigma_z)$ are the Pauli spin matrices. When confined to 2D, subband quantization causes the g factor to decrease and the Hamiltonian can be expressed in its components

$$\mathcal{H} = \frac{g^*_{\parallel}}{2}\mu_B \left(B_x\sigma_x + B_y\sigma_y\right) + \frac{g^*_{zz}}{2}\mu_B B_z\sigma_z \tag{2.43}$$

As the 2D quantum well becomes narrower, the g factor becomes smaller and eventually changes sign [284]. Moreover the reduced symmetry of a 2D system compared to bulk, leads to the out-of-plane Zeeman spin splitting arising from coupling between

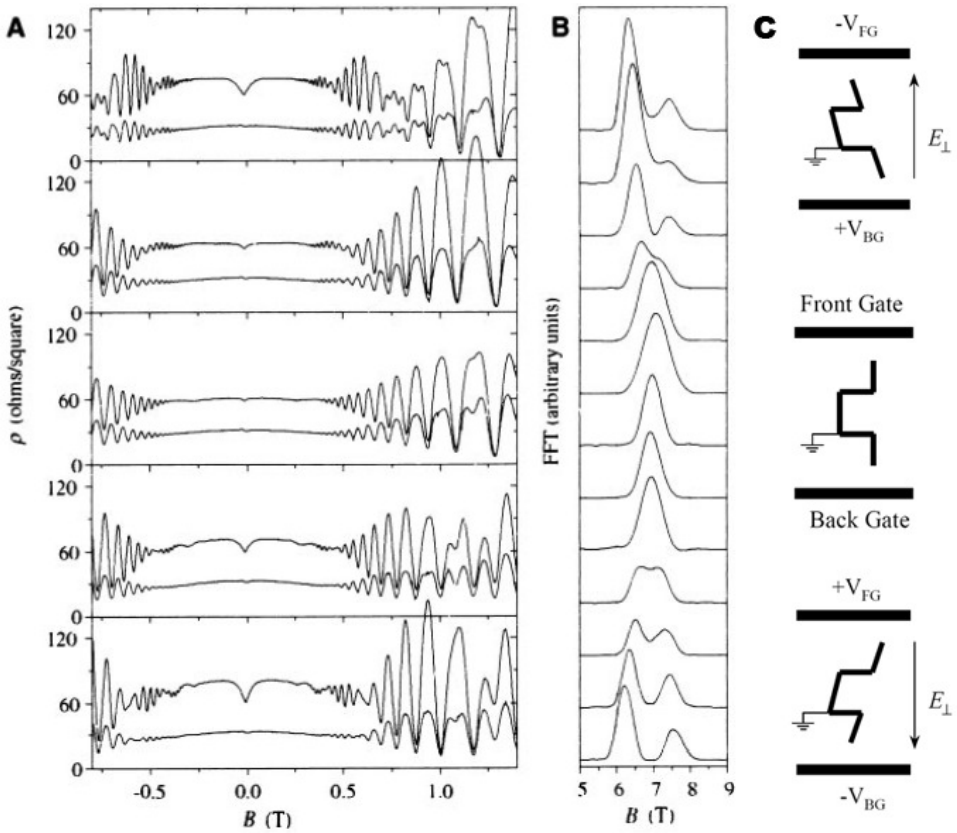

Figure 2.13: Tuning the Rashba SO over a 20nm GaAs quantum well at a temperature of 25mK. Figure reproduced from [204]. (a) Oscillations in magnetoresistivity as a function of perpendicular field, taken at different front/back gate biases along the $[01\bar{1}]$ (top) and $[\bar{2}33]$ (bottom) directions. (b) Corresponding Fourier transforms of the SdH oscillations showing 2 distinct frequencies for asymmetric confining potentials and only one for a symmetric well (c) Schematic of the shape of the confining potential corresponding to the 3 main biasing conditions, with the symmetric condition in the middle.

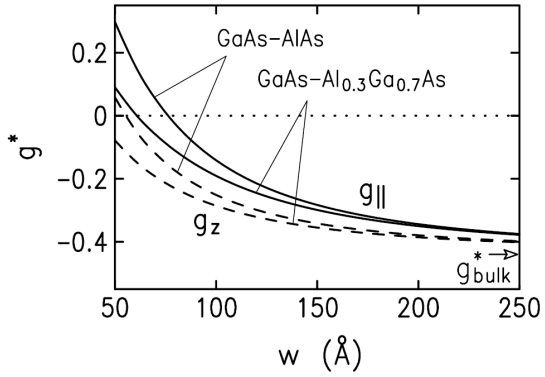

Figure 2.14: Theoretical plot of the electron g^* over quantum well width, exhibiting a slight anisotropy [284].

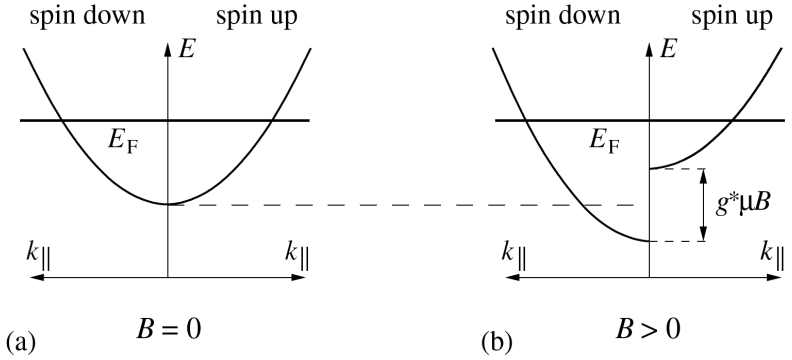

Figure 2.15: (a) Two-fold spin degenrate subband in the absence of a magnetic field. (b) When a parallel field is applied the Zeeman effect causes the bands to split by $\Delta E = g^*\mu_B B$ and become spin polarised [284].

adjacent energy bands, and hence g^*_{zz} is larger than the in-plane $g^*_{\|}$. The variation of the two g^* components are presented for a range of well widths in Fig. 2.14 [284].

For a quantized 2D system in the absence of a magnetic field, the subbands are spin degenerate, equally occupied and no spin-polarization is present, shown in Fig. 2.15a. When an in-plane field $B_{\|}$ is applied, the bands split by an amount proportional to the field, increasing the number of occupied states in one spin subband and decreasing the number of occupied states in the other (illustrated in part b). An electron system is considered fully spin polarized when the Zeeman energy from an in-plane magnetic field is greater than the Fermi energy i.e. $g^*\mu_B B \gg E_F$.

This results in two distinctly different areas covered by the Fermi circle for each spin subband. Since the total carrier density must remain constant, the Fermi energy

adjusts itself as one spin subband becomes depopulated, and the system becomes fully spin polarized. By measuring the energy splitting between the subbands, we can calculate the effective g factor and hence characterize the spin properties of the system.

2.7.1 Zeeman splitting in 2D holes

Similar to the electron case, using a first-order approximation the Zeeman splitting for bulk holes is isotropic, where g^* is equivalent to the Luttinger band parameter $\kappa = 1.2$ in GaAs [284]. The general Zeeman Hamiltonian to lowest order is

$$\mathcal{H} = -2\kappa\mu_B \boldsymbol{B} \cdot \boldsymbol{J} \tag{2.44}$$

where the quantization axis $\hat{J}_z$ is determined by the momentum $\boldsymbol{k}$. Holes in a quantum well, have a pre-defined quantization axis $\hat{J}_z$ perpendicular to the 2D plane, when a magnetic field is applied along $\hat{J}_z$, we get a large Zeeman splitting of heavy hole (HH) states. The most commonly accepted value for the out-of-plane hole g factor is [271, 284]:

$$g_{zz}^{HH} = 6\kappa = 7.2 \tag{2.45}$$

This out-of-plane g factor applies to 2D heavy-holes in GaAs for any crystal growth direction. However, in the case of in-plane Zeeman splitting, the growth direction becomes important due to crystallographic anisotropy, and higher order terms in the Hamiltonian are required to fully describe the underlying physics.

2.7.2 In plane Zeeman splitting for 2D heavy holes on high symmetry growth directions

When an in-plane field $\boldsymbol{B}_{\|} = (B_x, B_y, 0)$ is applied, at the band edge there is no direct coupling between HH states as they remained locked to $\hat{J}_z$, meaning there is no $B_{\|}$-linear Zeeman splitting term. The lowest order term is proportional to $B_{\|}^3$ at $k_{\|} = 0$:

$$\Delta E_z(\|) \propto \frac{B_{\|}^3}{\Delta_{HH-LH}} \tag{2.46}$$

This yields an effective in-plane $g^*_{\parallel} \approx 0$ for heavy-holes. However this is only applicable at the $\boldsymbol{k}_{\parallel} = 0$ band edge. At finite $\boldsymbol{k}_{\parallel}$, HH-LH mixing results in a non-zero g factor and we obtain a linear Zeeman splitting at $\boldsymbol{k}_{\parallel} > 0$ [284]:

$$\Delta E_z(\parallel) \propto \frac{k_{\parallel}^2 B_{\parallel}}{\Delta_{HH-LH}} \tag{2.47}$$

2.7.3 Experimental review of hole g factor anisotropy in high-symmetry GaAs

The anisotropy of hole g factors, was first discovered by van Kesteren *et al.*, whose measurements on optically excited electron-hole pairs (excitons) for different quantum well thicknesses grown on a high symmetry (100) GaAs crystal, yielded values of $g^*_{zz} = 2.5$ and $g^*_{xx} = g^*_{yy} < 0.01$ [271]. Measurements of the g factors in confined excitons have also been conducted using photoluminesence [88, 230]. These measurements exhibit a large variation in the out-of-plane g factor, $-0.7 < g^*_{zz} < 2.9$, and are much lower than the theoretically predicted value of 7.2. This discrepancy has been attributed to the bound state of the exciton which is effectively zero-dimensional, thus suppressing the in-plane momentum. On this basis, excitons are not a good representation of a 2D system. Faraday/Kerr rotation experiments [152, 255] also yield small values of g^*_{zz}, due to admixing between the HH and LH exciton states which can dramatically reduce the g factor [255].

Other studies of GaAs g factors include transport measurements of the out-of-plane bulk g factor using 2D devices [201, 282], quantum point contacts (QPCs) and 1D quantum wires where the quasi-1D channel width has been widened to reach higher subband indexes, approaching the 2D-limit [53, 141, 144, 251]. Despite numerous attempts, it was only recently that the theoretical out-of-plane $g^*_{zz} = 7.2$ bulk limit was experimentally verified in a [001] GaAs, 1D device for higher subbands $N = 6, 7$ [192]. Other transport experiments in QPCs and quantum wires yield small in-plane g factors for holes, which is consistent with theoretical predictions for both high-symmetry (100) [39, 148] and lower-symmetry (311) growth planes [50, 53, 141, 144].

An experimental review of the anisotropic g factors in low-symmetry GaAs crystals is provided in Chapter 4.2.3 as a prelude to our magnetic field studies of a (311) 2D

hole system.

Chapter 3

Fabricating 2D hole systems

3.1 Introduction

In this chapter we shall briefly introduce the high mobility electron transistor, a two-dimensional system which forms the basic underlying structure of the low-dimensional devices under study in this thesis. We shall compare and contrast two main methods used to generate a 2D gas within a heterostructure - doping versus electrostatic induction, followed by two main types of induced structures. We then outline the basic steps used to fabricate these induced 2D transistors followed by some preliminary tests, characterizing hysteresis in such devices.

3.2 Background

3.2.1 High mobility electron transistors (HEMT)

The earliest two-dimensional electron gas (2DEG), was realized in a Silicon metal-oxide-semiconductor field–effect transistor (MOSFET) at Bell Labs in the 1960s, based upon the working principle of a FET from a US patent filed in 1925. The cross-section of a typical device consists of a p-type Si substrate covered by a SiO_2 layer which acts as an insulator between the Si substrate and a metal electrode gate. Applying a positive bias to the gate causes an inversion layer to form at the Si/SiO_2 interface, resulting in a conducting channel connecting the source and drain electrodes. In 1957

Schrieffer [233] proposed that charge carriers confined in the inversion layer do not behave classically since the confining potential is so narrow that motion perpendicular to the interface becomes quantized and if only a few quantum states are occupied, the system effectively becomes a 2DEG.

An alternative semiconductor material to Silicon is GaAs, a III-V semiconductor with a zinc blende crystal structure and unlike Silicon has a direct bandgap of 1.424eV at room temperature, which eliminates complications from inter-valley scattering. In particular, further work on lattice matched GaAs/Al_xGa_{1-x} heterojunctions has eventually led to the achievement of high mobilities up to $11.7\times10^6 cm^2V^{-1}$ [209], making it a popular system from which to fabricate High Electron Mobility Transistors (HEMT). In such semiconductor-insulator-semiconductor (SIS) structures, the AlGaAs layer replaces the SiO_2 layer in the MOSFET.

The fabrication of a high quality HEMT relies upon the ability to grow epitaxial heterojunctions between different semiconductors, forming a single crystal with an artificially engineered band structure and doping profile. One of the most popular growth methods is Molecular Beam Epitaxy (MBE), where epilayers of semiconductor material are grown with controlled chemical composition and levels of dopants. The ability to engineer the bandstructure of such semiconductors has led to a wide range of different structures and layer compositions. For the purposes of this thesis, we shall focus upon two main methods for introducing charge carriers into these heterostructures - doping and inducing.

3.2.2 Induced versus doped 2D HEMT architectures

The method of doping involves the deliberate introduction of "impurity" atoms into a layer, usually the $Al_xGa_{1-x}As$. This is typically followed by a $Al_xGa_{1-x}As$ spacer layer before contact to the GaAs layer is made. Although techniques such as modulation doping have led to unprecedented mobilities [209], it is not without its deficiencies. Disorder is inevitably introduced into the material by the presence of remote ionized dopants, which can be a limiting factor to the mobility in high quality modulation-doped samples [8, 66] and Random Telegraph Signal (RTS) noise. Moreover, both the

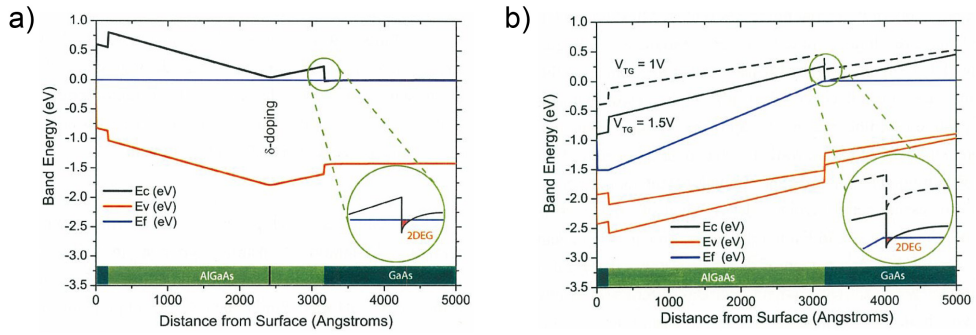

Figure 3.1: Energy band diagrams for GaAs modelled with a Poisson-Schrödinger solver reproduced from Ref. [231]. (a) δ-doped 300nm 2DEG with an 80nm spacer layer between the heterojunction and the doping layer. (b) Induced device with a 500nm thick polyimide insulating layer, giving a threshold voltage of $V_{th} \sim 1.5$V.

carrier type and density of doped structures are fixed once the material is grown.

An alternative to doping which removes the problems caused by doping altogether is to induce carriers into the $Al_xGa_{1-x}As$/GaAs interface via an externally applied electric field, through a metallic gate [130]. This technique is much more flexible as it allows both carrier types (holes and electrons) to be produced with adjustable carrier densities, which are limited only by tunnelling through the $Al_xGa_{1-x}As$ barrier. Once the bias on the top gate (used to induce carriers) goes over a certain threshold voltage, conductance through the channel increases linearly with gate voltage until a saturation point is reached.

The difference between modulation doped and induced heterostructures can also be seen in their band structures, shown in Fig. 3.1 [231]. Here the chemical potential is discontinuous and not well defined in the insulator, and for the purposes of the calculation it is varied linearly for simplicity. Doped systems contain a dip in the conduction band towards the narrow region of doping. At the $Al_xGa_{1-x}As$/GaAs heterointerface the conduction band drops below the Fermi level and the 2D electron gas can form. Panel (a) shows a δ-doped 300nm 2DEG with an 80nm spacer layer between the interface and the dopant layer. For induced systems, the chemical potential is not constant throughout the structure, shown in panel (b). Here an accumulation gate (top gate) modulates the conduction band. If the bias voltage V_{TG} is sufficiently high (over the threshold voltage) the conduction band dips below the Fermi level at

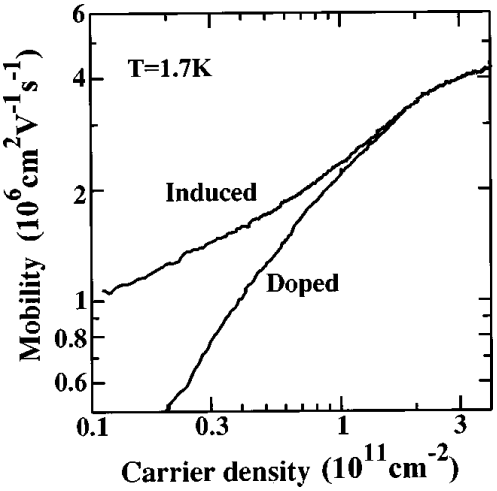

Figure 3.2: A graph of mobility vs density for an induced 2DEG vs a modulation doped 2DEG [104], exhibits a distinct drop in the mobility of a doped device compared to the undoped structure.

the heterojunction and populates with electrons forming a 2DEG. If $V_{TG} < V_{th}$, the conduction band remains above the Fermi energy (dashed black line) and no 2DEG is formed [231].

3.2.3 Random telegraph signals and charge noise

A major contributor to disorder in shallow HEMTs where the 2D layer is close to the surface are dopants in the AlGaAs layer of a modulation-doped or δ-doped structure [31, 212]. These ionized dopant impurities can significantly lower the mobility in a 2D system at low carrier densities [232] as charge carriers scatter due to their Coulomb interaction with these impurities. Fig. 3.2 [104] demonstrates the effect of these impurities on mobility, plotted vs carrier density for 2 samples: one with modulation doping and the other undoped. Each wafer was grown in the same chamber via Molecular Beam Epitaxy (MBE), resulting in similar background impurity levels. At carrier densities below 10^{11}cm^{-2} there is a significant drop in the mobility of the doped device compared to the undoped device, indicating that remotely ionized impurity scattering is dominant in the low density limit [104].

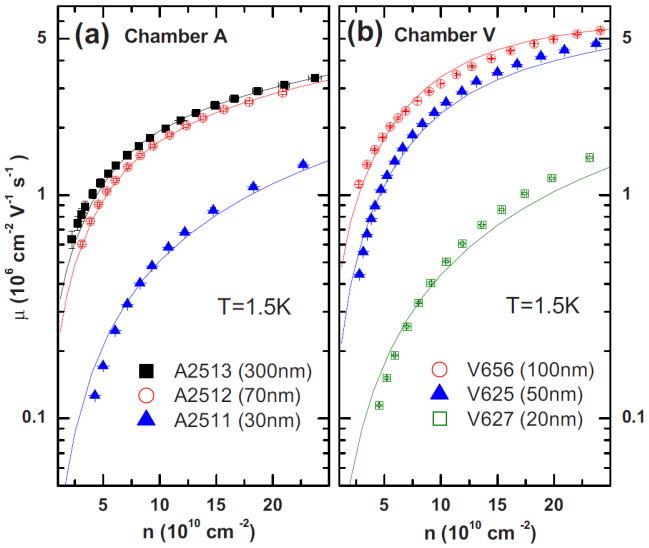

Figure 3.3: Comparison of the effect of surface states upon mobility as a function of density, in devices with different shallow 2DEG depths from the wafer surface.

3.2.4 Surface states

Another potential source of noise comes from surface states, located at the top of the heterostructure where the lattice abruptly terminates, resulting in a number of dangling bonds; some of which join with those from adjacent atoms to reconstruct the surface, thus minimizing the surface energy; some react to atmospheric species such as oxygen; whilst others remain free. The end result of this complex surface chemistry is a large peak in the density of states at the wafer surface, in the middle of the band gap of the semiconductor, effectively pinning the Fermi energy at this peak, leading to the characteristic Schottky barrier of deposited metallic surface gates [54, 84]. The net charge associated with these unwanted surface states causes charge carriers in the 2DEG to scatter, and their impact upon mobility becomes more prominent in shallower 2DEGs shown in Fig. 3.3. In this study by Mak *et al.*, samples with a small $(20 - 30\text{nm})$ AlGaAs thickness, were found to have a substantially lower mobility than samples with thicker AlGaAs layers, an effect which saturates when the 2DEG is over 100nm below the surface. Although such surface states lower mobility in 2D systems, their direct impact on quasi-stationary systems like quantum dots in induced heterostructures is still unclear.

3.2.5 Types of induced architecture

Although the technique of modulation doping has led to the fabrication of higher quality devices [209] the main drawback is the inevitable introduction of disorder and charge noise, due to the presence of remote ionized dopants. This also limits the mobility of such devices as charge carriers scatter off these dopants due to the Coulomb interaction [130]. Furthermore, the dopant layer may partially screen surface gates (via hopping conduction) and/or facilitate gate leakage, rendering many such heterostructures ungateable by metallic gates [175] deposited directly onto the wafer surface.

One way to bypass this problem is to eliminate the need for modulation doping altogether by using an "induced" or "undoped" structure, first pioneered by Solomon *et al.* in 1984 [247] and further developed by Kane *et al.* [130]. In such a semiconductor-insulator-semiconductor FET (SISFET) design, a heavily doped GaAs cap layer functions as a gate, drawing charge carriers to form a 2DEG at the heterojunction interface, below the $Al_xGa_{1-x}As$ insultating barrier [130] and above the GaAs substrate (see 3.4b). Ohmic contacts are made to electrically connect to the 2D gas. Such induced devices were found to be more stable and reproducible between thermal cycles [239] and also possess higher mobilities at lower carrier densities than devices fabricated on modulation doped wafers with a small AlGaAs spacer layer [104].

In this thesis we will take this one step further and focus upon a type of induced hetrostructure which removes the need for doping altogether. This provides an important platform for creating stable hole dots as discussed later in this thesis, since the level of noise in a modulation doped system may potentially become problematic when detecting the flow of single charges through the dot.

The metal-insulator-semiconductor FET (MISFET), was first developed by Harrell *et al.* [104], which relies upon a global metal surface gate to electrostatically induce the charge carriers. A cross-section of the heterostucture is shown in Fig. 3.4a.

A titanium gold (Ti/Au) global top gate, used to induce holes to form the 2DHG, is deposited on top of an insulating layer (polyimide or aluminium oxide in our case), to reduce the chance of current leakage directly to an ohmic. Fig. 3.5 illustrates the

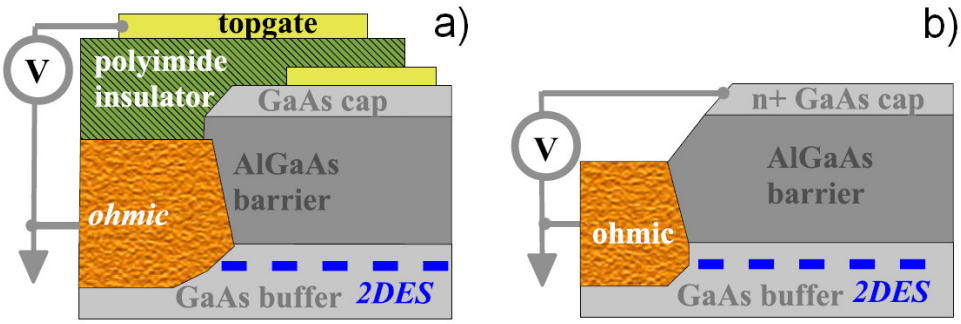

Figure 3.4: Comparison of two induced architecture types [174]. (a) MISFET induces via an overall top gate, followed by a polyimide insulating layer to reduce the chance of current leakage between the ohmics and the top gate. (b) SISFET induces via a degenerately doped GaAs cap just above the AlGaAs barrier and has a higher chance of leakage between the ohmics and the doped cap compared to the MISFET structure.

difference in the energy band diagram of a MISFET, under different biasing conditions.

In Fig. 3.5a with zero voltage applied to the top gate, the Fermi energy remains in the middle of the energy band gap. When a negative voltage is applied as in Fig. 3.5b, the bands bend upwards, and eventually the valence band crosses the Fermi energy, forming a triangular well just below the heterojunction sandwiched between the AlGaAs and GaAs layers, populated with holes. If a positive voltage is applied as in Fig. 3.5c, the opposite occurs i.e. the conduction band bends downwards below the Fermi energy and electrons accumulate in the well.

The advantage of such MISFET structures is their ability to easily switch between charge carrier types, simply by changing the sign of the voltage applied to the global top gate (and the corresponding type of ohmic metal contacts). One example of its use includes a study conducted into ambipolar devices [40]. Moreover in order to create fine structures like quantum dots, it is important to define small features at the 2D gas, which is much easier to accomplish if the 2DEG is close to the surface. However in the SISFET design, it is more difficult to form ohmic contacts to such shallow 2DEGs without directly shorting to the doped cap.

More recently, Mak *et al.* have demonstrated that these undoped, shallow GaAs/AlGaAs MISFET heterostructures can be used as a basis to fabricate stable, single-electron quantum dots 30nm from the GaAs surface [175], defined electrostaically by metal sur-

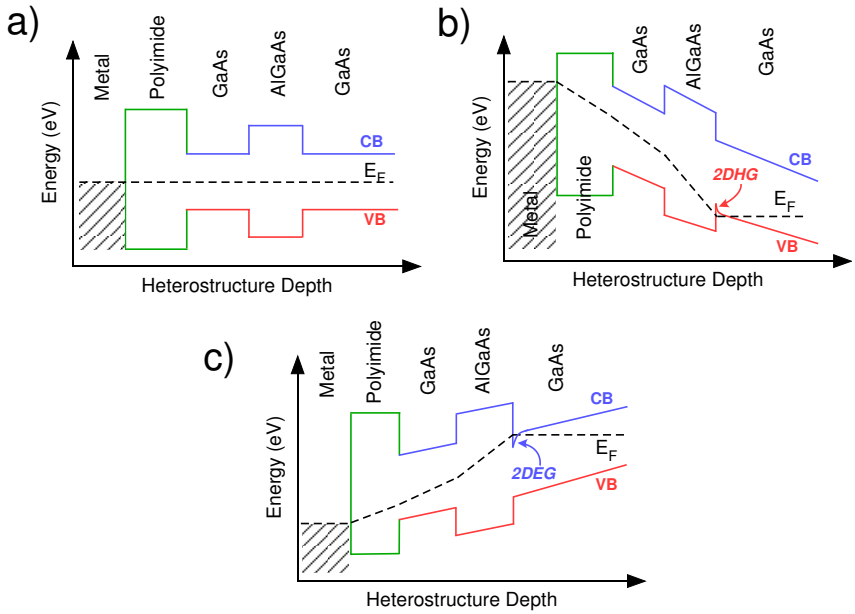

Figure 3.5: Schematic band structure illustrating the response of the MISFET to different top gate voltage biasing configurations. (a) At zero bias the FET is nominally off, (b) applying a negative bias induces holes to form a 2DHG, (c) whilst a positive bias induces electrons into the 2DEG.

face gates on top of the wafer, beneath the insulating layer. Moreover, the flexibility of the induced MISFET architecture combined with its potential for reduced charge noise, has seen it extended to create few-electron quantum dots in other material systems such as Silicon Metal-Oxide-Semiconductors [196, 291] and electron double-dots in Si/SiGe [29, 181] and Silicon [164].

3.3 Fabricating induced 2D transistors

3.3.1 Fabrication process flow

The standard process of fabricating induced 2D transistors has been used to create 2D systems from which a wide range of nanostructure devices can be fabricated, and can be found in other theses e.g. Refs. [38, 103, 142, 216, 231]. A brief outline of the major processing steps performed in a cleanroom (provided by the Australian Nanofabrication Fabrication Facility at UNSW) are given below. A photo of the end result of each of the corresponding steps is given in Fig. 3.6.

Mesa

After scribing and cleaving a piece of the GaAs wafer of the correct size, the first step is the definition of a mesa from the wafer via wet etching. The shape of the mesa typically takes the form of a Hall bar as shown in Fig. 3.6a. The process of photolithography is used to define a mesa pattern: this involves spinning a UV sensitive photoresist (S1813 or AZnLOF2020) onto a cleaned sample surface, pre-baking it at 110°C to allow it to harden, exposing the surface to UV light through an appropriate mesa mask pattern, developing the pattern (in AZ300MIF or AZ826MIF), rinsing the developer off in deionized water and blow-drying the sample with nitrogen. The definition of the mesa is necessary in induced structures to electrically isolate the conducting regions of the 2D device. To achieve this isolation we typically etch the pattern below the 2DEG, removing some of the AlGaAs spacer layer. Different etchants are available, but for our purposes we typically use a $H_3PO_4(85\%)$:$H_2O_2(31\%)$:H_20 (2:2:40) acid mix, as it etches both GaAs and AlGaAs isotropically. The target etch depth depends upon the depth of the heterojunction below the surface and for extra precision, the etch time is usually calibrated using a spare piece of GaAs or wafer if available. The etching process is halted by rinsing the sample in deionized water, after which the sample is N_2 blow-dried.

Ohmic contacts

Achieving a good electrical connection to the 2D gas is critical to the quality of the 2D device. Electrical contact is realized by thermal annealing of surface electrodes deposited in the shape of bonding pads. These electrodes have a typical area of $150 \times 150\mu m^2$ and are placed around edge of the mesa such that no edge currents can flow around an ohmic contact. Depending on whether the device is to be n-type or p-type, an appropriate eutectic mixture of metal compound is deposited. To create p-type ohmic contacts we typically evaporate 0.2g AuBe. For n-type ohmic contacts we evaporate a tri-metallic stack consisting of Ni/AuGe/Ni. The intial, 10nm nickel layer acts as a diffusion barrier, promoting lateral diffusion towards the 2DEG interface, followed by the gold germanium (290mg:40mg) layer hosting the n-type dopants, then

a thicker 120nm nickel capping layer to reduce surface roughness of the ohmics and hence reduce shorting to the top gate after annealing.

Next the metal is annealed into the semiconductor at a temperature of 530°C for 90s for AuBe and 470°C for 120s for Ni/AuGe/Ni, in a quartz tube oven using N_2 flow to prevent oxidation.

Metallic surface gates

This step involves the definition of nano-structures such as QPCs and quantum dots and is skipped during the fabrication of 2D transistors. Since the wavelength used in optical lithography does not provide enough resolution to define features on the nano-scale, the method of electron beam lithography (EBL) is used to write the pattern in the center of the mesa. The procedure for preparing the sample with EBL resist is very similar to that used in optical lithography where the step involving exposure to UV via a mask, is replaced by the EBL writing process. Once the nano-pattern is developed metal is evaporated onto the surface - first a thin layer of titanium used as a sticking agent, followed by gold for conduction. Extra care should be taken during the metal lift-off process to ensure the fine features are not damaged and sometimes the sample is left in a heated NMP solvent for several hours. Sometimes a combination of optical lithography and EBL is necessary to extend the gate pattern from the electrical contact pads at the edges of the mesa to the middle of the mesa where the nano-pattern is located.

Insulating dielectric

The two main dielectrics explored during fabrication of our devices are polyimide and aluminium oxide.

To use polyimide, the polyimide (HD4104) is first mixed with a thinner (T9039) in a ratio of (2:1). The polyimide is treated like a resist undergoing optical lithography - it is spun onto the sample until it reaches a thickness of $\sim 1\mu$m and baked at 65°C for 90s, placed under the insulating dielectric pattern and exposed to UV light, before being developed (401D) and rinsed (400R). Once completed, the sample with

the polyimide covering is baked at 250°C for 1hr to cure and set. During the baking process the solvent is evaporated and the polyimide layer shrinks to $400-600$nm thick.

The aluminium oxide layer on the other hand is deposited over the entire sample conformally to the required depth via atomic layer deposition (ALD). To open windows in the AlOx layer to contact the ohmic and surface gate pads, optical photolithography is used to define the areas to be opened and the sample dipped in a buffered HF acid mix, which is designed to stop etching once the GaAs surface is reached. After a pre-calibrated etch time, the sample is rinsed thoroughly in deionized water and N_2 blow-dried. The device after the AlOx has been deposited and etched is shown in Fig. 3.6d.

Metallic top gate

Standard optical photolithography is used to define the pattern of the global top gate, which covers the hall bar shaped mesa. Enough metal needs to be deposited to climb the mesa to connect the top gate and the contact gate pads below the mesa without breaking. We typically deposit 20nm of titanium to act as a sticking layer followed by 80nm of gold for good electrical conduction.

Wire bonding

The device is finally cleaved to fit within an LCC20 chip carrier and held down using resist or low-temperature compatible GE-Varnish. An Au-ball wire bonder is used to make electrical contact between the contact pads of the device and the bonding pads of the LCC20 chip carrier.

3.4 Characterizing 2D heterostructures

Initial characterization of the devices under study involves dipping them into a cryostat of liquid helium and measuring the 4-terminal conductance through each pair of ohmics. Data showing the response of an induced electron device and an induced hole device for different top gate voltages are given in Fig. 3.7 and Fig. 3.8 respectively.

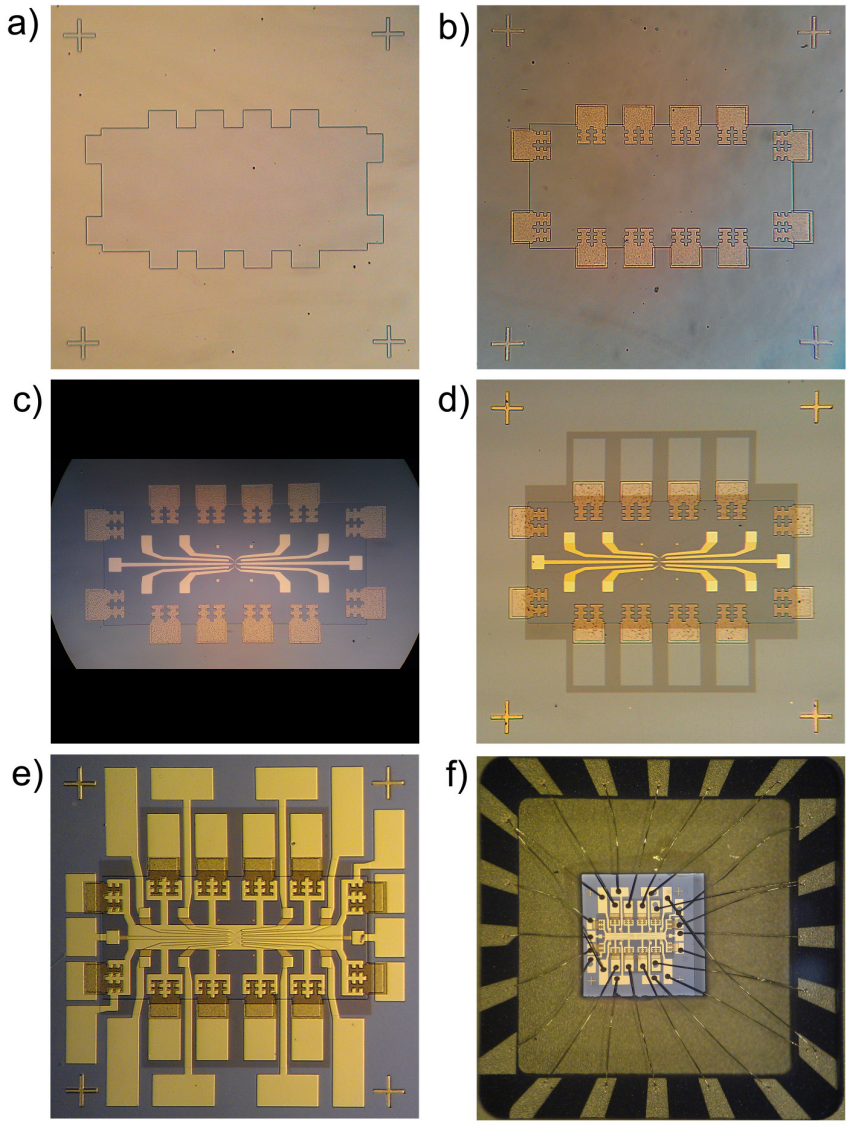

Figure 3.6: Photos of a low-dimensional induced device taken at the end of each main fabrication step. (a) Resulting mesa pattern in the shape of a hall bar shown after etching the wafer surface. (b) Addition of ohmics to enable electrical contact to the 2D gas after annealing. (c) Definition of the 'Sunbeam' quantum dot nano-structure (to be used later in Chapter 7) via a combination of optical and EB lithography. This step for creating lower dimensional (¡2D) nanostructures is bypassed when fabricating 2D transistors. (d) Application of the insulating dielectric layer, photo depicts AlOx. (e) Picture of the final device after the top gate metal has been evaporated and lifted-off. (f) Photo of the final device within an LCC20 chip carrier with Au wire bonds providing the electrical connection between device to the chip carrier.

The 2D electron transistor in Fig. 3.7 was fabricated from wafer W0639 (single heterojunction located 160nm below the surface), grown in the Cavendish Laboratory by the Semiconductor Physics group, using the electron recipe for ohmics. A 600nm thick layer of polyimide was used as the insulating dielectric to prevent direct shorting between the ohmics and the global top gate (TG). This style of 2D device will be used as a basic platform to create an electron quantum dot later in Chapter 6.1.

For this test, the top gate was swept to a larger bias voltage, and swept back to zero bias. This was repeated for increasingly larger values of TG. For target top gate voltages below $V_{TG} = -12$V, the threshold voltage beyond which the device turns on, remains constant at $V_{th} = +1.5$V. Beyond the threshold voltage, the conductance (lower panel) shows a linear increase until it hits a saturation point at $V_{sat} = +12$V beyond which the conductance remains at a maximum of 2mS despite any increase in top gate bias, behaviour similar to a typical transistor characteristic curve.

For mid-range top gates of -8V, -10V and -12V closed-loop hysteretic behaviour in the 2-terminal current is observed between the forwards and backwards sweeps, although none in seen when converted into 4-terminal conductance. At higher top gate voltages above $V_{TG} = -12$V, the hysteretic behaviour is no longer closed i.e. the return sweep to zero bias no longer reaches zero conductance/current at the same threshold voltage as the forward sweep. Hysteretic behaviour can also be observed in the 4-terminal conductance as well as the 2-terminal current. Sweeping to higher top gate targets shifts the threshold voltage to larger values. Despite this shift, no leakage current between the ohmics and the global top gate was detected.

Similarly a 2D hole transistor was fabricated from wafer W0640 (110nm deep single heterojunction) grown in the Cavendish Laboratory by the Semiconductor Physics group, using the AuBe hole recipe for ohmics. The 600nm thick layer of polyimide was replaced with a 30nm thick, conformal Aluminium oxide dielectric layer, which allowed for the 2D hole gas to be induced at lower top gate voltages (due to the higher dielectric constant of AlOx ($\epsilon = 8$) compared to polyimide ($\epsilon = 3.5$)). This 2D device will be used later in Chapter 6.5 to fabricate an induced hole quantum dot.

The same series of tests with different top gate targets was conducted on this device

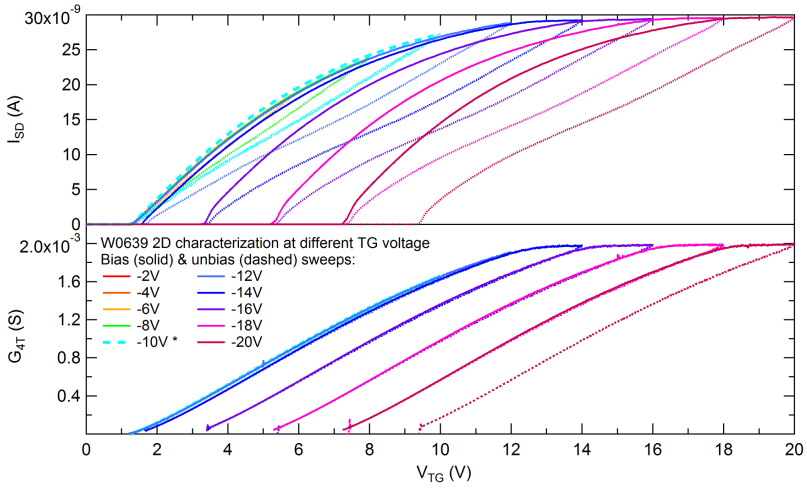

Figure 3.7: Plot of raw 2-terminal current (top panel) and 4-terminal conductance (bottom panel) as a function of top gate voltage for different target voltages. Solid lines correspond to sweeps towards increasing bias, to induce more carriers, whilst dashed lines correspond to sweeps back to 0V. Measurements were taken at 4K for a 160nm deep 2DEG created from wafer W0639, with a 600nm thick layer of polymide as an insulating dielectric. The top gate voltage marked with an asterisk indicates the largest top gate bias which can be applied before the onset of hysteresis.

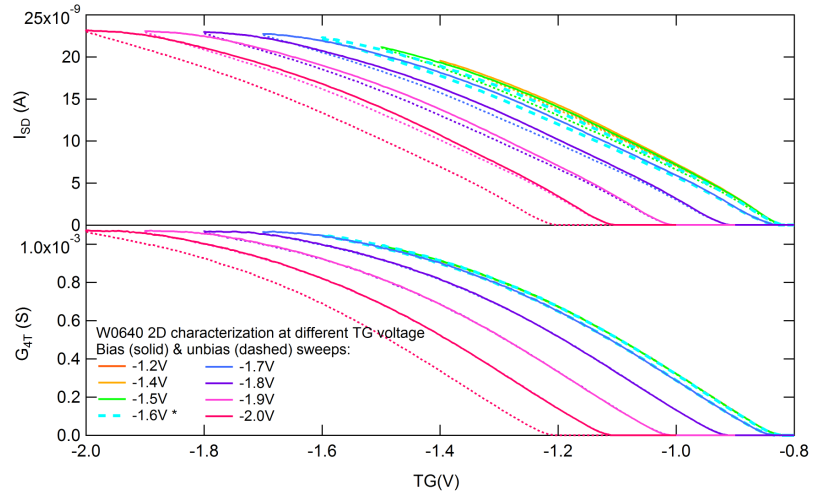

Figure 3.8: Plot of raw 2-terminal current (top panel) and 4-terminal conductance (bottom panel) as a function of top gate voltage for different target voltages. Solid lines correspond to sweeps towards increasing bias, to induce more carriers, whilst dashed lines correspond to sweeps back to 0V. The device under study is a 110nm deep 2DHG created from wafer W0640, with 30nm of Aluminium Oxide as an insulating dielectric, taken at a temperature of 4K. The top gate voltage marked with an asterik indicates the largest top gate bias which can be applied before the onset of hysteresis.

and the results shown in Fig. 3.8, where the sign of the bias applied to the top gate is reversed to induce holes. This device exhibited similar behaviour to the electron 2D transistor. An initial $V_{th} = -0.82$V remained constant for both forward bias and reverse bias sweeps until the saturation voltage at -1.6V was reached. Beyond this voltage, hysteretic behaviour between forward and backwards TG sweeps appear in both the 2-terminal current and 4-terminal conductance traces, despite no leakage current to the top gate being detected.

Such behaviour occurring in two different types of dielectric with different thicknesses suggests that beyond the saturation voltage, the insulating dielectric may be charging up. A study done by Huang *et al.* [121] in a Si/SiGe undoped 2DEG heterostructure, with a metallic top gate separated from the wafer surface by a 90nm thick Aluminium oxide layer, reports a sudden drop in the density beyond a certain (saturation) voltage. The authors attribute this drop at higher gate voltages to the formation of a nearly immobile surface electron layer between the AlOx dielectric and the Silicon surface.

The rationale behind this mechanism is illustrated in Fig. 3.9 which depicts the change in the band structure in the 3 major operating regimes of the transistor. Fig. 3.9a corresponds to the regime where a non-zero top gate bias is applied, but $V_{TG} < V_{th}$, so although charge is accumulating in the quantum well, the 2D density n_{2D} lies below the critical density of the metal-insulation transition for the quantum well $n_{c,QW}$ so no current flows from the ohmic contacts into the quantum well. The 2D transistor behaves as an insulator. Panel (b) describes the regime where $V_{TG} > V_{th}$. Above this threshold voltage, the critical density for the metal-insulator transition (MIT) is reached and electrons begin to flow from the ohmic contacts through the quantum well, forming a 2DEG. However, since the critical density for the surface layer is much higher than the quantum well, no charges populate the surface layer [121]. Panel (c) is a schematic of the cross-section of the 2D heterostructure for the scenario depicted by the band structure in panel (d). Here the top gate bias is over the saturation voltage V_{sat}. At this point, electrons tunnel from the 2DEG into the surface layer, and the density is raised above critical density of the metal-insulator transition

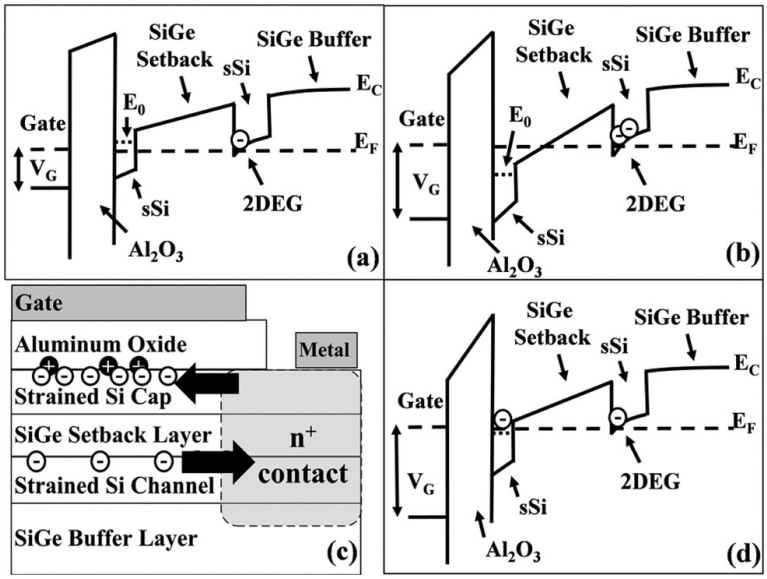

Figure 3.9: Schematic illustrating the formation of the surface layer, reproduced from Ref. [121]. Panel (a) corresponds to the regime $0 < V_{TG} < V_{th}$. Charge accumulates in the quantum well, but $n_{2D} < n_{c,QW}$ so the 2D transistor behaves as an insulator. In panel (b) $V_{TG} > V_{th}$ and $n_{c,QW} < n_{2D} < n_{c,SL}$, where current flows through the quantum well forming a 2DEG but no charges populate the surface layer. The regime of $V_{TG} > V_{sat}$ and $n_{2D} > n_{c,SL}$ is given in panels (c) which is a schematic of a cross-section of the 2D device, showing electrons in both the quantum well and the surface layer and the equivalent band structure in (d), where both the quantum well and the surface layer are populated with electrons at the same Fermi level.

for the surface layer, resulting in a current flowing from the ohmic contacts into the surface layer. From Gausss law, for a fixed gate voltage, the electron density of the 2DEG must be reduced as the density of electrons in the surface layer increases, in order for charge to be conserved. In this regime electrons exist in both the surface and the buried quantum well, with the same Fermi level for both layers.

These 3 regimes correspond to those seen in our data, where above the saturation voltage V_{sat}, this tiny current through the surface layer does not leak to the metallic top gate hence no leakage current is detect. Rather this surface layer serves to screen the 2DEG (or corresponding 2DHG) from the top gate, resulting in the observed shift in the threshold voltage towards larger bias.

For the quantum dot devices to be fabricated from the 2D heterostructure later in this thesis, we wish to prevent the formation of this surface layer charge as it may interfere with the operation of the dot. Hence we shall use operating voltages below the saturation voltage of $V_{TG} = +10$V for the W0639 2DES device and $V_{TG} = -1.6$V for the W0640 2DHS device.

Due to this shift, when characterizing the density and mobility of our wafers we did not push the top gate bias beyond the saturation voltage. Several 2D devices made from different wafers, were characterized for both holes and electrons, shown in Fig. 3.10 and Fig. 3.11 respectively. These measurements were taken at temperatures below 250mK.

3.5 Conclusion

In this section we outline the fabrication process of an induced 2D transistor (with and without low-dimensional nanostructures). We show characterization curves of two 2D transistors taken at 4K and found that if the top gate is biased beyond the saturation voltage, we enter a regime of hysteretic behaviour between the forward bias and reverse bias sweeps in conductance. This hysteresis and shift in the threshold voltage towards higher bias can be explained by the presence of an induced surface layer of charge between the insulating dielectric and the wafer surface, which screens the 2DEG from the top gate. For our quantum dot measurements in later chapters we wish to avoid

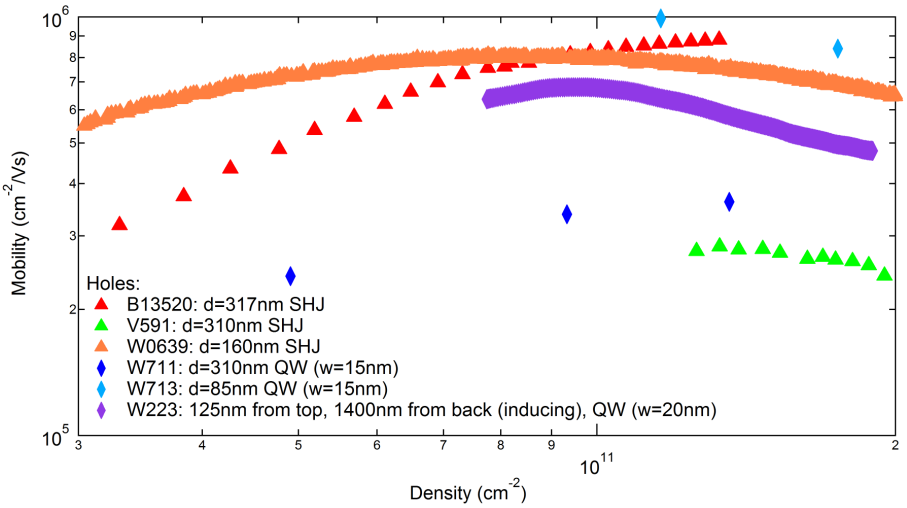

Figure 3.10: Plot of mobility versus density for a series of induced 2D hole transistors made from different wafers, for a combination of single heterojunctions and quantum wells, as marked in the legend. This data is a compilation of measurements performed by members of the QED group including, A. Srinivasan, D. Q. Wang and myself. Wafers were grown by different groups including the Semiconductor Physics group in Cavendish Laboratory and Bochum.

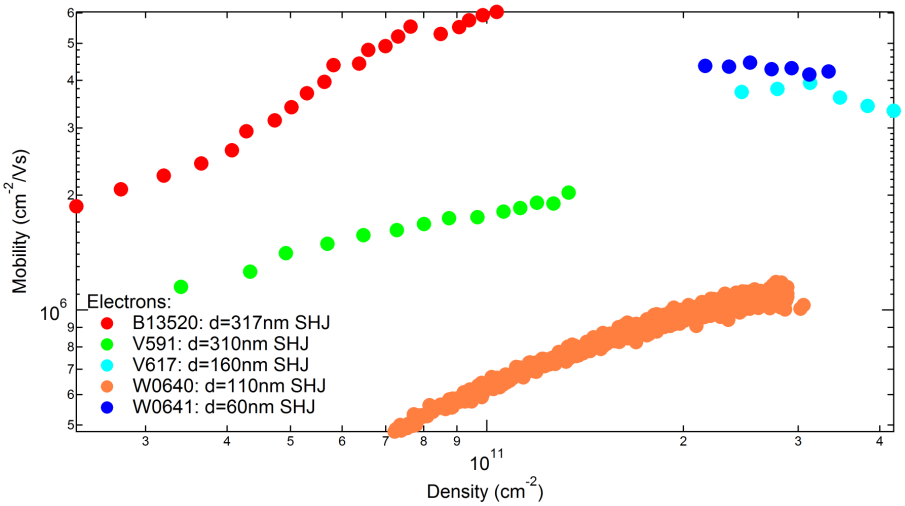

Figure 3.11: Plot of mobility versus density for a series of 2D electron transistors made from different wafers, for a combination of single heterojunctions and quantum wells, as marked in the legend. This data is a compilation of measurements performed by members of the QED group including, A. Srinivasan, D. Q. Wang and myself. Wafers were grown by different groups including the Semiconductor Physics group in Cavendish Laboratory and Bochum. Note: The mobility for wafer W0640 was much lower than expected (it should be similar to W0641) and is most likely due to the 2D device being fabricated from a piece near the edge of the wafer.

hysteretic behaviour in conductance and hence the top gate bias applied should remain well below this saturation voltage for any given 2D structure.

Chapter 4

Out-of-plane spin polarisation in a 2D hole system

4.1 Introduction

In the background Chapter 2.7.3, we briefly introduced literature describing the spin response of 2D GaAs heterostructures grown along high-symmetry crystal axes such as (100). It is well known that the spin-orbit interaction leads to anisotropy in the g factors $g^* = (g_x^*, g_y^*, g_z^*)$, such that the perpendicular g_z^* factor, is larger than the in-plane g factors $g_z^* \gg g_y^*, g_x^*$ [284] and that these in-plane g factors g_y^*, g_x^* are close to zero.

This chapter explores the concept of the anisotropic spin response and crystal symmetry, showing that the Landé g factor has a tensor structure, which is necessary to accurately describe the spin response of devices grown along low-symmetry crystal directions. We show that for a 2D system grown on a (311) substrate, applying an in-plane magnetic field B_x can generate a net spin polarization σ_z perpendicular to the applied field. This body of work constitutes one of the rare occasions in which we are able to directly probe off-diagonal elements in the gyromagnetic tensor and was recently published: L. A. Yeoh *et al.*, Phys. Rev. Lett. **113**, 236401 (2014).

We begin the chapter by introducing the unique properties of low-symmetry crystals in GaAs, and review measurements of the anisotropic g factor in such systems,

followed by tilted field measurements in 2D systems. This is followed by an explaination of the experimental concept, measurement setup and calibration. We then present our tilted field transport datasets, comparing the differences between data taken along a high-symmetry axis, to the data taken along a low-symmtry axis and discuss the complexities of modelling the band structure of a 2D hole system in tilted fields.

4.2 Background

4.2.1 Low symmetry crystals and non-collinear spin polarisation

A general (mmn) crystal lattice can be described by a Cartesian co-ordinate system with unit vectors $\hat{x}$, $\hat{y}$, $\hat{z}$, where $\hat{z}$ (which is the vector normal to the (mmn) plane) is rotated by an angle θ from the high-symmetry [001] crystal direction, illustrated in Fig. 4.1. The corresponding g factors can be expressed as a function of this angle θ between the high symmetry [100] direction and the arbitrary growth direction $[nmm]$ [286]:

$$g^*_{xx} = g^*_{yy} = -6K(2 - 3\sin^2\theta)\sin^2\theta, \tag{4.1}$$

$$g^*_{xz} = 12K(2 - 3\sin^2\theta)\sin\theta\cos\theta, \tag{4.2}$$

and $g^*_{zz} = 6\kappa = 7.2$ is the same as that given in the background Chapter 2.7 [284]. Here K is a coefficient based upon the Luttinger parameters scaled by θ [286].

These numerical calculations of g factors at the $k_{\|} = 0$ band edge, along the two orthogonal in-plane directions are given in Fig.4.1b. From this figure, higher symmetry growth directions such as [100] have zero in-plane g factors $g^*_{xx}(k{=}0) = g^*_{yy}(k{=}0) = 0$ (indicated by a purple diamond). However, for the lower symmetry [311] direction, the g factors exhibit a distinct in-plane anisotropy such that $g^*_{xx} = g^*_{yy} = -0.16$ and $g^*_{xz} = 0.65$ (shown by green circles) [286].

$\boldsymbol{k \cdot p}$ theory predicts that 2D hole quantum wells grown along a low symmetry surface, within a non-centrosymmetric zinc blende crystal structure, possess strong spin-orbit (SO) interaction, leading to exotic spin behaviour [284, 286]. One such surface is the experimentally popular (311) growth plane, due to its higher mobilities compared to other crystal directions [111]. The reduced symmetry results in non-

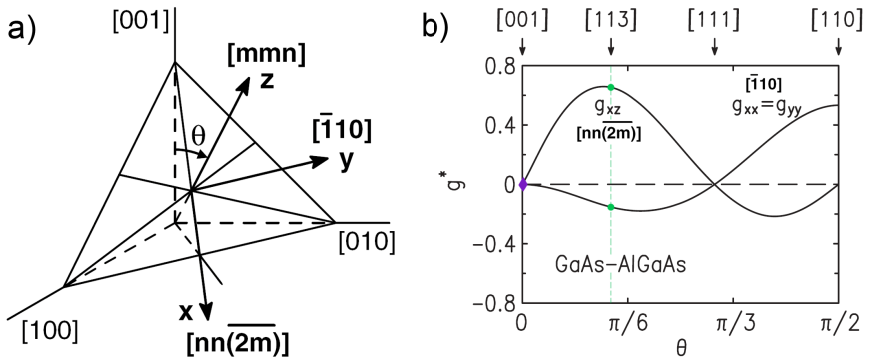

Figure 4.1: Crystal anisotropy of the hole g factor (a) Schematic of the co-ordinate system for lower-symmetry crystal directions as a function of angle θ with respect to a high symmetry [001] lattice orientation reproduced from Ref. [282]. (b) Numerical diagonalization of the 4×4 Luttinger Hamiltonian $\mathcal{H}_{8v8v}$ adapted from Ref. [286], demonstrating the anisotropic behaviour of the effective g factor of the first hole subband, for a GaAsAlGaAs quantum well, plotted as a function of crystal orientation where θ is the angle between [001] and the growth directions as defined in panel (a). Note: Refs. [282, 284], also plot g^* as a function of θ similar to that in panel (b). For our purposes the figure from Ref. [286] is preferred for greater clarity - it provides a segregates the g factor contribution from the off-diagonal elements of the gyromagnetic tensor (in the form of g^*_{xz}), from the diagonal element contributions (g^*_{xx},g^*_{yy}), unlike the other two references which plot the sum of g^*_{xx} and g^*_{xz}.

vanishing $B_{\|}$-linear Zeeman terms and finite g factors at $k_{\|} = 0$, resulting in the need for higher order terms in the Hamiltonian to be taken into consideration in order to fully describe the underlying spin behaviour.

Quantum wells grown along the low-symmetry [311] direction exhibit spatial symmetries described by the point group $\mathcal{C}_{2h}$ - this includes mirror symmetry in the plane perpendicular to the $[01\bar{1}]$ direction and two-fold rotational symmetry within that plane [284]. To describe these lower symmetries, we define a Cartesian co-ordinate system where the unit vectors $\hat{x}$, $\hat{y}$, $\hat{z}$ are parallel to crystal directions $[\bar{2}33]$, $[01\bar{1}]$ and [311] respectively. The most general effective Zeeman Hamiltonian describing the lowest heavy hole subband that is consistent with this symmetry [210, 284], in the presence of a magnetic field $\boldsymbol{B} = (B_x, B_y, B_z)^T$ is given by

$$\mathcal{H}_Z = \frac{\mu_B}{2} \boldsymbol{B}^T \cdot \underline{g}^* \cdot \boldsymbol{\sigma} \quad , \tag{4.3}$$

where $\boldsymbol{\sigma} = (\sigma_x, \sigma_y, \sigma_z)^T$ are the spin-1/2 Pauli matrices, T denotes the transpose of

the matrix and $\underline{g}^*$ is a tensor of the form [287, 298]

$$\underline{g}^* = \begin{pmatrix} g^*_{xx} & 0 & g^*_{xz} \\ 0 & g^*_{yy} & 0 \\ g^*_{zx} & 0 & g^*_{zz} \end{pmatrix} \quad . \tag{4.4}$$

This general Hamiltonian Eq. 4.3 makes a few predictions about the anisotropic in-plane response of g^* to the direction of the magnetic field. If the field is applied along the higher symmetry $[01\bar{1}]$ direction, the only Zeeman splitting contribution would come from g^*_{yy}. On the other hand, if the field is applied along the lower symmetry $[\bar{2}33]$ direction, there is an in-plane Zeeman contribution from g^*_{xx} plus an extra g^*_{xz} contribution.

4.2.2 Anomalous out-of-plane spin polarisation on low symmetry (311) substrates

As seen from Eqs. 4.3 and 4.4, the Zeeman Hamiltonian for any arbitrary crystal growth direction $[nmm]$ at $k_{\|} = 0$, can be expressed as [286],

$$\mathcal{H}^{HH}_{[nmm]} = \frac{\mu_B}{2}(g^*_{xx}B_x\sigma_x + g^*_{xz}B_x\sigma_z + g^*_{yy}B_y\sigma_y + g^*_{zx}B_z\sigma_z + g^*_{zz}B_z\sigma_z) \quad . \tag{4.5}$$

The Hamiltonian contains an unusual off-diagonal term $g^*_{xz}B_x\sigma_z$, which couples the in-plane field B_x to the out-of-plane spin σ_z when the in-plane field is applied along the low symmetry $[\bar{2}33]$ direction, i.e. $B_x \rightarrow \sigma_z$. This generates an additional, anomalous out-of-plane spin polarization on top of the in-plane component denoted by $g^*_{xx}B_x\sigma_x$. The value of $g^*_{xz} = 0.65$ is >4 times larger than its corresponding in-plane counterpart $|g^*_{xx}| = |g^*_{yy}| = 0.16$. This non-collinear spin response phenomenon is unique to low symmetry zinc blende structures and does not occur for 2D systems grown in the high symmetry [100] direction[1].

[1] At present not much is known about the effect of the g^*_{zx} term contained within the general g tensor, since most magnetic field studies to date have been performed with either a fully perpendicular field (where g^*_{zz} dominates over g^*_{zx}) or a fully in-plane field, in which there is no B_z, resulting in a non-existent $g^*_{zx}B_z\sigma_z$ term, such as Eq.10a in Ref. [286]. From symmetry considerations one may anticipate g^*_{zx} to be of the same order of magnitude as g^*_{xz}. However in our 2D system, this term is negligible within the high parallel field, low perpendicular field parameter space considered in our experiment as demonstrated in the supplementary material of Ref. [298], and thus this term will be discarded from subsequent Hamiltonians in the remainder of this chapter.

4.2.3 Experimental review of hole g factor anisotropy for low-symmetry GaAs crystals

Demonstrations of the in-plane g^* anisotropy in a low symmetry (311) hole system have been performed by Papadakis *et al.* [201] and Winkler *et al.* [282], in a 20nm GaAs quantum well. Two hall bars were fabricated to form a L-shaped pattern, aligned along the two orthogonal in-plane directions $[\bar{2}33]$ and $[01\bar{1}]$. Magnetoresistance traces taken for two current directions along each crystal axes, indicated by dashed and solid lines in Fig. 4.2 [286]. Although the resistivity traces have different slopes due to mobility anisotropy between the two crystal directions [111, 202], changing the current direction (parallel and anti-parallel) does not affect the subband depopulation point B_d (indicated by arrows). However, the depopulation field is significantly larger when the field is applied along $[01\bar{1}]$ ($B_d \sim 10T$) compared to along $[\bar{2}33]$ ($B_d \sim 4T$). In such 2D transport measurements, g^* is averaged over $g^*(\boldsymbol{k}_\parallel)$ up to the Fermi wave vector k_F, due to the dependence of g^* upon $\boldsymbol{k}_\parallel$, rather than representing a pure g^* at $\boldsymbol{k}_\parallel = 0$.

Despite this, the result provides evidence for the in-plane anisotropy where $g^*_{[\bar{2}33]} > g^*_{[01\bar{1}]}$. The $\boldsymbol{k} \cdot \boldsymbol{p}$ calculations by Winkler suggest this large anisotropy was due to the presence of a non-collinear spin response stemming from the reduced symmetry of the lattice. Despite this theoretical understanding of the origins of the anisotropic in-plane g factor, to-date there has been no direct observation of the non-collinear contribution to spin-splitting due to the off-diagonal g^*_{xz} component.

4.2.4 Tilted field measurements and the coincidence method

One way to probe the non-collinear spin response stemming from the off-diagonal $g^*_{xz}B_x\sigma_z$ component is to measure its contribution to Zeeman spin splitting of the Shubnikov-de Haas (SdH) oscillations for a series of different in-plane fields. This can be achieved by performing transport measurements of the longitudinal magnetoresistance whilst tilting the sample within a magnetic field.

When studying spin splitting in the longitudinal magnetoresistance (Shubnikov-de Haas, SdH) oscillations of a 2D system in a perpendicular magnetic field, a naïve ap-

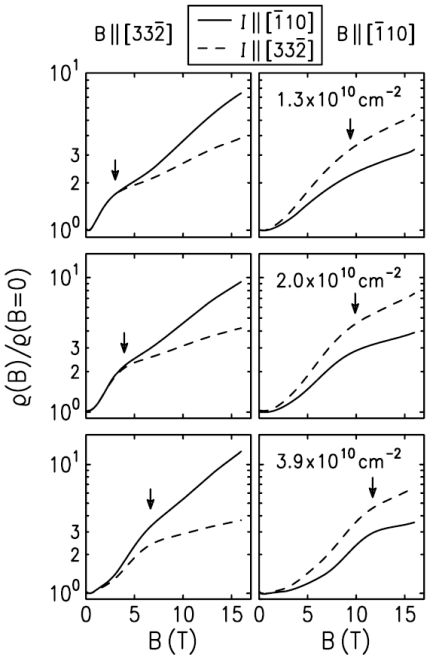

Figure 4.2: Anisotropy of the depopulation field B_d (arrows) along the two crystal directions [$\bar{2}$33] and [01$\bar{1}$]. No change in B_d occurs when the direction of the current is switched, indicating this in-plane anisotropy is purely a crystal symmetry effect [286].

proach may be to derive the spin splitting energies, through comparing the separation of the two spin states in field, to the separation of adjacent energy levels $\hbar\omega_c$. However, due to the discontinuity in the Fermi energy as it jumps between spin states in a 2D system, the peak positions of the SdH oscillations cannot be directly related to the energy spacing.

This can be overcome by using the tilted field Landau level 'coincindence method', developed by Fang and Stiles for 2D electrons in silicon [75] which involves rotating a 2D sample in a magnetic field by a known angle θ. Applying a total magnetic field B_{tot} at an angle θ with respect to the normal of the 2D plane, the perpendicular field component becomes $B_z = B_{tot}\cos\theta$. Since the formation of Landau levels are exclusively dependent upon B_z, and described by $\hbar\omega_c \equiv \hbar\frac{eB_z}{m^*}$, whilst the Zeeman splitting is dependent upon the magnitude of the total field B_{tot} [75], the spin splitting can be calculated at certain critical angles, where the Zeeman splitting is equal to half

the Landau level separation [75, 193]

$$|g^*\mu_B B_{tot}| = r\frac{1}{2}\hbar\omega_c \tag{4.6}$$

where the parameter $r = (1, 2, 3, ...)$ corresponds to a ladder of *coincident* spin-up and spin-down energy levels from different Landau levels, and $r = (\frac{1}{2}, \frac{3}{2}, \frac{5}{2}, ...)$ corresponds to a ladder of *alternating* spin-up and spin-down energy levels [193]. From this the g factor can be calculated provided m^* is known

$$g^* = \frac{1}{2}\frac{e\hbar}{m^*\mu_B}\cos\theta \tag{4.7}$$

This analysis rests upon the assumptions of an isotropic g^* and ignores orbital coupling of the in-plane field due to the finite thickness of the quantum well width.

4.2.5 Experimental review - tilted field measurements of 2D systems

The tilted field coincidence angle technique has been successfully used to study the evolution of the Landau level energy gaps in a variety of 2D electron systems such as: InAs [246], GaAs [193, 203, 307] and paired with other material combinations [143], InGaAs [60, 61], ZnO [267], Graphene [304] and HgTe [292] to name a few. Some were performed in conjunction with cyclotron resonance to provide an independent measure of the effective mass [60, 193, 203] and hence calculate the g factor, whilst others have instead focused upon the evolution of anticrossings due to SO coupling in narrow gap heterostructures [61] and the fractional quantum hall effect [73].

In comparison there have been fewer tilted field studies performed in 2D hole systems. Preliminary research into the Landau level spectrum of GaAs include studies into the symmetry of the confining potential [125] and the effect of strain [177] in narrow quantum wells. Both studies discovered that the amplitude of the spin-split (odd) minima remains constant and unaffected by the increase in total field, which was interpreted in terms of decoupling between light and heavy holes. A brief study into the effect of the in-plane field upon magnetoresistance oscillations by Heuring *et al.* comparing theory with transport data, also showed that only certain minima are affected by the parallel field, whilst the rest remain unchanged [112]. The authors attribute this effect to strong level mixing.

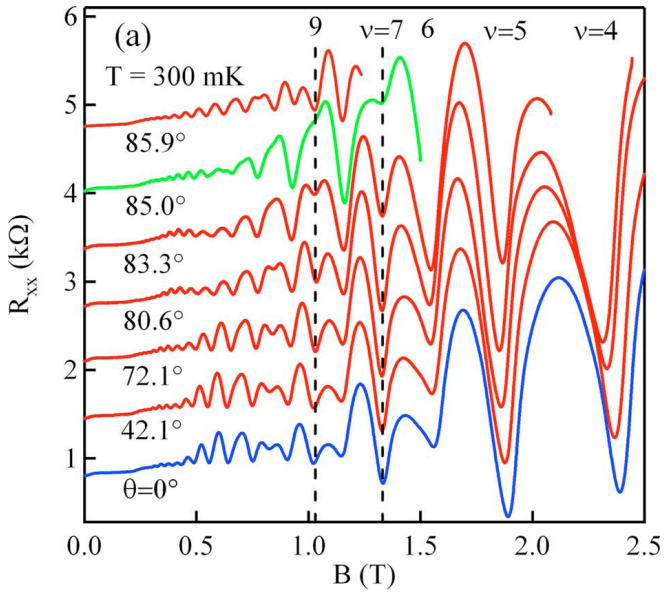

Figure 4.3: Tilted field SdH traces for a (100) asymmetrically doped 15nm GaAs quantum well showing coincidence at 85° [300].

A few tilted field measurements have been performed to study the g factor of GaAs 2D hole devices grown on a (100) surface. Rahimi *et al.* [218] performed compressibility studies in tilted fields and found that despite the application of a 10T in-plane field, there was no systematic dependence of the spin splitting for Landau level filling factors $\nu = 1$ and $\nu = 3$, upon the parallel component of the field, which suggests that the in plane g factor for high symmetry zinc blende crystals is close to zero [218]. On the other hand, transport measurements in a (100) carbon-doped 15nm GaAs quantum well were performed by Yuan *et al.* to study the SdH oscillations at different tilt angles, shown in Fig. 4.3 [300]. The authors measured $m^* \approx 0.4$ in a separate cyclotron resonance experiment (taken at 4K), and for a coincidence angle of 85° calculated the out-of-plane g factor to lie between $7.2 > g^*_{zz} > 5$ [300]. However, the coincidence method assumes equally spaced energy levels, isotropic g^* and parabolic energy bands, so although this method works well for electron systems, the authors mentioned that difficulties arose when applying this method to hole systems due to their complex, non-parabolic band structure. The non-linear behaviour of the Landau levels and the anisotropy of both g^* and m^* in hole systems will be discussed in greater depth in Section 4.6.2.

More recent transport studies into the effective mass of holes in a dilute low-

symmetry (311)A GaAs quantum well 20nm wide have shown that $m^* \sim 0.2$ [41]. Using a sufficiently strong parallel magnetic field (up to 16T) to fully depopulate one of the spin subbands, and measuring m^* for the populated subband, the authors found that m^* obtained from the spin polarized subband is very close to the unpolarized value, and concluded that in contrary to expectations stemming from previous work in 2D electrons [268], the perpendicular field has the greatest effect upon m^*. This is a suprising contradiction to theoretical expectations which predict that a large in-plane field should couple to the hole's orbital motion leading to an enhancement in m^* compared to the electron case [268], although the reason behind this lack of m^* enhancement in 2D holes is not obvious [41]. However Chiu *et al.* [41] measured an increase in m^* with increasing perpendicular field, a similar trend to that previously reported by [68, 96]. Once again, the authors mentioned that the origin of this is not fully understood [41], but is likely related to the non-linear dependence of the 2D hole Landau levels [48, 200, 217].

From these experiments, Chiu *et al.* [41] also deduced the spin susceptibility ($\chi^* \propto g^* m^*$) of the 2D hole system from the depopulation field and obtained a value of $g^* m^* \cong 0.19$ which is an enhancement of 1.5 when compared to the theoretical values of $m^* \sim 0.2$ and $g^*_{xz} = +0.65$ at the k=0 band edge [284]. The authors remarked that this enhancement in $g^* m^*$ is smaller than the factor of two seen in equivalent electron systems and suggest that this lack of enhancement could be due to the holes band structure and large effective spin [285].

These experiments show that much still remains unknown about the unusual spin behaviour of holes in low symmetry 2D systems and further investigation is needed. Although magnetic depopulation studies have suggested the presence of an off-diagonal contribution to spin polarization from g^*_{xz}, no direct measurement of its effect has been made to date.

4.3 Detecting non-collinear spin polarization

In this section we demonstrate that the interplay between quantum confinement and the crystal structure means that the Zeeman splitting in confined hole systems is not

merely anisotropic, but that a magnetic field applied in one direction can generate a net spin polarisation of the delocalised 2D holes at right angles to the applied magnetic field. Since the number of holes in a 2D quantum well is low, it is hard to directly detect this polarisation with torque magnetometry or SQUID techniques [69, 182, 279]. Instead we use tilted field transport measurements to achieve the required sensitivity.

4.3.1 Experimental concept

To access the off-diagonal elements of the g tensor in Eq. 4.4 and hence observe the unusual out-of-plane spin polarisation via transport measurements, we use tilted fields shown in Fig. 4.4 to control the interplay between the terms contributing to the out-of-plane spin polarisation in the Hamiltonian described by Eq. 4.5. In transport measurements of the SdH oscillations in perpendicular field, we effectively detect the density of states at the Fermi energy which are affected by both an orbital component and a Zeeman component. Applying a large in-plane field B_x along the $[\bar{2}33]$ direction generates a spin polarization in the out-of-plane [311] direction due to the non-collinear $g^*_{xz}B_x$ term. Simultaneously, a perpendicular magnetic field B_z can be applied along the [311] direction which generates a perpendicular spin polarization proportional to $g^*_{zz}B_z$. The resulting total Zeeman energy can be expressed as,

$$\Delta E = \sqrt{(g^*_{xx}B_x)^2 + (g^*_{zz}B_z + g^*_{xz}B_x)^2} \quad . \tag{4.8}$$

Tilting the sample with respect to a total magnetic field $B_{tot} = B_{\|} + B_z$, by an angle θ changes the total Zeeman energy, which manifests as a splitting in the SdH oscillations at larger in-plane fields. Varying this tilt angle enables us to control the sign of the ratio B_x/B_z through the sign of θ, as the total Zeeman energy is being varied. If θ is positive as depicted in Fig. 4.4a, a positive B_x results in the term $g^*_{xz}B_x$ adding to $g^*_{zz}B_z$, enhancing the anomalous out-of-plane spin polarization arising from the in-plane field, which increases the spin-splitting in the SdH oscillations. In contrast, if θ is negative as shown in Fig. 4.4b, the negative sign of B_x means that $g^*_{xz}B_x$ is subtracted from $g^*_{zz}B_z$ resulting in a suppressed out-of-plane spin polarization and a reduction in the splitting of the SdH oscillations. The amount of interplay between the two terms can also be studied by changing the magnitude of θ.

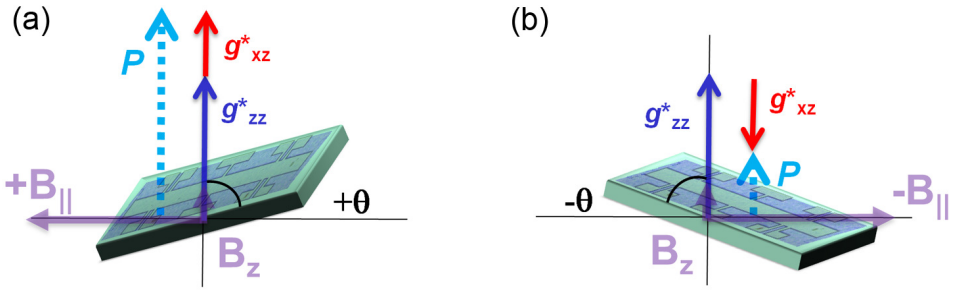

Figure 4.4: Experimental concept for detecting the out-of-plane spin polarisation. (a) Positive tilt angles $+\theta$ correspond to $+B_{\|}$ and g^*_{xz} adds to g^*_{zz} resulting in a net spin polarization $\mathcal{P}$. (b) The opposite occurs for negative tilt angles $-\theta$ which introduces a $-B_{\|}$, so g^*_{xz} subtracts from g^*_{zz} and $\mathcal{P}$ is reduced.

4.3.2 Device details and measurement setup

The high-mobility 2D hole system (2DHS) samples, fabricated by Prof. A. R. Hamilton, were grown on a low-symmetry (311)A surface, from a GaAs/$Al_{0.33}Ga_{0.67}As$ heterostructure in a T335 wafer by the Semiconductor Physics group at Cavendish Laboratory. The conducting substrate doubles as an *in situ* back-gate, located 2.6μm away from a symmetrically modulation Si-doped 20nm wide GaAs quantum well [243]. At zero gate bias the device has a density of $p_{2D} = 1.33 \times 10^{11}\text{cm}^2$ and a corresponding mobility of $\mu = 0.678 \times 10^6\text{cm}^2\text{V}^{-1}\text{s}^{-1}$. The energy spacings between subbands are large enough that only the lowest HH band is occupied.

To perform transport measurements in tilted magnetic fields, the sample was mounted on a 'home' built *in situ* piezoelectric rotation system, featuring an in-built angle readout mechanism with an accuracy of $\pm 0.01°$ [299], shown in Fig. 4.5c. This allowed for single-axis rotation to be conducted at a base temperature of 35mK cooled by an Oxford K100 dilution refrigerator, within the bore of a 15T superconducting magnet (refer to Appendix A.1 for more information about the system). The magnitudes and relative signs of B_x, B_y and B_z are controlled by tilting the sample with respect to the total field of the magnet by some angle θ, shown in Fig. 4.5(a,b).

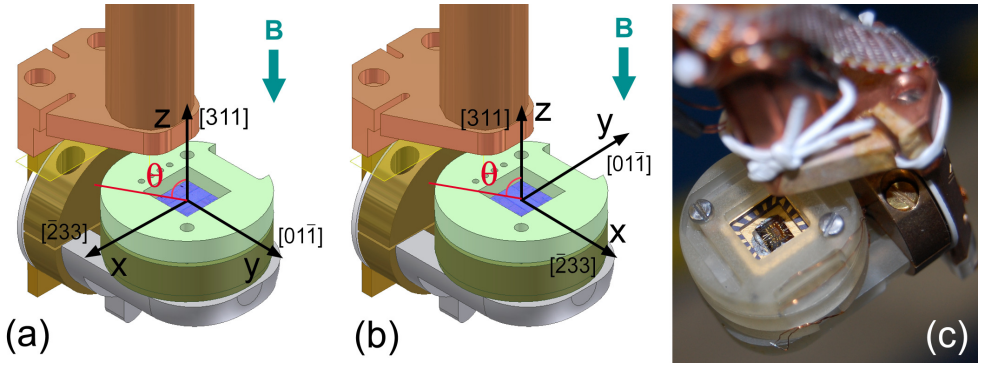

Figure 4.5: (a) 3D model with co-ordinate axes, showing sample orientation aligned to rotate between the [311] perpendicular direction and the [$\bar{2}$33] in-plane direction within a magnetic field. (b) Sample oriented to rotate between the [311] and [01$\bar{1}$] directions. (c) Photo of a device within sample holder mounted onto the piezoelectric rotator.

Electrical setup for 2D transport measurements

To study the Shubnikov-de Haas (SdH) oscillations transport measurements were performed using standard ac lock-in techniques, with a constant ac current of 10nA at a frequency of 5Hz. The measurement setup is depicted in Fig. 4.6.

4.4 Preliminary measurement setup, calibration and device checks

4.4.1 Characterizing the measurement setup

Before beginning the experiment, the following calibration and characterization checks were performed at a temperature of 4K prior to cooling the fridge to its base temperature.

1. Calibrating the angle readout of the sample and rotator with respect to the magnetic field: achieved by using the 2D Hall bar as a Hall sensor and rotating it in field to find the exact angles where the plane of the 2D sample is parallel and perpendicular with respect to the total field. Refer to Appendix B for calibration graphs and more details.

2. Characterize magnet hysteresis: with the sample oriented perpendicular to the

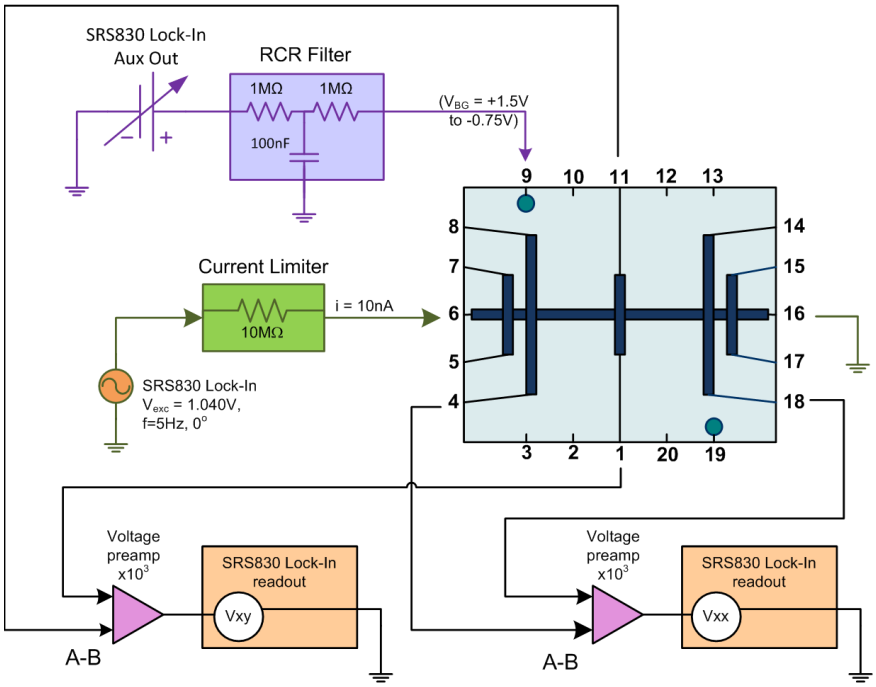

Figure 4.6: Electrical setup used to perform the tilted field transport measurements. A SRS830 lock-in amplifier provides an ac excitation current to the source ohmic which travels along the length of the hall bar, as well as a DC voltage via a RCR filter to the back gate to tune the confining potential. Separate probes were used to simultaneously measure the Hall and longitudinal voltages.

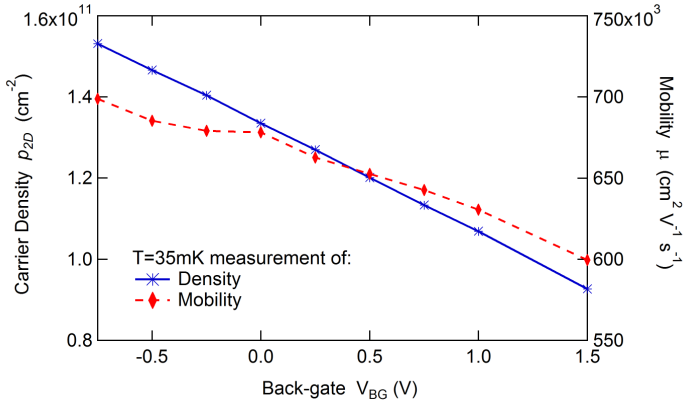

Figure 4.7: Plot of 2D density (blue) on the left axis, and mobility (red) on the right axis, versus back-gate voltage for our 20nm wide GaAs quantum well heterostructure fabricated from a T335 wafer and measured at 35mK.

magnetic field, the magnetic field was swept through $B = 0$ to a series of different $\pm B$ targets at different sweep rates and the Hall resistance measured. We discovered a small hysteresis of ± 35mT at $B = 0$. As the area enclosed by the hysteresis loop is constant, a hysteresis correction procedure was written which was then applied to the longitudinal resistivity measurements taken at tilted fields, scaled for tilt angle. More details on the correction procedure and hysteresis characterization are given in Appendix B.

4.4.2 Characterizing the 2D hole device

As the device is modulation doped, it is nominally on (non-zero density and mobility at $V_{BG} = 0$V), though the 2D hole density increases linearly with more negative back-gate bias and the device effectively behaves as a transistor. Measurements of density and mobility taken at 35mK are given in Fig. 4.7. The density was obtained from the Hall resistance and the mobility μ calculated from the density and measured zero field longitidinal resistivity ρ_{xx} according to $\mu = \frac{1}{\rho_{xx}(B=0)p_{2D}e}$, where e is the electronic charge.

The mobility in this device increases with density. At $V_{BG} = +1.50$V, corresponding to $p_{2D} = 9.26 \times 10^{10}\text{cm}^{-2}$, the hole mobility is $0.6 \times 10^{6}\text{cm}^2\text{V}^{-1}\text{s}^{-1}$, which gives a mean free path $l \approx 3\mu$m at this gate voltage.

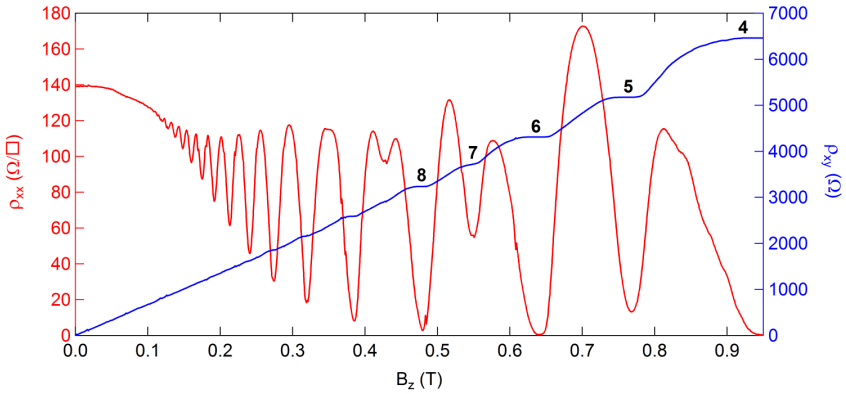

Figure 4.8: Plot of SdH oscillations ρ_{xx} (in red) and corresponding Hall plateaus (in blue) as a function of perpendicular field B_z, taken at the symmetric operating point of $V_{BG} = +1.50$V, where the 2D carrier density is $p = 9.26\times10^{10}\text{cm}^{-2}$ and the mobility $\mu = 0.6\times10^{6}\text{cm}^{2}\text{V}^{-1}\text{s}^{-1}$.

4.4.3 Aligning sample axes to the magnetic field

Initially the 2D sample was rotated to $\theta = 90°$, so the magnetic field lay perpendicular to the sample plane, $B_z \neq 0$, $B_{\|} = 0$. The sample orientation was confirmed by the rotator's pre-calibrated angle readout mechanism, detailed in Appendix B. An initial measurement was taken at $\theta = 90°$, of the Hall plateaus as a function of perpendicular field, shown in Fig. 4.8 (blue) to check the device was functioning at base temperature. The corresponding low-field oscillating longitudinal resistivity is shown in red, with spin splitting appearing for $B_z > 0.35$T. This alignment was performed at the start of every cooldown and the hall plateaus were also used to independently verify the angle of rotation readout for every change in tilt angle θ.

4.4.4 Tuning the confining potential via Rashba SO

Once the sample was aligned such that the 2D plane is fully perpendicular to the magnetic field, we tuned the symmetry of the confining potential.

To minimize the $B = 0$T spin splitting due to inversion asymmetry, Rashba SO coupling was used to compensate the splitting due to Dresselhaus SO, by tuning the electric field across the quantum well using the *in situ* back-gate, such that their combined effect upon the spin splitting seen in the SdH oscillations ρ_{xx} and hence

the total SOI is minimized. The longitudinal resistivity was measured for a series of different back-gate biases, and plotted as a function of inverse filling factor $1/\nu$, shown in Fig. 4.9. Here $\nu = \frac{h}{e}\frac{p}{B_z}$, where h is the Planck constant, e the electronic charge and p is the 2D density at a given back gate voltage. The column on the right is the corresponding Fourier transform of each SdH trace, with the x-axis (frequency) scaled by the 2D carrier density to align the $1f$ and $2f$ peaks associated with the presence of two spin species.

The optimum operating point was identified as the back-gate bias where beating in the low field SdH oscillations was minimized, and the classical magnetoresistance dip at $B = 0$T arising from two-band transport (due to two different carrier densities and mobilities from the two spin species of heavy holes (σ_+ and σ_-)) was eliminated [68, 99, 190, 204].

This symmetric point was found to be $V_{BG} = +1.50$V, where the 2D hole density was $p_{2D} = 9.26\times10^{10}\text{cm}^{-2}$ with a mobility of $\mu = 0.6\times10^{6}\text{cm}^2\text{V}^{-1}\text{s}^{-1}$. At this point the Fourier transform shows a single peak and the dip at $B = 0$ in the SdH is reduced compared to the others. For this experiment only the lowest HH band is occupied.

To confirm the symmetric operating point, we examined the low field SdH oscillations in greater detail to check that the beatings of the SdH at this point were minimal. Fig. 4.10 plots the corresponding SdH traces for each back-gate voltage showing their periodicity in $1/B_z$. The amplitudes of these oscillations are normalized for clarity by multiplying the datasets by $e^{\frac{0.33T}{B_z}}$ to remove the envelope. From these traces we confirm that the operating voltage of $V_{BG} = +1.50$V exhibits the least amount of beatings, indicating that the combined effect of the Dresselhaus and Rashba SO interactions adequately compensate one another and are thus both minimized at $B = 0$. This operating point was selected as the final voltage used throughout the rest of the experiment.

4.5 Experimental Data

The low symmetry (311)A heterostructure under study possesses both a high symmetry axis $[01\bar{1}]$, and a low symmetry $[\bar{2}33]$ axis within the same sample, making it an

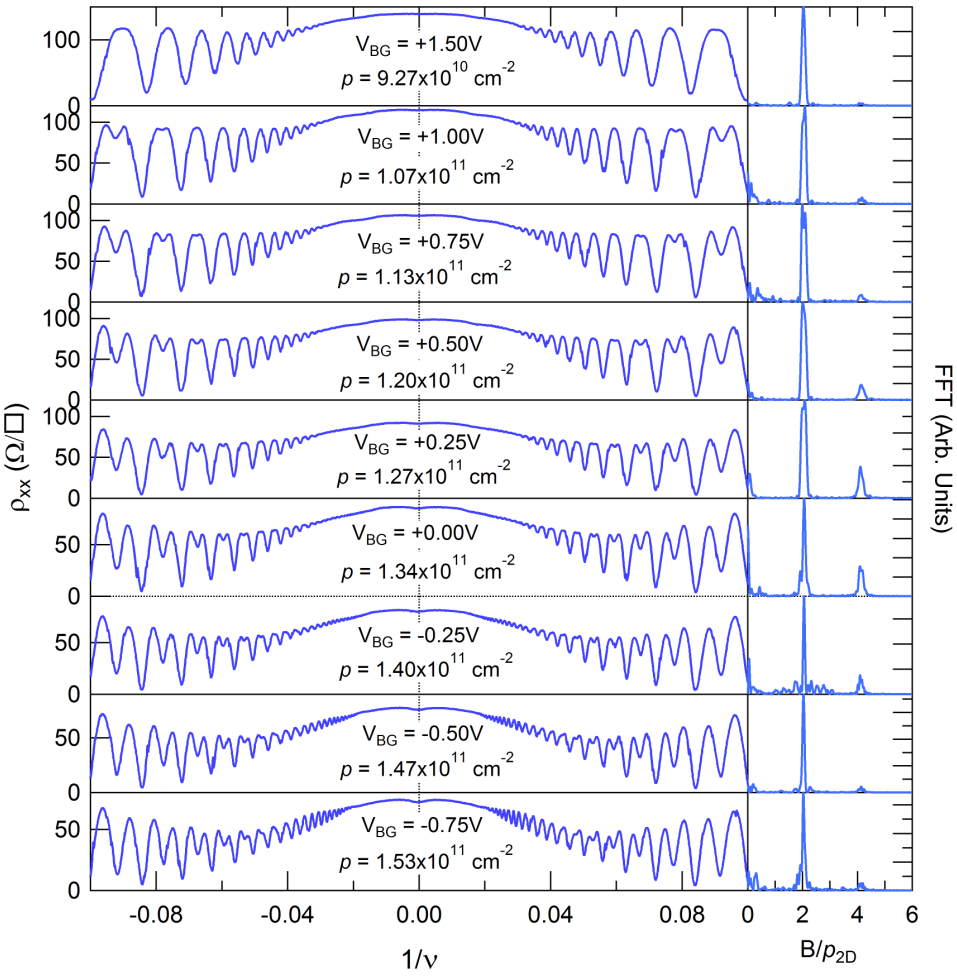

Figure 4.9: Tuning the confining potential via Rashba SO (a) SdH traces versus inverse filling factor taken at different back gate voltage biases, to tune the symmetry of the confining potential over the quantum well. In the top panel at $V_{BG} = +1.50$V, the 2D carrier density is $p = 9.26{\times}10^{10}\text{cm}^{-2}$ and $p = 1.53{\times}10^{11}\text{cm}^{-2}$ at $V_{BG} = -0.75$V at the bottom. (b) Corresponding Fourier transform of each SdH trace, where the x-axis is scaled by carrier density according to $B \times 1/p_{2D}$ for clarity in order to line up the $1f$ and $2f$ peaks.

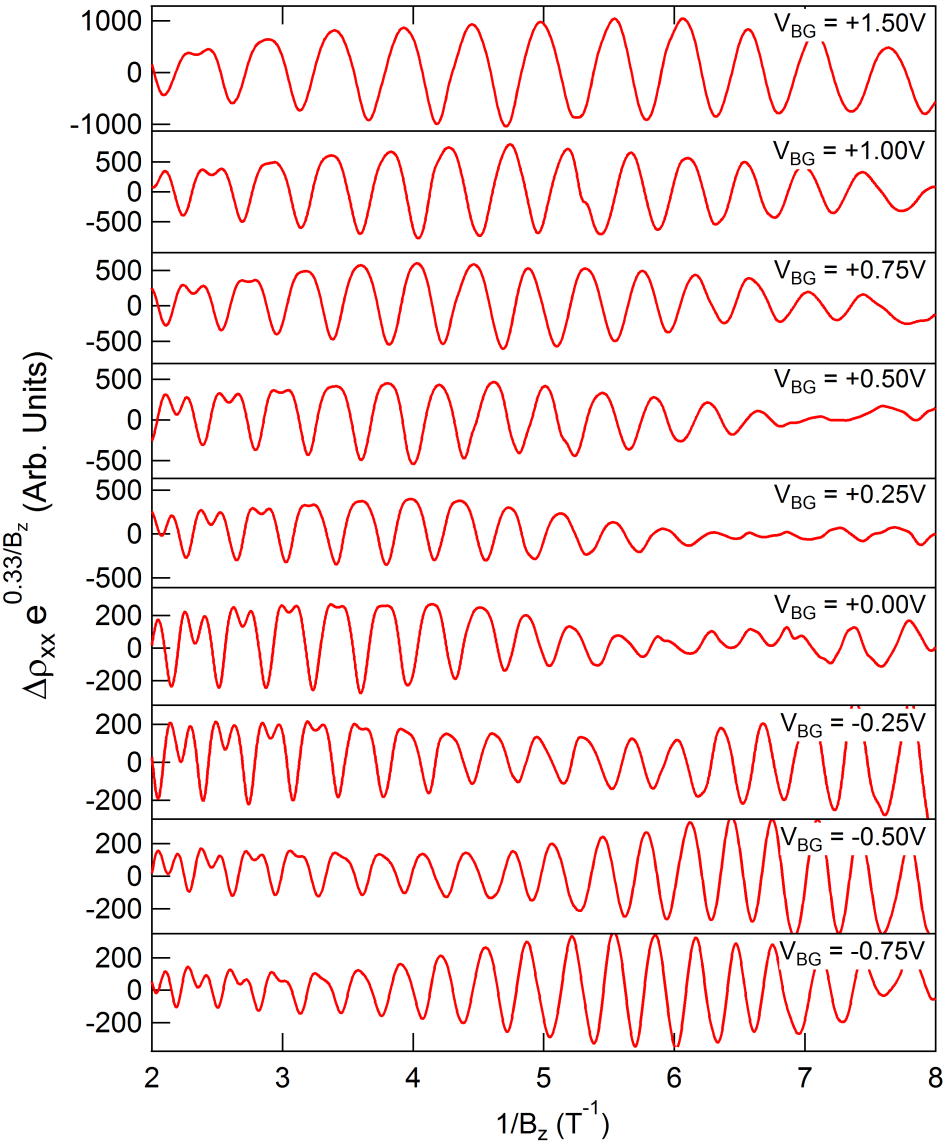

Figure 4.10: Corresponding plots of the SdH oscillations ρ_{xx} in Fig. 4.9 periodic in inverse B_z, for different back-gate biases, with their amplitudes normalized by $e^{\frac{0.33T}{B_z}}$. The tilt angle $\theta = 90°$, so that $B_{\|} = 0$T. In the top panel where $V_{BG} = +1.50$V, the 2D carrier density is $p = 9.26\times10^{10}$cm^{-2} and increases to $p = 1.53\times10^{11}$cm^{-2} at $V_{BG} = -0.75$V in the bottom panel. The back gate voltage $V_{BG} = +1.50$V, produces SdH oscillations with the least beating and hence this was selected as the operating point for the rest of the experiment.

ideal candidate for this study.

The experiment was conducted on two separate cooldowns, during one cooldown the sample was oriented within the sample holder, such that the total applied field B rotated between the crystal axes [311] in the perpendicular direction and the $[01\bar{1}]$ in-plane direction as depicted in Fig. 4.5b. The sample was rotated to its target angle and the total magnetic field swept both positive and negative, whilst the longitudinal resistivity was measured. This was repeated for a series of different angles. To study the other crystal axis, the sample was warmed back to room temperature, rotated by 90° and reinserted into the sample holder to tilt the total applied field B between the [311] perpendicular direction to the $[\bar{2}33]$ in-plane direction, illustrated in Fig. 4.5a. The series of measurements with field sweeps were repeated.

4.5.1 Tilted field results along high symmetry direction $[01\bar{1}]$

In this section we shall first consider the effect of tilted fields along a high symmetry crystal axis, where there is no out-of-plane spin polarization. In the case of high symmetry axes, there are no off-diagonal components in the g tensor and Eq. 4.4 can be reduced to $\underline{g}^* = (g^*_{xx}, g^*_{yy}, g^*_{zz})$.

Along the high symmetry $[01\bar{1}]$ crystal axis direction in our system, the effective Hamiltonian used in Eq. 4.5 becomes

$$\mathcal{H}^{HH}_{[01\bar{1}]} = \frac{\mu_B}{2}(g^*_{yy}B_y\sigma_y + g^*_{zz}B_z\sigma_z) \quad , \tag{4.9}$$

and the equivalent Zeeman energy splitting is described by

$$\Delta E_Z = \sqrt{(\frac{1}{2}g^*_{yy}\mu_B B_y\sigma_y)^2 + (\frac{1}{2}g^*_{zz}\mu_B B_z\sigma_z)^2} \quad . \tag{4.10}$$

For the first part of this experiment, we orient the sample with respect to the total magnetic field as shown in Fig. 4.11a, so that the sample rotates along the yz-plane (and $B_x = 0$). The field is first aligned along the [311] crystal growth direction and the sample rotated to introduce a field component parallel to the $[01\bar{1}]$ direction.

The magnetoresistance ρ_{xx} data are plotted as a function of B_z in Fig. 4.11c, for different tilt angles $\pm\theta$. Starting with the magnetic field fully perpendicular to the quantum well (top trace, $\theta = 0°$), the SdH oscillations show no sign of beating at

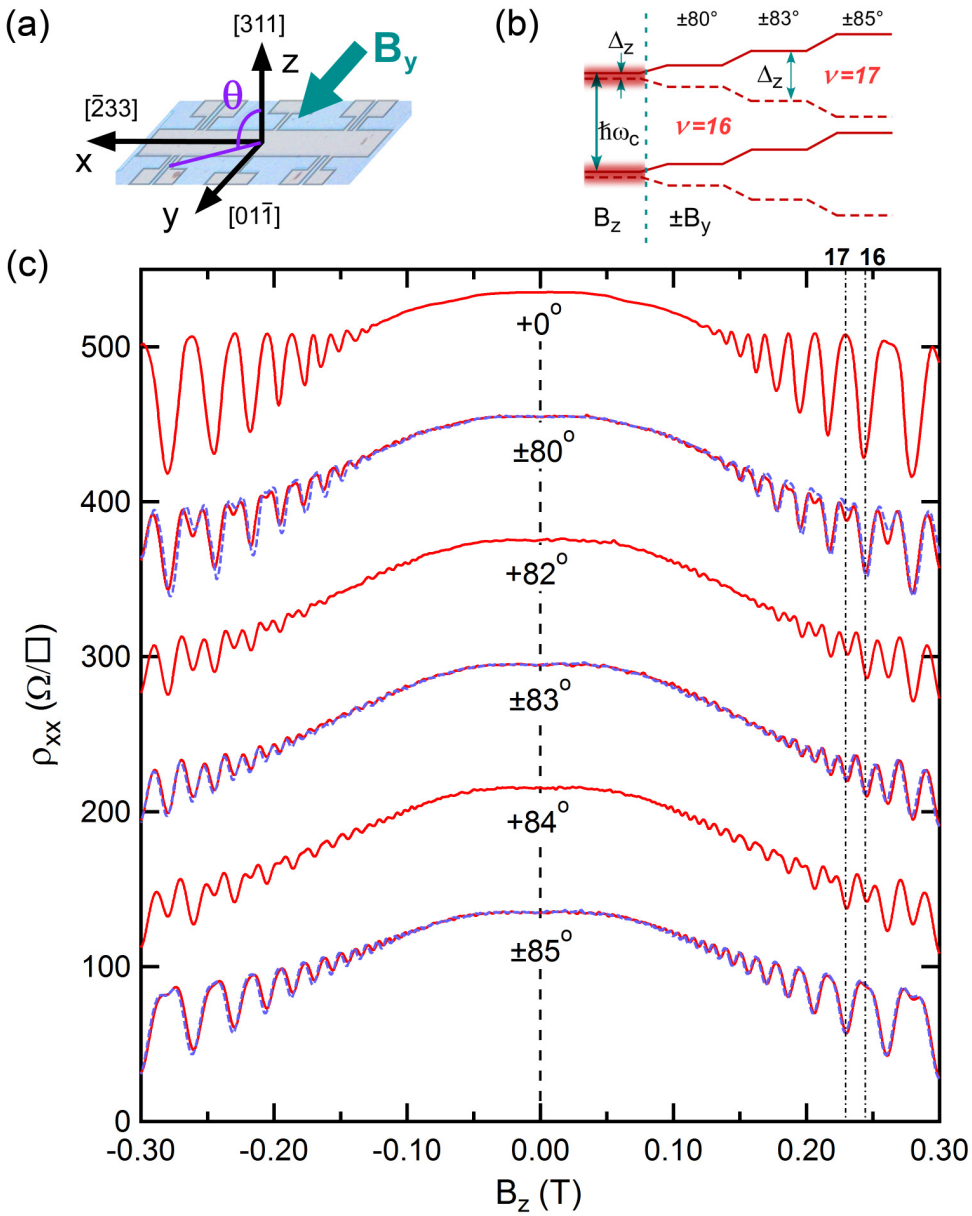

Figure 4.11: (a) Sample orientated in magnetic field, to rotate along the yz-plane ($B_x = 0$). Initially the total field was aligned along [311] ($B_{tot} = B_z$, $\theta = 0°$) and was rotated by θ to increase the component of field B_y along [01$\bar{1}$] and study the higher symmetry direction. (b) Schematic of the Landau level fan chart, starting with a purely perpendicular field B_z and illustrating the spin splitting introduced by a parallel field component B_y as the sample is tilted. (c) Magnetoresistivity traces taken at a series of tilt angles for $+\theta$ (solid red) and $-\theta$ (dashed blue). Filling factors ν=16 and ν=17 are marked by dashed vertical lines and the traces are offset by 80Ω/□ for clarity.

low fields and the even filling factors ν_{even} are dominant. The Landau levels remain spin degenerate up to $B_z \approx 0.25$T, with a well-defined ρ_{xx} minima at ν=16 and a ρ_{xx} maxima at ν=17. This is qualitatively different to the result of Yuan *et al.* [300] for an asymmetrically doped quantum well, who observed a dominant ν_{odd} throughout their dataset.

By tilting the sample, an in-plane field component B_y is introduced along $[01\bar{1}]$, which lifts the spin degeneracy of the Landau levels as indicated schematically in Fig. 4.11b. This can be seen by following the odd filling factors ν_{odd} such as ν=17 in Fig. 4.11c, where the peak at $\theta = 0^\circ$ evolves into a weak minimum at $\theta = \pm 80^\circ$. This dip becomes more prominent with increasing in-plane field and by $\theta = \pm 85^\circ$ the ν=17 ρ_{xx} maximum has evolved into a ρ_{xx} minimum. The opposite happens for even filling factors ν_{even}. For example, ν=16 starts as a well defined ρ_{xx} minimum at $\theta = 0^\circ$ and evolves into a ρ_{xx} maximum at $\theta = \pm 85^\circ$.

The most striking feature of the Fig. 4.11 dataset is its symmetry between traces taken at the same $|\theta|$, which is remarkably similar to what is expected for a 2D electron system. The SdH data are identical for both positive tilt $+\theta$ (solid red) and negative tilt $-\theta$ (dashed blue) angles. Moreover, the traces remain symmetric for both signs of $\pm B_z$, for both combinations of $\pm\theta$, and changing the sign of the ratio B_y/B_z has no effect (demonstrated in Fig. 4.13). This result reflects the symmetry of the Hamiltonian where the corresponding g tensor contains no off-diagonal elements.

A naïve approach is to analyse the data and attempt to extract g factors using the 'coincidence' method for 2D electrons [75, 203], by comparing the cyclotron energy gap (dependent on B_z) to the Zeeman energy gap (dependent on total field), to calculate the product $|g^* m^*|$. However as previously mentioned, this coincidence method assumes parabolic bands (constant m^*) and an isotropic g factor, neither of which is the case for 2D holes.

Nevertheless, a crude estimate of the product $|g^*_{zz} m^*|$ can be obtained from the $\theta = 0^\circ$ data by comparing the magnetic field at which the SdH oscillations first become visible ($\Delta\nu_{even} = \hbar\omega_c - g^*_{zz}\mu_B B$ at 0.12T) with the field at which spin splitting first appears ($\Delta\nu_{odd} = g^*_{zz}\mu_B B$ at 0.35T). This suggests that $g^*_{zz} m^* \sim 0.5$, which is much

lower than the theoretical expectation of $g^*_{zz}m^* = 1.4$ (where $m^* = 0.2$ and $g^*_{zz} = 7.2$ [284]. The reason for this apparent discrepancy will be addressed in later Section 4.6.2.

4.5.2 Tilted field results along low symmetry direction $[\bar{2}33]$

Having checked the SdH oscillations are symmetric despite a change in the sign of the parallel field along the high symmetry $[01\bar{1}]$ orientation (i.e. $\rho_{xx}(B_y) = \rho_{xx}(-B_y)$), we now turn our attention to the low symmetry direction to observe the effect of the out-of-plane spin polarization due to the presence of off-diagonal elements in the g tensor described by Eq. 4.4. In this case, we expect to detect the presence of a non-zero g^*_{xz} component as an asymmetry between corresponding SdH traces of $\pm\theta \equiv \pm B_x/B_z$.

In our system, Eq. 4.5 can be rewritten so the first-order Zeeman Hamiltonian specific for the low symmetry direction $[\bar{2}33]$ is expressed as

$$\mathcal{H}^{HH}_{[\bar{2}33]} = \frac{\mu_B}{2}(g^*_{xx}B_x\sigma_x + g^*_{xz}B_x\sigma_z + g^*_{zz}B_z\sigma_z) \quad , \tag{4.11}$$

and the corresponding Zeeman energy as

$$\Delta E_Z = \sqrt{(\frac{1}{2}g^*_{xx}\mu_B B_x)^2 + (\frac{1}{2}g^*_{zz}\mu_B B_z + \frac{1}{2}g^*_{xz}\mu_B B_x)^2} \quad . \tag{4.12}$$

To perform the second part of the experiment, the sample was thermal cycled and reoriented to rotate along the xz-plane (so $B_y = 0$). Once again the total magnetic field was first aligned along the [311] direction and the sample rotated to increase the in-plane field component B_x applied along the low symmetry $[\bar{2}33]$ direction, as shown in Fig. 4.12a. The back gate bias was then re-tuned to symmeterise the confining potential, with the symmetry point occuring under similar conditions to the previous cooldown (the back-gate bias applied differs by 1.3% and the hole density by 0.6%).

The low-field magnetoresistance data taken at different tilt angles are shown in Fig. 4.12d. The top trace was taken at $\theta = 0°$, where the field is perpendicular to the quantum well and is identical to the corresponding $[01\bar{1}]$ trace in Fig. 4.11c, where B_z causes the Landau levels to split and generate an out-of-plane spin polarisation.

When an in-plane field component B_x is introduced by tilting the sample, an additional out-of-plane spin polarization proportional to $g^*_{xz}B_x$ is generated, that either adds to or subtracts from, the out-of-plane spin polarization due to B_z. This difference

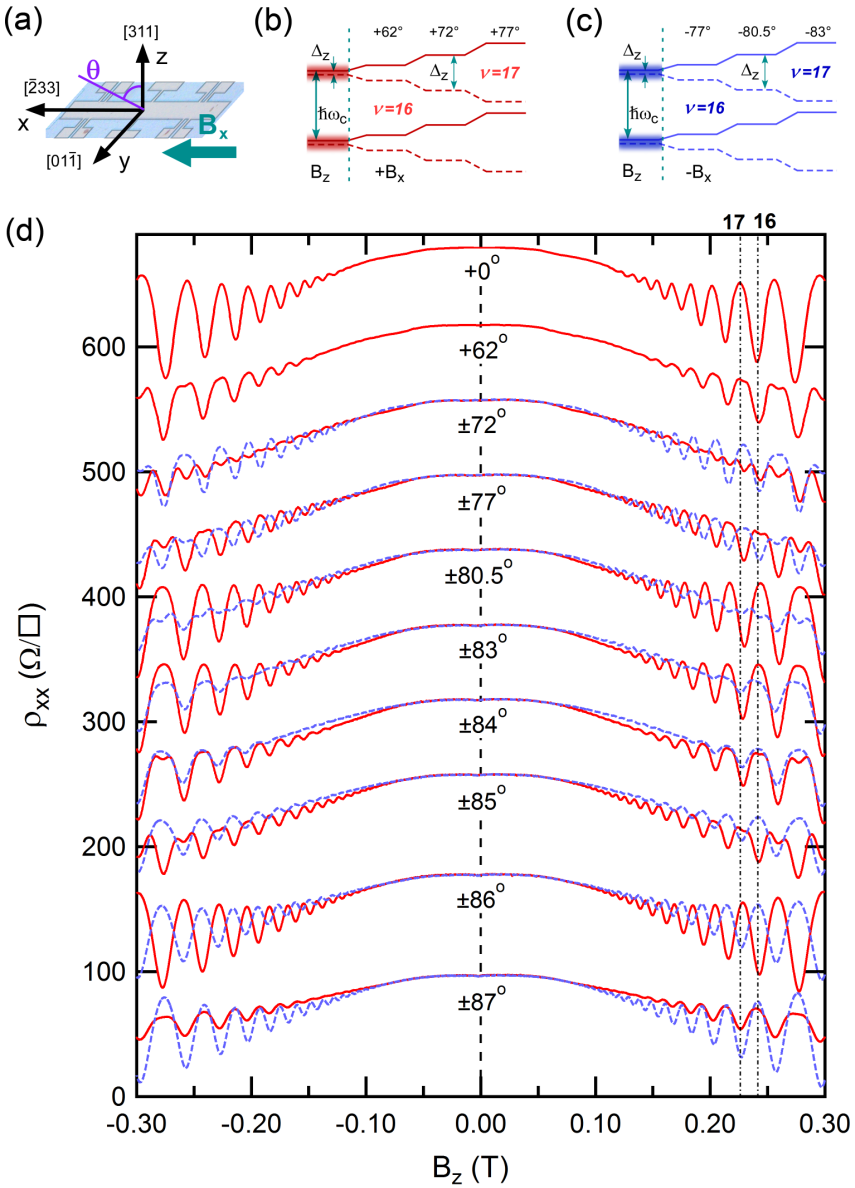

Figure 4.12: (a) Sample orientated in magnetic field, to rotate along the xz-plane ($B_y = 0$) and study the low symmetry direction. Initially the total field is aligned along the [311] crystal direction ($B_{tot} = B_z$, $\theta = 0°$) and is rotated by θ to increase the field component B_x parallel to [$\bar{2}$33]. (b,c) Schematic of the Landau level fan chart, starting with a purely perpendicular field B_z and illustrating the spin splitting introduced by a parallel field component as the sample is tilted to $+B_x$ by $+\theta$ in (b) and $-B_x$ by $-\theta$ in (c). (d) Magnetoresistivity traces taken at a series of tilt angles for $+\theta$ (solid red) and $-\theta$ (dashed blue). Filling factors ν=16 and ν=17 are marked by dashed vertical lines and the traces are offset by 40Ω/□ for clarity.

in behaviour is most pronounced at high in-plane fields, such as $\theta = \pm 85°$ and $\theta = \pm 86°$ where the SdH oscillations for opposite signs of $\pm\theta$ are completely out of phase with each other. This is in stark contrast to the equivalent SdH trace in the $[01\bar{1}]$ dataset (e.g. $\theta = \pm 85°$ in Fig. 4.11c) which is completely symmetric, i.e. $\rho_{xx}(B_y) = \rho_{xx}(-B_y)$.

We can obseve this asymmetry by following the evolution of ρ_{xx} maximum at ν=17 starting with zero tilt angle in Fig. 4.12. For the $-\theta$ traces (dashed blue lines) we can identify three main regimes (similar to the $[01\bar{1}]$ but occuring at different angles):

i) A small spin splitting at ν=17 is first noticeable at $\theta = -77°$.

ii) By $\theta = -80.5°$ the minima for both odd and even filling factors (ν=16 and ν=17) are equally well defined.

iii) Going to larger tilt angles, the ρ_{xx} maximum at ν=17 evolves into a minimum, while the ρ_{xx} minimum at ν=16 becomes a maximum. These three regimes correspond to the three regimes shown in Landau level schematic of Fig. 4.12c. Here the negative in-plane field component $-B_x$ (due to $-\theta$), results in $g^*_{xz}B_x$ subtracting from $g^*_{zz}B_z$ reducing the effective Zeeman splitting.

In contrast to the negative tilt angles, the $g^*_{zz}B_z$ and $g^*_{xz}B_x$ terms in Eq. 4.12 add for positive tilt angles, and the spin splitting develops more rapidly for corresponding $+\theta$, illustrated in Fig. 4.12b. By comparing the evolution of ν=17 for $+\theta$ (solid red lines) to their equivalent $-\theta$:

i) The onset of spin splitting at ν=17 is first resolvable at a much lower in-plane field, at $\theta = +62°$.

ii) At $\theta = +72°$ the minima at ν=16 and ν=17 are equally well defined.

iii) At $\theta = +77°$ the ρ_{xx} maxima at ν=17 has evolved into a minima, whilst the minima at ν=16 has become a maxima. Tilting the sample further causes the oscillations to invert a second time at $\theta = +86°$ and a third time at $\theta = +87°$.

From this dataset, we observe that the spin splitting of the Landau levels evolve much faster for positive tilt angles than it does for negative tilt angles. This suggests

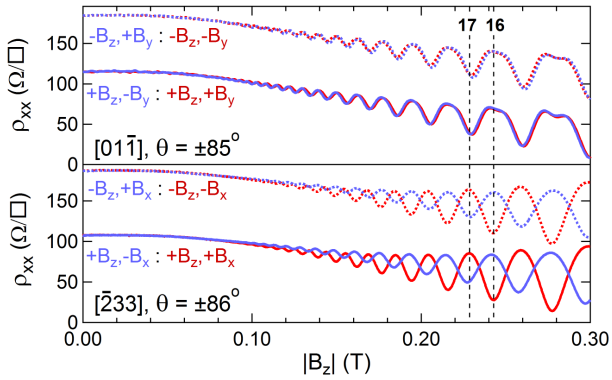

Figure 4.13: Magnetoresistance data plotted versus $+B_z$ (solid lines) comparing the sign of the ratio $\frac{B_x}{B_z}$ where $+\theta \equiv \frac{+B_x}{+B_z}$ (solid red), $-\theta \equiv \frac{-B_x}{+B_z}$ (solid blue) and corresponding traces plotted versus $-B_z$ (dashed lines) for $+\theta \equiv \frac{-B_x}{-B_z}$ (dashed red) and $-\theta \equiv \frac{+B_x}{-B_z}$ (dashed blue). Part (a) shows symmetric SdH traces along $[01\bar{1}]$ for $\theta = \pm 85°$ in all four cases (here the parallel field is denoted B_y rather than B_x). In part (b) along $[\bar{2}33]$ the traces are distinctly different for $+\frac{B_x}{B_z}$ compared to $-\frac{B_x}{B_z}$. Traces in each panel are offset vertically by $70\Omega/\square$.

that this difference between $+\theta$ and $-\theta$ traces stems from the interplay between the g^*_{xz} and g^*_{zz} terms in Eq. 4.11.

To confirm that this asymmetric behaviour with respect to the sign of $\pm\theta$ is not an artefact or a measurement error, we compare the symmetry of the datasets with respect to the sign of B_z by plotting both $\pm B_z$ on the same axis $|B_z|$ in Fig. 4.13. Here, all four combinations of the signs of $\pm B_x$ and $\pm B_z$ are given for a tilt angle of $|5°|$. Along the $[\bar{2}33]$ direction, the resistivity traces are symmetric only when the signs of both B_x and B_z are reversed, so that the total sign of the ratio B_x/B_z remains the same. This striking result suggests that effect of the non-collinear spin polarization due to the off-diagonal element g^*_{xz} is a maximum when the two terms of the Hamiltonian $g^*_{xz}B_x\sigma_z$ and $g^*_{zz}B_z\sigma_z$ are added together, whilst the effect of the non-collinear spin polarization can likewise be reduced when the same terms act to counterbalance each other. This rules out the possibility of measurement artefacts and confirms the existence of the unusual non-collinear g^*_{xz} contribution to the spin response of a low-symmetry 2D hole system.

4.6 Discussion - Modelling the hole bandstructure

Although we can experimentally verify that the non-collinear spin polarization due to the off-diagonal element g^*_{xz} is a maximum when a positive in-plane field is applied along the $[\bar{2}33]$ crystal direction, a quantitative comparison of g^*_{xz} with the theoretical value would be ideal. However we discovered that achieving such a quantitative comparison between the tilted field experimental data and numerical calculations performed using the traditional approach is currently impractical.

In this section we attempt to extract values for the g factors and compare them with theory. Due to the complexity of the hole bandstructure, the standard approach of determining Landau level energies by diagonalizing the effective Hamiltonian in a large basis of harmonic oscillator functions [58, 74, 83], becomes a non-trivial task for holes in tilted fields, with both components of magnetic field B_z and $B_{\|}$ applied simultaneously [287]. We shall first introduce the naive 'electron-like' approach to extracting g factors using the 'coincidence' method, assuming parabolic bands (constant m^*) and an isotropic g factor and discuss the limitations of this model. This is followed by full $\boldsymbol{k} \cdot \boldsymbol{p}$ calculations of the energy fan diagram and dispersion relations where we explore the anisotropic behaviour of both m^* and g^* in the presence of a magnetic field.

4.6.1 'Electron-like' parabolic band model

A naïve approach is to analyse the data and attempt to extract g factors using the 'coincidence' method described in Section 4.2.4 for 2D electrons [75, 203], by comparing the cyclotron energy gap (dependent on B_z) to the Zeeman energy gap (dependent on total field) and extracting the product $|g^*m^*|$.

As a first approximation to modelling a simple non-interacting Landau fan diagram of the 2D hole system, we assume parabolic bands (constant m^*) and constant g factors, replacing the electron $g^* = -0.44$ with the relevant hole g factor in each crystal direction, where the nth energy level can be expressed for the $[01\bar{1}]$ and $[\bar{2}33]$

respectively as:

$$E_{[01\bar{1}]} = (n+\frac{1}{2})\hbar\frac{eB_z}{m^*} \pm \sqrt{(\frac{1}{2}g^*_{zz}\mu_B B_z)^2 + (\frac{1}{2}g^*_{yy}\mu_B B_y)^2} \tag{4.13}$$

$$E_{[\bar{2}33]} = (n+\frac{1}{2})\hbar\frac{eB_z}{m^*} \pm \sqrt{(\frac{1}{2}g^*_{xx}\mu_B B_x)^2 + (\frac{1}{2}g^*_{zz}\mu_B B_z + \frac{1}{2}g^*_{xz}\mu_B B_x)^2} \tag{4.14}$$

A schematic model is shown in Fig.4.14, where the parameters used are $g^*_{zz} = 3.0$, $g^*_{xx} = g^*_{yy} = -0.16$, $g^*_{xz} = 0.65$ and $m^* = 0.19$. The Landau levels for a small, purely B_z field up to 0.1T are shown in panels (a) and (c). If the theoretical values of $g^*_{zz} = 7.2$ and $m^* \sim 0.2$ are applied directly to this model, we obtain a Zeeman gap which is much larger than the cyclotron gap. However for our experimental data taken at $\theta = 90°$ ($B_\parallel$=0), we observe that the cyclotron gap is larger than the Zeeman gap. To achieve agreement with the experimental data, g^*_{zz} was reduced to ~ 3 in order for the Landau levels to exhibit a smaller Zeeman gap ($\Delta\nu_{odd} \equiv \Delta E_z = g^*\mu_B B$) so $\Delta\nu_{even} > \Delta\nu_{odd}$. Panel (b) models the Landau levels along the high-symmetry $[01\bar{1}]$ direction. The levels behave symmetrically for both signs of the in-plane field, as expected from the symmetric form of Eq. 4.13. On the other hand panel (d) shows a distinct shift in the Landau level crossings when an in-plane field is applied along $[\bar{2}33]$. For $+B_x$ the crossings appear earlier (at smaller values of B_x) compared to equivalent $-B_x$ level crossings, due to the presence of the $g^*_{xz}B_x$ term interacting with a fixed $g^*_{zz}B_z$ term.

Although the simple model yields a reasonable approximation in electron systems, the behaviour of g^*_{xz} in holes is far from a simple offset in $B_\parallel$, and despite numerous tweaks we were unable to achieve a match for coincidence angles between the simple Landau model and the experimental data. This discrepancy clearly demonstrates that this simple model cannot be directly compared with the experimental data, since its basic assumptions of constant m^* and parabolic energy bands alone, do not take into account HH-LH couplings, interaction and higher order effects, arising from the highly non-parabolic band structure of spin-3/2 holes. In the following section we will show that, both g^* and m^* are anisotropic and vary with parallel field, which has a significant impact upon the Landau level structure of a 2D hole system.

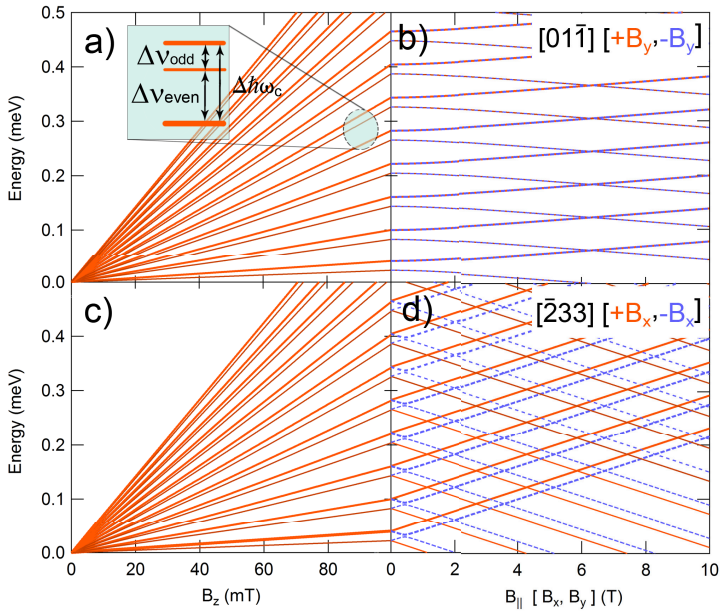

Figure 4.14: Landau fan chart produced using a naïve approximation. (a) A small perpendicular field B_z is first applied along $[01\bar{1}]$, which spin resolves the Landau levels. (b) Next, adding an in-plane field B_y splits the Landau levels at the same rate for both signs of $\pm B_y$. (c) Similarly a small B_z is first applied along $[\bar{2}33]$ (d) followed by an in-plane field B_x which shows a distinct offset between $\pm B_x$.

4.6.2 $\boldsymbol{k \cdot p}$ models - 8×8 Kane Hamiltonian

To obtain a more complete description for our low-symmetry tilted field 2D hole data, the $\boldsymbol{k \cdot p}$ method was applied to model our system. The non-parabolicity of the hole band structure for quantum wells grown along low symmetry GaAs directions, is already present at zero-field and is further enhanced with the application of an in-plane field. Theoretical calculations of the energy versus in-plane wave-vector $\boldsymbol{k}_{\|}$ dispersion curves, for bound hole states in shallow (311)A GaAs quantum wells (<10nm), reveal an enhanced anisotropy for some hole subbands compared to equivalent subbands in (100) quantum wells [108, 269], with some higher bands exhibiting a pronounced 'camel-back' structure with a saddle point at $\boldsymbol{k}_{\|} = 0$. Other dispersion calculations for a 15nm quantum well along different crystal growth directions, also yield much richer and complex bandstructure effects along [311] compared to higher symmetry directions [284].

Dispersion relations for our 20nm GaAs quantum well, were calculated using the $\boldsymbol{k \cdot p}$ method with an 8×8 Kane Hamiltonian, by R. Winkler. These calculations account for Dresselhaus SO by including the remote band contributions to second-order in $\boldsymbol{k}$. Fig. 4.15(a) illustrates the dispersion relation for the lowest five hole bands: HH1 (at -0.67meV), HH2, LH1, HH3 and HH4 respectively along both $[\bar{2}33]$ (solid purple) and $[01\bar{1}]$ (dashed blue). Here the presence of 2D confinement pushes the unoccupied HH2 band down to -4.31meV, and the LH1 band to -6.73meV. In the case of zero in-plane field, the HH1 bands are nearly isotropic in the 2D plane, although there is a tiny spin-orbit splitting of HH1 at finite $\boldsymbol{k}_{\|}$, seen as the bands cross the Fermi energy, due to the presence of bulk inversion asymmetry.

Fig. 4.15b and c, show the effects of applying an in-plane magnetic field upon the dispersion relations for two orthogonal in-plane crystal axes. For an in-plane field applied along $[01\bar{1}]$ there is almost no splitting of the HH1 subbands ($\Delta E = 0.025$meV) at the $\boldsymbol{k} = 0$ band edge in Fig. 4.15(b), as the heavy hole spins are locked along the [311] confinement axis due to the HH-LH splitting. However, at finite $\boldsymbol{k}_{\|}$ the in-plane field couples to the orbital momentum due to the finite well width, distorting the Fermi surface and lifting the spin degeneracy. In contrast when the magnetic field is

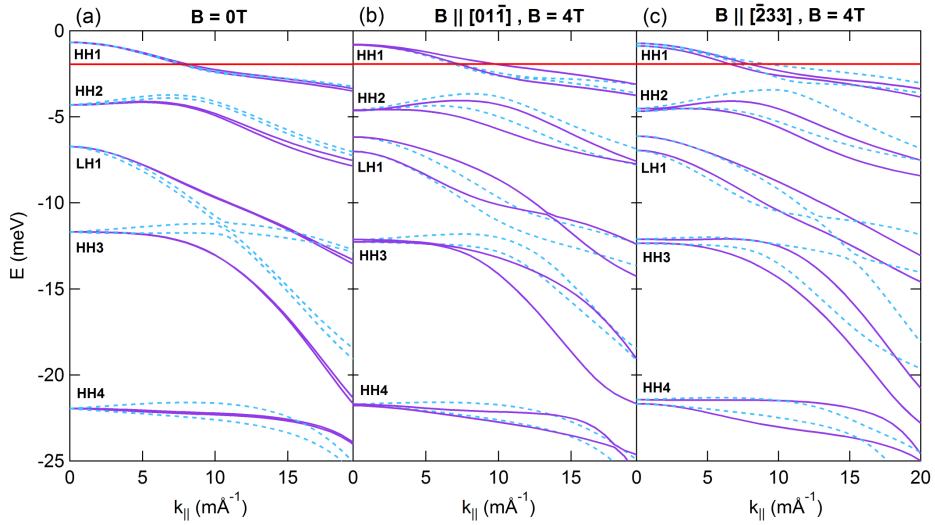

Figure 4.15: (a) 2D Hole dispersion relations for a 20nm wide GaAs quantum well from 8×8 $\boldsymbol{k} \cdot \boldsymbol{p}$ calculations, showing the Fermi energy (horizontal red line at -1.95meV) and $E(\boldsymbol{k})$ along $[\bar{2}33]$ (solid purple) and $[01\bar{1}]$ (dashed blue) at zero field. (b) Dispersion plot for $B_y = 4$T along $[01\bar{1}]$, exhibits a tiny $\boldsymbol{k}_{||} = 0$ spin splitting ΔE in the HH1 subbands, (c) Dispersion relation with $B_x = 4$T along $[\bar{2}33]$ shows a comparatively larger $\boldsymbol{k}_{||} = 0$ spin splitting due to the presence of g^*_{xz} [R. Winkler].

applied along the lower symmetry $[\bar{2}33]$ axis (Fig. 4.15(c)) the $\boldsymbol{k}_{||} = 0$ splitting is ~ 6 times larger, $\Delta E = 0.145$meV. Since the states at $\boldsymbol{k} = 0$ are locked perpendicular to the quantum well by the 2D confinement, this enhanced spin-splitting is due to the out-of-plane spin-polarization generated by the in-plane field due to g^*_{xz} as described in Eq. 4.11.

In the case of a purely perpendicular field, the non-parabolicity of the band structure and HH-LH coupling also yield a more complex hole Landau fan diagram compared to that for electrons. A Landau fan chart of our system is presented in Fig. 4.16(a), obtained from an equivalent $\boldsymbol{k} \cdot \boldsymbol{p}$ calculation, taking into account the self-consistent Hartree potential, and bulk inversion asymmetry through remote-band contributions to second order in $\boldsymbol{k}$ in the 8×8 Kane Hamiltonian. The calculations show the spin splitting of the Landau levels is highly non-linear with increasing field.

Fig. 4.16b plots the product $|g^*_{zz} m^*|$, extracted from the energy gaps between Landau levels at the Fermi energy E_F. Here m^* is extracted from the Landau fan diagram of Fig. 4.16a in a similar manner to how it is determined from temperature

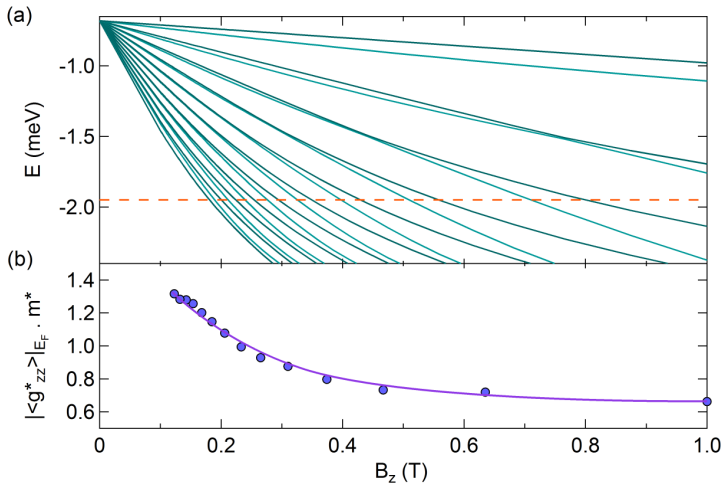

Figure 4.16: (a) 8×8 $\boldsymbol{k} \cdot \boldsymbol{p}$ calculations of the first 20 energy levels in the Landau fan diagram for a 20nm GaAs quantum well in a purely perpendicular field. The dashed orange line marks the position of the Fermi energy. (b) Plot of the product $|g^*_{zz}m^*|$ where g^*_{zz} is extracted from the Zeeman energy gap between adjacent even-odd-indexed energy levels around the Fermi energy, and m^* from the cyclotron gap between adjacent odd-indexed energy levels, from panel (a) [R. Winkler].

dependent SdH measurements. For a fixed B, m^* is extracted from the gap between adjacent energy levels with the same spin. Likewise, $\langle g^*_{zz} \rangle$ is determined from the Zeeman gap ($\Delta\nu_{odd}$) between adjacent even and odd indexed Landau levels at a fixed B, $\Delta E_Z = g^*_{zz}\mu_B B_z$. From these values the product $|g^*_{zz}m^*|$ could be calculated.

Due to the non-parabolicity of the bandstructure, the product $|g^*_{zz}m^*|$ decreases from 1.32 (where $g^*_{zz} = 6$, $m^* = 0.22$) at $B_z = 0.12$T, to 0.88 (where $g^*_{zz} = 3.7$, $m^* = 0.23$) at 0.3T, in Fig. 4.16b. The 8×8 $\boldsymbol{k} \cdot \boldsymbol{p}$ calculations show that $g^*_{zz}m^*$ trends to ~ 0.6 at higher perpendicular fields, due to the anisotropy of both g^*_{zz} and m^* in the presence of a perpendicular field. This result is more consistent with $g^*_{zz}m^* \sim 0.5$ obtained from the experimental data at $\theta = 0°$ and is much lower compared to that predicted by the naïve theory described in the 'electron-like' model.

Another contributing factor to the non-parabolic band structure is the anisotropic behaviour of g^* and m^* in a parallel magnetic field. Calculations of these are plotted as a function of in-plane field along $[01\bar{1}]$ in Fig. 4.17a and along $[\bar{2}33]$ in panel (b), courtesy of R. Winkler.

Along the $[01\bar{1}]$ direction, g^*_{yy} decreases to ~ 0 at large in-plane fields, whilst one

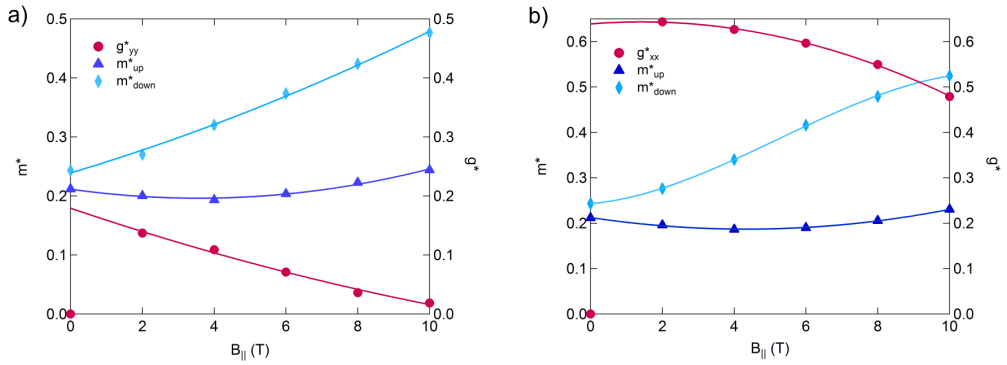

Figure 4.17: Plot of the anisotropy of two species of m^* (blue) on the left axis, and g^* (red) on the right axis versus an in-plane field applied along the $[01\bar{1}]$ direction in (a) and along $[\bar{2}33]$ in (b). These values were taken from $\boldsymbol{k}\cdot\boldsymbol{p}$ calculations of our sample's 20nm QW, based upon the numerical diagonalization of the 8×8 Kane Hamiltonian accounting for the self-consistent Hartree potential. Calculations were performed by R. Winkler.

effective mass species, m^*_{up}, remains about constant and the other, m^*_{down}, approximately doubles. For the $[\bar{2}33]$ direction, g^*_{xx} decreases slightly with in-plane field, m^*_{up} remains mostly constant, whilst once again m^*_{down} roughly doubles in value. These plots suggest that the anisotropy of g^* and m^* are non-negligible in our system, as most of our data was collected at large in-plane fields.

However, the problem of achieving realistic $\boldsymbol{k}\cdot\boldsymbol{p}$ calculations taking into account the variation in g^* and m^*, for both $B_{\|}$ and $B_{\perp}$ simultaneously, remains outstanding and further theoretical investigation is required.

4.7 Conclusions and future work

In summary, we report the direct observation of an out-of-plane spin polarization of itinerant 2D holes generated by an in-plane magnetic field applied along the low symmetry $[\bar{2}33]$ direction. This non-collinear spin polarization is due to a non-zero off-diagonal element g^*_{xz}, whose combined effect upon the spin splitting of the SdH oscillations reaches a maximum when the two terms of the Hamiltonian $g^*_{xz}B_x\sigma_z$ and $g^*_{zz}B_z\sigma_z$ are added together. This phenomenon is unique to 2D holes formed in a low symmetry zinc blende crystal structure such as GaAs, and stems from the in-

terplay between quantum well confinement and lattice symmetries. Our experiment constitutes one of the rare ocassions where off-diagonal elements in the gyromagnetic tensor $\underline{g}^*$ are accessible to experimental study. From our numerical calculations of the bandstructure, the complex and highly anisotropic behaviour of g^* and m^* in both perpendicular and parallel fields, means that the coincidence method using tilted fields cannot be directly applied to extract g factors.

Of further interest would be to repeat the same experiment in a 2D system with both a front and back gate, as this would allow one to independently tune the density (and keep it constant) and the confining potential (and hence the Rashba SO). The experiment could be performed at different densities and for differing confining potential symmetries for comparison. Moreover, performing the experiment within a 3-axis vector magnet system would allow for independent control of each field component being applied.

Finally, on top of a method to perform $\boldsymbol{k} \cdot \boldsymbol{p}$ calculations which accounts for both $B_{\parallel}$ and $B_{\perp}$ simultaneously, another aspect of low-symmetry systems which requires further consideration, both theoretically and experimentally is, g^*_{zx}, of which very little has been mentioned in the literature.

Chapter 5

Non-abelian spin dynamics in a 2D hole system

5.1 Introduction

In the previous chapter we examined the static properties of hole spins and showed the presence of an unusual non-collinear spin-polarization caused by the presence of an off-diagonal g^*_{xz} contribution in the g tensor. For this chapter we now explore the dynamics of 2D hole spins, concentrating upon how the spins behave in tilted magnetic fields. Previous studies have predicted the presence of Berry phase in systems with strong spin-orbit coupling [13, 189], and holes which intrinsically possess strong spin-orbit coupling provide a convenient platform to study this phenomena. In particular, we demonstrate that holes undergo non-abelian spin evolution in tilted magnetic fields, which can be modelled using the paradigm of the non-abelian gauge field.

This chapter begins with an overview of the key concepts underpinning the abelian and non-abelian gauge formalisms and their generalizations, followed by examples of experiments conducted to observe the Berry phase, with an emphasis on semiconductor systems. Section 5.3.2 outlines a non-abelian formalism for our 2D hole system and describe the conditions needed to generate and detect the elusive non-abelian Berry curvature in a semiconductor system. In section 5.4 we use a 2D GaAs hole system grown on a low-symmetry plane to present tilted-field transport measurements taken

along two crystal axes and study the phase changes in Shubnikov-de Haas oscillations. We found that unlike the 'electron-like' model discussed in the previous chapter, the adapted non-abelian formalism predicts the position of the coincidence angles correctly, thus providing the first experimental evidence for the existence of the non-abelian Berry curvature in a solid-state semiconductor system.

This work (to be published) was done in collaboration with theorists T. Li and O. P. Sushkov, who derived the non-abelian formalism to explain the unusual behaviour of our 2D hole system (to be published). Note that the theoretical formalism and all calculations in this chapter were performed by T. Li. The experiment was performed by the author of this thesis and the analysis was a joint effort.

To highlight the difference between a system with no spin dynamics, one with abelian behaviour and one with non-abelian behaviour, the spin trajectories of a particle moving around a circular path (in momentum space) are illustrated in Fig. 5.1. Each of the 3 panels corresponds to the 3 different situations:

a) *No spin dynamics*: There is no spin-orbit interaction and the spin (red) simply aligns with the external magnetic field $\boldsymbol{B}_{ext}$ (blue), e.g. the trajectory followed by a non-relativistic electron in the presence of an external magnetic field.

b) *Abelian (adiabatic) spin dynamics*: Although spin is precessing, it remains aligned with the driving field $\boldsymbol{B}_{eff}$ which itself is parallel to the momentum, $\boldsymbol{B}_{eff} \approx \boldsymbol{B}_{so} \propto \boldsymbol{k}$. The abelian picture assumes the adiabatic limit holds for the system under study [167], i.e. the spin precession frequency is much larger than the orbital frequency around the closed loop due to the presence of $\boldsymbol{B}_{ext}$. This precession of spin around a closed orbit generates a geometric Berry phase which appears as the π-phase shift observed in Shubnikov-de Haas oscillations [6, 198]. e.g. in the case of an ultra-relativistic Dirac electron.

c) *Non-abelian spin dynamics*: Describes a system where corrections to the adiabatic scenario are required, e.g. a system where the spin is effectively rotating around two axes simultaneously, such as 2D holes with strong spin-orbit (SO) coupling, undergoing non-adiabatic spin precession in the presence of an external magnetic

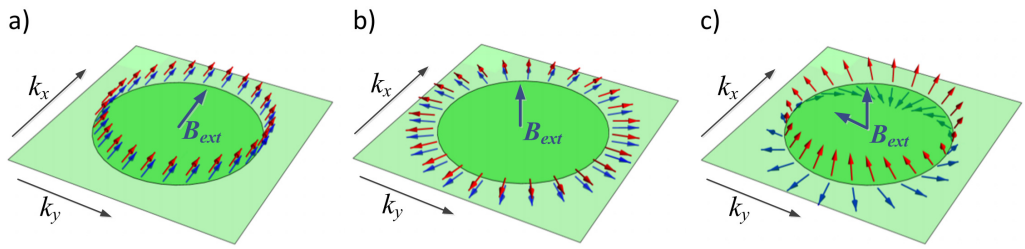

Figure 5.1: Spin dynamics along the closed trajectory in momentum space (green circle) due to $\boldsymbol{B}_{ext}$ in three qualitatively different situations, where spin (red arrows) is driven by a local effective magnetic field $\boldsymbol{B}_{eff}$ (blue arrows). (a) Absence of spin dynamics. This corresponds to the case of an electron moving within an external magnetic field in the absence of spin-orbit interaction. (b) Abelian spin dynamics. Spin is changing, but it remains parallel to the driving field $\boldsymbol{B}_{eff} \propto \boldsymbol{k}$. (c) Non-abelian spin dynamics. The spin is parallel to the vector sum of the driving field $\boldsymbol{B}_{eff}$ and the non-abelian gauge field.

field with non-zero in-plane and perpendicular components. In this instance the particle's spin (red) is driven by a local effective magnetic field $\boldsymbol{B}_{eff}$ (blue), which consists of both the external magnetic field $\boldsymbol{B}_{ext}$ and the momentum-dependent SO field $\boldsymbol{B}_{so}$ (not shown). Here, the driving field $\boldsymbol{B}_{eff}$ is not collinear with spin and this non-collinearity is proportional to the non-abelian gauge field.

5.2 Background

In this literature review we cover the key concepts used to formulate the non-abelian gauge field derivation for our experimental data and provide context for this body of work. This includes: introducing the concept of gauge theory, the geometric Berry phase and its generalization, followed by the non-abelian paradigm. Finally we highlight experiments conducted and proposed in solid-state systems to observe the abelian Berry phase and detect the non-abelian gauge field.

Gauge theories are a class of field theories possessing a local (continuous) symmetry. The symmetry transformations do not change observable quantities. In classical physics, the gauge field which appears in the Lagrangian (e.g. the vector potential in the case of electromagnetism) cannot be measured directly and different configurations of the field can result in identical observable quantities (e.g. the electric and magnetic

fields). Cornerstone to all gauge theories is a property called *gauge invariance* (or gauge symmetry), which is the invariance of the Lagrangian with respect to group transformations of a gauge field. The continuous group of transformations form a Lie group. Locally the Lie group is described by the Lie algebra which consists of the group generators. A gauge field is considered *abelian* if the group generators commute. On the other hand, if the symmetry group of transformations are non-commutative, the gauge field is *non-abelian*, such as in the Yang–Mills theory [293].

Although the gauge field is not a physically meaningful object in classical physics, it results in a shift of the phase of the quantum wavefunction which may be directly observed in quantum interference measurements [23]. Let us consider, as an example, the case of electromagnetism. The phase shift in the semiclassical wavefunction is equal to the integral of the magnetic vector potential $\boldsymbol{A}$ along the classical path l, $\frac{e}{\hbar}\int \boldsymbol{A}\cdot d\boldsymbol{l}$. For an electron moving around a closed loop, the phase accumulated in the vector potential is equal to the magnetic flux in units of $\frac{\hbar}{e}$, which results in a shift of the Bohr-Sommerfeld quantisation condition. This flux appears even when the electron is confined to move in a region which is unpenetrated by the magnetic field; this surprising result is known today as the Aharonov-Bohm effect [3, 23]. In this thesis, the analogous flux for a non-abelian gauge field due to the spin-orbit interaction has been observed for the first time via the quantum interference of holes moving along a cyclotron trajectory (i.e. Shubnikov-de Haas oscillations), and appears as a modulation to the phase of these oscillations. This will be detailed in Section 5.3.2.

Although originally conceived to describe the interactions of elementary particles [89, 293], through the principle of 'emergence', gauge fields have been extended to describe the behaviour of a wide variety of quantum systems. The concept of emergent gauge fields arise naturally in many geometrical contexts, giving rise to the idea that physical systems can be classified according to their geometrical properties. One example of such an abelian gauge theory is the *geometric phase*, more commonly known as the *Berry phase* [23], which describes the adiabatic evolution of a *non-degenerate* quantum state. The emergence of non-abelian gauge fields in *degenerate* quantum systems was first proposed by Wilczek and Zee [280]. The concept of the abelian gauge

field has been used to describe a broad range of physical phenomena such as the topological Chern number formulation of the quantum Hall effect [145, 262], 3D topological insulators [82, 117, 118, 290], superconductors [79, 214] and superfluids [98, 215]. Similarly the non-abelian gauge field has been theoretically predicted to exist in a number of many-body systems e.g. fractional quantum Hall liquids [187], spin-orbit coupled systems [13, 189], self-assembled quantum dots [253], cuprate semiconductors and ensembles of ultracold atoms [156] (see review Ref. [87] for more examples). But to date there has been no experimental evidence for the non-abelian gauge field in a semiconductor system.

In this literature review we shall begin with a classical interpretation of Berry phase, followed by Berry's original derivation and its generalization to an abelian gauge field, followed by the non-abelian Berry phase derivation and its generalization into a gauge field and an observable trace. We briefly cover how Berry curvature can be used to describe spin and charge transport through a crystal lattice and highlight some experiments and proposals to measure and detect the abelian and non-abelian Berry phase.

Note that we shall only be providing a brief summary of the theoretical results and their implications. For more details of the derivations for the abelian and non-abelian Berry phase, connection and curvature, refer to Appendix D.

5.2.1 The geometric Berry phase

In 1984 Berry [23] discovered that a phase difference can be acquired over the course of a cycle, when a system is subjected to cyclic adiabatic processes, resulting from the geometrical properties of the parameter space of the Hamiltonian. This additional phase factor is now known as the Berry phase.

Since the conception of Berry phase, many generalizations have been proposed to the original definition. In this chapter we shall focus on two main extensions: 1) the relation between Berry phase, Berry connection and Berry curvature; 2) the generalization from a single non-degenerate state to m degenerate states evolving together, resulting in a whole matrix rather than a single phase factor, giving rise to

non-abelian behaviour [280]. Such a flexible theory can be used to explain the spin and charge transport of electrons/holes through a semiconductor crystal by taking the periodic lattice potential into consideration and the effect of spin-orbit interaction upon the Landau level structure. Moreover the semiclassical formalism can be amended to include quantization effects such as Bloch oscillations and cyclotron orbits via the Onsager quantization condition [199]. More recent developments have shown that the Berry connection plays an explicit role in spin dynamics and is related to the spin-orbit interaction e.g. applications include the relativistic Dirac electron and the Kane model in semiconductors [91, 289].

Classical Berry phase

The Berry phase has been observed in classical systems such as the Foucault pendulum [105] and the Pancharatnam phase in optical fibers [265]. In these systems, the classical analog to Berry phase highlighting its geometrical origin is the geometric angle, which can be explained as follows [7]:

We now describe how the Berry phase can manifest in a classical system. Suppose we travel along a closed path $\mathcal{C}$ on the surface of a sphere. Initially we define a vector $\boldsymbol{v_i}$ tangential to the surface along the direction of travel, illustrated by the long vector in Fig. 5.2 at position (1) marked in red. As we move along the curve we apply the principle of parallel transport of $\boldsymbol{v}$ around $\mathcal{C}$, i.e. for each infinitesimal displaced point along the curve, we ensure that $\boldsymbol{v}$ remains parallel to its previous state. Once back at the starting point (7), we find that final vector $\boldsymbol{v_f}$ has rotated and is now at an angle γ with respect to its initial direction Fig. 5.2. The underlying cause for this rotation is purely geometrical and is connected to the intrinsic curvature of the sphere. This geometric angle depends on the path enclosed and is related to the integral of the curvature on the surface bounded by the loop. In this case, the geometric angle γ equals the solid angle Ω subtended from the center of the sphere. In this example the loop covers 1/8th the surface area such that $\Omega = \frac{\pi}{2} = \gamma$.

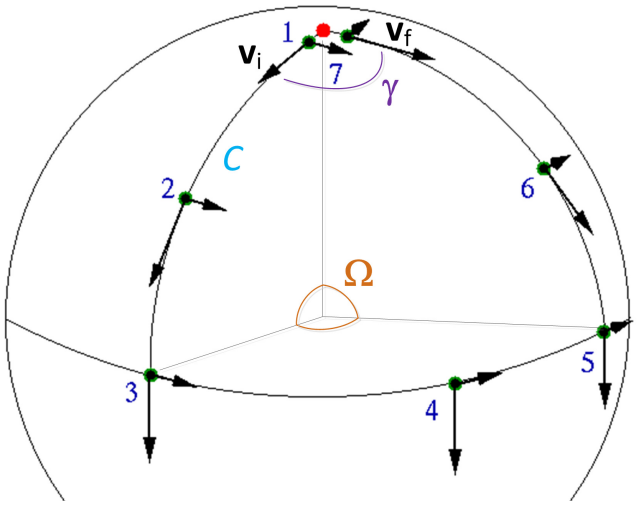

Figure 5.2: Classical analog of Berry phase depicting parallel transport of vector $\boldsymbol{v}$ around a closed path $\mathcal{C}$ on the surface of a sphere, where the difference in angle γ between the vector's initial $\boldsymbol{v_i}$ and final $\boldsymbol{v_f}$ state is equal to the solid angle enclosed by $\mathcal{C}$, where $\gamma = \Omega$. Figure reproduced from Ref. [90].

Cyclic adiabatic evolution

We shall briefly outline the concept of Berry in terms of cyclic adiabatic evolution and introduce the local description of the Berry phase in terms of the Berry curvature. For a full set of derivations please refer to Appendix D.1.

For a quantum system in an eigenstate, of a Hamiltonian $\mathcal{H}$ with time varying parameters $\boldsymbol{R} = (R_1, R_2, ...)$, such that between time $t = 0$ to time $t = T$, $\boldsymbol{R}$ circulates around a closed path denoted $\mathcal{C}$ in the parameter space [23].

If the environment and hence $\mathcal{H}$ is slowly altered (i.e. the characteristic frequency $2\pi/T$ is much smaller than the energy spacing between adjacent levels, $\mid E_n - E_{n'} \mid$), the effects of the slowly changing degrees of freedom upon faster moving degrees of freedom can be estimated using the adiabatic approximation. The adiabatic theorem [135, 186] predicts that a system starting off in one of its eigenstates $|n(\boldsymbol{R}(0))\rangle$ will remain as an instantaneous eigenstate $|n(\boldsymbol{R}(t))\rangle$ of the Hamiltonian $\mathcal{H}(\boldsymbol{R}(t))$ during the whole process, at any time t. So the only degree of freedom available to change is the phase $\gamma_n(t)$ of the quantum state, whose wave-function can be expressed as

$$|\psi_n(t)\rangle = exp\left\{-i\int_0^t \mathrm{d}t'\, E_n(\boldsymbol{R}(t'))\right\} e^{i\gamma_n(t)}\, |n(\boldsymbol{R}(t))\rangle \ . \tag{5.1}$$

The first exponent is the dynamical phase factor, which describes the slowly varying time evolution of the stationary state. This dynamical phase is not geometrical, rather it depends only upon $\boldsymbol{R}(t)$ which parameterizes the path followed, and on the arbitrary gauge choice of a "zero phase" of the basis state at each point along the path. The second exponent is the additional geometrical phase factor of interest, which is acquired by the quantum state during adiabatic evolution. Its phase $\gamma_n(t)$ cannot be written as a function of $\boldsymbol{R}$ only and is path dependent.

The total phase change of state $|\psi\rangle_n$ around a path $\mathcal{C}$ is given by the evolution of the wave-function between $t = 0$ and $t = T$, where the geometrical phase change is described by a path integral in parameter space and is independent of how the circuit is traversed in the adiabatic approximation [23]

$$\gamma_n(\mathcal{C}) = \oint_{\mathcal{C}} \mathrm{d}\boldsymbol{R} \cdot \boldsymbol{A}_n(\boldsymbol{R}) \ , \tag{5.2}$$

where $\boldsymbol{A}_n(\boldsymbol{R})$ is a vector-valued function now known as the Berry connection (or Berry vector potential) [289]

$$\boldsymbol{A}_n(\boldsymbol{R}) = i \left\langle n(\boldsymbol{R}) \,|\, \boldsymbol{\nabla}_{\boldsymbol{R}} \,|\, n(\boldsymbol{R}) \right\rangle \ , \tag{5.3}$$

and $\gamma_n(\mathcal{C})$ is defined up to an integer multiple of 2π under the gauge transformation. For any closed path, $e^{i\gamma_n}$, the *geometric Berry phase* $\gamma_n(\mathcal{C})$ is gauge invariant and is given by

$$\gamma_n = \oint_{\mathcal{C}} \mathrm{d}\boldsymbol{R} \cdot \boldsymbol{A}_n(\boldsymbol{R}) \quad . \tag{5.4}$$

From this defintion, the Berry phase only depends on the geometry of the closed path and is independent of the time variation of $\boldsymbol{R}(t)$ in the adiabatic limit. The Berry phase is a measurable quantity. Unlike the Berry phase, the local Berry connection $\boldsymbol{A}_n(\boldsymbol{R})$ is gauge dependent and hence can never be physically observable. Due to the geometric character of the Berry phase, in systems where electrons/holes behave as ultrarelativistic particles, Berry phase directly reflects the shape of the spin trajectory. Measurements of the Shubnikov-de Haas oscillations in graphene [198, 305] and in topological insulators [227] have highlighted the contribution of this geometric phase arising from the internal degrees of freedom (pseudospin and spin respectively) of the systems under study.

Berry curvature and gauge fields

The Berry phase can be generalized into a field by defining an anti-symmetric second-rank, gauge invariant field (curvature) tensor, derived from the Berry vector potential $\boldsymbol{A}_n(\boldsymbol{R})$ in Eq. 5.3 [289], $F^n_{\mu\nu}(\boldsymbol{R})$ which is called the *Berry curvature*,

$$\begin{aligned} F^n_{\mu\nu}(\boldsymbol{R}) &= \frac{\partial}{\partial R^\mu}\mathrm{A}^n_\nu(\boldsymbol{R}) - \frac{\partial}{\partial R^\nu}\mathrm{A}^n_\mu(\boldsymbol{R}) \\ &= i\left[\left\langle \frac{\partial n(\boldsymbol{R})}{\partial R^\mu} \middle| \frac{\partial n(\boldsymbol{R})}{\partial R^\nu} \right\rangle - (\nu \leftrightarrow \mu)\right] . \end{aligned} \tag{5.5}$$

From Stoke's theorem, for a closed path $\mathcal{C}$ forming the boundary of a surface $\mathcal{S}$, the Berry phase can be expressed as a surface integral

$$\gamma_n = \int_{\mathcal{S}} \mathrm{d}R^\mu \wedge \mathrm{d}R^\nu \; \frac{1}{2} F^n_{\mu\nu}(\boldsymbol{R}) \; , \tag{5.6}$$

where $\mathcal{S}$ is the surface enclosed by the path $\mathcal{C}$. Unlike the Berry vector potential (Berry connection), the Berry curvature described by Eq. 5.5 is gauge invariant and observable. In a 3D parameter space, we can recast the Berry curvature Eq. 5.5 and the closed-loop Berry phase 5.6 into pseudovector form

$$\begin{aligned} \boldsymbol{F}_n(\boldsymbol{R}) &= \boldsymbol{\nabla}_{\boldsymbol{R}} \times \boldsymbol{A}_n(\boldsymbol{R}) \; , \\ \gamma_n &= \int_{\mathcal{S}} \mathrm{d}\boldsymbol{S} \cdot \boldsymbol{F}_n(\boldsymbol{R}) \; . \end{aligned} \tag{5.7}$$

The abelian Berry paradigm covers the situation where a single energy level is separated out in the adiabatic evolution, but if the energy levels are degenerate, then the corresponding dynamics must be projected onto a subspace spanned by these degenerate eigenstates, resulting in a non-abelian Berry curvature [280].

5.2.2 Non-abelian Berry paradigm

In contrast to a system where electrons/holes behave as ultrarelativistic particles, the concept of Berry phase is not as straightforward in 2D semiconductors due to the existence of two coupled Fermi surfaces with opposing spins.

The following section briefly summarizes how the concept of Berry phase can be extended to such systems, comprising of degenerate (or nearly degenerate) energy

bands. Since degenerate Bloch states possess multiple components, the Berry curvature becomes a matrix with a non-abelian gauge structure, ultimately resulting in a non-abelian Berry curvature (i.e. the non-abelian *field*).

Non-abelian Berry phase

Beginning with the adiabatic problem, Wilczek and Zee [280] derived the non-abelian Berry phase in a similar manner to that for the geometric Berry phase for multiple, M, degenerate states. For a full derivation please refer to Appendix D.2.

For a closed path the Wilson loop is obtained, which is a matrix analogy to the geometric Berry phase and can be expressed as

$$\mathcal{U} = \mathcal{P}\ exp\left\{ i \oint \mathcal{A}_\mu \mathrm{d}R^\mu \right\} \quad . \tag{5.8}$$

Note that $\mathcal{U}(t)$ and $\mathcal{A}(\tau)$ are now matrices, where $\mathcal{U}(t)$ and $\mathcal{A}(\tau)$ do not commute with $\mathcal{U}(t^{'})$ and $\mathcal{A}(\tau^{'})$ respectively.

$\mathcal{A}$ is the corresponding non-abelian analog for the Berry connection defined in Eq. 5.3 and can be expressed as [91]

$$\mathcal{A}^\mu_{ab} = i \left\langle n_a \,|\, \partial_\mu \,|\, n_b \right\rangle \quad . \tag{5.9}$$

The non-abelian Berry connection $\mathcal{A}^\mu_{ab}(\boldsymbol{R})$ is now a matrix-valued vector indexed by (a, b) for all indices of the degenerate subspace $(1, ..., M)$, where μ refers to a set of matrices $\mathcal{A}$ and ∂_μ is shortened notation for $\frac{\partial}{\partial \boldsymbol{R}_\mu}$. The specific form of $\mathcal{A}$ from Eq. 5.9 depends upon the choice of basis states $|n_a(\boldsymbol{R}(t))\rangle$. For a different choice e.g.

$$n(\boldsymbol{R}(t)) = \Omega(t)\psi(t) \ , \tag{5.10}$$

the set of fields $\mathcal{A}^\mu$ then transform as full gauge potentials

$$\mathcal{A}^{\mu^{'}}_{ab}(t) = \partial^\mu \Omega \Omega^{-1} + \Omega \mathcal{A}^\mu \Omega^{-1} \ . \tag{5.11}$$

Deriving the non-abelian Berry curvature

When considering a set of degenerate bands, conventional adiabatic theorem is no longer valid and we can extend the non-abelian Berry formalism to describe a non-abelian Berry curvature, as done for the Berry phase. For the semiclassical framework,

a correct treatment of the system involves a wave packet constructed from the degenerate levels [52, 241]. Thus, the Berry curvature tensor $F^n_{\mu\nu}(\boldsymbol{R})$ from the abelian Eq. 5.5 must be extended to a matrix definition $\mathcal{F}^{ab}_{\mu\nu}(\boldsymbol{R})$ in analogy to non-abelian gauge theories [280], by substituting the curl with the covariant derivative [91, 241]

$$\begin{aligned}\mathcal{F}^{ab}_{\mu\nu}(\boldsymbol{R}) &= \partial_\mu \mathcal{A}^{ab}_\nu - \partial_\nu \mathcal{A}^{ab}_\mu + i\left[\mathcal{A}_\mu, \mathcal{A}_\nu\right]^{ab} \\ &= \{i\left\langle \partial_\mu n_a(\boldsymbol{R}) \,|\, \partial_\nu n_b(\boldsymbol{R})\right\rangle - i\left\langle \partial_\nu n_a(\boldsymbol{R}) \,|\, \partial_\mu n_b(\boldsymbol{R})\right\rangle\} \\ &\quad + i\left[\left\langle \partial_\nu n_a(\boldsymbol{R}) \,|\, n_c(\boldsymbol{R})\right\rangle \left\langle n_c(\boldsymbol{R}) \,|\, \partial_\mu n_b(\boldsymbol{R})\right\rangle\right] \\ &\quad - i\left[\left\langle \partial_\mu n_a(\boldsymbol{R}) \,|\, n_c(\boldsymbol{R})\right\rangle \left\langle n_c(\boldsymbol{R}) \,|\, \partial_\nu n_b(\boldsymbol{R})\right\rangle\right] \end{aligned} \tag{5.12}$$

Just as in the abelian scenario where the Berry connection (Berry curvature) have the same mathematical structures as the vector potential (magnetic field), this correspondence also holds for the non-abelian gauge theory e.g. $SU(2)$ gauge theory [280]. The non-abelian Berry connection $\mathcal{A}^\mu_{ab}(\boldsymbol{R})$ under the gauge transformations, is transformed according to Eq. 5.11 and the corresponding non-abelian Berry curvature $\mathcal{F}^{ab}_{\mu\nu}(\boldsymbol{R})$ to [91]

$$\mathcal{F}^{ab'}_{\mu\nu}(\boldsymbol{R}) = \mathcal{U}^\dagger(\boldsymbol{R})\; \mathcal{F}^{ab}_{\mu\nu}(\boldsymbol{R})\; \mathcal{U}(\boldsymbol{R}) \quad . \tag{5.13}$$

Thus the non-abelian Berry curvature matrix $\mathcal{F}^{ab}_{\mu\nu}(\boldsymbol{R})$ is changing under a gauge rotation and therefore cannot be directly observed [36]. But we can derive gauge invariant quantities from it which are physically meaningful, such as the trace of the Berry curvature matrix, $\mathrm{tr}\mathcal{F}$. This trace will play a crucial role in interpreting our experimental data which we will discuss in Sections 5.3.2 and 5.4.

5.2.3 Gauge fields in crystal lattices

The advent of Berry connection and curvature allows the non-abelian gauge field to be extended to describe the spin and charge transport of electron wave packets in crystals, using the semiclassical approach [91, 289].

The abelian gauge field

For the case of a crystal lattice, the crystal momentum vector $\boldsymbol{k}$ is equivalent to the general parameter $\boldsymbol{R}$ used in the previous sections of this chapter. Starting with the

Schrödinger equation for the Bloch state $\psi_{n\boldsymbol{k}}(\boldsymbol{r}) = e^{i\boldsymbol{k}\cdot\boldsymbol{r}}u_n(\boldsymbol{r},\boldsymbol{k})$ (where n and $\boldsymbol{k}$ are the band index and crystal momentum and $u_n(\boldsymbol{r},\boldsymbol{k})$ is a cell-periodic function),

$$\left\{-\frac{\hbar^2}{2m}\boldsymbol{\nabla}_{\boldsymbol{r}}^{\boldsymbol{2}} + V(\boldsymbol{r})\right\}\psi_{n\boldsymbol{k}}(\boldsymbol{r}) = \varepsilon_{n\boldsymbol{k}}\psi_{n\boldsymbol{k}}(\boldsymbol{r}) \ . \tag{5.14}$$

Rewriting it for the periodic part of the Bloch function we arrive at

$$\left\{-\frac{\hbar^2}{2m}(\boldsymbol{\nabla}_{\boldsymbol{r}} + i\boldsymbol{k})^2 + V(\boldsymbol{r})\right\}u_n(\boldsymbol{r},\boldsymbol{k}) = \varepsilon_{n\boldsymbol{k}}u_n(\boldsymbol{r},\boldsymbol{k}) \ . \tag{5.15}$$

Generally the differential equation for $\psi_{n\boldsymbol{k}}(\boldsymbol{r})$ is a simultaneous eigenfunction of the translation operator and the Hamiltonian, and so it does not depend on the wave vector $\boldsymbol{k}$, since it only labels eigenvalues of the translation operator. However for the above scenario, $\boldsymbol{k}$ appears as a parameter and hence the Berry phase, connection and curvature now apply directly to the periodic part of the wave function $u_n(\boldsymbol{r},\boldsymbol{k})$ as well [91]. So for each band n, there is now an abelian Berry connection associated with every $\boldsymbol{k}$ of the form

$$\boldsymbol{A}_n(\boldsymbol{k}) = i\int_{uc} d^3r u_n^*(\boldsymbol{r},\boldsymbol{k})\boldsymbol{\nabla}_{\boldsymbol{k}}u_n(\boldsymbol{r},\boldsymbol{k}) \ , \tag{5.16}$$

where integral is made over one unit cell uc. And the corresponding abelian Berry curvature can be expressed as

$$\boldsymbol{F}_n(\boldsymbol{k}) \ = \ \boldsymbol{\nabla}_{\boldsymbol{k}} \times \boldsymbol{A}_n(\boldsymbol{k}) \quad , \tag{5.17}$$

which is the quantity that appears in the semiclassical equations of motion for the wave packet (see Ref. [91] for further details of the derivation). Hence the Berry connection and curvature associated with band n are properties of the periodic $u_n(\boldsymbol{r},\boldsymbol{k})$ part of the Bloch function.

For vanishing periodic potentials the Bloch functions reduce to plane waves and constructing the wave packet from plane waves results in $u_n(\boldsymbol{r},\boldsymbol{k}) = 1$. This means that both $\boldsymbol{A}_n(\boldsymbol{k})$ and $\boldsymbol{F}_n(\boldsymbol{k})$ also disappear. Hence the physical origin of the Berry connection and curvature stems from the periodic crystal potential breaking up the full spectrum of the parabolic, free-particle dispersion relation into bands. These bands are usually separated by gaps, and states are selected only from a limited number of these bands to represent the wave packet [91, 289].

The non-abelian gauge field

As briefly discussed for the abelian case, the non-abelian Berry connection and curvature can also be used to describe the spin and charge transport of particles through crystal lattices as demonstrated by Culcer *et al.* [52] and Shindou *et al.* [241]. The authors describe the coherent wave packet evolution of a particle in the valence band, for M degenerate bands, under the action of an electric field and show that this leads to the separation of spins (denoted by indices i, j), which require non-abelian corrections due to the additional degree of freedom stemming from the spin-orbit interaction [52]. The matrix described by the Wilson loop now takes the form of

$$\mathcal{U} = P\ exp\left\{ i \oint \mathcal{A}_{ij}(\boldsymbol{k}) \mathrm{d}\boldsymbol{k} \right\} \ . \tag{5.18}$$

The non-abelian Berry connection from Eq. 5.9 can be rewritten as

$$\mathcal{A}_{ij}(\boldsymbol{k}) = i \left\langle u_i(\boldsymbol{k}) \,|\, \boldsymbol{\nabla}_{\boldsymbol{k}} u_j(\boldsymbol{k}) \right\rangle \ . \tag{5.19}$$

The corresponding non-abelian Berry curvature from Eq. 5.12 becomes

$$\mathcal{F}_{ij}(\boldsymbol{k}) = \partial_\mu \mathcal{A}_\nu^{ij} - \partial_\nu \mathcal{A}_\mu^{ij} + i \left[\mathcal{A}_\mu, \mathcal{A}_\nu\right]^{ij} \tag{5.20}$$

Likewise the matrices describing the non-abelian Berry connection $\mathcal{A}_{ij}(\boldsymbol{k})$ and curvature $\mathcal{F}_{ij}(k)$ can be transformed according to [91]

$$\begin{aligned} \mathcal{A}^{'}(\boldsymbol{k}) &= \mathcal{U}^{\dagger}(\boldsymbol{k})\ \mathcal{A}^{'}(\boldsymbol{k})\ \mathcal{U}(\boldsymbol{k}) + i\mathcal{U}^{\dagger}(\boldsymbol{k})\ \boldsymbol{\nabla}_{\boldsymbol{k}}\ \mathcal{U}(\boldsymbol{k}) \quad , \\ \mathcal{F}^{'}(\boldsymbol{k}) &= \mathcal{U}^{\dagger}(\boldsymbol{k})\ \mathcal{F}(\boldsymbol{k})\ \mathcal{U}(\boldsymbol{k}) \quad . \end{aligned} \tag{5.21}$$

5.2.4 Experimental evidence for abelian and non-abelian Berry phase

In this section we review existing experimental literature in which the abelian Berry phase has been observed with an emphasis on semiconductor systems. This is followed by proposals to detect the presence of the non-abelian Berry curvature.

Abelian Berry experiments

The abelian Berry phase has been experimentally observed in a wide variety of physical systems ranging from optical fibers [265], to neutron spin rotation [26, 254], Bose condensates of ultra cold atoms [165], graphene [198, 305] and topological insulators [227].

There are many more examples of experiments and corresponding extensions and generalizations of theory which can be found in reviews [7, 36, 191, 219, 220, 289].

Although such experimental evidence for Berry phase was obtained shortly after the theory was proposed, its observation in a solid-state condensed-matter system proved to be more challenging. More recently the Berry phase has been observed in the ensemble average spectrum of Aharonov-Bohm (AB) conductance oscillations in 2D semiconductor rings within an InAs 2D electron gas, in the presence of strong Rashba spin-orbit interaction [188, 195]. In its rest frame, a electron moving in the plane of a 2DEG "sees" the Rashba SO interaction as an inhomogeneous, momentum-dependent intrinsic in-plane magnetic field B_{int} that is perpendicular to the particle's momentum. The total magnetic field experienced by the carrier is $B_{tot} = B_{ext} + B_{int}$ where B_{ext} is an external field perpendicular to the 2D plane, shown in the insert of Fig. 5.3a. The particles spin precesses around B_{tot} and accumulates an additional geometric phase upon completing one cyclic evolution. In the adiabatic limit, the precession frequency of the spin around the local field B_{tot} is much faster than the orbital frequency [167], and the ring can be considered to consist of two uncoupled types of carriers with opposite spins [94]. The total phase acquired by the electron is determined by the angle (η) between the net field and the normal to the plane, and is composed of the AB phase and the SO induced geometric phase, which is different for the two spin species, $\Phi_{tot} = \Phi_{AB} + \Phi_{SO}$, and the superposition of the oscillatory contributions from both spin species is detected in the magnetoresistance of the ring.

Due to the requirement of strong SO interaction to create a sufficiently strong B_{eff} for spin precession to follow momentum, another semiconductor material in which Berry phase has been observed is in GaAs 2D hole systems, in semiconductor rings via Aharonov-Bohm oscillations [94, 295, 296] and Aharonov-Bohm-like oscillations in a GaAs hole antidot array [132]. Holes naturally possess strong SO coupling at $B = 0$, with an inversion asymmetry resulting from its zinc blende crystal structure. This leads to significant spin splitting of the energy bands in the absence of an applied magnetic field and the basic behaviour of holes in the ring is virtually same as that described in the previous paragraph for the electron case.

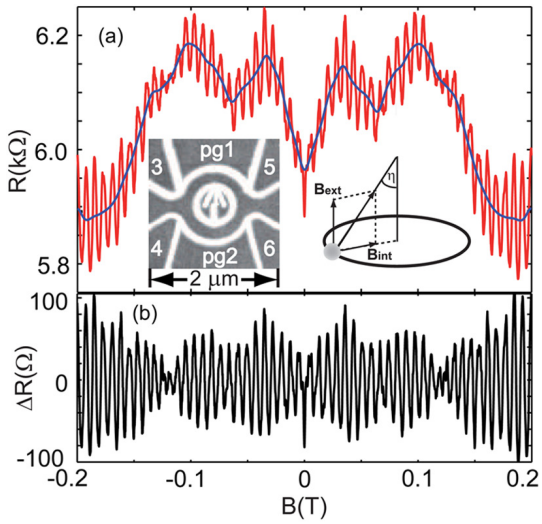

Figure 5.3: Aharanov-Bohm oscillations in a mesoscopic ring in a GaAs 2D hole system. (a) Insert shows an SEM image of the ring, and the effect of the fields felt by a particle as it travels through the ring. Low field oscillations in the magnetoresistance as a function of perpendicular field. (b) Normalized magnetoresistance oscillations showing a distinct beating pattern. Reproduced from Ref. [94].

Non-abelian gauge field experiments

The non-abelian gauge field has been theoretically predicted to exist in a number of many-body systems e.g. fractional quantum Hall liquids [187], spin-orbit coupled systems [13, 189], self-assembled quantum dots [253], cuprate semiconductors and ensembles of ultracold atoms [156] (see review Ref. [87] for more examples). One of the earliest examples of a non-abelian gauge field is Thomas precession [260], which describes the geometric precession of a spinning axis due to a non-abelian gauge field. In this case, the gauge field is precisely equal to a local Lorentz transformation projected onto the co-moving frame [180]. Just like the abelian Berry phase, detecting the non-abelian gauge field in a solid-state system is challenging. To-date the only experimental evidence of non-abelian Berry behaviour in such a system was found in the nuclear quadrupole resonance of ^{35}Cl in a single crystal of sodium chlorate [311].

One of the conditions to observe a non-abelian gauge structure is the need to map a path in parameter space where the spin varies by two angles. In the aforementioned experiments on Berry phase, mesoscopic rings were used to curve the particle's trajectory along a single axis (in the adiabatic limit B_{eff} follows the particle's orbital

momentum), thus varying one angle and exploiting only one parameter subgroup of the full non-abelian structure. To achieve a change in two axes, Zwanziger *et al.* use a double rotor where the sample holder containing the crystal spins freely on an air bearing and is contained in a larger spinner, which itself spins about a different axis from the sample holder [311]. A radio-frequency coil around the larger spinner of the double rotor is used to excite and detect the Cl resonance. A nonzero magnetization is prepared with a radio-frequency pulse and its time evolution monitored as the crystal undergoes the double rotor trajectory. The experiment was conducted in the adiabatic regime where the frequency of both rotors (360Hz for the spinner and 2020Hz for the sample holder) were much lower than the transition frequency of the quadrupole splitting at 29.94MHz. Under double rotation this spectrum breaks up into five lines, which required simulations to use the path-ordered integration of the full non-abelian gauge potential to match the dataset, and could not be reduced to the simplified abelian Berry form [311], thus providing evidence for the non-abelian geometric phase.

Since the experiment by Zwanziger *et al.*, experimental proposals have been made to detect the non-abelian Berry phase in systems with strong spin-orbit coupling such as p-type semiconductors [13, 189], however confirmation is yet to be established. The effective Luttinger Hamiltonian for bulk holes in the spherical approximation can be expressed as [189]

$$\mathcal{H}_0 = \frac{\hbar^2}{2m}\left\{\left(\gamma_1 + \frac{5}{2}\gamma_2\right)k^2 - 2\gamma_2(\boldsymbol{k}\cdot\boldsymbol{S})^2\right\}\ , \tag{5.22}$$

where S is the spin-3/2 matrix and γ_i are the Luttinger parameters. For a given wave vector $\boldsymbol{k}$ the Hamiltonian has 2 eigenvalues which form Kramers doublets, corresponding to the light- ($J = \pm\frac{1}{2}$) and heavy- ($J = \pm\frac{3}{2}$) hole bands. Rather than being characterized by an B_{eff} as in the electron case, the hole Hamiltonian is characterized by the effective quadrupole tensor field, leading to non-abelian effects [13].

Murakami *et al.* predicted that an electric field can induce a substantial amount of dissipationless spin current at room temperature, in hole-doped semiconductors [189]. One example uses an external electric field applied in the 2D plane (along z) of a p-GaAs semiconductor material, to induce a spin current along y. In order to detect

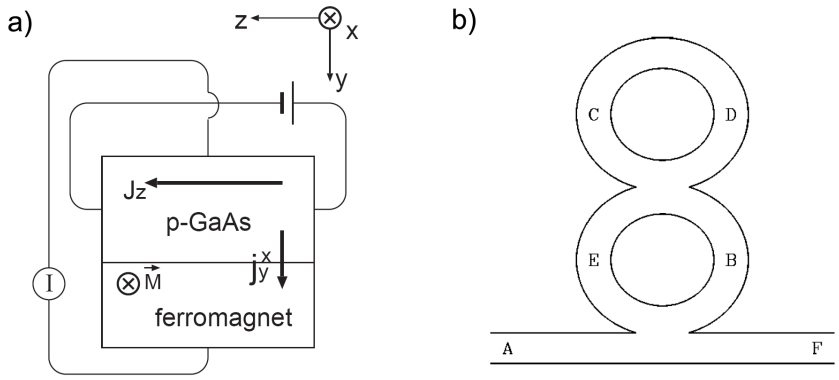

Figure 5.4: Proposals to detect non-abelian spin dynamics in p-type zinc blende semiconductors. (a) Experimental setup proposed by Murakami *et al.* to detect non-abelian effects by attaching a ferromagnetic electrode to a GaAs semiconductor, and measuring the dependence of current I flowing into the electrode on the direction of the magnetization $\boldsymbol{M}$ [189]. (b) Arovas *et al.* propose to use figure-8 mesoscopic rings within an external in-plane electric field to detect the non-abelian Berry phase through interference [13].

spin-dependent transport, a ferromagnetic electrode with magnetization $\boldsymbol{M}$ along $\pm x$ is attached to the positive y side of the sample and the other connecting lead attached to the p-GaAs as shown in Fig. 5.4 to complete the circuit [189]. The authors predict a change in the electric current I depending on the direction of $\boldsymbol{M}$.

A different approach to studying non-abelian spin dynamics was suggested by Arovas *et al.* who propose an experiment which uses a figure-8 mesoscopic ring to bend the trajectory of the holes along the 2D plane [13]. To achieve rotation in another axis, the authors effectively place the system in a rotating frame by imposing a static magnetic field in the plane of the ring. Transport measurements in this setup operate in a similar fashion to previous single ring structures in which Aharanov-Bohm oscillations were observed. Unlike the examples previous mentioned to detect the abelian Berry phase, the figure-8 ring like structure is designed to isolate non-abelian interference effects and cancel out the abelian effects [13].

In the rest of the chapter, we shall outline a new Onsager-like theory which predicts the existence of the non-abelian gauge field in a 2D hole system and discuss an alternative experimental setup to detect its presence. We then compare the experimental data with the predictions of the outlined theory, thus providing the first experimental

evidence for the non-abelian gauge field in a solid-state semiconductor system.

5.3 Non-abelian gauge fields in a GaAs 2D hole system

In this section we shall describe how the non-abelian gauge field manifests itself in a 2D hole system. We begin with outline of the semiclassical formalism which generalizes the Onsager quantization condition, where the quantum evolution equations are explicitly solved for non-abelian spin dynamics, and the spin-dependent phases appear alongside the Aharanov-Bohm contribution in the Lifshits-Kosevich formula. Such a semiclassical picture provides an effective technique to elucidate the role of spin-orbit coupling in transport and provides evidence for the matrix-valued phase, a signature of the non-abelian gauge field. Next we describe the conditions under which the non-abelian gauge field can be detected in a 2D hole system, using transport measurements in tilted magnetic fields to rotate the spins along two different axes, and control the magnitude of the spin-orbit coupling. This forms the basis of our experimental setup.

Note that the theoretical formalism and all calculations in this chapter were performed by T. Li. The experiment was performed by the author of this thesis and the analysis was a joint effort.

5.3.1 Conditions for generating and detecting the non-abelian gauge field

In order to generate and detect a non-abelian gauge field in a semiconductor system, the following conditions need to be met:

1. The system must possess degenerate (or nearly degenerate) energy bands to make use of the full matrix structure of the non-abelian Berry curvature. Valence band holes are ideal candidates as they naturally possess a four-fold degeneracy at k=0. This strong spin-orbit coupling term is unique to holes and is represented by the term $(\boldsymbol{k} \cdot \boldsymbol{S})^2$ in the spherical approximation of the Luttinger Hamiltonian 5.22.

2. Particles should follow a closed loop trajectory and according to Onsager [199], for a stationary state to exist the total phase accumulated along the trajectory

must be quantized. Rather than using mesoscopic patterned rings as in Ref. [13], we apply a small (<1T) magnetic field perpendicular to the 2D hole plane to curve the hole trajectories and form a closed cyclotron orbit. The perpendicular field induces quantum magnetic oscillations which can be detected with transport measurements.

3. The momentum relaxation length l of the particle must be larger than the cyclotron radius $l > r_c$ so that $\omega_c\tau > 1$, in order for the particle to complete one cyclotron orbit without being scattered. Likewise the phase coherence length $l_\phi = v_F\tau_\phi$ should be much greater than the mean free path of a carrier, which is greater than the sample length, in a ballistic system.

4. In order to probe non-abelian effects, the spin degree of freedom must undergo double axis rotation. To achieve this, in addition to the perpendicular field, an in-plane field component (of several Tesla) is introduced, which is coupled to the spins via the Zeeman effect. The combination of the in-plane Zeeman contribution to the Hamiltonian and the intrinsic spin-orbit coupling of holes introduces the other degree of freedom to the spin precession, resulting in non-abelian behaviour. This behaviour can be observed in the phase of the quantum magnetic oscillations generated by the perpendicular field, as an additional matrix-valued phase, which is the gauge-invariant observable trace of the $SU(2)$ matrix describing the non-abelian gauge field.

5.3.2 Non-abelian Berry curvature formalism for a GaAs 2D hole system

The theoretical formalism describing the author's data was developed by T. Li and O. P. Sushkov (to be published). In this section we only summarize the main aspects of this derivation.

Hole states in GaAs originate from atomic $p_{3/2}$ orbitals and hence possess an angular momentum J=3/2. The electric quadrupole interaction leads to strong coupling between the angular momentum ($\boldsymbol{J}$) and the linear momentum ($\boldsymbol{k}$), which is described by the Luttinger Hamiltonian [172]. The z-confinement in a low-dimensional 2D het-

erostructure enforces quantization of $\boldsymbol{J}$ along the z-axis. Therefore, a hole quantum state with a given in-plane momentum $\boldsymbol{k} = (k_x, k_y)$ splits into two doublets with $J_z = \pm 3/2$ (heavy holes) and $J_z = \pm 1/2$ (light holes). Since light holes lie significantly higher in energy, we shall only consider heavy holes for the low energy dynamics in our work.

The heavy-hole Kramers doublet can be described by an effective spin $s = 1/2$, $|J_z = +3/2\rangle \equiv |\uparrow\rangle$, $|J_z = -3/2\rangle \equiv |\downarrow\rangle$. The Hamiltonian describing heavy holes consists of three parts – the kinetic energy, the Zeeman interaction and the spin-orbit interaction, $\mathcal{H} = \mathcal{H}_K + \mathcal{H}_Z + \mathcal{H}_{so}$ (hereafter we set $\hbar = 1$),

$$\begin{aligned} \mathcal{H}_K &= (\boldsymbol{k} - e\boldsymbol{A})^2/2m \\ \mathcal{H}_Z &= -\frac{\Delta}{2}\sigma_z, \quad \Delta = g_{zz}\mu_B B_z \\ \mathcal{H}_{so} &\equiv -\boldsymbol{\beta}(\boldsymbol{k})\cdot\boldsymbol{\sigma} = -\frac{1}{2}\alpha\left[\sigma_+ B_- k_-^2 + \sigma_- B_+ k_+^2\right] \end{aligned} \tag{5.23}$$

where $\sigma_\pm = \sigma_x \pm i\sigma_y$, $B_\pm = B_x \pm iB_y$, $k_\pm = k_x \pm ik_y$; m is mass of the heavy-hole, $\boldsymbol{A}$ is the in-plane vector potential created by B_z, e is the electronic charge, σ_i are Pauli matrices describing the spin, $\mu_B = e/2m_e$ is Bohr magneton, $g_{zz} \approx 7.2$ [284], m_e is the electron mass and α is the spin-orbit coefficient. Note that for holes, the sign of the energy compared to Ref. [284] has been reversed. The SO interaction arises purely from a small mixing between heavy and light holes due to the presence of the in-plane field, and does not describe Dresselhaus SO or Rashba SO. The kinematic structure of $\mathcal{H}_{so}$ in Eq. 5.23 is dictated by the fact that the Pauli matrices $\sigma_\pm$ correspond to $\Delta J_z = \pm 3$. A more detailed derivation of the SO interaction $\mathcal{H}_{so}$ is presented in Appendix C.

If the perpendicular magnetic field is zero, $\boldsymbol{A} \propto B_z = 0$, then the hole trajectories are straight lines and $\mathcal{H}_{so}$ in Eq. 5.23 simply splits the doubly degenerate band, $\epsilon_k = k^2/2m$, into a pair of chiral bands. In the presence of the perpendicular field, the hole trajectory forms a closed circle, $\boldsymbol{k} = k(\cos\theta, \sin\theta)$.

Semiclassically, using the wave packet picture, the angle of the orbit enclosed by the hole trajectory is, $\theta = -\omega_c t$ (the sign corresponds to $B_z > 0$), where $\omega_c = e|B_z|/m$ is the cyclotron frequency. The spin-orbit field $\boldsymbol{\beta}(\boldsymbol{k})$ varies along the trajectory. This variation can be removed by a local gauge transformation of the spinor wave function

$\psi \to \psi' = g^{-1}(\boldsymbol{k})\psi$. Taking $g(\boldsymbol{k}) = e^{-i\theta\sigma_z}$ we gauge out the angle dependence of the SO field,

$$\boldsymbol{\beta}'(\boldsymbol{k}) \cdot \boldsymbol{\sigma} = g^{-1} \left[\boldsymbol{\beta} \cdot \boldsymbol{\sigma}\right] g \ , \quad \boldsymbol{\beta}' = \alpha k^2 \boldsymbol{B}_{\parallel} \ . \tag{5.24}$$

Since our choice of $g(\boldsymbol{k})$ ensures that we perform a transformation to the co-rotating frame of the hole, it follows that $\boldsymbol{\beta}'$ does not vary along the trajectory. The gauge transformation results in the covariant derivative $\boldsymbol{\nabla} \to \boldsymbol{\nabla} - i\mathcal{A}_{\boldsymbol{k}}$, where $\mathcal{A}_{\boldsymbol{k}}$ is the non-abelian gauge field (or vector potential) possessing a vortex structure in 2D momentum space

$$\mathcal{A}_{\boldsymbol{k}} = ig^{-1}\boldsymbol{\nabla}_{\boldsymbol{k}} g = \left(-\frac{k_y\sigma_z}{k^2}, \frac{k_x\sigma_z}{k^2}\right) \ . \tag{5.25}$$

The field tensor corresponding to this gauge field is zero, $\mathcal{F}_{\mu\nu} = \partial_\mu \mathcal{A}_\nu - \partial_\nu \mathcal{A}_\mu - [\mathcal{A}_\mu, \mathcal{A}_\nu] = 0$. However, the gauge field has a nonzero circulation along the hole trajectory

$$\oint \mathcal{A}_{\boldsymbol{k}} \cdot \boldsymbol{dk} = 2\pi\sigma_z \ \ , \tag{5.26}$$

and this circulation manifests as quantum magnetic oscillations.

In order to appreciate the full dynamics which underlies quantum magnetic oscillations, we need to consider the impact of the SO interaction ($\mathcal{H}_{so}$) upon the Landau level structure. For this analysis, we restrict ourselves to a semiclassical approximation, where the Landau levels are determined by the Onsager quantization condition. Consider a hole traversing the circular trajectory, where the hole is initially prepared in a polarization state $\psi(0)$. Under the combined action of $\mathcal{H}_{so}$ and $\mathcal{H}_Z$ spin will precess along the trajectory, as shown in Fig.5.1c. After one full cycle the spin wave function becomes $\psi(2\pi) = \mathcal{U}\psi(0)$, where $\mathcal{U} \in \mathrm{SU}(2)$ is a unitary evolution matrix. In order to form a standing wave (and hence satisfy the semiclassical quantization condition), it is necessary for $\psi(0)$ to be an eigenvector of $\mathcal{U}$, i.e. $\psi(2\pi) = e^{\pm i\Phi}\psi(0)$. Here $e^{\pm i\Phi}$ are the complex conjugate eigenvalues of $\mathcal{U}$. Hence, depending on the spin state, an additional phase $\pm\Phi$ appears in the Onsager quantization condition due to spin dynamics.

SdH oscillations in the resistivity are described by the Lifshits-Kosevich formula [163]. Accounting for the additional phase Φ we obtain,

$$\Delta\rho_{xx} = \rho_{xx}(B) - \rho_{xx}(0) = \mathcal{D}(B)\cos\Phi\cos\frac{2\pi E_F}{\omega_c} \ \ . \tag{5.27}$$

Here E_F is the Fermi energy and the amplitude factor $\mathcal{D}(B)$ depends on the hole scattering time τ, $\mathcal{D}(B) \propto e^{-\frac{\pi}{\omega_c \tau}}$. Spin dynamics enters only via the spin evolution phase factor $\mathrm{tr}\,\mathcal{U} = 2\cos\Phi$. For the semiclassical approximation we assume large filling factors $\nu = \frac{E_F}{\omega_c} \gg 1$, hence only the lowest harmonic of magnetic oscillations is taken into consideration.

The matrix phase $\mathcal{U}$ may be explicitly expressed as a path-ordered exponential which can be calculated using the gauge transformation from Eq.(5.24)

$$\begin{aligned} \mathcal{U} &= \mathcal{P}\exp\left\{-\frac{i}{\omega_c}\oint\left[\boldsymbol{\beta}\cdot\boldsymbol{\sigma}+\frac{\Delta}{2}\sigma_z\right]d\theta\right\} \\ &= \exp\left\{i\oint\mathcal{A}_{\boldsymbol{k}}\cdot\boldsymbol{dk} - i\frac{2\pi}{\omega_c}\left[\boldsymbol{\beta}'\cdot\boldsymbol{\sigma}+\frac{\Delta}{2}\sigma_z\right]\right\}\ . \end{aligned} \tag{5.28}$$

It is this matrix phase $\mathcal{U}$ that we detect via transport measurements, which is comprised of both a geometrical (the first term) and a dynamical (the second term) component. In our experiment these terms can be identified individually due to the fact that the path-ordered exponential can be evaluated in a simple form as described in the equation above. So by using Eqs. 5.26 and 5.24 we find the prefactor Φ in Eq.(5.27) for the amplitude of the SdH oscillations, $2\cos\Phi = \mathrm{tr}\,\mathcal{U}$,

$$\Phi = \frac{2\pi}{\omega_c}\sqrt{\left(\omega_c - \frac{\Delta}{2}\right)^2 + |\alpha k_F^2|^2(B_x^2+B_y^2)}\ . \tag{5.29}$$

Here k_F is Fermi momentum and the geometric contribution is simply equal to ω_c (inside the square root), which comes from the non-abelian gauge field. As previously mentioned, the gauge field cannot be observed without the in-plane field. This is evident from Eq. 5.29: if $\boldsymbol{B}_\parallel = 0$ the gauge contribution is exactly 2π and hence the phase shift is determined only by the Zeeman splitting, $\mathrm{tr}\,\mathcal{U} = 2\cos(\pi\Delta/\omega_c)$. The Zeeman splitting with $\boldsymbol{B}_\parallel \neq 0$ is $\delta E_Z = \sqrt{(\frac{\Delta}{2})^2 + |\alpha k_F^2|^2(B_x^2+B_y^2)}$. A naive expectation for the spin accumulated phase draws a direct relation to the Zeeman splitting $\Phi_{naive} = 2\pi\delta E_Z/\omega_c$, however Eq. 5.29 differs from this. A semi-naive expectation takes into account the abelian Berry phase φ_B on top of the Zeeman splitting. The phase φ_B is given by the first term of the square root expansion in Eq. 5.29 in powers of ω_c, yielding

$$\Phi_{AB} = \frac{2\pi\delta E_Z}{\omega_c} + \varphi_B = \frac{2\pi\delta E_Z}{\omega_c} - \frac{\pi\Delta}{\delta E_Z}\ . \tag{5.30}$$

The subscript "AB" in Φ stands for "abelian Berry". Although this abelian Berry phase approach has been shown to provide a good description for magneto-oscillations in Dirac fermion systems [6, 198], and quantum interference in mesoscopic rings [94, 296], we discover that both the "naive" Φ_{naive} and abelian Berry phase Φ_{AB} approaches are inconsistent with our data.

As shown in the previous chapter for a GaAs 2D hole system grown on the low-symmetry (311)A crystal plane, the gyromagnetic tensor is not diagonal in the x, y and z axes. Hence we need to account for this in the expression for Δ presented in Eq. 5.23, which is now replaced by

$$\Delta = \mu_B(g_{zz}B_z + g^*_{xz}B_x) \quad . \tag{5.31}$$

This off-diagonal tensor component g^*_{xz} causes the magnetic response to be asymmetric between $B_x \rightarrow -B_x$.

Substituting the effect of the low-symmetry crystal directions upon the gyromagnetic tensor into the spin evolution phase in Eq. 5.29, the additional phase can be expressed as

$$\Phi = \frac{2\pi}{\omega_c}\sqrt{\left(\omega_c - \frac{\mu_B(g_{zz}B_z + g^*_{xz}B_x)}{2}\right)^2 + |\alpha k_F^2|^2(B_x^2 + B_y^2)}. \tag{5.32}$$

5.4 Experimental Results

5.4.1 Experimental concept and methodology

In order to meet the stringent conditions outlined in Section 5.3.1 to generate and detect a non-abelian gauge field, we conduct transport measurements using high-mobility 2D hole system (2DHS) samples with standard Hall bar geometry, fabricated by Prof. A. R. Hamilton. These were made from a GaAs/$Al_{0.33}Ga_{0.67}As$ heterostructure, grown on a low-symmetry (311)A surface, from a T335 wafer, by the Semiconductor Physics group at Cavendish Laboratory. A conducting substrate doubles as an *in situ* back-gate, located 2.6μm away from a symmetrically, modulation Si-doped 20nm wide GaAs quantum well [243].

Control over the individual components of the magnetic field, was achieved using a tilted-field measurement technique, similar to that performed by Fang and Stiles [75].

The sample was mounted on an *in situ* piezoelectric rotator, featuring an in-built angle readout mechanism with an accuracy of $\pm 0.01^\circ$ [299], detailed in Chapter 4.3.2. This allowed for single-axis rotation to be conducted at a base temperature of 35mK cooled by an Oxford K100 dilution refrigerator, within the bore of a 15T superconducting magnet. Transport measurements were performed using standard ac lock-in techniques, with a constant ac current of 5nA at a frequency of 5Hz. For this experiment only the lowest heavy hole band is occupied.

The relative positions of the magnetic field and the crystal axes of the sample was first calibrated by rotating the 2D Hall bar at a fixed field through an angle of 90° and noting the positions where the sample plane is fully perpendicular to the field, $\theta_{tilt} = 90^\circ$ and fully parallel $\theta_{tilt} = 0^\circ$. For details see Chapter 4.4.3 and Appendix B.

As the spins travelling through the quantum well are free to evolve kinematically under the effect of several competing interactions, including the Zeeman, Rashba and Dresselhaus couplings further tuning of the sample was necessary to eliminate unwanted parasitic effects in this study. Despite the symmetric doping on either side of the quantum well, there was still in beatings of the Shubnikov-de Haas even without any tilting of the magnetic field [68]. As the Rashba interaction is sensitive to the confining potential, by varying the bias voltage applied to the *in situ* back-gate, we tune the system by compensating the fixed effect of the Dresslehaus SO using the Rashba SO, to the point where their combined influence on the spin dynamics is negligible. This was detected by finding the back-gate bias at which the beating in the low field SdH oscillations were minimized as described in Chapter 4.4.4. A back gate voltage of +1.50V was selected where the carrier density is $p = 9.26\times10^{10}\mathrm{cm}^{-2}$ and a mobility of $\mu = 0.6\times10^{6}\mathrm{cm}^{2}\mathrm{V}^{-1}\mathrm{s}^{-1}$. This back-gate voltage is the operating point used for the rest of the experiment.

If we fix the perpendicular field and vary only an in-plane field, we will observe the effect of the non-abelian gauge field as a phase shift. But due to the tilted-field nature of the experiment, as the in-plane component is varied in proportion with the cyclotron frequency (controlled by the perpendicular component), the effect of the gauge field is manifested as a modulation to the amplitude of the magnetoresistivity

oscillations in the form of beatings. At certain tilt angles where the frequency of the oscillations double, the phase simultaneously undergoes a π-phase shift (as seen in the coincidence method [75]). Several such angles are observed in our experiment.

The crystallographic anisotropy of the low-symmetry (311) surface leads to an orientation-dependent response to the in-plane field component and in Chapter 4.5 we discovered that the off-diagonal g tensor component g^*_{xz} causes the magnetic response to be asymmetric with respect to $B_x \to -B_x$. Such a low symmetry crystal enables us to study the effect of the non-abelian gauge field along a high symmetry $[01\bar{1}]$ direction and compare this case to its effect upon the spin dynamics in the low symmetry $[\bar{2}33]$ and $[2\bar{3}\bar{3}]$ directions, allowing for 3 sets of independent tests of the non-abelian theory.

5.4.2 Tilted field transport measurements

To perform tilted field transport measurements, the device was first mounted on the rotator such that the total magnetic field rotates, between the crystal axes [311] and $[01\bar{1}]$, where the 2D plane is perpendicular to the field at θ_{tilt}=90°, shown in Fig. 5.5. The sample was then rotated towards the $[01\bar{1}]$ direction till $\theta_{tilt} = +10°$ to introduce a parallel field component B_x, and the total field B_{tot} swept, changing the sign of the in-plane field $\pm B_x$. This procedure was repeated for a number of different $+\theta_{tilt}$ with increasing in-plane field components. The experiment was then repeated for an equivalent $-\theta_{tilt}$ and the results shown in Fig. 5.5.

During a second cool down, the sample was reoriented to perform tilted measurements along the [311] and low symmetry $[\bar{2}33]$ crystal axes. The quantum well was re-symmetrized using the procedure described in Chapter 4.4.4 and the measurement procedure was then repeated for both $\pm\theta_{tilt}$. The results are graphed in Fig. 5.6.

From the experimental results shown in Fig. 5.5 and Fig. 5.6, we are interested in the changing phase of the magnetoresistivity oscillations. For the purposes of our analysis we will focus upon the low field oscillations between $B_z = 0.16$T and 0.5T. Both Figs. 5.5 and 5.6 plot resistivity versus $1/B_z$ where the sample is tilted with respect to the magnetic field over a range of angles θ_{tilt}, such that $B_z = |B_\parallel| \tan\theta_{tilt}$. Fig. 5.5 corresponds to tilting in the yz-plane ($B_x = 0$) and Fig. 5.6 corresponds to

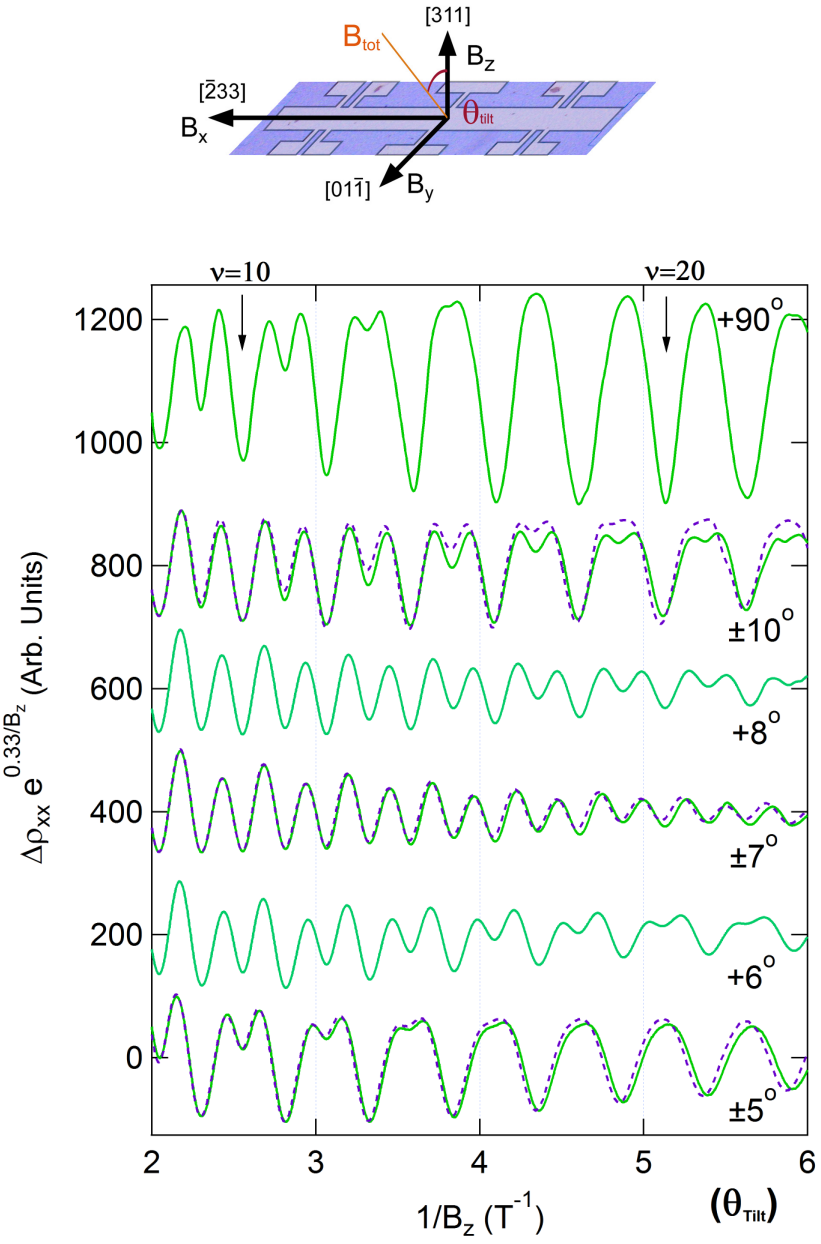

Figure 5.5: Sample orientation in the magnetic field when the in-plane field B_y is applied along the $[01\bar{1}]$ crystal direction. The sample rotates in an external magnetic field $\boldsymbol{B}_{tot}$ by an angle θ_{tilt} to the 2D heterostructure, $|B_y| = B_z \tan\theta_{tilt}$. SdH oscillations are plotted as a function of $\frac{1}{B_z}$ for an applied field of $B_y > 0$, $B_x = 0$ (green solid lines $\equiv +\theta_{tilt}$) and $B_y < 0$, $B_x = 0$ (purple dotted lines $\equiv -\theta_{tilt}$). SdH traces are offset for clarity. The amplitude of the oscillations was normalized by multiplying the data by $e^{0.33/B_z}$. At $\theta_{tilt} = 7.5 \pm 0.5°$ the oscillations exhibit an inversion corresponding to the change in sign of $\cos\Phi$ in Eq.(5.27). The data in (c) is identical to that presented in Fig. 4.11, where $\theta_{tilt} = 90°$ is defined for the sample in perpendicular field to maintain consistency with the new calculations, rather than the $\theta_{tilt} = 0°$ reference in Fig. 4.11.

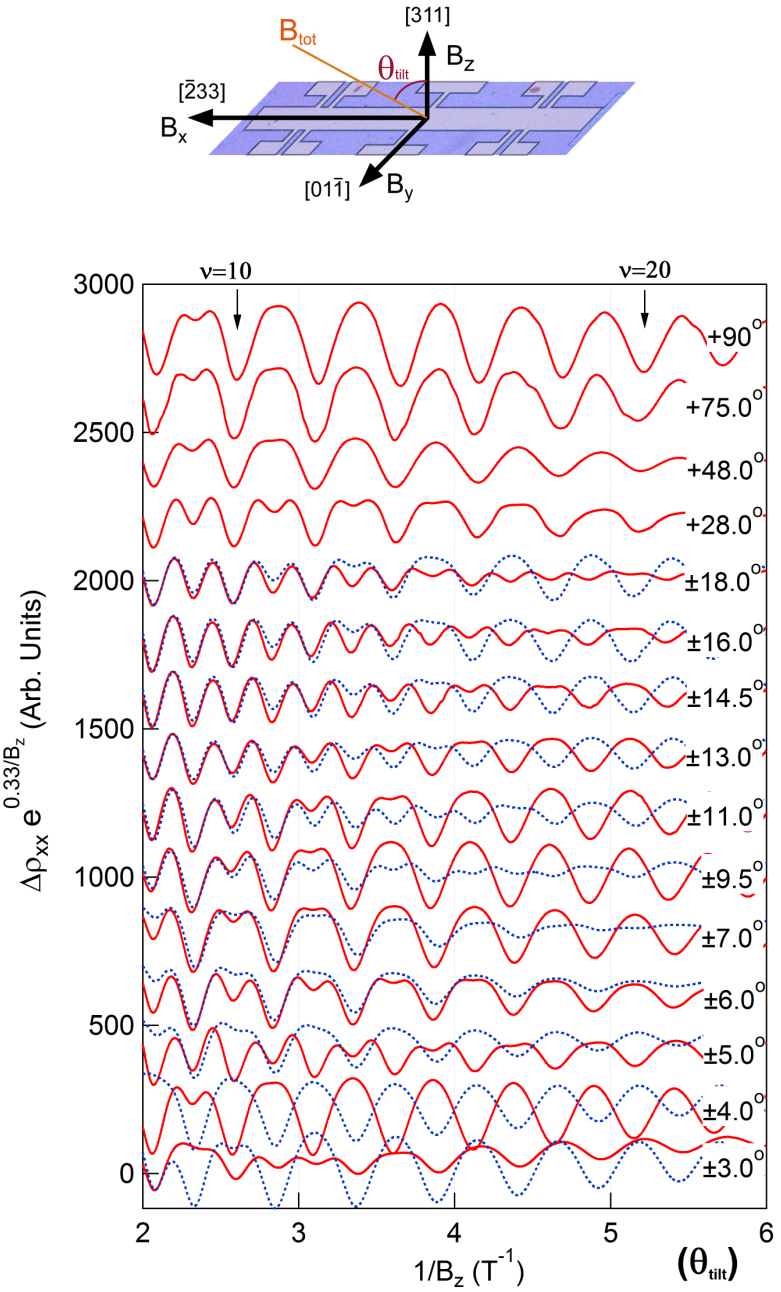

Figure 5.6: Dataset where the relative orientation of the magnetic field components to the sample axes is such that B_x lies along the [2̄33] crystal direction. The sample rotates in an external magnetic field $\boldsymbol{B}_{tot}$ by an angle θ_{tilt} to the 2D heterostructure, $|B_x| = B_z \tan\theta_{tilt}$. SdH oscillations are shown where the applied field is $B_x > 0$, $B_y = 0$ (red solid lines $\equiv +\theta_{tilt}$) and $B_x < 0$, $B_y = 0$ (blue dotted lines $\equiv -\theta_{tilt}$). Due to crystallographic anisotropy, the oscillations are distinctly different for different signs of B_x. The filling factors ν are indicated by arrows at the tops of panels (b,c). In these panels we indicate negative B_x or B_y by negative tilt angles. The data in (c) is identical to Fig. 4.12, with the perpendicular field orientation of the sample defined as $\theta_{tilt} = 90°$, to maintain consistency with the new calculations, as opposed to $\theta_{tilt} = 0°$ in Fig. 4.12.

tilting in the xz-plane ($B_y = 0$). The magnetoresistivity oscillations in Fig. 5.5 are symmetric with respect to $B_y \to -B_y$, whilst the traces in Fig. 5.6 exhibit asymmetry with respect to $B_x \to -B_x$ due to the nonvanishing g^*_{xz} in Eq. 5.31.

To visualize the phase evolution of the SdH oscillations along the $[\bar{2}33]$ direction i.e. xz-plane ($B_y = 0$), the positive tilt data and negative tilt data are plotted in separate panels in Fig. 5.7. The top of both panels begins with the sample plane fully perpendicular to the field ($B_x = 0$), with subsequent SdH traces taken at tilts with an increasing parallel field component ($B_x \neq 0$). To observe where the phase changes occur, each SdH trace can be compared with that taken in the fully perpendicular orientation (dashed black). If we follow the $\nu = 20$ minimum for $+\theta_{tilt}$ starting at 90°, we find this minimum evolves into a maximum at $+\theta_{tilt} = 18°$, back into a minimum between $5 - 6°$ and a maximum between $3 - 4°$. In contrast, the $\nu = 20$ minimum for $-\theta_{tilt}$ undergoes a single phase change between $-6°$ to $-7°$, where the feature appears nearly flat. Interestingly for $-\theta_{tilt}$ the exact angle at which this phase flip occurs appears to change with filling factor, trending slightly towards smaller $-\theta_{tilt}$ values at lower fields.

According to Eqs. 5.27 and 5.29, the normalized amplitude of resistivity oscillations $\cos\Phi$, is a function only of θ_{tilt} and is independent of the magnitude of the total magnetic field $\boldsymbol{B}$. At tilt angles corresponding to changes in the sign of $\mathrm{tr}\,\mathcal{U} = 2\cos\Phi$, the first harmonic of the SdH oscillations invert (i.e. maxima become minima, and vice versa). At these "coincidence" angles the phase Φ must coincide with a half-integer multiple of π.

To determine these angles of coincidence, we extract the phase difference for every filling factor between $\nu = 6$ and $\nu = 26$, with respect to its original position at 90°, for each subsequent $+\theta_{tilt}$. The corresponding phase evolution versus tilt angle plots are given in Fig. 5.8.

From these phase plots, the coincidence angles are observed at the tilt angle $\theta_{tilt} = 7 \pm 0.5°$ for the field applied along the yz-plane in Fig. 5.8(a,b) for both signs of the tilt angle. For the field applied in the xz-plane in Fig. 5.8(c,d), there are multiple coincidence angles at $\theta_{tilt} = 18 \pm 1°$, $5.5 \pm 0.5°$, $3.5 \pm 0.25°$ for $B_x > 0$ and a single

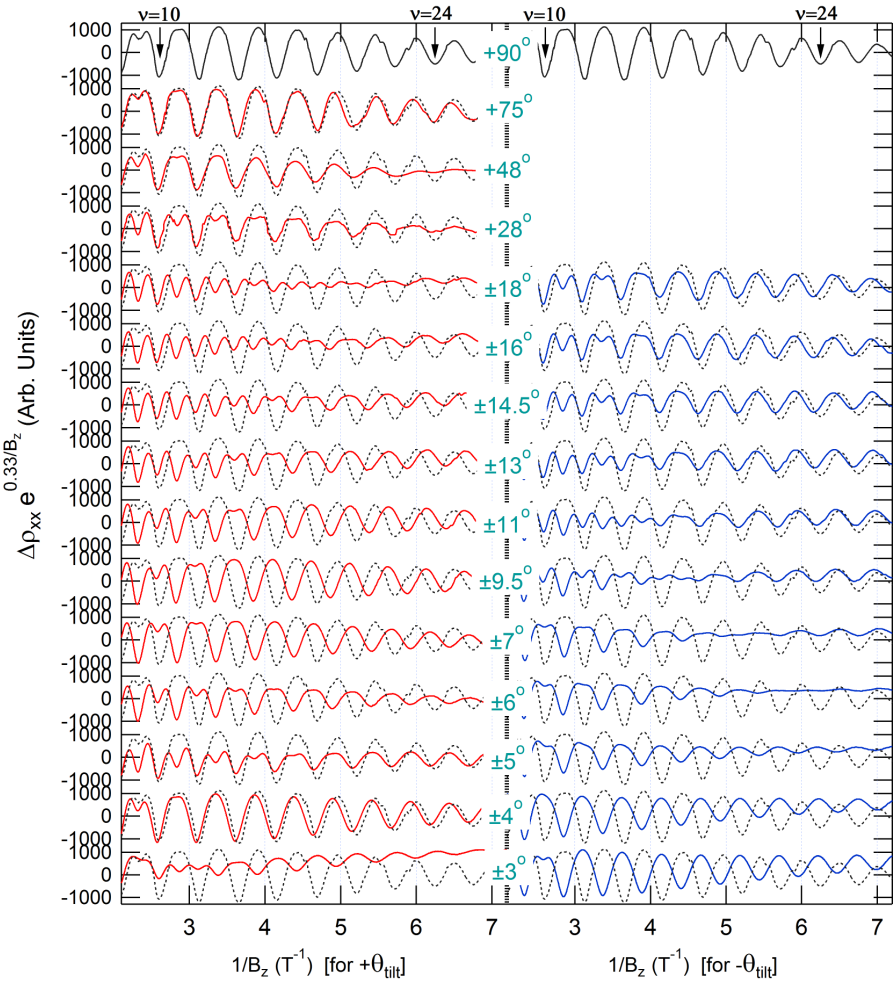

Figure 5.7: SdH oscillations in the magnetoresistance ρ_{xx} plotted versus $1/B_z$ where the field component B_x is aligned along the $[\bar{2}33]$ crystal direction as shown in Fig. 5.6, obtained from tilting in the xz-plane ($B_y = 0$). Here $+\theta_{tilt}$ traces (red) are plotted in a separate panel (left) from $-\theta_{tilt}$ traces (blue, right panel) for clarity. To visualize the phase evolution at each θ_{tilt}, the ρ_{xx} trace taken at $\theta_{tilt} = 90°$ is plotted in dashed black for each tilt angle. In this orientation, the oscillations invert at angles $+\theta_{tilt} = 18 \pm 1°, 5.5 \pm 0.5°, 3.5 \pm 0.25°$ for $B_x > 0$ and $-\theta_{tilt} = 6.5 \pm 0.5°$ for $B_x < 0$.

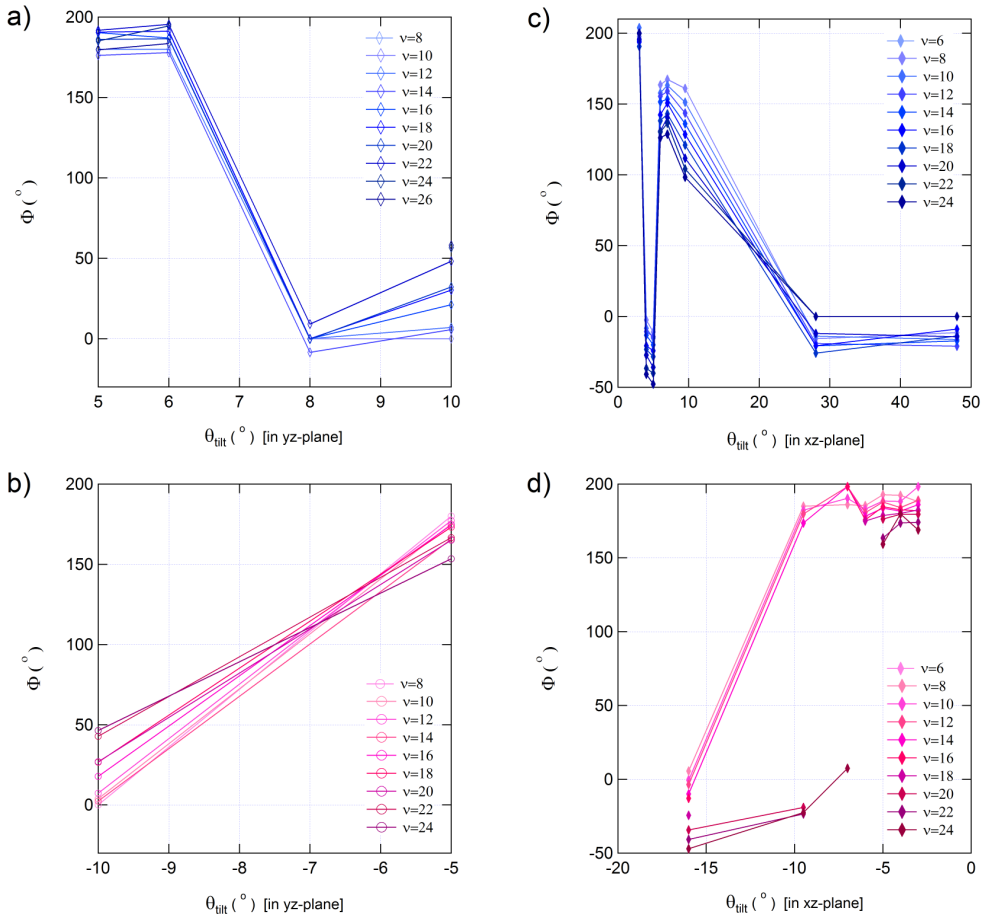

Figure 5.8: Phase evolution of the SdH resistivity oscillations Φ versus tilt angle, for all 4 combinations: (a) $B_{\|} \equiv B_y$ along $[01\bar{1}]$ for $+\theta_{tilt}$ and (b) $B_{\|} \equiv B_y$ along $[01\bar{1}]$ for $-\theta_{tilt}$, extracted from SdH resistivity oscillations in Fig. 5.5. (c) $B_{\|} \equiv B_x$ along $[\bar{2}33]$ for $+\theta_{tilt}$ and (b) $B_{\|} \equiv B_x$ along $[\bar{2}33]$ for $-\theta_{tilt}$, extracted from SdH resistivity oscillations in Fig. 5.7. For any filling factor between $\nu = 6$ and $\nu = 26$, the phase for each tilt angle is compared to its initial position at 90°.

coincidence angle at $\theta_{tilt} = 6.5 \pm 0.5^\circ$ for $B_x < 0$. Thee angles of coincidence can be described using Eqs. 5.32, which are based upon three independent, device-specific parameters: $g_{zz}m^*$, $2\alpha k_F^2/(g_{zz}\mu_B)$, and g_{xz}^*/g_{zz}. A commonly accepted value for the diagonal g-factor is $g_{zz} = 7.2$ [284]. We adopt this value and are hence left with unknowns m^*, $\lambda = 2\alpha k_F^2/\mu_B$, and g_{xz}^*. Numerical calculations with realistically shaped quantum wells yield an effective mass of $m^* \approx 0.2m_e$, although due to significant uncertainty in such calculations we will also set m^* as a free fitting parameter, with possible values in the range of $0.1m_e < m^* < 0.5m_e$. Calculations of λ and g_{xz}^* are even less reliable than that of m^*, therefore we also treat them as free fitting parameters, as described in the following section.

5.4.3 Modelling the data - abelian vs non-abelian paradigm

We now turn our attention to modelling the experimental data in order to draw a comparison between our experimental results and the non-abelian gauge field theory. Altogether we have 3 fitting parameters to describe 5 coincidence angles. To compare the experimental coincidence angles to those of theory, a least squares fit to the phase of the SdH resistivity oscillations, Φ, was performed using the observed 4 coincidences angles for the orientations $[\bar{2}33]$: $B_x > 0, B_y = 0$ and $[01\bar{1}]$: $B_y \neq 0, B_x = 0$. We then use these fitting parameters to predict the coincidence angles for the orientation $[2\bar{3}\bar{3}]$: $B_x < 0, B_y = 0$. Fitting the data in Fig.5.9a, gives the fitting parameters: $m^* = 0.21m_e$ (in good agreement with the numerical prediction), $|\lambda| = 1.1$ and $g_{xz}^* = -0.9$. Substituting these parameters into Eq. 5.32 allows us to predict the coincidence angles for $B_x < 0, B_y = 0$, graphed in Fig. 5.9b as an open circle. Here, a single coincidence angle is predicted at $\theta_{tilt} = 4.5^\circ$, which is in good agreement with the only observed coincidence at $\theta_{tilt} \approx 6.5^\circ \pm 0.5^\circ$. The small discrepancy is most likely due to a third-order in-plane field correction to the effective Hamiltonian which only becomes apparent at low tilt angles, i.e. large in-plane fields (see Appendix C for details).

Show that the data cannot be described without non-abelian spin dynamics, we have attempted to fit the observed data using the abelian Berry formula Eq. 5.30 instead of Eq. 5.32. Using Eqs. 5.30 and 5.31 we repeat the same procedure de-

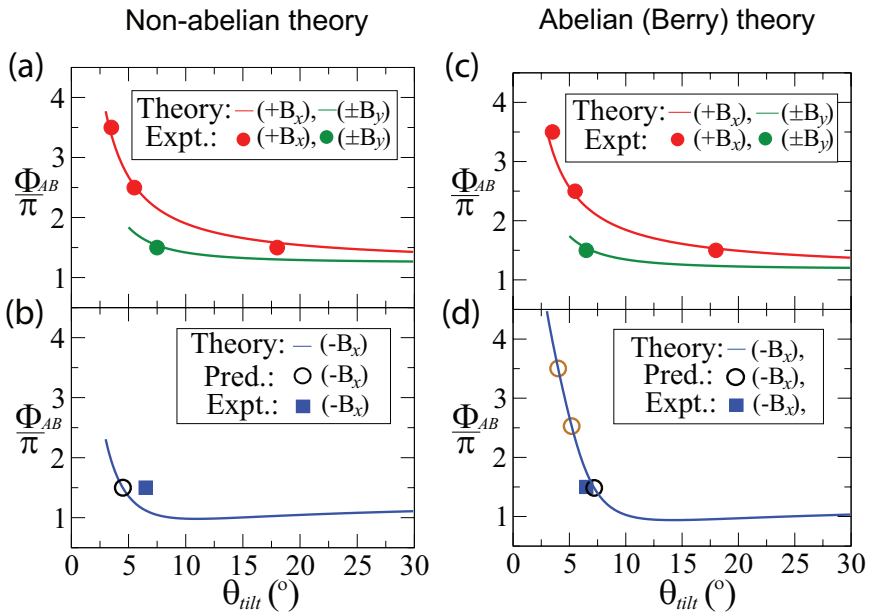

Figure 5.9: Comparison of experimentally observed coincidences angles to the non-abelian (a,b) and abelian (c,d) theories. Expressing the envelope of the SdH oscillations as $\cos\Phi$, we find that Φ/π becomes a smooth function of tilt angle. This function is plotted for the experimental range of tilting angles. Angles at which Φ crosses a half-integer multiple of π correspond to inversions of the SdH oscillations. Both theories contain three unknown parameters m^*, g^*_{xz}, λ. In (a,c) we show the least squares fits of Φ to the observed coincidence angles for an applied $B_x > 0, B_y = 0$ (red) and $B_y \neq 0, B_x = 0$ (green). The plots of Φ in (b,d) show the predicted coincidences for $B_x < 0, B_y = 0$. The non-abelian gauge theory (b) predicts a single angle of coincidence (open circle) which is close to the observed coincidence point (square). In contrast, the abelian theory (d) predicts three coincidences whilst experimentally only one angle of coincidence was observed. The two coincidence angles predicted by theory but are not present in the experimental data are marked in orange circles.

scribed above and fit Φ_{AB} to the observed 4 coincidence angles for the orientations $B_x > 0, B_y = 0$ and the single angle for $B_y \neq 0, B_x = 0$, as shown in Fig. 5.9c. These parameters were then used to predict the coincidence angles occurring for the orientation $B_x < 0, B_y = 0$, shown in Fig. 5.9d as open circles. The fitting parameters obtained are $m^* = 0.33m_e$, $|\lambda| = 0.41, g^*_{xz} = +0.61$. Unlike the non-abelian case, 3 coincidence angles are predicted for the $B_x < 0, B_y = 0$ direction (the extra 2 are coloured orange), compared to the single coincidence angle observed in the experiment. This discrepancy suggests that the experimental data cannot be reconciled with the paradigm of abelian Berry phases alone and provides evidence for the existence of non-abelian gauge fields in 2D hole systems in tilted fields.

The number of coincidence angles is a robust prediction of the abelian theory which could not be changed even after significant variation of the fitting parameters. This can be seen in Fig. 5.10 where we compare the calculated phase for different fitting parameters (lines) against the experimentally observed coincidence angles (circles and squares). Here the phase $\frac{\Phi}{\pi}$ is graphed as a function of tilt angle for varied parameters λ, g^*_{xz} and m^*. The top panel shows the calculated phase and the experimental coincidence points for orientations of the external field $B_x > 0$, $B_y = 0$ (red) and $B_y \neq 0$, $B_x = 0$ (green). The bottom panels show the calculated phase and experimental coincidence points for the field orientation $B_x < 0$, $B_y = 0$ (blue). The solid lines correspond to fitting parameter values $\lambda = 1.1$, $g^*_{xz} = -0.90$ and $m^* = 0.21$ used in Fig. 5.9 to fit the data. Dashed and dotted lines corresponds to variations in λ by $\pm 30\%$ in panels (a,b), g^*_{xz} by $\pm 30\%$ in panels (c,d) and m^* by $\pm 10\%$ in panels (e,f). Only one green line is present in panel (c) since at $B_y \neq 0$, $B_x = 0$ the phase is independent of g^*_{xz}.

Similarly, to demonstrate the robustness of the abelian Berry fit, the fitting parameters used in the abelian Berry model were varied by the same amount as in the non-abelian case and the results plotted in Fig. 5.11. Despite this variation in the fitting parameters, the abelian Berry paradigm still predicts three coincidence angles for the $B_x < 0$, $B_y = 0$ direction, compared to the single coincidence actually observed in experiment.

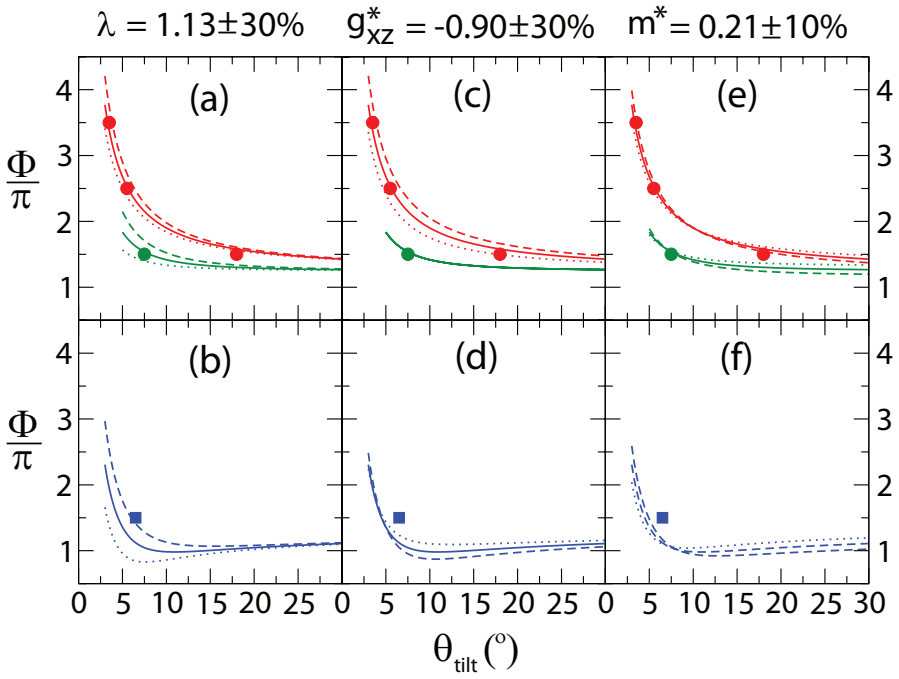

Figure 5.10: Plot of phase $\frac{\Phi}{\pi}$ (defined by the envelope of the resistivity oscillations $\rho_{xx} \propto \cos\Phi$) as a function of tilt angle (θ_{tilt}) for varied parameters λ, g^*_{xz} and m^* using the non-abelian model. The top panel shows the calculated phase and the experimental coincidence points for orientations of the external field $B_x > 0$, $B_y = 0$ (red) and $B_y \neq 0$, $B_x = 0$ (green). The bottom panels show the calculated phase and experimental coincidence points for the field orientation $B_x < 0$, $B_y = 0$ (blue). The solid lines correspond to fitting parameter values $\lambda = 1.1$, $g^*_{xz} = -0.90$ and $m^* = 0.21$ used in Fig. 5.9 to fit the data. Dashed and dotted lines corresponds to variations in λ by $\pm 30\%$ in panels (a,b), g^*_{xz} by $\pm 30\%$ in panels (c,d) and m^* by $\pm 10\%$ in panels (e,f).

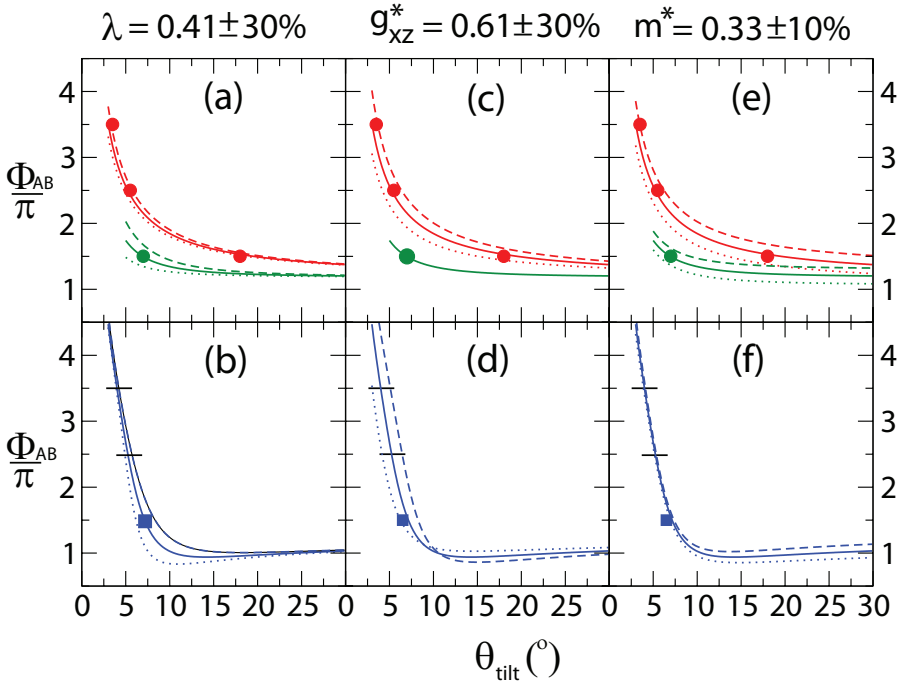

Figure 5.11: plot of $\frac{\Phi}{\pi}$ (defined by the envelope of the resistivity oscillations $\rho_{xx} \propto \cos\Phi$) as a function of tilt angle for varied parameters λ, g^*_{xz} and m^* using the abelian Berry model. The top panel shows the calculated phase and the experimental coincidence points for orientations of the external field $B_x > 0$, $B_y = 0$ (red) and $B_y \neq 0$, $B_x = 0$ (green). The bottom panels show the calculated phase and experimental coincidence points for the field orientation $B_x < 0$, $B_y = 0$ (blue). The solid lines correspond to fitting parameter values $\lambda = 0.41$, $g^*_{xz} = 0.61$ and $m^* = 0.33$ used in Fig. 5.9 to fit the data. Dashed and dotted lines corresponds to variations in λ by $\pm 30\%$ in panels (a,b), g^*_{xz} by $\pm 30\%$ in panels (c,d) and m^* by $\pm 10\%$ in panels (e,f).

5.5 Conclusions and future work

In summary, we have observed the effect of the non-abelian gauge field in a low-symmetry 2D hole system with strong spin-orbit coupling, using the technique of tilted field transport measurements to observe the matrix phase of the non-abelian gauge field as a modulation in the Shubnikov-de Haas oscillations as the magnetic field is varied. This result is one of the few measurements of the non-abelian gauge field and the first of its kind in a semiconductor crystal lattice.

Due to the nature of the system, as future work one suggestion may be to extend the tilt angle range in the $[01\bar{1}]$ to cover the same angle range as $[\bar{2}33]$ to achieve more phase flips. Another suggestion would be to gather data at lower angles in both directions. However, this would require a significantly larger in-plane field component around ≥ 10T, which would lead to significant distortion of the band structure due to orbital effects stemming from the finite width of the quantum well. Instead it may be of interest to repeat the experiment within a similar parameter space, but use samples with different quantum well widths and hence energy spacings between the light-hole and heavy hole subbands and mixing probabilities which should influence the spin dynamics. Another alternative is to perform a similar set of measurements at different densities.

Chapter 6

Induced quantum dots

6.1 Introduction

In the previous 2 chapters, we discuss the unusual spin dynamics of 2D hole systems, in this chapter we turn our attention to isolating single spin states by fabricating quantum dots using an induced architecture. The chapter begins by introducing quantum dots as artificial atoms and a quick overview of the development of electrostatically induced, lateral gated quantum dots in a variety of material systems. We describe the concept of using a quantum point contact as a charge sensor to independently determine dot occupancy in the few-N regime and introduce the concept of shell filling in electron systems. We highlight the unique challenges involved in creating robust, reproducible small quantum dots due to charge noise and random telegraph signals, and show how these challenges can be overcome by using a flexible, induced-style of architecture for such devices.

The final goal is to demonstrate a working few-hole, induced quantum dot which can be operated down to the last hole with integrated charge sensing. Due to the challenges of fabricating quantum dots, we achieve this using a two-stage approach:

1. We begin by demonstrating the fabrication of an induced GaAs electron quantum dot and characterizing it to see how well the dot design works with an induced, global-top gate architecture. Since electron dots possess larger energy scales than hole dots, they are easier to measure and we can draw comparisons with

results from other dots in literature. Once the geometry for the electron dot works well, the plan was to use the same quantum dot gate pattern to create a hole dot. During characterization, however, we found that although we were able to demonstrate Coulomb blockade behaviour, current directly through the dot was lost very shortly after the gates were defined and the charge detector was not sensitive.

2. To understand the role of the quantum dot confining potential within an induced architecture better, we perform simulations in Nextnano++ and discovered that the depth of the 2D gas below the surface, combined with the type of insulating dielectric, plays a critical role in the definition of good tunnel barriers. We also explore an alternative gate pattern using a symmetric design with increased coupling between the charge detector and the quantum dot, and make small adjustments to optimize the dot design for an electrostatically induced, small single-dot geometry.

3. Finally we apply this new design to a hole quantum dot and demonstrate the ability to tune the dot down to the last hole with charge sensing.

6.1.1 Quantum dots as artificial atoms

When a two-dimensional system is spatially confined along its remaining free directions, a 'zero-dimensional' quantum dot is formed, which possesses the unique ability to trap charge carriers on a small conducting island. The term "artificial atom" was coined to describe quantum dots [16, 133] as the energy spectrum of the trapped charges exhibit discrete, bound states similar to those seen in naturally occurring atoms, and electrons fill each discrete orbital according to Hund's rules [258]. Quantum dots are typically larger than natural atoms and can be easily manipulated and studied by applying electric and/or magnetic fields, making them ideal candidates for isolating and studying single spin states.

The first demonstration of single electron tunnelling behaviour was discovered by Scott-Thomas *et al.* in a 1D Silicon Field Effect Transistor (FET) [236], followed shortly by the first controllable single electron transistor by Meriav *et al.* in GaAs [184].

Since then extensive transport experiments have been conducted in electron quantum dots and summarised in reviews [100, 101, 134, 150].

6.2 Background

Since their conception, many experiments have been performed to study the charge [150] and spin states [101] of electron quantum dots. The idea to use semiconductor dots as spin qubits [166] has fuelled the development of well-controlled, small quantum dots operating down to the few-electron regime [150]. Due to the wide variety of different styles, types and single-to multi-dot architectures, for the purposes of this thesis we will narrow the focus to electrostatically defined lateral gated quantum dots and induced FET structures.

6.2.1 Few electron regime and single electron dots

Few-electron quantum dots [101] are ideal systems in which to study the behaviour of single spin states, where the ability to confine, manipulate, and probe individual electrons is a prerequsite to such studies. The ability to construct a quantum dot where one can simultaneously tune the number of electrons and interrogate them spectroscopically is important. This capability was first achieved in GaAs vertical quantum dots in the 1990's where the number of confined electrons was successfully controlled down to zero, resulting in the discovery of the shell filling structure and spin effects, studied using both capacitance and Coulomb blockade transport techniques [14, 258].

Despite the flexibility provided by lateral gated dots, achieving high tunability in this dot type proved to be more difficult, since reducing the electron number by driving the gate voltage to more negative values tended to decrease the tunnel coupling to the leads. The resulting current through the dot can become unmeasurably small before the few-electron regime is reached [101]. However, by optimizing the design of the surface gate geometry, it is possible to compensate for this decrease in the tunnel coupling. The very first demonstration of a small *lateral* dot, controllably emptied down to the last electron was performed by Ciorga *et al.* [43]. The dot was defined in a

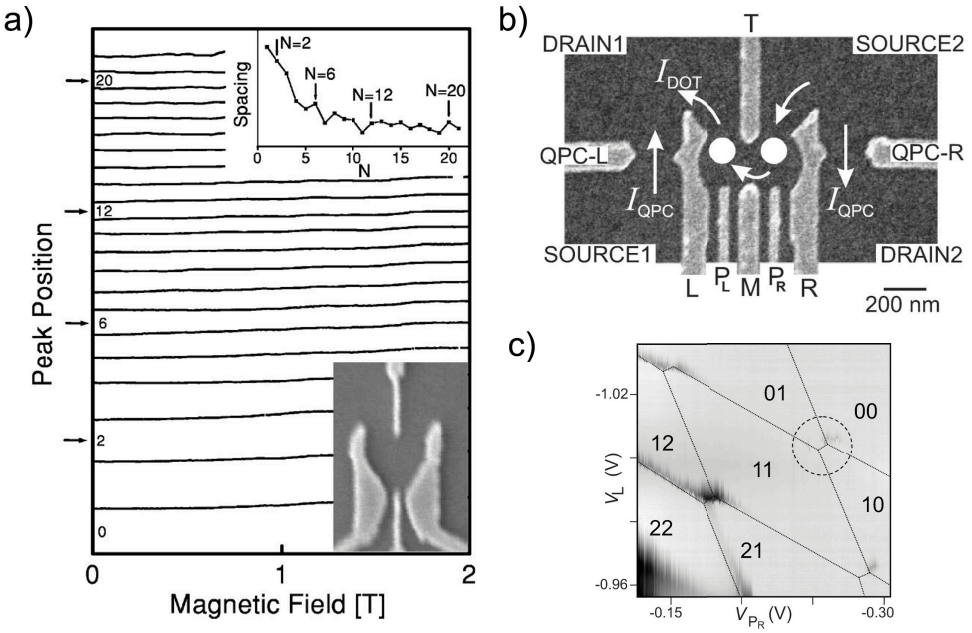

Figure 6.1: Lateral quantum dot designs. (a) Lateral dot design by Ciorga *et al.* [43], shown in the bottom right insert, used to measure the addition spectrum, shown in the top right insert, via magnetospectroscopic measurements up to 2T. (b) Scanning electron micrograph of the first lateral, coupled double-dot design by Elzerman *et al.* [71] with integrated QPC charge detectors. White circles indicate the two quantum dots and white arrows indicate possible current paths. (c) Greyscale log plot of dot current, showing the honeycomb charge stability diagram of V_L vs V_{PR} from the double-dot in (b) over the last few electrons, as both dots are tuned until both are emptied.

GaAs 2DEG, where the authors used a combination of Coulomb blockade spectroscopy measurements to construct the addition spectrum of the first 20 electrons. The device shown in Fig. 6.1, uses two types of gates designed to have different functionalities. The set of gates used to define the dot is large and thick, enclosing the electrons. The second type of gate is thin and the corresponding voltage applied has a very small effect on the dot potential, which makes it ideal for setting the tunnel barrier. This gate combination allowed for the dot potential and hence number of electrons on the dot to be tuned over a wide range, whilst keeping tunnel rates high enough for electron transport directly through the dot to be detected.

The small-dot design was later adapted by Elzerman *et al.* [71], who created a few-electron lateral double dot in GaAs with integrated charge sensing and demonstrated control over the electron number in both dots whilst maintaining tunable tunnel cou-

pling to the reservoir. By sweeping the two barrier gates and observing conductance through the double dot, the authors were able to obtain a charge stability "honeycomb" diagram over the first few electrons in the dot, showing the point at which both dots are emptied of electrons. This was followed shortly after by a number of studies including; demonstration of excited-state spectroscopy in a nearly closed quantum dot [71] and the electrical single-shot read-out of an individual electron spin [72] with a long single-spin energy relaxation time (up to $T_1 = 0.85$ ms at a magnetic field of 8T) due to its isolated state.

This small double-dot design by Elzerman *et al.* has since become the standard for lateral coupled double-dots in the GaAs material system and has been used with minor adjustments in a number experiments such as: coherent quantum control of a logical qubit based on two-electron spin states with an average spin dephasing time of $T_2^* = 10$ns [127, 206–208], singlet-triplet spin blockade in few-electron lateral double quantum dot [128, 211]. More recently the design has been extended to demonstrate coherent control of three-spin states in a triple quantum dot [85]. Similar device designs for double- and triple- dots [234] in GaAs have been used to study the QPC back action upon the quantum dot [92, 102].

The double-dot design has also been successfully used to fabricate and study electron quantum dots in the Si/SiGe material system, examples including the demonstration of tunable spin loading through an orbital excited state and a $T_1 = 136$ms. [242], and a double dot in an isotopically enriched ^{28}Si quantum well [281].

More examples on studies performed in electrostatically induced, lateral gated few-electron quantum dots, can be found in reviews [100, 101, 134, 150].

6.2.2 Major types of hole quantum dots

The first single hole quantum dot transistor was made by Leobandung *et al.* in 1995 [157], etched into Silicon and contained a single gate, plus source and drain leads. Since then, hole quantum dots have been fabricated and characterized in a variety of different structures and materials, each with their own set of advantages and disadvantages. Similar to the electron dots mentioned in the previous chapter, lateral

hole quantum dots have also been electrostatically defined within a 2D hole gas in GaAs [93, 137, 146, 147, 266] and multiple well GaAs heterostructures [264]. Similar hole dot structures have also been created in Silicon [62, 160, 249].

Transport measurements in GaAs quantum dots

Despite the recent resurgence of interest in hole quantum dots, surprisingly little work has been done in GaAs electrostatically defined hole dots compared to other systems. In this subsection we explore existing literature related to the theory, fabrication and characterization of GaAs lateral hole quantum dots.

Initial theoretical studies in GaAs hole quantum dots predicted that spin relaxation and decoherence due to the heavy-hole phonon interaction could be comparable to or longer than that of equivalent electron dots [33]. For HHs, it was shown that the form of the nuclear-spin interaction is predominantly Ising-like in quasi-2D hole systems [77] and that it is possible to operate in a regime where the hyperfine decoherence can be effectively "switched off" [78], so that the dynamics of hole dots are dominated by other interactions such as spin-orbit (SO) and nuclear dipole. Later it was shown that in such a regime, the BIA spin-orbit interaction becomes more dominant than the LH-HH mixing in lateral gated quantum dots [45]. The Rashba SO interaction also has a profound effect particularly on hole quantum dots [176]. It appears that the relative dominance of each of the SO mechanisms is strongly influenced by the shape of the confining potential and varies dramatically with the type of quantum dot under study, and much still remains unknown.

The first single-hole transistor in GaAs was created by Grbić *et al.* [93], with the quantum dot pattern defined using local anodic oxidation (LAO). This oxidization process locally etches the GaAs wafer slightly, depleting the 2D hole gas directly below the oxidized regions. The LAO technique was used instead of directly depositing metal onto the wafer surface, as Grbić *et al.* found current leakage from the surface Schottky gates to the 2DHG led to instabilities in the dot. From the Coulomb blockade peaks, Grbić estimated the hole dot to have a charging energy of $E_C \approx 1.5$ meV and its size to be similar to its lithographic dimensions.

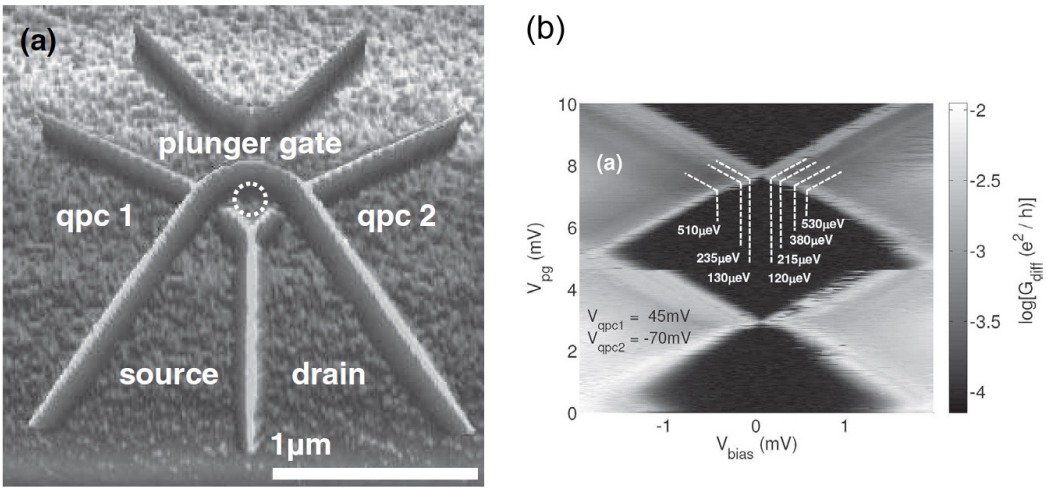

Figure 6.2: GaAs quantum dot formed by Komijani *et al.*, which was later extended to include QPC charge sensing (CS circuit not shown) [147]. (a) AFM image of the quantum dot topology. The oxide lines break up the 2DHG into different regions, and a dashed circle indicates the location of the quantum dot with respect the a source and drain regions. Coupling between the dot and its leads is tuned via in-plane gates QPC1 and QPC2 and the quantum dot occupancy tuned with the plunger gate. (b) Observed excited states through the quantum dot.

The LAO technique was next used by Komijani *et al.* to study a hole dot with smaller dimensions on a C-doped (100) GaAs wafer, possessing sufficiently large energy spacings for excited states to be observed [147], see Fig. 6.2. Whilst determining the number of holes in the small quantum dot, Komijani *et al.* found that the dot size calculated directly from the single-particle level spacing ($\Delta E \approx 20\mu$eV) was noticeably different from that estimated using the charging energy via the constant interaction model. They thus concluded that the simple constant interaction model breaks down in the small-N regime, and other effects such as hole-hole interactions may be more dominant [147]. Hence another method such as charge sensing is required to determine the exact number of holes for dots with small occupation numbers. Further studies were performed which combined the $p-$type GaAs quantum dot with an additional charge sensing circuit to observe dot counting statistics as well as perform time-averaged and time-resolved charge detection [146].

More recent work in GaAs hole dots have included the development of a large induced hole dot using a SISFET architecture [137] and more recently, an induced

SISFET double dot [266]. As well as studies into the Kondo effect [139, 140].

Hole quantum dots in other material systems

Another more recently developed popular type of quantum dot are self-assembled quantum dots (SAQDs) in InAs [27, 221], InGaAs [30, 64] and SiGe [12] as well as hybrid superconductor-semiconductor SiGe devices [136]. Although small, pyramidal shaped quantum dots with heavy-hole ground states could be formed in these experiments, studies in SAQDs so far have been patterned with source and drain contacts plus a single gate. Attaching an external charge detector to an SAQD to independently verify when the last hole has been reached, is non-trivial due to their self-assembled nature, with results reported in existing literature solely relying upon the small size of the SAQD to ensure operation the few-hole regime.

Another major class of hole dots are made from $p-$type nanowire structures in Ge/Si [119, 120, 171, 223], NiSi-Si-NiSi [310] and InSb [213]. These nanowire structures also exhibit sharp Coulomb blockade peaks and multiple, distinct excited states. Unlike SAQDs they are gateable and hence easy to tune electrically. The shape of such dots are generally elongated and cylindrical, leading to the dominance of light-hole like states as opposed to heavy-hole states, depending upon the height-to-diameter ratio of the dot under study [308]. From a fabrication point of view, the main disadvantage of nanowires is the difficulty in controlling the precise location of the dot on the semiconductor surface. To perform charge sensing on nanowire style dots, 2 nanowires located within reasonable proximity of each other are used, where a coupling gate is patterned from the nanowire containing the dot circuit to the second wire, where a separate quantum dot style of electrometer is created, demonstrated by Hu *et al.* [119, 120]. An alternative method developed by Choi *et al.* [42] involves using a vertically coupled charged detector, realized by etching a QPC into a GaAs/AlGaAs 2DEG directly below an InAs nanowire which houses the gate-defined quantum dot (although this was performed in an electron system it could be also implemented in a hole system).

More recently hole dots have been created using single acceptor dopant atoms

embedded in a bulk semiconductor such as silicon FinFET devices [270]. These possess a symmetric dot shape more akin to that of a natural atom and hence a unique bulk fourfold hole spin degeneracy [24, 25]. As this result is fairly recent, to date no external charge sensing has been reported in such systems.

6.2.3 Charge sensing with quantum point contacts

The push towards the few-electron regime to study single spin states in quantum dots has resulted in some unexpected challenges. One of these is that the current through the dot can become unmeasurably small before the few-electron regime is reached [101]. To overcome this, external charge sensors can be integrated into the quantum dot setup, to provide a non-invasive method to monitor the occupancy of the quantum dot, making it possible to verify when the last electron has been isolated [122, 226]. Although the concept of charge sensing was first demonstrated by Ashoori *et al.* in 1992 [15] and Field *et al.* in 1993 [76], the potential of the charge detector as a spectroscopic tool has only been recently fully developed [71, 126].

To date several implementations of electrometers coupled to a quantum dot have been explored. These include; a single-electron transistor fabricated on top of the heterostructure [15, 170], a second electrostatically defined quantum dot [80, 114] and a quantum point contact (QPC) [76, 248]. Out of all the implementations, the QPC is most commonly used because of its ease of fabrication and experimental operation. In the following section we shall detail the operation of a QPC as a charge detector, which we implement later in our device design.

The technique of using a quantum point contact (QPC) as a charge sensor to monitor the charging of a quantum dot by individual electrons was first introduced by Field *et al.* in 1993 [76]. Fig. 6.3a shows the device developed by Field *et al.*. It consists of 2 separate circuits (one for the charge sensor, the other for the quantum dot) in sufficiently close proximity to allow for direct coupling. The QPC charge detector can be tuned to its most sensitive operating point by changing the bias voltage applied to the QPC gate, until the QPC conductance lies between the first conductance plateau $G = \frac{2e^2}{h}$ and complete pinch-off, shown in Fig. 6.3b. As the plunger gate is swept the

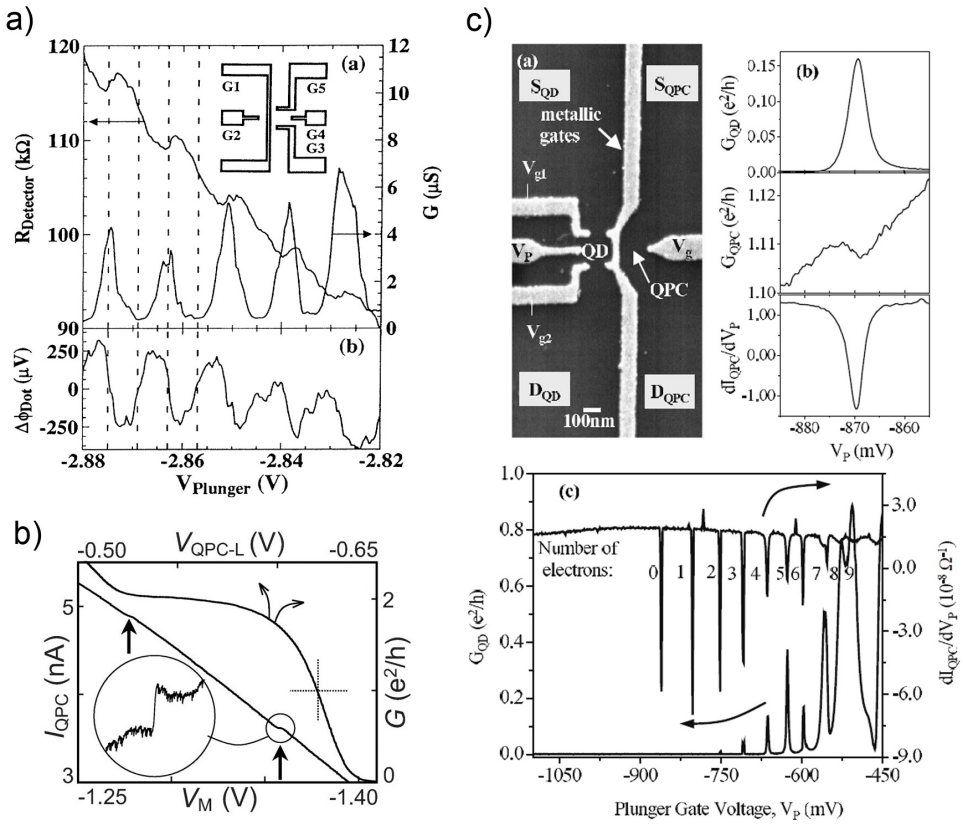

Figure 6.3: (a) First charge sensing circuit and initial measurements by Field *et al.* showing direct correspondence between the charge sensing sawtooth signal and Coulomb blockade peaks [76]. (b) Data from Elzerman *et al.* where the cross marks the most sensitive operating point of the QPC charge sensor at e^2/h [70]. (c) Circuit design and data from Sprinzak *et al.* shows that charge sensing can be used to sense the last electron, even when the current through the dot is too weak to be detected [248].

occupancy of the dot is changed, inducing a corresponding change in potential in the QPC detector. As electrons tunnel in and out of the dot, we see a series of Coulomb peaks in the dot conductance and a corresponding sawtooth feature in the conductance of the QPC on top of a falling background. As charge enters (leaves) the quantum dot island, conductance through the dot increases (decreases), whilst corresponding conductance through the charge detector decreases (increases). This is more clearly seen in the rightmost panel of Fig. 6.3c, which zooms into a single Coulomb blockade peak and corresponding charge sensor sawtooth feature.

The main advantage of the charge sensor is that it allows one to determine the absolute number of electrons in a dot, even when current passed directly through the

dot is too small to be measured [248].This can be seen in the bottom-most panel of Fig. 6.3c, where the derivative of the charge sensor current shows dips which persists beyond the last Coulomb blockade peak, down to the last electron. Further work was also conducted to optimize the response of the QPC to single electron charging events in small quantum dots [302, 303]. Such integrated QPC charge detectors are now routinely used in double quantum dot devices as they provide a simple method to establish the regime where each of the two dots are occupied with a single electron [70, 206].

The advent of QPC charge sensing has made it possible to study a variety of different types of quantum mechanical behaviour in a quantum dot, which cannot otherwise be accessed e.g. excited states in a nearly closed dot [71, 126]. In particular the charge sensor is able to measure extremely slow electron dynamics, when current directly through the quantum dot itself (charge per unit time) becomes too small to be detected for systems with slow moving electrons. Replacing the measurement of current with a time-resolved measurement of charge has enabled studies into the counting statistics of single electron transport [95], the electrical control of spin relaxation [5], the spin dynamics of random telegraph signals [116] and many others [122].

6.2.4 The electronic structure of quantum dots

In this section we briefly introduce shell filling and the constant interaction model which has been used to successfully explain the behaviour of electron quantum dots in different systems. We compare this to existing experiments conducted in different types of hole dots with different geometries and describe how their behaviour differs from the electron case and from each other.

Electron shell filling and the constant interaction model

Like all quantum low dimensional systems, the symmetry of a quantum dot is also responsible for degeneracies in the energy spectrum. The 3D spherically symmetric confining potential of natural atoms, gives rise to degeneracies known as shells (1s, 2s, 2p, 3s, 3p...), which are most stable when completely filled with electrons. These

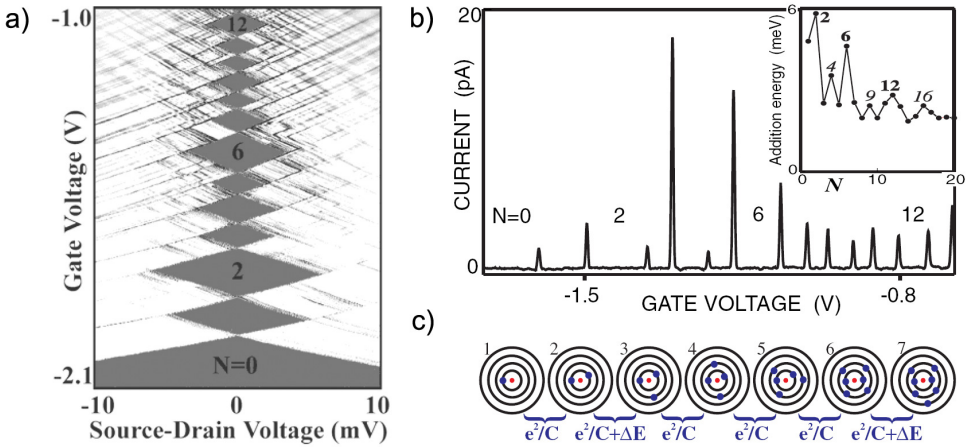

Figure 6.4: Illustrations introducing shell filling. (a) Greyscale plot of quantum dot current versus gate and source-drain bias voltage, showing a distinct enlargement of the Coulomb diamonds (and therefore addition energies) at the magic numbers $N = 2, 6, 12$. Figure adapted from Ref. [134]. (b) Single trace of quantum dot current versus gate voltage, exhibiting enlarged spacing between Coulomb blockade peaks at the magic numbers. Insert depicting a plot of addition energy versus quantum dot occupancy, with enlarged energy spacings at the magic numbers. (c) Illustration of the shell filling sequence for a quantum dot in terms of atomic orbitals, where the N=2 electron must overcome the charging energy $E_C = e^2/C$ of the first electron to fill the same shell. The N=3 electron, on top of the charging energy requires an additional single-particle energy ΔE to jump to the next orbital. Panels (b,c) are reproduced from Ref. [150].

occur at the atomic magic numbers of 2, 10, 18, 36... [150]. In the case of an artificially induced quantum dot in a 2D gas, the quantum dot shape is more akin to a 2D disc - assuming a circularly symmetric confining potential which can be described by a harmonic oscillator with a r^2-dependence rather than $\frac{1}{r}$ in the case of natural atoms. This lower degree of symmetry leads to a 2D shell structure with a lower magic number sequence of 2, 6, 12, 20... [150] as explained in Fig. 6.4.

One way to understand these magic numbers is to treat them as single-particle states in a 2D harmonic oscillator, ignoring Coulomb interaction between electrons on the dot. Extending the 1D harmonic oscillator spectrum (described by $E_n = (n+\frac{1}{2}\hbar\omega)$) to 2D yields $E_{n,l} = (2n+|l|+1)\hbar\omega_o$, where $n = (0, 1, 2...)$ is the radial quantum number, $l = (0, \pm1, \pm2, ...)$ is the angular momentum quantum number and ω_o is the oscillator frequency.

The eigenenergies $E_{(n,l)}$ as a function of magnetic field can be solved for a 2D

parabolic confining potential $V(r) = \frac{1}{2}m^*\omega_o^2 r^2$, giving rise to the Fock-Darwin spectrum [150]:

$$E_{n,l} = (2n + |l| + 1)\hbar(\omega_o^2 + \frac{1}{4}\omega_c^2)^{1/2} - \frac{1}{2}l\hbar\omega_o \tag{6.1}$$

The electrostatic confinement energy is described by $\hbar\omega_o$ and the cyclotron energy by $\hbar\omega_c = \hbar eB/m^*$. Each orbital state $E_{(n,l)}$ is two-fold spin-degenerate, which is lifted at non-zero B and a single-particle state with a positive (negative) l will shift to lower (higher) energy. The lowest energy state $(n, l) = (0, 0)$ is two-fold spin degenerate (neglecting Zeeman splitting in B). The second state has double-orbital degeneracy $E_{(0,1)} = E_{(0,-1)}$, which forms the second shell and is full with a total of N=4 electrons. The third shell possesses triple-orbital degeneracy $(1, 0)$, $(0, 2)$ and $(0, -2)$ and can hold another 6 electrons, leading to a magic number of N=12. When the field is increased, the electron occupying the highest energy state is forced into a different orbital state and transitions occur in the spectrum where energy levels cross, with an increase in the number of crossings at larger N. After the last crossing, electrons occupy states forming the lowest orbital Landau level characterized by $(0, l)$ such that $l \gg 0$ and including spin degeneracy is denoted with filling factor ν=2, analogous to the quantum Hall effect in a 2DEG [150]. However, unlike a 2D system the presence of the electrostatic confining potential defining the dot lifts this degeneracy. The Fock-Darwin spectrum provides a comprehensive method to study the evolution of the ground states of an electron dot in field, especially towards the few-N regime.

For the Constant Interaction model, a Coulomb charging energy is added to the non-interacting Fock-Darwin states as a first order approximation to model electron-electron interactions [150]. This modifies the addition spectrum such that the topmost filled state is added to the charging contributions, resulting in the spin-degenerate states appearing twice, separated by the charging energy. The magic numbers are visible as an anomalous enhancement in the energy separation at B=0. An even-odd parity effect is observed where energy spacings for N_{even} are larger than those for N_{odd}. These wiggles approximately in phase with B (which stop at ν=2), suggesting that the Nth and (N+1)th electrons occupy the same single-particle state but possess opposite spin.

6.2.5 Hole shell filling and magnetic field dependence studies

We now turn our attention to studies of the shell structure in different types of hole quantum dots to-date and provide a brief overview of the literature. Valence band holes are much more complex and possess stronger spin-orbit coupling than electrons [33, 78], arising from bulk inversion asymmetry (Dresselhaus spin-orbit) [63], structural inversion asymmetry (Rashba spin-orbit) [35] plus additional spin-orbit coupling between light-hole (LH) and heavy-hole (HH) subbands [67]. Recently it has been shown that both the quantum dot geometry and spin splitting energy [45] play a critical role in determining the interplay between these spin-orbit mechanisms and much still remains unknown about the spin behaviour of hole quantum dots.

One such phenomena is the incomplete shell filling observed in InAs self-assembled quantum dots (SAQD) resulting in a highly polarized few hole ground state. This was first observed by Reuter *et al.* [221, 222], through capacitance-voltage (C-V) spectroscopy measurements, who discovered that once the *s*-like ground state is completely filled with two holes, the *d*-shell starts filling before the *p*-shell is full. The authors attribute this behaviour to the increased Coulomb interaction and smaller quantization energies of holes due to their larger effective mass. A different explaination for the anomalous filling was proposed by He *et al.* [109, 110] who address the limits of a 2D-EMA parabolic model of the confining potential, by combining an atomistic pseudopotential description of the electronic structure with a many-body configuration interaction description. Their model involves sequential shell filling (like the 2D-EMA parabolic model), but rather than filling all shells sequentially, once the first *p*-shell is filled, the second *p*-shell is skipped completely and the first *d*-shell starts to fill instead. A third alternative provided by Climente *et al.* [44], suggests that the interaction between heavy hole and light hole subbands is the key factor in explaining the anomalous behaviour, rather than the Coulomb interaction and the shell fillings are actually sequential, as opposed to Reuter's proposal.

A later experiment employing both C-V and polarized photoluminescence spectroscopy in InAs SAQDs, also confirmed that holes in InAs SAQDs cannot be described purely by the Fock-Darwin model and spin-orbit coupling effects in the valence band

need to be considered to fully describe the system [27]. More recent optical studies in InAs SAQD holes have mapped out an anisotropic g factor and noted its strong variance with orbital level [21, 235, 256, 257]. Optical experiments have been extended to other types of self-assembled quantum dots such as InGaAs [30, 64] and GaSb/GaAs [86, 106, 197].

Transport experiments in SAQDs such as SiGe [12] and hybrid superconductor-semiconductor SiGe devices [136] have also reported larger, anisotropic g factors of $2 \sim 3$. Furthermore, due to their pyramidal dot shape, these g factors are highly sensitive to a vertical electric field [12].

On the other hand, experiments in $p-$type nanowire dots have demonstrated sequential spin filling, in stark contrast to that reported for self-assembled quantum dots in both Ge/Si core shell structures [119, 223] and single-crystal p-type silicon [306, 310]. Magneto-transport measurements in these nanowires yield g^* between $1-2$ in both material systems, characteristic of a spin-1/2 particle where the dominance of LH as opposed to HH states in nanowires is dependent upon the quantum dot height to diameter ratio [308]. Electric-dipole spin resonance (EDSR) experiments in hybrid ambipolar InSb nanowires [213] have observed a g^* anisotropy varying between $1.5-4.5$ depending upon the in-plane magnetic field angle to the nanowire axis. Similarly to the other types of nanowire dots, the g^* of InSb nanowires is also suppressed compared to the bulk hole g-factor, which the authors attribute to hole subband mixing. Pribiag *et al.* also demonstrate a significant difference in hole double-dot spin-blockade anisotropy compared to electron double-dots [213].

Recent magneto-transport measurements of a single acceptor atom in a silicon FinFET [270], have observed the lifting of the bulk hole fourfold spin degeneracy [24, 25] with an applied magnetic field, into its four spin states [270]. Their degenerate HH and LH subbands stem from their more symmetric dot shape which is closer to that of a natural atom than the other types of hole dots mentioned [149, 185, 259].

6.2.6 Quantum dot challenges: random telegraph signals, charge noise and reproducibility

As the size of nanostructure devices continue to decrease, they become more susceptible to local charge fluctuations. Such noise in the signal can exhibit ubiquitous $1/f$ [65, 115, 276] or random telegraphic behaviour, where $1/f$ noise can stem from the summation of many random telegraphic signals (RTS), and each RTS is formed when the measured current switches between 2 distinct states [129]. In particular the precision of the state readout of QPC charge sensors, used to detect changes in the state of individual charges on quantum dots, can be affected by fluctuations in conductance caused by the motion of background charges [113]. This background charge noise may lead to fluctuations in the energy levels of the quantum dots themselves, resulting in decoherence in both charge [107, 124, 205] and spin states [51, 159].

Several mechanisms have been suggested as the origin of this low-frequency noise in GaAs-based devices:

1. *Electron hopping between the two-dimensional electron gas (2DEG) and charge trap sites*: Charge traps with energy levels within a few k_BT of the Fermi energy can capture (trap) or emit (detrap) single electrons, causing fluctuations in the Coulomb potential of the 2DEG, and contributing to RTS noise when the current switches between two states, demonstrated in both GaAs QPCs [59, 229] and electron dots [228]. Such trap centers may come from; crystal dislocations or damage incurred during the fabrication process [229] and deep traps from metastable DX centers [32].

2. *Current leakage through the Schottky barrier*: Other sources of charge traps contributing to noise include, tiny current leakages through the Schottky barrier, where electrons tunnel from the gate into the 2DEG. In the process, some electrons become trapped in long-lived localized states near the active region of the device and cause RTS before they reach the 2DEG [212]. Such switching behaviour due to leakage exhibits a strong, direct dependence upon gate voltage unlike switching behaviour stemming purely from impurities [46, 161]. It is also

possible to determine the spatial distribution of such traps if their switching behaviour is gate voltage dependent [47, 162].

3. *Charge hopping between ionized impurities in the remote-doping layer*: This is detected by the charge sensor and/or quantum dot via the Coulomb interaction. Their effects have been observed as discrete time dependent changes in the conductance of a 1D wire [263]. Kurdak *et al.* [153] have observed their presence as fluctuations in both QPC measurements and 2D Hall voltage measurements in field. By comparing the conditions needed to observe fluctuations in both QPCs and the 2D Hall voltage, the authors conclude that the only possible source of their measured noise comes from remote impurities. A major contributor to such impurities are dopants in the AlGaAs layer of a modulation-doped or δ-doped structure [31, 212]. Ontop of contributing to RTS noise, the proximity of these ionized dopant impurities to the 2DEG significantly lowers mobility at low carrier densities [232] as charge carriers scatter due to their Coulomb interaction with these impurities, as discussed in Fabrication Chapter 3.2.2.

Common to all 3 noise sources mentioned above, the low-frequency charge noise increases as the voltage applied V_g to the surface Schottky gate is decreased (more negative). Since the Schottky barrier becomes less opaque with decreasing V_g, the observed noise dependence upon V_g was interpreted as evidence that the current leakage through the Schottky barrier was responsible for charge noise [113].

This strong V_g dependence of the noise, allowed for the reduction of charge noise by employing techniques such as bias cooling (which involves applying a voltage to the Schottky gates at room temperature and holding it as the sample is cooled, which effectively freezes out charge traps) [162, 212]. Another option is to apply an additional global top gate [31] both of which shift the operation point to a less negative voltage. Other experimentalists have also employed thermal cures [81], to reduce RTS noise. These techniques have been used with varying degrees of success between devices.

A more recent study by Hitachi *et al.* [113], have proposed a totally different origin to RTS noise, where rather than being an intrinsic feature of doped devices, RTS noise comes from external sources and is related to damage incurred during the fabrication

process which induces charge trap sites. In contrast to previous reports, the authors observed no switching noise or random telegraphic noise, originating from tunneling through a Schottky barrier, for measurements obtained over a number of hours in their δ-doped structures [113] and that these RTSes were virtually gate independent and not affected by the presence of the superlattice barriers. Gate-dependent RTS appear only in devices fabricated with a high-damage process that induces charge trap sites.

Ontop of a robust, damage-free fabrication technique, one effective way to eliminate the charge noise associated with doping is to avoid doping the heterostructure altogether. Recently, single-electron transistors based upon undoped structures have been fabricated [175, 238] and will be discussed in the following section.

6.2.7 Induced vs doped architecture for quantum dots

As discussed in Chapter 3.2, although the technique of modulation doping has led to the fabrication of higher quality devices [209], however the main drawback is the inevitable introduction of disorder and charge noise, due to the presence of remote ionized dopants as discussed in the previous section, on top of reduced mobility. Furthermore, the dopant layer may partially screen surface gates (via hopping conduction) and/or facilitate gate leakage, rendering many such heterostructures ungateable by metallic gates [175] deposited directly onto the wafer surface. One way to bypass this problem is to eliminate the need for modulation doping altogether by using an "induced" or "undoped" structure, as discussed in Chapter 3.2.2. Such structures provide a starting platform from which to fabricate eletrostatically induced, lateral gated quantum dots.

Recent work in such induced devices created from a SISFET architecture by See *et al.* [239] use billiards to probe the disorder potential, and demonstrate that by removing the ionized dopants and populating the dot electrostatically, the device becomes more stable and the electronic properties of the dot become reproducible between thermal cycles. The authors measure low temperature magnetoconductance of two billiards with identical geometry, one undoped and one modulation-doped, before and after thermal cycling to room temperature. The magnetoconductance traces exhibit quantum interference fluctuations stemming from the dot geometry, plus artifacts due

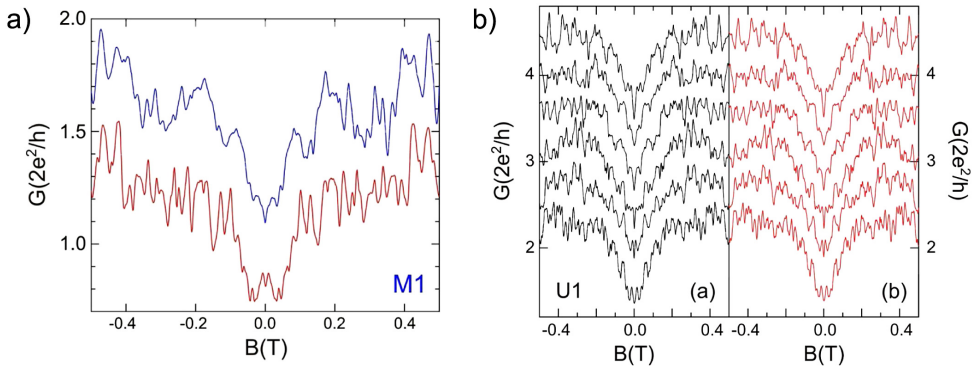

Figure 6.5: Magnetoconductance fluctuations versus perpendicular magnetic field in quantum dots of identical geometry fabricated from (a) modulation doped before (blue) and after (red) thermal cycling to room temperature; and (b) induced structures before (black) and after (red) thermal cycling. The sequence of traces was taken at increasing top gate voltage, from +930 (top) to +955 mV (bottom) in 5mV steps. Figure reproduced from Ref. [239].

to the disorder distribution with the latter changing between different cool downs. The results are reproduced in Fig. 6.5.

These plots show that the magnetoconductance is reproducible after thermal cycling for the undoped device, but not for the modulation doped device, suggesting that the disorder due to remote ionized impurities in doped devices cannot be ignored. The authors suggest that such disorder produces small-angle scattering (which is not accounted for in mobility measurements as they are heavily weighted towards large-angle scattering) which has a major effect upon transport at smaller length scales approaching those used in quantum dots and can potentially explain the lack of reproducibility under thermal cycling in modulation-doped dots.

More recently, Mak *et al.* have demonstrated that undoped, shallow GaAs/AlGaAs MISFET heterostructures can be used as a basis to fabricate stable, single-electron quantum dots 30nm from the GaAs surface [175], defined electrostaically by metal surface gates on top of the wafer, beneath the insulating layer. The authors observed an improvement of more than one order of magnitude in mobility (a $2 \times 10^{11}\text{cm}^{-2}$) with respect to doped heterostructures with similar depths, due to the absence of dopants [175].

Such shallow two-dimensional electron gases (2DEGs) have 2 main advantages

over their deeper cousins for quantum dot fabrication: Firstly, finer features can be transferred from the surface metallic gates to the 2DEG without the confining potential broadening or smearing out at the level of the 2DEG. Secondly, the energy scales of the dot levels tend to be larger, which enable more robust operation at higher temperatures. Such shallow induced structures have the advantage that the 2DEG can be brought much closer to the surface without sacrificing mobility.

The flexibility of the induced MISFET architecture combined with its potential for reduced charge noise, has seen it extended to create few-electron quantum dots in other material systems such as Silicon Metal-Oxide-Semiconductors [196, 291] and electron double-dots in Si/SiGe [29, 181] and Silicon [164].

6.2.8 Induced hole quantum dots

Due to problems with unstable gates, the first stable gated defined *p*-type GaAs/AlGaAs quantum dots [93] were only created 15 years after their *n*-type counterparts [184]. The first induced SISFET style hole dot was fabricated on a high-mobility (311)A GaAs heterostructure [137] with a Si-doped p^+-GaAs cap, that was wet-etched to create 7 gates, to independently control the entry and exit barriers and the dot density. Random telegraph signals were observed in the source-drain bias data, which were attributed to surface state traps in the etched trench [137].

A different style of lateral (planar) induced, silicon metal-oxide-semiconductor (MOS) hole dot was trialled by Li *et al.* [160]. Rather than using a doped cap to induce the dot, the dot and tunnel barriers were formed using a combination of metallic gates, similar to a MISFET style architecture, except rather than using a global top gate to induce carriers in both the leads and the dot, there are separate inducing gates for the source and drain reservoirs and the dot. This multiple gate design allows for considerable flexibility over device operation, including independent control of the carrier density in the dot and reservoirs [160]. A similar design has also been adopted by Ref. [249], who also report the observation of instabilities in the dot current which were attributed to disorder or roughness at the disorder at the Si/SiO_2 interface, or impurities and charge traps within the silicon oxide dielectric itself.

During measurement of our hole quantum dot, we have become aware of recently published work, in which a double quantum dot with charge sensing was fabricated using a similar MISFET style architecture in an undoped (100) GaAs wafer with an aluminium global top gate [266]. Unlike the source-drain bias plot in Fig. 6.2b, taken from the doped device by Komijani *et al.* [147], the source-drain bias map from Tracy *et al.* [266] shows no discontinuities or jumps, which are signatures of random telegraph signals. The authors report little to no electrical instabilities as anticipated for such an induced architecture, and demonstrated the transition between a large single-dot, into a small double-dot regime, using two QPC charge sensors to detect the occupancy of each dot [266].

Although the architecture of the devices presented in the following sections, are similar to that reported by Tracy *et al.* the focus of this thesis chapter is to characterize a single rather than a double dot and observe excited states in the charge detector signal.

6.3 Electron quantum dot characterization

In the remainder of this chapter, we shall borrow the best of both worlds and build upon the concepts from the background review, starting off by fabricating and characterizing an induced single electron quantum dot before moving onto hole dots. We begin by using a variation of the standard small-quantum dot design pattern developed by Elzerman *et al.* [70, 72] with QPC charge sensing in order to reach the few-N regime, combined with an undoped MISFET architecture similar to that used by Mak *et al.* [175].

This is followed by Nextnano++ simulations of the confining potential for our given dot geometry, and some adjustments made to optimize the dot design for an induced small dot geometry.

6.3.1 Device design and measurement setup

The induced electron dot was fabricated from wafer W0639 (100) GaAs from the Semiconductor Physics group at Cavendish Laboratory, its layout shown in green in

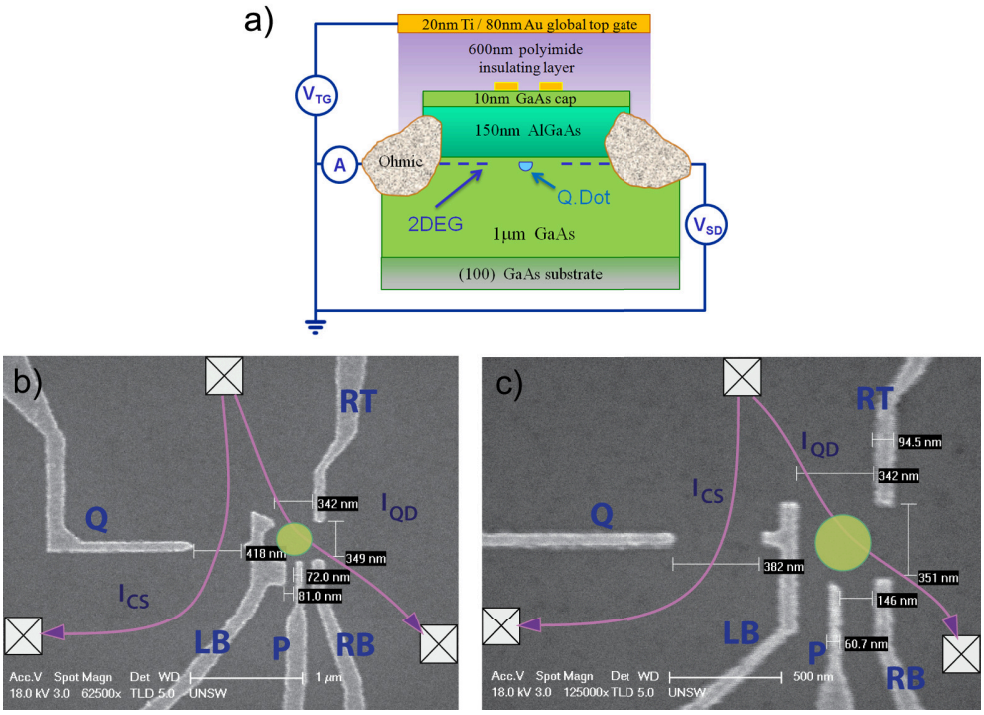

Figure 6.6: (a) W0639 wafer layout for the 160nm deep 2DEG, together with the etched ohmics and the EBL gates defining the quantum dot pattern on the wafer surface. The structure is covered by a 600nm thick Polyimide insulating dielectric followed by an overall top gate. (b) SEM image of the "asymmetric curved quantum dot" pattern scaled for a deeper 2DEG, replicated from the design by Elzerman *et al.* [70]. The quantum dot location is highlighted by a green circle. A separate QPC charge sensing circuit is created using gates Q and LB, and the 2 current paths for the quantum dot and charge sensor are shown in green, where the crossed-boxes represent the ohmic contacts. (c) SEM image of a variation to the design in (b) the "asymmetric square dot" pattern, in which the large gate LB is replaced by a small, thinner, straight gate for easier fabrication.

Fig. 6.6a. A tri-metallic stack consisting of Ni/AuGe/Ni was evaporated to create $n-$type ohmic contacts and annealed into the heterostructure. Next the quantum dot pattern was defined by electron beam lithography (EBL) and deposited with a thin layer of titanium followed by gold. This was then covered by an insulating polyimide dielectric layer followed by an overall Ti/Au global top gate (TG), which we use to induce carriers into the 2DEG.

A scanning electron microscope image of the 2 patterns trialled are shown in Fig. 6.6b,c. Panel (b) shows a direct translation of the standard design created by Elzerman *et al.* [70] for electron dot systems. This version only contains half of the

original double-dot pattern, similar to Refs. [71, 72] as we are interested in single dots for this study. The lithographic dimensions have been scaled up by $\frac{dotlength}{depth} \sim 2.2$, to a dot length of $\sim$ 350nm, to compensate for the deeper 2DEG at 160nm from the surface metallic gates (compared to a $\sim$ 200nm dot length for a 90nm depth in the original design [70]). The lithographic dimensions of the quantum dot and QPC charge sensor width are: 342 $\times$ 349nm and 418nm respectively. Fig. 6.6c is a simplified variation of (b) which uses the same geometry and layout but replaces the wide, curved gate LB with a straight thin gate. A 2DEG depth of 160nm was initially chosen due to fabrication challenges in obtaining a 100% yield of working ohmics in shallower structures, although a depth closer to the 90nm used by Elzerman *et al.* would have been preferred to allow a more direct comparison to be drawn.

These designs use 4 gates to define the quantum dot: LB and RT to define the top (entry) tunnel barrier, RT and RB define the right (exit) tunnel barrier, whilst the plunger gate P is a thin gate used to tune the occupancy of the quantum dot. An extra gate Q on the left of the dot defines the QPC charge sensor together with LB. The metal gates screen the 2DEG directly underneath them when a voltage is applied to the global top gate, forming the quantum dot and a 1D constriction.

During the course of measuring both devices with the two slight variations in design, we found that both devices (if operated at similar voltages) behaved in a very similar fashion to one another, so for the measurement results we shall concentrate on and present data for the simplified variation, design (c).

Using the constant interaction model for a large dot, we make some ball park estimates and set boundaries for the quantum dot parameters. From measurements of density versus top gate from an equivalent W0639 electron Hall bar, an operating point of $V_{TG} = +6.0V$ was selected which gave a 2D density of $n_{2D} = 1.4 \times 10^{11} cm^{-2}$. This value was chosen as it was high enough to give a reasonable density, and yet remain well below the onset of hysteresis in the 4 terminal conductance across the 2D hall bar, as discussed in Chapter 3.4. From the lithographic area of the square dot, we estimate the dot can hold no more than $\sim$ 500 electrons. A Fermi wavelength of $\lambda_F = \sqrt{\frac{2\pi}{n_{2D}}} \approx 67$nm gives a maximum of $\frac{2W_{QPC}}{\lambda_F} \approx 10$ conductance modes through

the right tunnel barrier of the quantum dot and a maximum of ≈ 11 through the charge sensor, where W_{QPC} is the width of the 1D channel. However due to the larger depth of the 2DEG below the surface, we anticipate the lateral depletion to also be increased by a similar scale factor of ~ 2.2 and hence estimate that the actual number of conductance modes through both the QPC and the dot should be halved (or less), down at the 2DEG.

To observe single electron transport through the dot (as Coulomb blockade peaks) the quantum dot charging energy must be larger than its thermal energy, $E_C \gg k_B T$. E_C can be approximated using a simple parallel plate capacitor model such that $E_C \equiv e^2/C_\Sigma$, where C_Σ is dominated by the sum of capacitances between the dot and its defining gates. Given that the top gate has the largest overlapping area A with the quantum dot, and is located a total distance of $d = d_{AlGaAs} + d_{PI} = 760nm$ directly above it, we can make a first-order approximation which assumes that the top gate is the dominant contributor to the total capacitance, hence $C_{TG} \approx C_\Sigma$. Applying the series plate capacitor model to sum the capacitances across both the Polyimide and AlGaAs layers we get;

$$\frac{1}{C_\Sigma} \approx \frac{d_{PI}}{\epsilon_{PI}\epsilon_0 A} + \frac{d_{AlGaAs}}{\epsilon_{AlGaAs}\epsilon_0 A} \quad , \tag{6.2}$$

where $\epsilon_{PI} = 3.5$ is the dielectric constant of Polyimide, $\epsilon_{AlGaAs} = 12.5$ is the dielectric constant of AlGaAs [1], $\epsilon_0 = 8.854 \times 10^{-12} F/m$ the electric permeability of free-space and A is the lithographic dot area $0.377\mu\text{m}^2$.

This gives us a $C_\Sigma \approx 18aF$, corresponding to a charging energy of $E_C \sim 8.9$meV or an equivalent temperature of $T_E = \frac{E_C}{k_B} \sim 100K$. The average single particle spacing $\Delta E \approx \frac{2\pi\hbar^2}{m^* A}$ is estimated to be 19μeV (or ~ 2.2K), where $m^* = 0.067 m_e$ is the effective mass of electrons in GaAs and spin degenracy is ignored [11]. These ball-park values act as upper limits, since at 160nm below the wafer surface, the effective quantum dot dimensions due to broadening of the confining potential are expected to be different i.e. much smaller.

The quantum dot was characterized inside a Kelvinox 100 dilution refrigerator at a base temperature of 20mK, using standard two-terminal ac lock-in techniques which simultaneously readout both quantum dot and charge sensing signals (see Appendix A.1

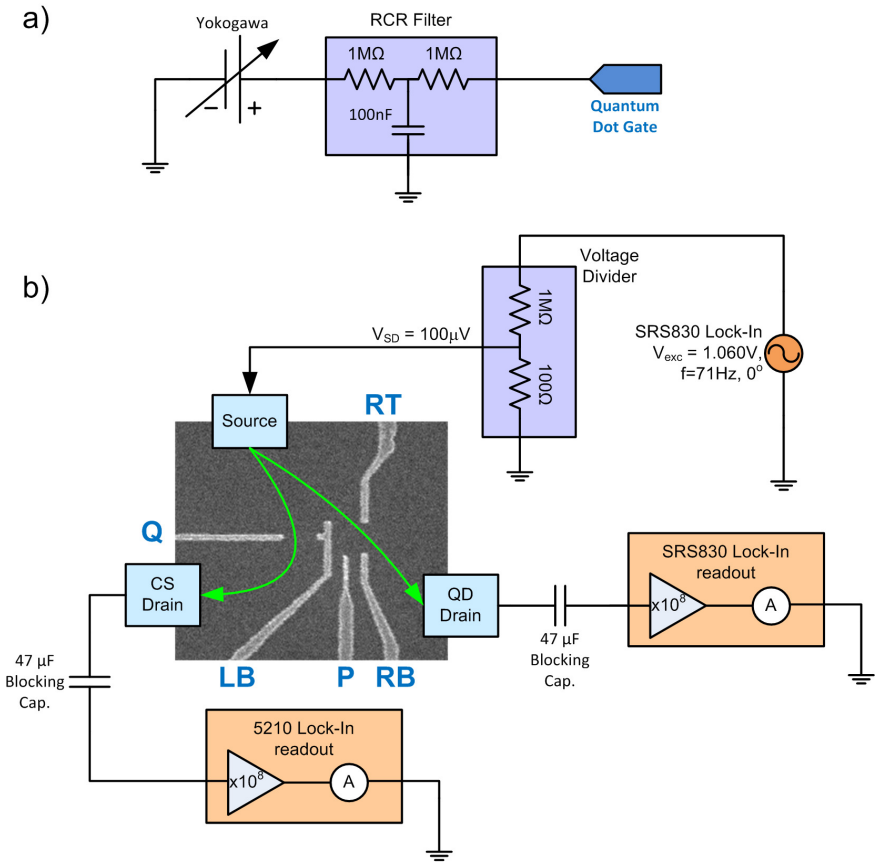

Figure 6.7: Part (a) shows a Yokogawa DC voltage source followed by a low pass RCR filter, used to apply a bias to tune each of the EBL gates (Q, RT, LB, P, RB), labelled in blue in Part (b). A SRS830 lock-in amplifier provides a $100\mu V$ ac excitation voltage to the source ohmic on the device. Here the circuit splits into two parts: One path travels through the quantum dot, out through the dot drain, into a SRS830 lock-in amplifier current readout via a $47\mu F$ blocking capacitor. The other leg goes into the charge sensor drain, to a secondary SRS830 lock-in amplifier for simultaneous readout of the charge sensor.

for further information on the K100). The measurement setup is illustrated in Fig. 6.7. In this setup we have a common source for both the dot and the charge sensing circuits and two separate drains. This configuration was selected over that with two sources and a common drain, to reduce noise in the common drain. We adopted a common ohmic for this design as it gave us enough ohmics to fit two quantum dots onto the same Hall bar, rather than one dot to one Hall bar.

6.3.2 Experimental Data and Results

To study single electron transport through the quantum dot, the tunnel barriers between the quantum dot and its source and drain reservoirs need to be sufficiently opaque (generally $G < \frac{2e^2}{h}$). To achieve this condition, we first investigate the behaviour of different pairs of gates by applying a negative bias simultaneously to them, with unused gates set to 0V, and measuring the current through the quantum dot to find their pinch-off points. The drain contact was then swapped over to the charge sensing (CS) circuit and the measurement repeated for the QPC charge sensor. The data is shown in Fig. 6.8.

From this first set of data, the top barrier pinches-off before the right barrier and both of them exhibit small features below the first conductance plateau $G \approx \frac{2e^2}{h} \approx 77\mu$S which suggests that some of the gates may be partially defined at 0V, as they screen the 2DEG from the top gate.

To investigate the pinch-off characteristics of the asymmetric dot geometry, we paired the gates and swept the pair to pinch-off, whilst all unused gates were unbiased to +1V to ensure they are not defined in the 2DEG. With both gates at the pinch-off voltage, one of the gates was unbiased whilst the other was held fixed at the pinch-off point. The same procedure was then repeated for the other barrier gate. All 3 gate pair combinations are plotted in Fig. 6.9. The right barrier (green sweeps) exhibit a similar profile between both pairs of gates, due to the symmetric geometry of the barrier. On the other hand the top barrier (red/pink), exhibits distinctly different behaviour for each gate - the top barrier closes off shortly after RT is defined (red), whilst LB appears to be strongly defined with little rise in current until the unbiasing

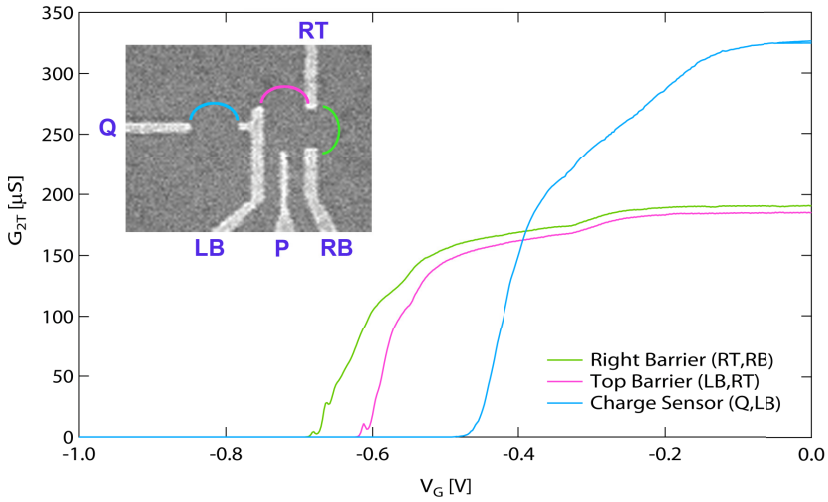

Figure 6.8: Pinch-off characteristics of the quantum dot where the raw dot current is converted to 2-terminal conductance for the; right barrier (green), top barrier (pink) and the QPC charge sensor (blue). For each pinch-off curve, the corresponding pairs of gates were simultaneously swept to a more negative bias, whilst the others remained at 0V. This was done at a top gate of $V_{TG} = +6.0$V. Note the data is plotted in 2T conductance rather than units of the conductance quantum in order to observe the full behaviour of the gates as they are unbiased to 2D.

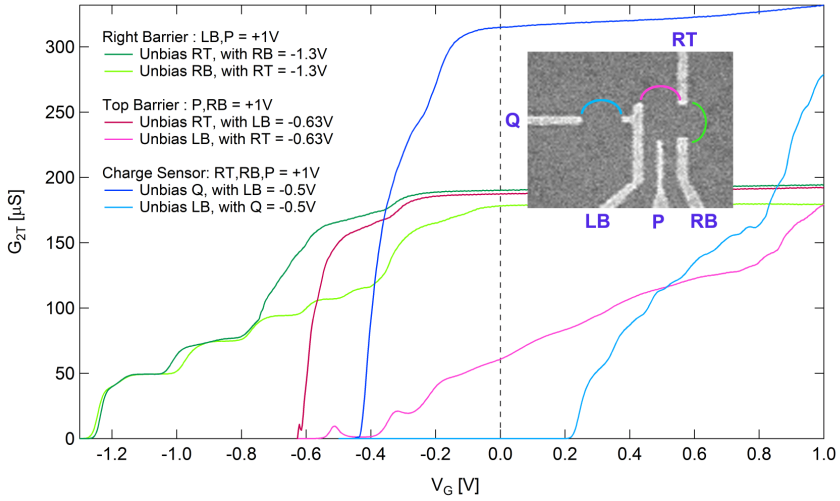

Figure 6.9: Pinch-off characteristics of the quantum dot where the quantum dot current is converted to 2-terminal conductance. For each pinch-off curve, the corresponding pairs of gates were simultaneously swept to a more negative bias, whilst the others remained at 0V. This was done at a top gate of $V_{TG} = +6.0$V. Note the data is in 2T conductance rather than units of the conductance quantum in order to observe the full behaviour of the gates as they are unbiased to 2D.

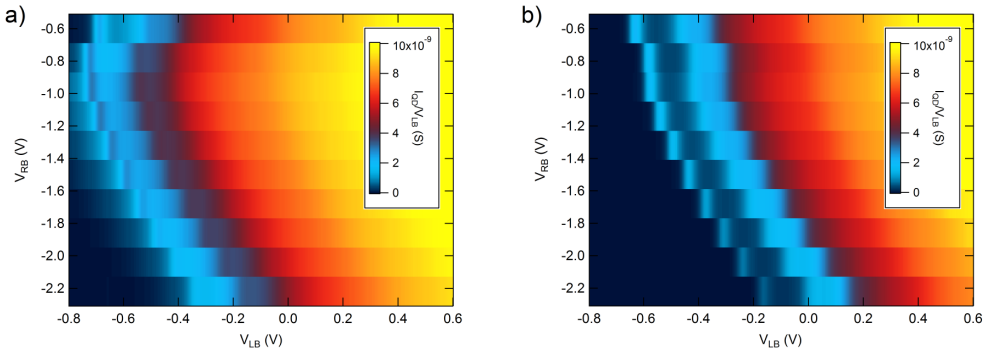

Figure 6.10: Colour maps of transconductance through the dot with varying barrier gates RB vs LB. (a) with $V_{RT} = -0.60$V (b) and $V_{RT} = -0.62$V. In both cases $V_Q = V_P = 0$V. Both graphs indicate that the moment gate RT is defined, current through the dot disappears rapidly. Both maps barely show any Coulomb blockade like behaviour before the dot barriers are closed off.

point at +1V (pink). The charge sensor (blue sweeps), which shares LB as a common gate with the top barrier, also exhibits an unexpected asymmetric pinch-off profile, which could be explained if the depletion region underneath gate LB is much broader than originally anticipated.

To understand the gate behaviour better, we conducted a series of barrier maps where we stepped RB and swept LB, shown in Fig. 6.10. As gate RT defines both entry and exit tunnel barriers, we kept this fixed at a voltage where the gate is just defined ~ -0.6V in (a) and ~ -0.62V in (b). Between the two colour maps, we observe that a small change in RT (compared LB and RB) shifts the active region of the dot significantly. Moreover, both panels do not exhibit a series of 'diagonal lines' alternating with clear regions of zero current, as expected from a typical stability diagram which would result in well defined Coulomb blockade peaks. Rather the current through the dot dramatically drops from 10nA to zero. This suggests that once gate RT is defined, current through the dot is almost immediately cut off. This behaviour remained despite varying combinations of gate voltages. Both colour map also exhibit a distinctively curved region of conductance, which suggests strong crosstalk between gates LB and RB, as the gates influence each other by coupling through the quantum dot.

To operate the dot in the single electron tunnelling regime, voltages were set on each

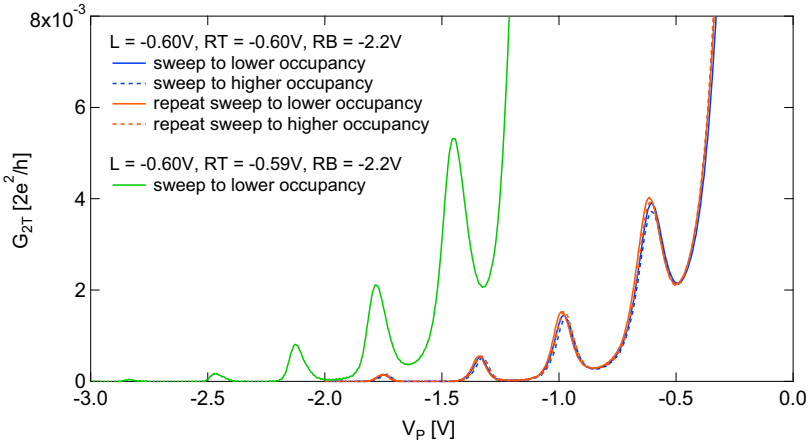

Figure 6.11: Coulomb blockade oscillations as a function of plunger gate voltage (blue), where $V_{LB} = -0.6$V, $V_{RT} = -0.6$V and $V_{RB} = -2.2$V. Subsequent repeat sweeps (orange), taken 10 minutes after the blue sweeps sit on top of the initial sweeps, indicating little hysteresis in the device as expected from an induced architecture. Unbiasing RT slightly to -0.59V (green) dramatically shifts the peak profile, suggesting that gate RT is highly coupled to the dot compared to P. The charge sensor gate Q remains unused at 0V.

gate corresponding to the points where the barriers were close to pinch-off but opaque enough to let some current through the dot. Initial values of $V_{RT} = -0.6$V, $V_{RB} = -2.2$V (so the voltage sum across the right barrier is -2.8V) and $V_{LB} = -0.60$V, were chosen and the plunger gate P, was swept towards pinch-off to decrease the occupancy of the quantum dot. The result is shown in Fig. 6.11 where a series of Coulomb blockade (CB) oscillations were observed on top of a falling conductance background. Beyond $V_P = -1.1$V the minima between CB peaks fall to zero conductance, indicative of single-electron tunneling. Subsequent repeat up-and-down sweeps showed little hysteresis in the behaviour of the dot and the CB traces taken 10minutes apart sit on top of each other, suggesting the device is reasonably stable as expected from an induced architecture. Beyond $V_P = -2.0V$ the current dies off rapidly due to strong crosstalk between the plunger and the barrier gates. As gate RT defines both dot barriers, we backed this off to $V_{RT} = -0.59$V, which resulted in sharper CB oscillations beginning at a larger plunger gate voltage (green), in Fig. 6.11.

To study the relative coupling of each gate to the quantum dot, we sweep each gate (including the top gate) over the same set of Coulomb blockade oscillations obtained

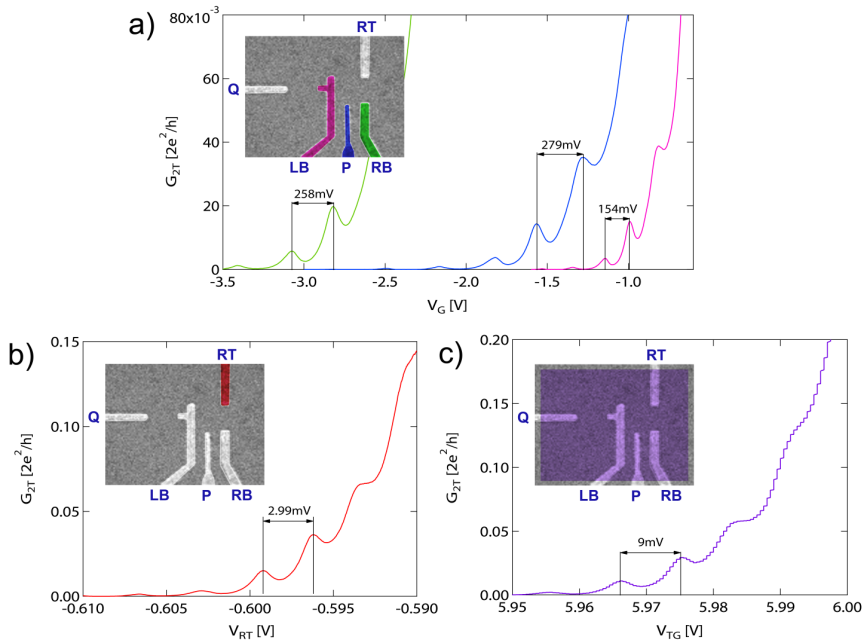

Figure 6.12: Plots of the same set of Coulomb blockade peaks swept using different quantum dot gates; gates LB, P and RB are displayed in (a) the short period gate RT in (b) and the overall top gate in (c) [the discrete steps are due to the lower resolution limit of the instrument voltage source for a larger total voltage range]. Bias voltages on all gates which are not being swept are $V_{TG} = +6\text{V}$, $V_{LB} = -0.6\text{V}$, $V_P = -1\text{V}$, $V_{RB} = -2.2\text{V}$ and $V_{RT} = -0.59\text{V}$.

Gate	ΔV_g	$C_g = e/\Delta V_g$	$\alpha = C_g/C_\Sigma$
RB	258mV	0.621aF	0.00843
P	279mV	0.574aF	0.00780
L	154mV	1.04aF	0.00141
RT	2.99mV	53.6aF	0.728
TG	9.00mV	17.8aF	0.242

Table 6.1: The period for each gate ΔV_g was obtained from the Coulomb blockade oscillations in Fig. 6.12. Corresponding gate capacitances C_g were calculated using the approximation $\Delta V_g = e/C_g$, and sum to $C_{\Sigma gates} = 73.6$aF. From this we estimate the charging energy to be $E_C \equiv e^2/C_{\Sigma gates} = 2.18$meV. The lever arms $\alpha = C_g/C_\Sigma$ for each gate are also given [1].

from the plunger gate. The data is displayed in Fig. 6.12, where the period of the oscillations is related to the gate capacitance via $\Delta V_g = e/C_g$ (assuming ΔE is negligible) shown in Table 6.1. From this table gate RT is the most capacitively coupled to the quantum dot, even more so than the top gate whilst the plunger gate has the weakest coupling. These numbers indicate that the quantum dot is not only small, but located much closer to gate RT than previously anticipated. Since $C_{TG} < C_{RT}$, our initial large dot estimate based upon the constant interaction model is not a good approximation, even though the value of C_{TG} is close to our first estimate. From the values in Table 6.1 we obtain a total capacitance of $C_{\Sigma gates} = 73.6$aF and a charging energy of $E_C \approx 2.18$meV (or ~ 25.3K), which is much smaller than the lower bound $E_C = 8.9$meV ($C_\Sigma \approx 18$aF) estimated in our model. [1] Comparing to literature, our charging energy is smaller than the $E_C = 3.7$meV obtained by Elzerman *et al.* [70], for adding a second electron to the dot. This suggests that although our dot is small, larger gate biases are required to squeeze the confining potential further in order to reach the last electron. However, beyond this point the tunnel barriers are quite high and current directly through the dot can no longer be detected, hence an independent method to determine the number of electrons remaining within the dot, such as a charge detector is essential.

To find out more about the dot, bias spectroscopy was performed on the Coulomb

[1] Note that this value of charging energy estimated by summing the gates, neglects the effect of capacitance contributions from the source and drain leads, which would increase C_Σ and thus decrease the value of E_C. It also means that decreasing the leverarm values calculated in Table 6.1 by a factor of 3 will give a more realistic set of values.

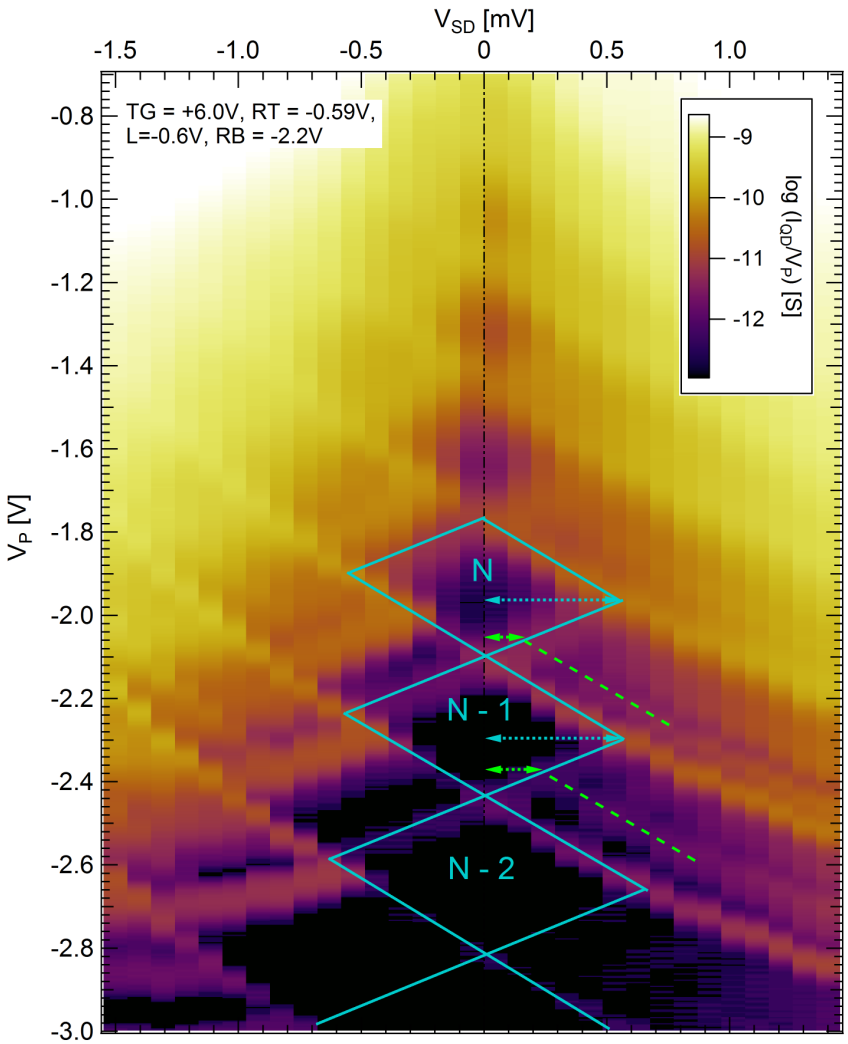

Figure 6.13: Source-drain bias spectroscopy of the Coulomb blockade peaks from Fig. 6.11. The colour scale is a log plot of differential conductance, versus plunger gate voltage V_P along the y-axis and dc source-drain bias voltage V_{SD} on the x-axis. For this measurement $V_{RT} = -0.59\text{V}$, $V_{RB} = -2.2\text{V}$, $V_{LB} = -0.6\text{V}$ at $V_{TG} = +6.0\text{V}$. The dashed green lines outside each coulomb diamond mark the location of the excited states.

blockade peaks in the quantum regime. Fig. 6.13 is a log-scale colour map of the differential conductance plotted against V_P and the DC source-drain bias V_{SD}. The colour map shows no indication of random telegraphic signals nor switching noise, demonstrating the stability of the MISFET architecture.

A series of Coulomb diamonds is highlighted by solid blue-green lines and their relative occupancy N labelled, starting from the first diamond where electron transport is fully blockaded (indicated by a dark, black region). The diamonds rapidly grow in size, indicating the dot is in the few-electron regime. Finer featured bright coloured lines, outside of the diamond running parallel to the diamond edge indicate transport through excited states [101]. From the source drain bias colour map we extract a single particle level spacing between the excited state and its parallel ground state using V_{SD}, of $\Delta E = 200\mu eV$ for diamond N and $\Delta E = 300\mu eV$ for the $N-1$ diamond ($T_{\Delta E} \sim 2.3 - 3.5K$). These values are once again much smaller than the 1.8 meV difference between the first excited state and the ground state measured by Elzerman *et al.* [70]. Recalculating the quantum dot size based upon $\Delta E = 300\mu eV$ via the relation $\Delta E \sim \pi\hbar^2/m^* l^2$ gives us a estimated $l \sim 110$nm in the $N-1$ state. This rough estimate assumes that $E_F^{2D} = E_F^{dot}$, which may not be the case for a small dot. Although it is possible to tune the dot to lower occupancies, the current directly through the dot soon becomes too small to measure, and a charge sensor is required.

Charge Sensing

For this particular device at a top gate of $V_{TG} = +6.0$V, we found that the charge sensor was not sensitive over the operating voltage ranges of the quantum dot. No distinctive sawtooth features coinciding with Coulomb blockade peaks in the dot conductance were detected.

To test the charge sensor, we first kept the same voltages used to define the quantum dot ($V_{LB} = -0.6$V, $V_{RT} = -0.59$V, $V_{RB} = -2.2$V at $V_{TG} = +6.0$V) and hooked up the charge sensing circuit. Despite pulling Q back to its maximum voltage $V_Q = -0.2$V (beyond which Q becomes undefined), the charge sensor conductance dropped dramatically as plunger gate is swept, tuning the dot to lower occupancies.

Moreover the charge sensor conductance appeared to exhibit Coulomb blockade oscillations of its own which were uncorrelated to the Coulomb blockade peak period in the dot, shown in Fig. 6.14a,b. This suggests that there may be an unwanted quantum dot forming within the 1D channel of the charge sensor as the channel width down at the 2DEG may be quite narrow, since the depletion region below LB may be broader than previously anticipated, as suggested by the unexpectedly large capacitive coupling of the dot to gate RT.

Attempts were made to widen the charge sensing channel to remove the undesired dot by incrementally unbiasing gate LB from -0.6V to $V_{LB} = +0.2$V, to reduce the depletion region under LB and retuning the other gate voltages to retain the original, wanted quantum dot. Gate Q was then set to its maximum operating voltage where the conductance through the charge detector was just below the first $\frac{2e^2}{h}$ plateau for maximum CS sensitivity.A corresponding simultaneous measurement of both the quantum dot and charge sensor conductance is shown in Figs. 6.14(c,d). In the region of Coulomb blockade through the dot where there minima do not reach zero, a peak in the Coulomb blockade corresponds to a slight dip in the CS (marked in dashed purple lines). However towards lower occupancy, the oscillations in the CS no longer coincide with the peaks through the dot. Rather double-peak like features start to appear in the dot conductance (starting from the dashed orange mark), as oscillatory behaviour in the CS becomes more pronounced, suggesting that the unwanted dot in the CS circuit may have formed despite the larger channel width and our wanted dot, may be behaving as a charge detector and 'back-sensing' the presence of the undesired dot in the 1D channel. Further tests were performed with different gate voltage configurations up to $V_{LB} = +0.4$V; beyond this point the top tunnel barrier of the dot becomes too transparent and no distinct zeros were obtained between Coulomb blockade peaks.

This was an unexpected result which suggested that the current quantum dot and charge sensing layout was not optimal for the 2DEG depth and voltage parameters available. We also characterized a quantum dot with a different configuration, the "asymmetric curved dot" device from Fig. 6.6b, using the same process as we have just described for the "asymmetric square dot" device in Fig. 6.6c. But we discov-

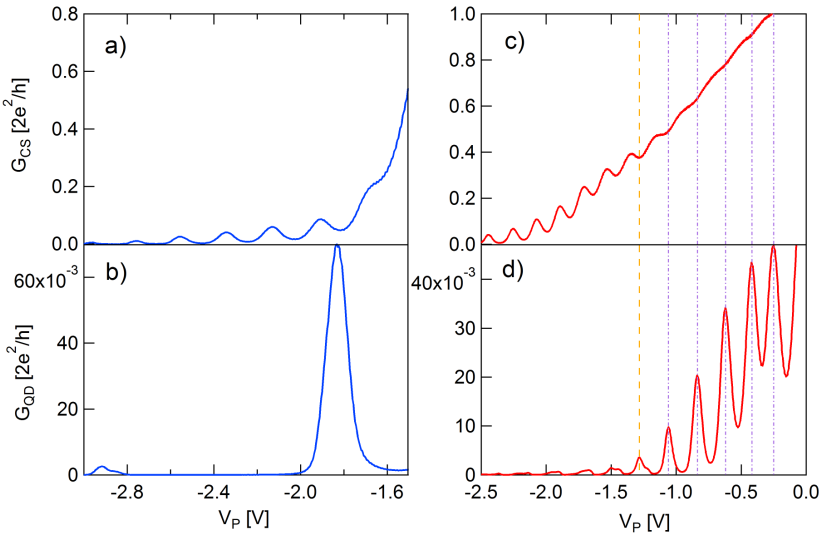

Figure 6.14: Simultaneous measurement of 2-terminal conductance, corrected for series resistance, through both the charge detector (top panels a,c) and quantum dot (bottom panels b,d) as the plunger gate is swept (x-axis, right to left) to reduce the occupancy of the dot. Left panels (a,b) with $V_{LB} = -0.6$V and the QPC charge sensor pulled back to a maximum of $V_Q = -0.2$V. The CS signal does not correlate with the quantum dot Coulomb blockade peaks but rather appears to behave as an unwanted dot within the 1D channel. Right panels (c,d) correspond to dot and charge sensor conductance respectively, with gate LB unbiased to $V_{LB} = +0.2$V, in an attempt to widen the CS 1D channel. Q is set to $V_Q = -0.460V$ so that G_{CS} lies just below the first conductance plateau to cover the range of maximum sensitivity over the range of V_P. However, the orange dashed line at $V_P = -1.03$V is the last position where Coulomb blockade peaks in G_{QD} are sensed as dips in the CS signal and beyond this the wanted quantum dot appears to still 'back-sense' the unwanted dot formed within the CS channel despite widening the CS channel. For more information about potential effects of the 3-terminal setup upon this dataset, please refer to Appendix E.

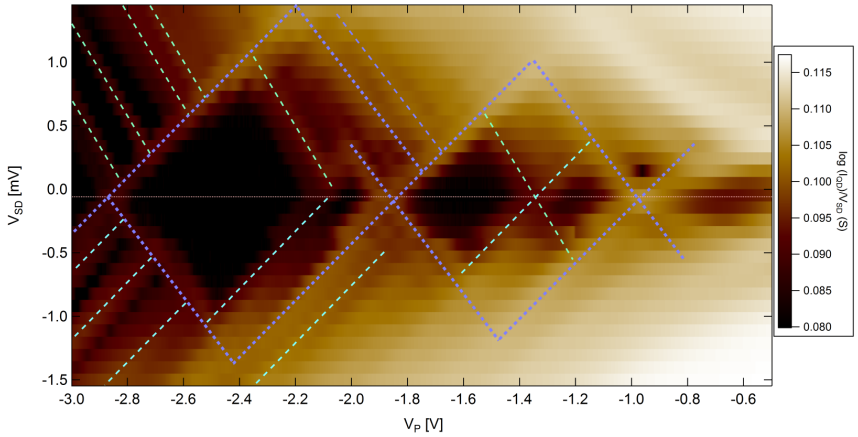

Figure 6.15: Source-drain bias spectroscopy of curved dot design from Fig. 6.6b. The colour scale is a log plot of differential conductance, versus plunger gate voltage V_P along the x-axis and dc source-drain bias voltage V_{SD} on the y-axis. For this measurement, the voltages used were $V_{RT} = -0.732$V, $V_{RB} = -0.712$V, $V_{LB} = -0.1$V at $V_{TG} = +6.0$V. The ground states forming Coulomb diamonds (dashed purple) appear broken into a series of smaller diamonds within what should be the blockaded region, suggesting parallel dot transport. Excited states are marked in dashed green.

ered that the behaviour of this curved design is virtually the same as the square dot design; including the non-sensitivity of the charge sensor, over the operating voltage range of the quantum dot. Unexpectedly, during source-drain bias measurements, the quantum dot appeared to fragment into two dots as seen in Fig. 6.15. Rather than exhibiting a single diamond with fully blockaded current within the enclosed region, lines of conductance taking the form of smaller diamonds with alternating, different sizes suggest that transport is occurring through two dots in series with each other. This could potentially have been caused by a nearby disorder potential near gate RT, however the exact cause is still unknown. After these measurements were performed, Tracy *et al.* published results on an induced hole double quantum dot [266] using a similar variation of the Elzerman double-dot design [70] in a 110nm deep quantum well without fragmenting.

6.3.3 Electron dot summary

In conclusion, we have demonstrated that we can electrostatically define a small, stable electron quantum dot of size $l \sim 110$nm, in a 160nm deep 2DEG using a completely

undoped heterostructure. However this design is still not fully optimized and we were unable to perform transport measurements down to the last electron as the charge sensor was not sensitive in the few-N regime and direct current through the dot was lost shortly after gate RT was defined. The unusual behaviour of gate LB suggests the depletion region beneath it was unexpectedly large, pushing the quantum dot away from the charge sensor towards gate RT and reducing the sensitivity of the QPC charge detector. Part of this could be due to a smeared out confining potential at a depth of 160nm below the metal gates defining the dot combined with an asymmetric dot geometry. Moreover the presence of a global top gate could screen coupling between the dot and charge sensor, further reducing its sensitivity. This suggests that there may be other subtleties involved in transferring a quantum dot pattern from a modulation doped architecture directly into an induced architecture, which requires finer tuning of the design. To investigate this further, in the following section we perform some simulations and suggest an alternative, more optimize the design of the dot geometry for an induced architecture.

6.4 Quantum Dot Simulations

To understand the behaviour of the electrostatic potential defining the quantum dot down at the 2DEG, some 3D simulations were performed in the Schrödinger-Poisson solver, Nextnano++ [273]. These allowed us to qualitatively examine the effect of the quantum dot gate geometry upon the shape of the confining potential and model the effect of insulating materials with different dielectrics. The dependence of broadening of the confining potential upon the distance between the 2DEG and the global top gate was also investigated. Details of the modelling parameters and setup are described in Appendix F.

The lithographic dimensions of the quantum dot pattern were transferred into a Poisson solver software package, Nextnano++, shown in Fig. 6.16a, where the accuracy of the result is limited by the grid resolution and computation time to run the simulation. Panel b) of the figure shows the resulting electron density at the 2DEG, below 160nm of AlGaAs and 600nm of Polyimide to the top gate, using the same

dielectric constants as in the previous section. Areas of white represent a maximum electron density $n_{2D} = 1.4 \times 10^{11} cm^{-2}$, modelled with a higher top gate voltage of $+8.0V$, whilst black regions represent areas where the 2DEG is depleted.

Biases have been applied to the the quantum dot gates to define the dot. From this picture, since the gates LB,P,RB are close and act together, forming a large depletion region at the 2DEG which pushes the quantum dot farther away from the charge sensor and up against gate RT, resulting in a small, irregular 'banana' shaped dot. This complements the experimental data which yielded a capacitive coupling of RT to the quantum dot which was even stronger than the capacitive coupling to the top gate.

In panels (d) and (f) of Fig. 6.16, we simulate the effect of reducing the distance of the 2DEG to the GaAs surface, by 110nm in panel (d) and 60nm in panel (f) whilst keeping the EBL gate biases the same for a direct 1:1 comparison of the effect of the 2DEG depth only. These depths were chosen as they correspond to wafers with reasonable density and mobility characteristics that we have available from which we could fabricate dots (see Chapter 3.4 for wafer characteristics). This reduction in 2DEG depth appears to have a drastic impact upon the spread of the depletion region and hence the shape of the quantum dot. At 110nm from the surface, the defining electrostatic potential is much sharper and the tunnel barriers as well as dot shape become more distinctly defined. Going further to 60nm results in an open quantum dot with undefined tunnel barriers and an open CS channel. This depletion width profile suggests that it is much easier to define a dot with a sharp, tunable confining potential using the 60nm deep 2DEG compared to 160nm, simply by increasing the gate voltage biases to close the gap (not shown).

The change in electron density caused by using an insulating material with a higher dielectric constant such as Al_2O_3 is explored in panels (c) and (e). All parameters are kept constant in both panels except that in panel (c) the Polyimide insulator with $\epsilon = 3.5$ (from panel (b)) is replaced with amorphous Aluminium Oxide (in panel (c)) modelled with $\epsilon = 8$ with an applied top gate bias of $-1.34V$ to keep the same density as the Polyimide simulations. Despite the increase in ϵ by a factor of 2, there

appears to be little difference between the two simulations (b,c), which could be due to the large 760nm effective distance between the top gate and the 2DEG. In panel (e) the thickness of the Aluminium oxide layer is reduced to 30nm. This shows that reducing the thickness of the insulating dielectric also helps to reduce broadening of the depletion region underneath the defining gates at the 2DEG, resulting in a better defined quantum dot becomes. Although its impact is not as drastic as bringing the 2DEG closer to the defining gates, as seen in panels (b,d,f).

From these sets of simulations, applying a combination of shallower 2DEG and a thinner insulating material with a higher dielectric constant should result in a better defined quantum dot with sharper tunnel barriers. As the study of surface charges [174], showed that their effect on mobility is minimized when the 2DEG is $\sim$ 100nm from the surface, we decided to use the W0640 wafer where the 2DEG is 110nm from the surface, rather than the 60nm and combine it with 30nm of Aluminium oxide for the insulating layer. This combination also worked better for us in a practical sense, since we were unable to obtain a 100% ohmic yield for heterojunctions shallower than 150nm using the 600nm thick polyimide dielectric for *p*-type ohmics. On the other hand, we were able to achieve this using an ALD dielectric, which had the added advantage of a lower ohmic turn-on (threshold) voltage, consistent for all ohmics with a 100% yield on shallower wafers including 60nm.

As we are interested in studying the behaviour of a single quantum dot rather than a double dot configuration, we also modelled a symmetric design, similar to that used in the Field paper [76] with a few minor changes, shown in Fig. 6.17a dubbed 'Sunbeam'. This pattern (along with minor variations and extensions) has also been used to successfully fabricate small electron dots down to the last electron [29, 158, 291]. In this configuration, an electrostatically defined barrier made from gates LT and RT, separates the charge sensing circuit from the quantum dot circuit. The quantum dot is formed via 3 gates pressing against the separating gates. The QPC charge sensor on the other side of the separating gates, is positioned so the 1D channel is squeezed directly against the quantum dot increasing the proximity between the two nanostructures. In this design we have also introduced a 20nm gap in the separating

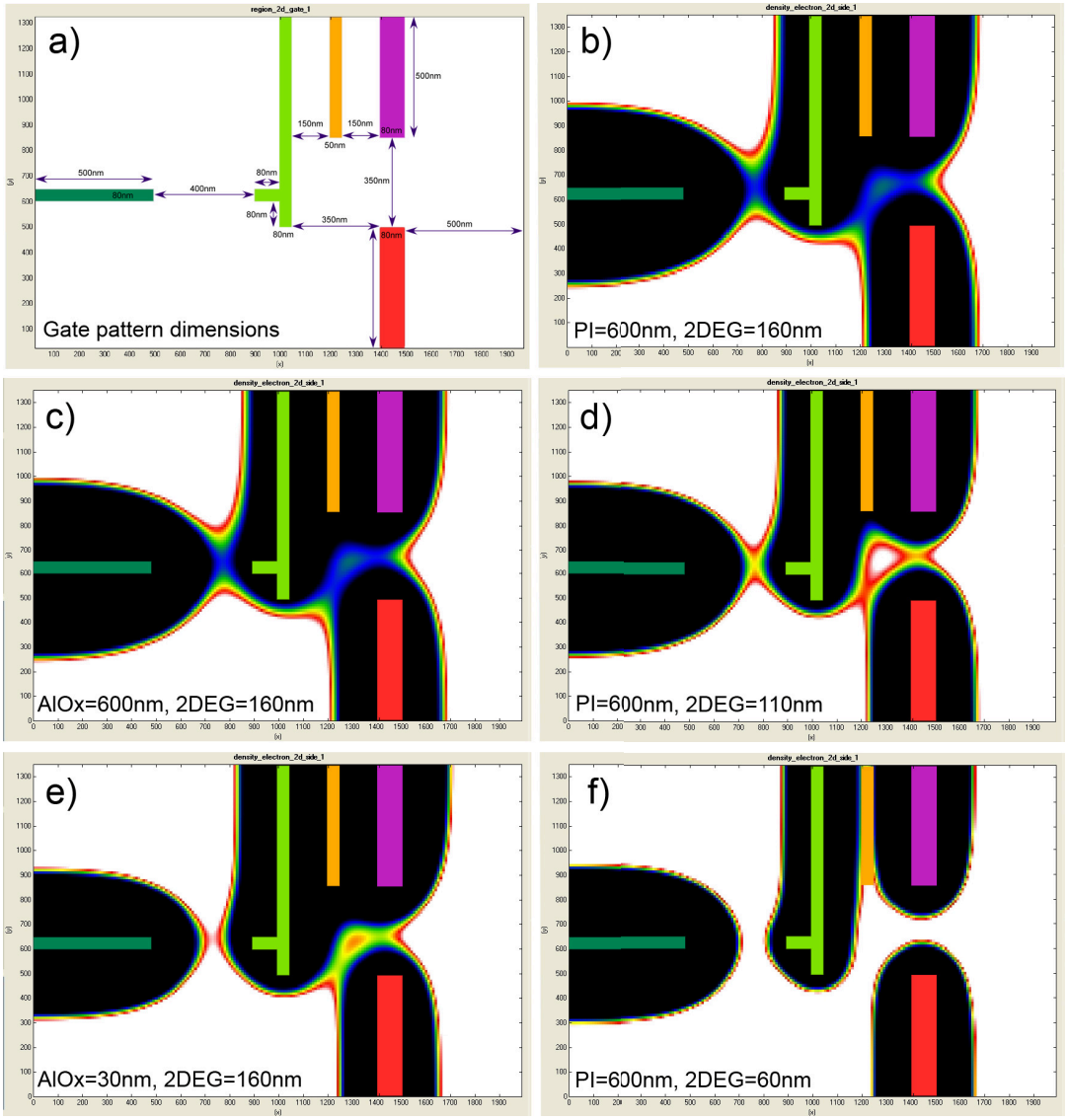

Figure 6.16: Nextnano++ simulations depicting the effect of changing different parameters upon the 2D electron density seen at the 2DEG for the asymmetric square dot design. Parameters affecting the confining potential profile include, the type and thickness of the insulating dielectric (Polyimide (PI) and Aluminium Oxide (AlOx) between the global top gate and wafer surface, and the depth of the 2DEG below the GaAs surface.

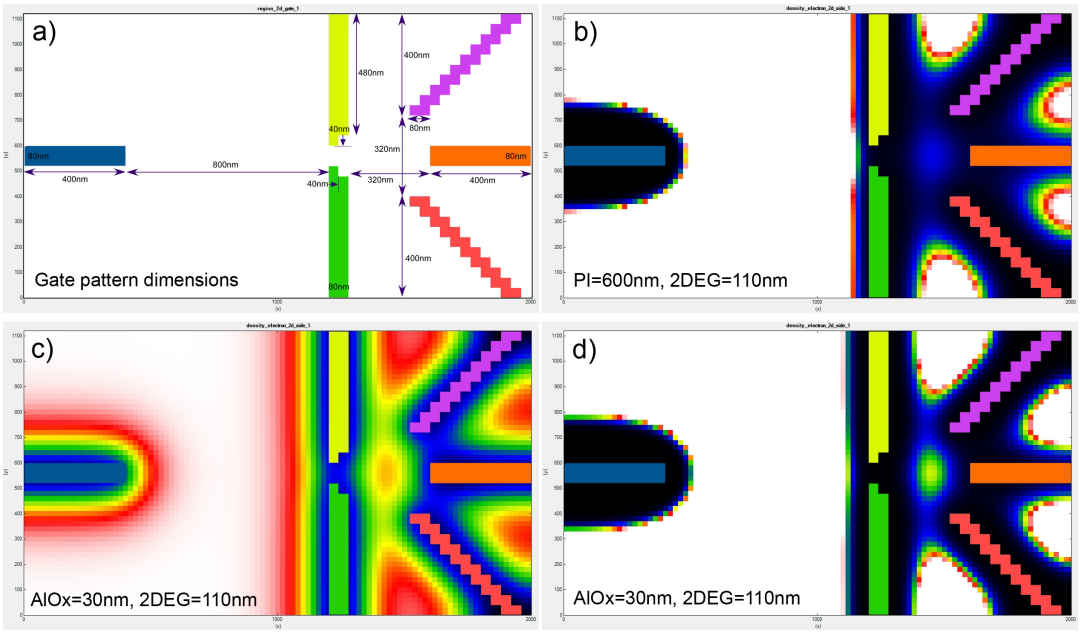

Figure 6.17: Nextnano++ simulations depicting the effect of changing different parameters upon the 2D electron density seen at the 2DEG for the adjusted symmetric 'sunbeam' dot design. Parameters affecting the profile of the confining potential include, the type and thickness of the insulating dielectric (polyimide (PI) and Aluminium Oxide (AlOx) between the global top gate and wafer surface, and the depth of the 2DEG below the GaAs surface.

barrier to increase coupling between the dot and the charge sensor as suggested by Rössler *et al.* [225], who demonstrated that the charge detector sensitivity increased by a factor of 4 when a small gap was introduced.

In the previous asymmetric design, we found that having 3 gates in parallel close to each other results in a much larger total effective depletion region. To reduce the size of this effective depletion region and the amount of crosstalk between the gates, we have deliberately angled LB, P and RB to increase the spacing in between them. In this simulation we also doubled the charge sensor channel width to 800nm, since in the previous experiment we had to operate the detector with gate Q nearly unbiased due to the unexpectedly large depletion region under LB.

The simulation for the symmetric design with a 110nm deep 2DEG and 30nm of AlOx is shown in Fig. 6.17c. Using the same top gate of -1.34V results in a maximum electron density of $n_{2D} = 1.4 \times 10^{11} cm^{-2}$ in the white regions of the image. Just like the case of the asymmetric design, the quantum dot gates are defined at zero bias, as their presence effectively screens the top gate. However even in this configuration, the region in which the quantum dot will be formed is distinct. Panel (d) simulates the same configuration as (c) but with EBL gate biases applied to define the quantum dot. In panel (b) we maintain the same EBL gate biases as in (c) but switch back to the polyimide insulator configuration for comparison. From this we can see that using the much thinner AlOx insulating dielectric is a much better choice compared to polyimide, since finer features such as surface metallic gates used to define the quantum dot, are not as smeared out by broadening of the confining potential down at the 2D gas.

Although we will be using a 30nm AlOx dielectric, we can compare the effect of the gate geometry upon the steepness of the confining potential of the dot, between the asymmetric square pattern in Fig. 6.16d with the symmetric sunbeam pattern in Fig. 6.17b, as both have a 600nm thick polyimide and a 110nm 2DEG. Between thee 2 patterns, we can immediately see that the confining potential is much steeper for the asymmetric square pattern and the corresponding tunnel barriers much thinner. The Sunbeam design appears to have thicker tunnel barriers, which makes them com-

paratively less tunable and possesses a shallower confining potential compared to the asymmetric design. However there are two main advantages to the Sunbeam design: firstly its symmetry means it is much easier and quicker to form a dot (in fact as shown in Fig. 6.17c, the dot is almost formed already even without any bias added to the gates) and to tune it. The second advantage is the two completely independent circuits of the charge detector and the quantum dot. This allows for greater operational flexibility e.g. the ability to lower the excitation voltage used on the dot circuit to enable excited states to be detected whilst raising the excitation voltage over the charge sensor to increase its signal to noise ratio.

From these simulations and the ease of operation of the symmetric design, we elected to use the Sunbeam design to fabricate our hole quantum dot. However the doubling of the charge sensor channel width to 800nm made it too large (the gaps of the QPC channel width in Fig. 6.17 is very large) and a very large voltage on gate Q was required to pinch-off the 1D channel. In the final design we reduced the QPC width back to 400nm.

6.4.1 Simulation summary

Simulations to visualize the quantum dot electrostatic confining potential, showed that a shallow 2DEG located closer to the metallic surface gates defining the dot pattern provides much better definition of the confining potential and sharper, more tunable barriers. Reducing the thickness of the insulating dielectric and selecting a material with a higher dielectric constant also increases the definition of the confining potential. A symmetric lateral gate geometry with a gap between the gates separating the charge sensor and quantum dot circuits may enhance the sensitivity of the CS and allow for operation of the dot in the few-N regime even after direct current through the dot is lost. Combined with the ease of operating a symmetric design plus the flexibility of completely independent quantum dot and charge detector circuits, in the following section we shall explore this design for an induced few-hole quantum dot, with a 110nm deep 2DHG and a 30nm thick AlOx insulating dielectric.

6.5 Hole quantum dot characterization

In this section we apply the Sunbeam design modelled in the simulation section and demonstrate the successful fabrication and characterization of a lateral, electrostatically induced, few-hole quantum dot, down to the last hole with an operational, integrated QPC charge sensor within a MISFET architecture. We observe Coulomb blockade with corresponding charge sensing features and use the technique of source drain bias spectroscopy to observe the presence of excited states through both the quantum dot circuit and the charge detector. Although the charge detector by itself does not provide information about the quantum dot energy spectra, since transport through the dot is not always available or desirable, combining the technique of source drain bias spectroscopy with charge detection offers a potential alternative to mapping out the energy spectra in the few-hole regime. Here we employ the use of a QPC charge sensor, compare its behaviour with measurements taken directly through the dot and demonstrate the presence of hole excited states via the charge sensor signal in an induced quantum dot.

6.5.1 Device design and electrical measurement setup

The induced hole dot was fabricated from wafer W0640 (100) GaAs, its cross-section depicted in Fig. 6.18a. Gold beryllium (AuBe) was evaporated to create $p-$type ohmic contacts and annealed into the heterostructure (as opposed to AuGe for electrons). This was followed by EBL gate definition of the 'Sunbeam' quantum dot pattern, deposited with a thin layer of Ti/Au. The metallic surface gates were then covered by 30nm of an insulating Al_2O_3 dielectric via atomic layer deposition (ALD), followed by an overall Ti/Au global top gate, which we use to induce carriers into the 2DHG.

A SEM image of the 'Sunbeam' pattern is shown in Fig. 6.18b, which uses 5 gates to define the quantum dot: LT and LB to define the left (exit) tunnel barrier, RT and RB define the right (entry) tunnel barrier, whilst the plunger gate P is used to tune the occupancy of the quantum dot. An extra gate Q is used to define the QPC charge sensor together with the gates LT and RT which separate the two circuits from each other. These metal gates screen the 2DHG directly underneath them, as a voltage is

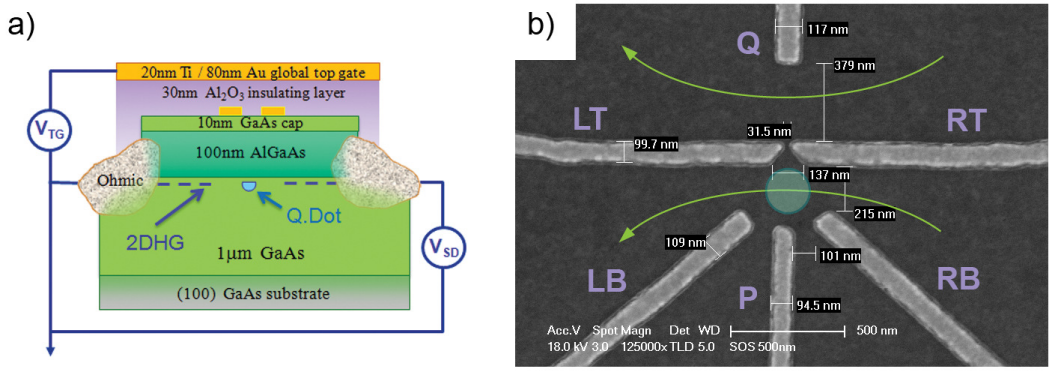

Figure 6.18: Part (a) shows the W0640 wafer layout for the 110nm deep 2DHG, together with the etched ohmics and the EBL gates defining the quantum dot pattern on the wafer surface. The structure is covered by a 30nm Al_2O_3 insulating layer followed by an overall top gate. Part (b) shows the SEM image of the symmetric quantum dot pattern, where the quantum dot location is highlighted by a green circle. A separate QPC charge sensing circuit is created using gates Q, LT and RT, and the 2 current paths for the quantum dot and charge sensor are shown with light green arrows.

applied to the global top gate, thus forming a quantum dot and a 1D constriction.

From these lithographic dimensions we once again begin with some initial, rough estimates about the quantum dot parameters. an operating point of $V_{TG} = -1.40V$ was chosen, which gave a 2D density of $p_{2D} = 2.33 \times 10^{11} cm^{-2}$ as it lay just below the onset of hysteresis. From the lithographic area of the dot pattern $297 \times 215nm$, we estimated the dot to hold a maximum of $\sim$ 400 holes. A Fermi wavelength of $\lambda_F = \sqrt{\frac{2\pi}{n_{2D}}} \approx$ 52nm would give a maximum of $\frac{2W_{QPC}}{\lambda_F} \approx 8$ conductance modes through each tunnel barrier and a maximum of ≈ 14 through the charge sensor, where W_{QPC} is the width of the 1D channel. However as demonstrated in the electron dot, down at the 2DHG due to broadening of the depletion region beneath the gates, we expect to see half the number of modes, i.e. ≈ 4 conductance modes through each tunnel barrier and ≈ 7 through the charge sensor.

A first-order estimate of E_C can be made using a simple series plate capacitor model as per the electron dot 6.2, with similar approximations so $E_C \equiv e^2/C_\Sigma$. $\epsilon_{AlOx} = 8$ is used as the dielectric constant of amorphous Al_2O_3 instead of ϵ_{PI}. The distance between the top gate and quantum dot is now shortened to $d = d_{AlGaAs} + d_{AlOx} =$

$140nm$. This gives us a $C_\Sigma \approx 138$aF, corresponding to a charging energy of $E_C \sim 1.2$meV or an equivalent temperature of $T_E = E_C/k_B \sim 14$K. The average single particle spacing $\Delta E \approx \frac{2\pi\hbar^2}{m^* A}$ [11] is estimated to be a minimum of 12μeV or ~ 0.14K. Due to the large effective mass of holes $m^* \approx 0.2$ compared to electrons, the single particle level spacing is much smaller and harder to resolve.

Measurements were once again performed inside a Kelvinox 100 dilution refrigerator at a base temperature of 45mK, using standard two-terminal ac lock-in techniques to simultaneously readout both quantum dot and charge sensing signals from each corresponding circuit. Unlike the asymmetric design used for the electron dot with a common source between the dot and charge detector circuits, this time the charge sensing circuit is independent of the quantum dot circuit for greater flexibility, allowing us to operate the charge sensor using a greater source excitation voltage for better signal-to-noise ratio and a reduced quantum dot excitation voltage to observe excited states. The measurement setup used is illustrated in Fig. 6.19. In this setup, an 8-channel Basel LNHR (Low Noise High Resolution) DC voltage source was used to obtain the small step increments necessary to resolve hole excited states.

6.5.2 Experimental data and results

Dot characterization and charge sensing

To determine a good set of initial operating voltages, once the top gate was biased to -1.4V (for a density of $p = 2.33 \times 10^{11}/cm^2$) we first investigate the behaviour of each gate (Q, LB, P, RB) as a QPC by pinching it off against the gates separating the dot circuit from the charge sensing circuit (LT and RT). The pinch-off traces for each gate are shown in Fig. 6.20 for different values of LT and RT (where LT and RT are kept at the same voltage due to design symmetry). For each trace, all unused gates were biased to $V_G = -0.8$V to induce holes underneath them.

For this small dot design, at a depth of 110nm below the surface, 3 to 4 conductance modes were present through the quantum dot gates in panels (b-d), as predicted by our initial estimates. The gates defining the dot (LB, P, RB) had to be unbiased to open up the channel and allow current to flow through the dot, with the 1D to 2D

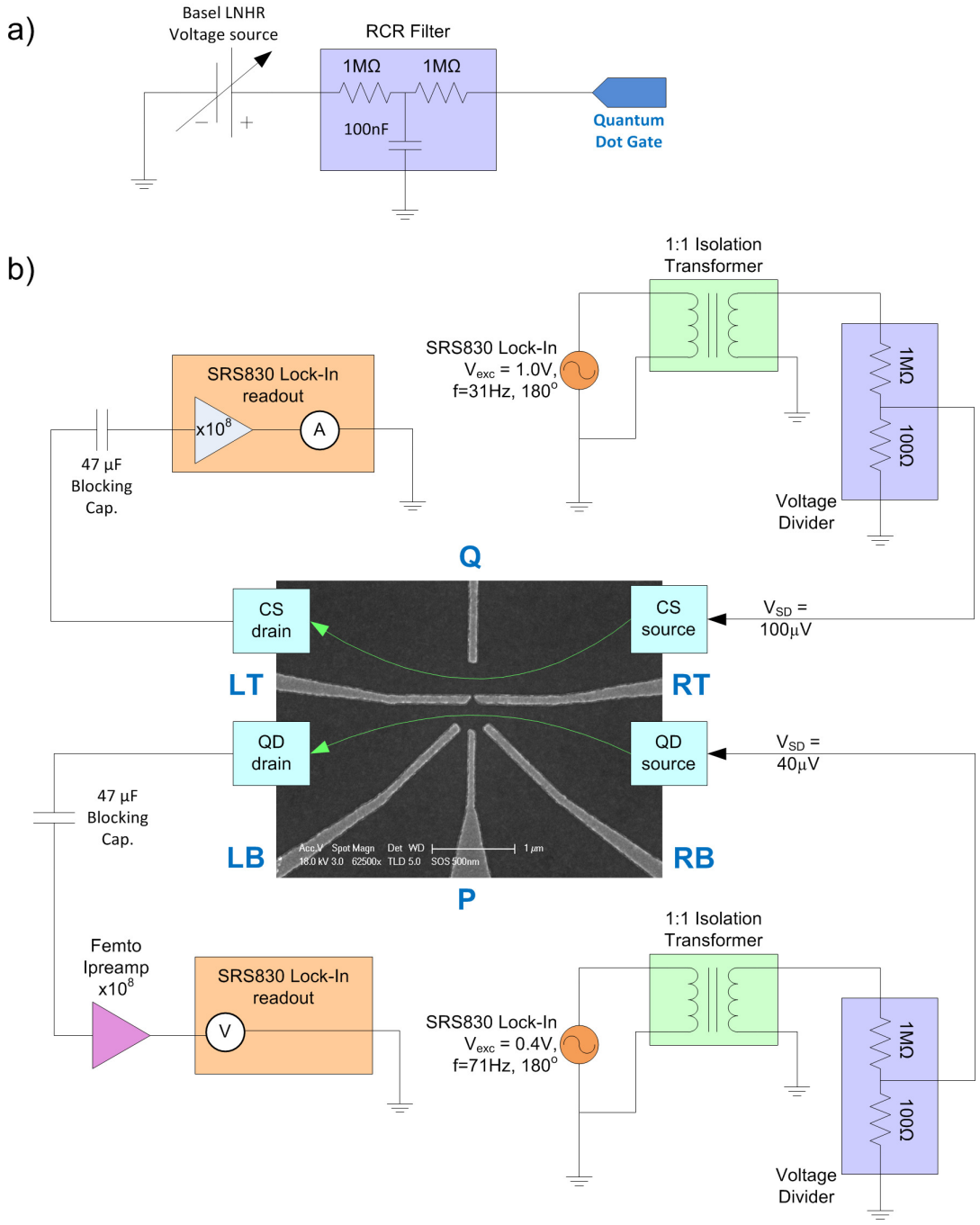

Figure 6.19: Part (a) shows a Basel LNHR DC voltage source followed by a low pass RCR filter, used to apply a bias to tune each of the gates (Q, LT, RT, LB, P, RB), labelled in blue in Part (b). Two completely separate circuits are used for the charge sensor and the quantum dot with different source frequencies and excitation voltages. In both cases, a SRS830 lock-in amplifier provides an ac excitation voltage, that is passed through an isolation transformer (to break a ground loop), into a $\times 10^4$ voltage divider through to the source ohmic on the device. From here it travels through the nanostructure, out through the drain and into a SRS830 lock-in amplifier current readout via a $47\mu F$ blocking capacitor. Due to the small dot signal, an external variable-gain, Femto current preamplifier was used to boost the signal before readout.

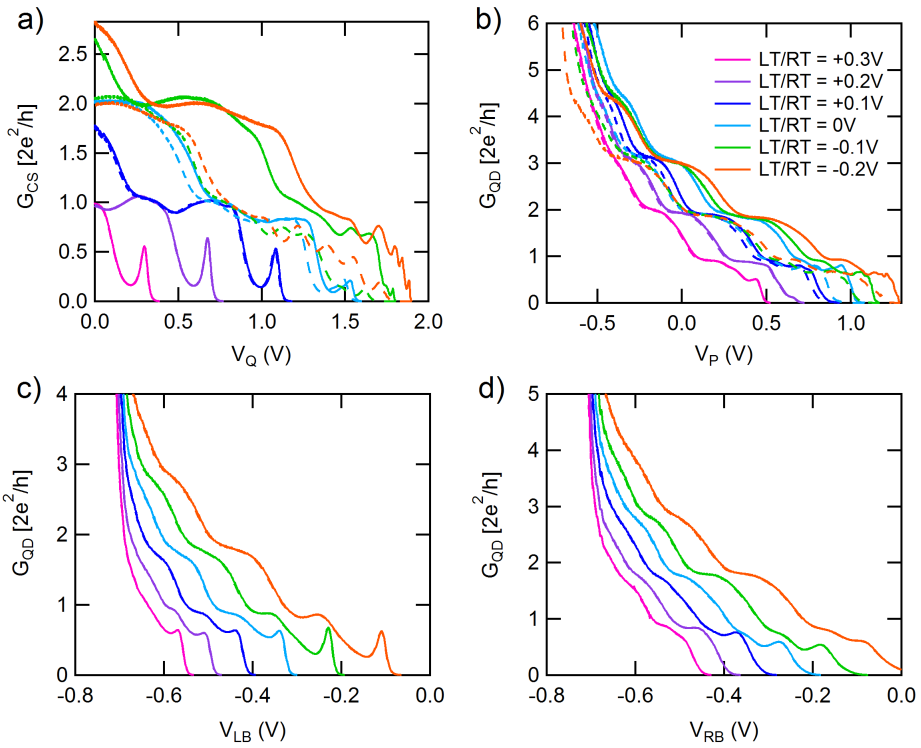

Figure 6.20: Pinch-off characteristics of the charge sensor gate Q (a) and quantum dot gates P (b), LB (c), RB (d); where the current is corrected for series resistance, converted to 2-terminal conductance and plotted in units of the conductance quantum. In all panels, each pinch-off trace was taken for different values of LT and RT, indicated in the legend of panel (b), for both forward (solid) and reverse (dashed) sweeps. All unused gates were unbiased to 2D region at -0.8V for a top gate of $V_{TG} = -1.4$V.

transition for each gate occurring at −0.72V. From these plots, for values of LT&RT smaller than +0.1V, we start to observe hysteretic behaviour in both the plunger gate and charge sensing gate traces. To maintain reproducible, stable gate behaviour, we do not operate LT&RT below this voltage for a top gate of −1.4V. An initial operating voltage of $V_{LT\&RT} = +0.20V$ was selected as it provided the best compromise, allowing current through the small dot (after all the gates were defined) whilst retaining good definition of the separating barrier.

To operate the dot in the single hole tunneling regime, voltages on LB, RB and P, were set so that $G_{QD} < \frac{2e^2}{h}$, i.e. close to pinch-off but transparent enough to let some current through the dot. The charge sensor Q was also moved to its sensitive operating point on the slope of the riser of the first conductance plateau. The dot excitation voltage was also lowered from 60μeV used in the pinch-off traces to 30μeV.

Fig. 6.21 shows a series of wall-wall plots of the quantum dot barriers, where gate P was kept fixed whilst stepping LB and sweeping RB. Panel (a) is a map of conductance directly through the dot, with $V_{LT\&RT} = 0.20$V and $V_P = -0.35$V whilst panel (b) shows the corresponding charge sensor transconductance conductance for greater clarity. The CS signal continues beyond the point where current through the dot disappears. Both barrier maps show a distinct wobbling in the lines, indicative of a strongly coupled double dot, due to the relatively larger bias on the plunger gate breaking up the single-dot into two dots, similar to Ref. [266]. In panels (c,d), the same barrier map is repeated over a larger range of LB, with the plunger gate pulled back to −0.42V. This yields straighter lines more akin to single-dot behaviour. The bias on the separating barriers LT&RT was backed off slightly to −0.18V to increase current through the dot. The lineshape and symmetry of the Coulomb blockade peaks and lower signal to noise ratio in the charge detector conductance suggest that the barriers of the dot are not symmetric. After further barrier tuning we arrive at the stability diagrams in panels (e,f), which exhibit distinct, well defined, straight lines in both the dot and CS maps, indicative of single hole tunnelling.

Keeping the dot barriers fixed whilst sweeping the plunger gate yields a series of Coulomb blockade peaks through the dot, with clear zeros and a distinct sawtooth

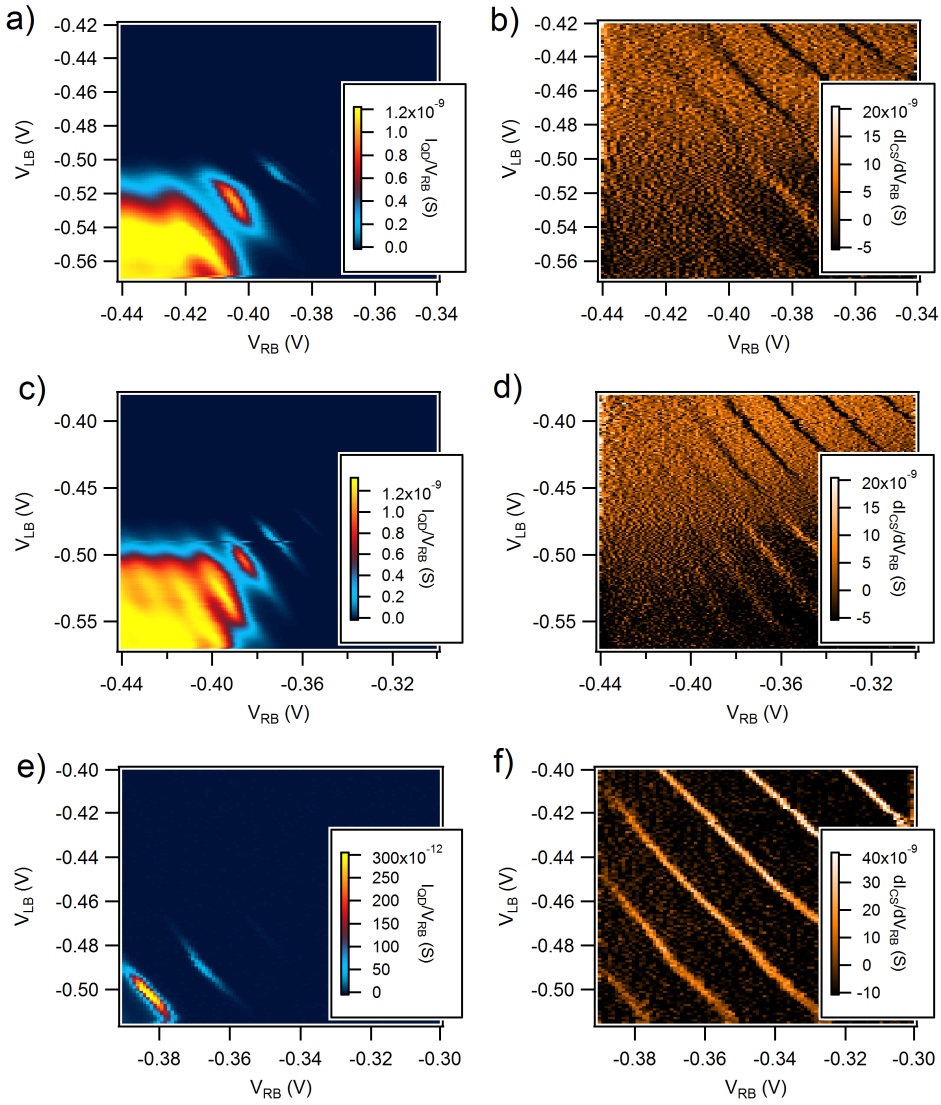

Figure 6.21: Colour maps of the entry and exit barriers to the quantum dot, stepping gate LB and sweeping RB. (a) Plot of conductance directly through the dot where $V_{LT\&RT} = 0.20$V and $V_P = -0.35$V. (b) shows its corresponding charge sensor response as a derivative of the conductance. Panels (c,d) similarly plot conductance through the dot and charge sensor for $V_{LT\&RT} = 0.18$V and $V_P = -0.42$V, yielding straighter lines. Stability diagrams in (e,f) show distinct straight lines in both quantum dot and CS maps after further barrier tuning, with $V_{LT\&RT} = 0.18$V and $V_P = -0.33$V.

signal in the charge sensor conductance, corresponding to each Coulomb blockade peak as shown in Fig. 6.22a. The step height of the charge sensor signal is about $\Delta G_{CS}/G_{CS} = 12\%$ at $V_P = -0.22$V, on the same order of magnitude as that reported in Ref. [226].

To extract the capacitance ratios and hence determine the lever arms α of each gate, each gate was swept over a voltage range to cover the same features as the plunger gate. The traces are plotted in Fig. 6.22b-d, and a table of values are provided in Table 6.2. From this table we see that the global top gate maintains the largest capacitive coupling to the dot, followed by gates LT&RT combined. The bottom gates LB and RB have very similar capacitances, consistent with the symmetry of our dot pattern. As LT and RT were swept simultaneously, from the symmetric geometry we estimate each gate to have a capacitive coupling to the dot equivalent to half the total i.e. $C_{LT} = C_{RT} = 5.7aF$ and $\alpha_{LT} = \alpha_{RT} = 0.027$, which is similar to that of the relatively symmetrically coupled bottom barrier gates LB and RB. Features with a red asterisk mark the starting point of the sweep, common to each panel. In panels (c,d) although distinct Coulomb blockade was present, barely any charge detector signal was observed as gates LT&RT, and TG were swept respectively. Perhaps the sensitivity of the charge sensor to the dot could have been reduced by the large capacitance of the gates which also couple to the dot, i.e. $\Delta q_{CS} \sim C_{QD-CS}/(C_{QD-gates} + C_{QD-reservoir} + C_{QD-CS})$. As these higher capacitance gates are swept, it effectively reduces (screens) the coupling between the charge sensor and the dot, resulting in a detector signal that is not visible over the steep falling background conductance. Fig. 6.22b shows the opposite case for the gates LT and RT, which define the entry and exit barriers of the dot - as the gate is swept to pinch-off the dot conductance shuts off very rapidly and only one Coulomb blockade peak can be seen before current through the dot is too small to be detected, whilst the charge detector is able to continue detecting the reduction of occupancy on the dot.

To extract the charging energy and single particle spacing of the dot, source-drain bias spectroscopy was performed on the same set of Coulomb blockade peaks in Fig. 6.22. Fig. 6.23 is a colour map of the differential conductance through the

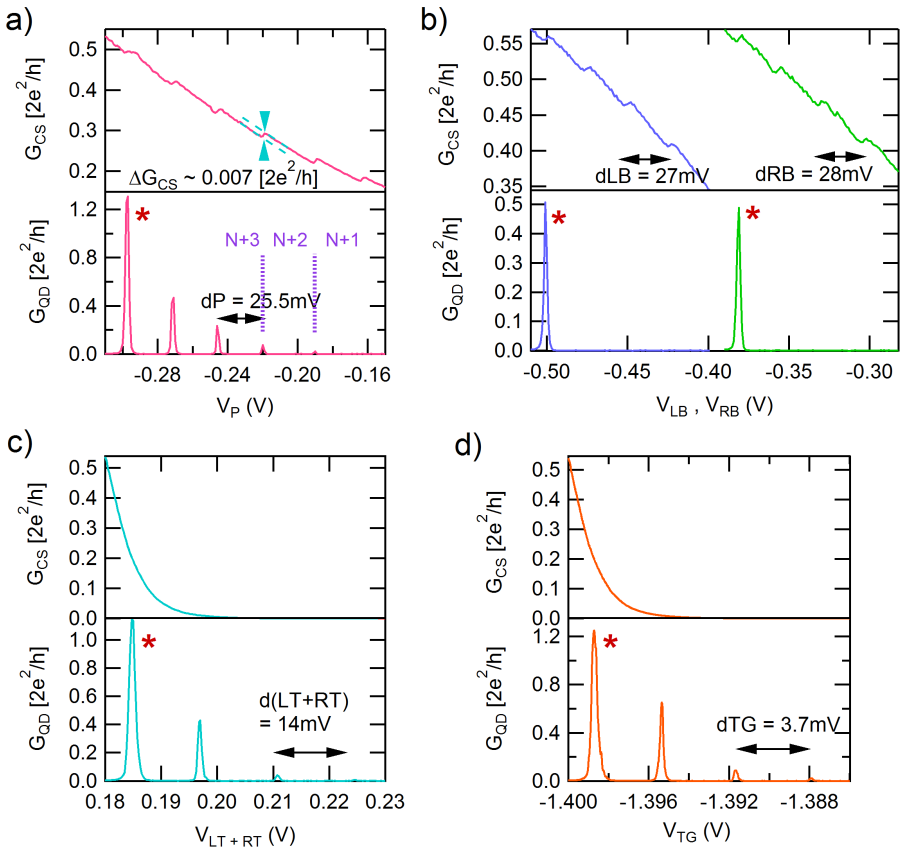

Figure 6.22: Conductance versus gate voltage plots generated to determine the capacitance ratios of each gate from the period for (a) plunger gate (pink) (b) LB (dark blue) and RB (green), (c) LT and RT simultaneously (aqua) and (d) top gate. Once again, current is corrected for series resistance, converted to 2-terminal conductance and plotted in units of the conductance quantum. When not being swept, each gate was kept at a fixed voltage of $V_{TG} = -1.4$V, $V_Q = -0.45$V, $V_P = -0.33$V, $V_{LT\&RT} = +0.18$V, $V_{LB} = -0.51$V and $V_{RB} = -0.39$V. Note the features from which dV_G are extracted from all gate traces, correspond to the N+3 Coulomb diamond in Fig. 6.23, as marked in purple in panel (a). The Coulomb blockade peak marked with a red asterisk corresponds to the first feature, common to each panel.

Gate	ΔV_g	$C_g = e/\Delta V_g$	$\alpha = C_g/C_\Sigma$
P	26mV	6.3aF	0.030
RB	28mV	5.7aF	0.026
LB	27mV	5.9aF	0.027
LT&RT	14mV	11aF	0.052
TG	37mV	43aF	0.20

Table 6.2: The period for each gate ΔV_g was obtained from the Coulomb blockade oscillations in Fig. 6.22. Corresponding gate capacitances C_g were calculated using the approximation $\Delta V_g = e/C_g$, and sum to $C_{\Sigma gates} = 73$aF. From this we estimate the charging energy to be $E_C \equiv e^2/C_{\Sigma gates} = 0.77$meV. The lever arms $\alpha = C_g/C_\Sigma$ for each gate are also given [1].

quantum dot plotted as a function of V_P and the DC source-drain bias V_{SD} in panel (a); the corresponding map of the charge sensor conductance derivative is given in panel (b). In both cases, 'N' refers to the dot occupancy.

For Coulomb diamond N+3 we extract an addition energy of $E_{add} = 0.98$meV (averaged from both arms of the diamond). Fainter lines outside of the diamond running parallel to its edge and terminating at the next highest diamond indicate transport through excited states [101], from which we obtain $\Delta E = 0.31$meV. Subtracting this from the addition energy yields a charging energy of $E_c = 0.67$meV, which is smaller than the ~ 1.2meV obtained from our initial estimate. This suggests once again that the series plate capacitor model breaks down for small dots. Recalculating the dot area based upon this new single particle energy spacing gives us an estimated quantum dot occupancy of ~ 18 holes in the N+3 state. This analysis provides an estimate on the lower bound of the quantum dot size and lies upon the assumption that the excited state comes from the same orbital as the corresponding Coulomb diamond and that the single particle spacing is not equal to zero.

The charging energies, single particle level spacings and corresponding leverarms for the remaining diamonds are extracted and shown in Table 6.3. Going from N+3 to N we see a general increase in the single particle level spacing towards lower dot occupancy, indicative of a small dot approaching the few-hole limit. For diamond N the charging energy is $E_C \sim 0.813$meV and from the excited state spacing $\Delta E \sim 419\mu$V, using $\Delta E \sim \pi\hbar^2/m^* l^2$, we roughly estimate the dot diameter to be $l \sim 100$nm at the 2DHG 110nm below the metal surface gates, where we use a value of $m^* \sim 0.5$ [169].

Occupancy	ΔV_p	E_C	$\alpha = \Delta V_{SD}/\Delta V_p$	ΔE
$N+2$	31mV	0.93mV	0.040	300μV
$N+1$	26mV	0.89mV	0.045	290μV
N	30mV	0.81mV	0.041	420μV

Table 6.3: Table of charging energies, leverarms and single particle level spacings obtained from the Coulomb diamond occupancies as labeled in Fig. 6.23.

In comparison, both our charging energy and single particle spacing is smaller that reported in recent literature i.e. $E_C \sim 1.6$meV and $\Delta E \sim 0.5$meV respectively [266], hence our estimated dot size is slightly larger, but of similar magnitude to $l \sim 100$nm reported by Tracy *et al.* [266]. Our smaller charging energy compared to Tracy *et al.* could be due to the difference in the shape of the confining potential between the two designs as discussed in the simulation Section 6.4. Our Sunbeam design tends to yield a shallower dot with a broader confining potential which leads to a smaller energy level spacing and hence reduced charging energies.

Source-drain bias measurements combined with charge sensing also allows us to gain further insight into the symmetry of the quantum dot tunnel barriers and their relative tunneling rates. When comparing the two arms of the equivalent Coulomb diamond in the charge sensor panel Fig. 6.24, at higher occupancies, the arm with a negative slope is dominant, whilst the arm with a positive slope is barely visible, despite it showing up in the quantum dot map. This effect can be explained in terms of the source (drain) tunnel barriers into (out of) the dot, as illustrated in Fig. 6.25. Panel (a) depicts a schematic source drain bias map similar to that introduced in Chapter 2.4.2 but adjusted for holes, which (unlike electrons) are sourced from the drain. Here the tunnel barriers are even, such that the tunnel rate of a hole from the source reservoir into the dot Γ_S, is equal to the tunnel rate from the dot into the drain reservoir Γ_D. A schematic energy diagram is given in Panel (b), showing alignment of the quantum dot ground states (GS) with respect to the source and drain electrochemical potentials as marked in panel (a). The negative slope (solid red circle) corresponds to the GS(N+1 $\leftrightarrow$ N) transition, whilst the positive slope (open blue circle) corresponds to GS($N \leftrightarrow N-1$). As the tunnel rates between the two barriers are similar, the hole spends an equal amount of time in both N+1 and N states,

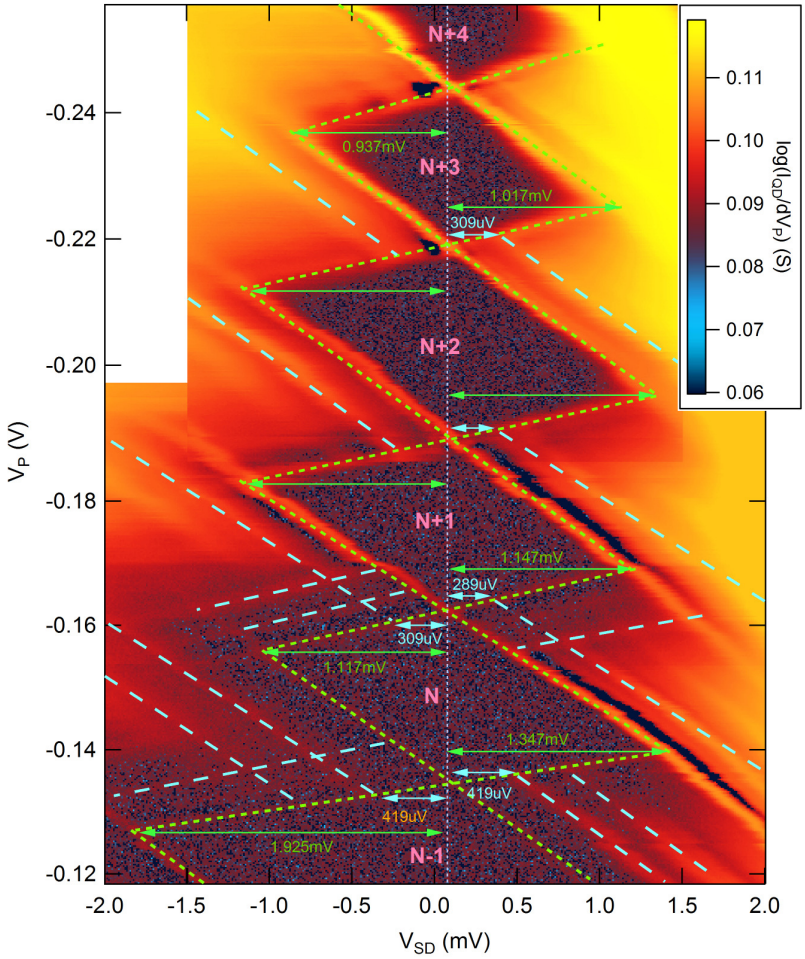

Figure 6.23: Source-drain bias spectroscopy starting with the last 3 Coulomb blockade peaks with corresponding states labelled in pink in Fig. 6.22a. The colour axis represents (a) log plot of differential conductance directly through the dot,versus plunger gate voltage along the y-axis and dc source-drain bias voltage on the x-axis. Dashed green lines highlight the Coulomb diamonds formed by the ground states and excited states are marked in longer period dashed blue lines. For this measurement $V_{LT\&RT} = +0.18\text{V}$, $V_{LB} = -0.51\text{V}$, $V_{RB} = -0.39\text{V}$ and $V_Q = -0.415\text{V}$.

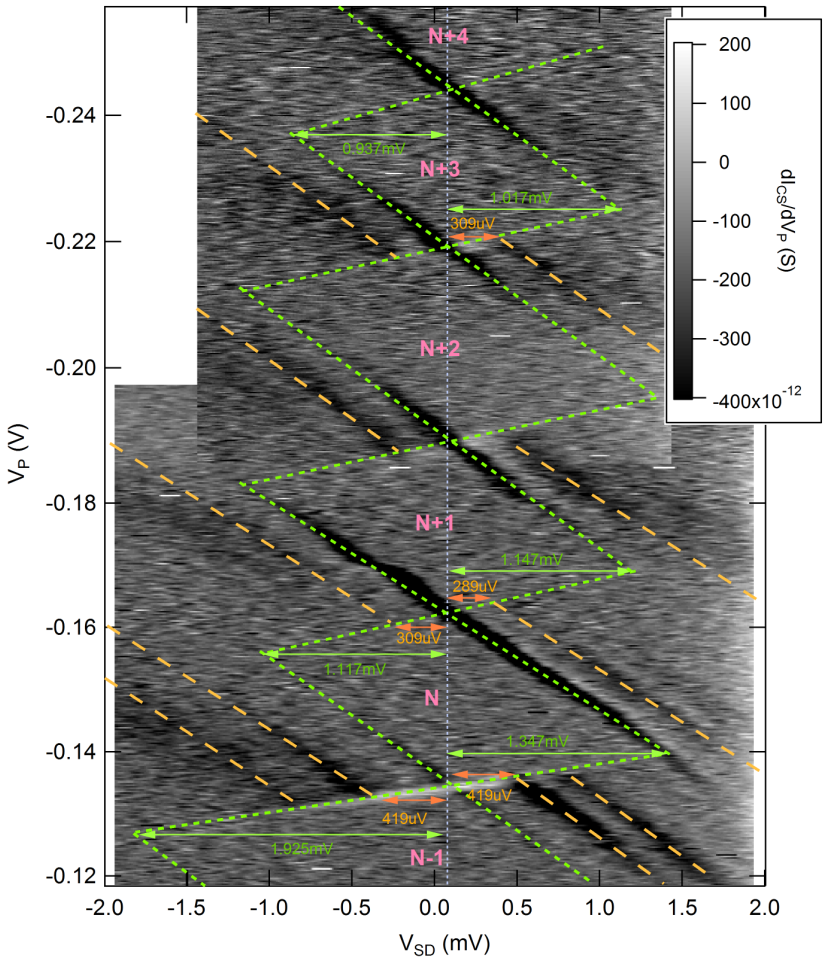

Figure 6.24: Derivative of differential conductance through the charge detector, corresponding to the dot conductance map in Fig 6.23. The derivative was taken with a moving average window of 13 datapoints to enhance the weaker signal of the excited states. Source-drain bias spectroscopy starting with the last 3 Coulomb blockade peaks with corresponding states labelled in pink in Fig. 6.22a. The charge sensor conductance is plotted against plunger gate voltage along the y-axis and dc source-drain bias voltage on the x-axis. Dashed green lines highlight the Coulomb diamonds formed by the ground states and excited states are marked in longer period dashed orange lines. For this measurement $V_{LT\&RT} = +0.18\text{V}$, $V_{LB} = -0.51\text{V}$, $V_{RB} = -0.39\text{V}$ and $V_Q = -0.415\text{V}$.

$t_{N+1} \sim t_N$ for the positive slope. The same goes for the negative slope $t_N \sim t_{N-1}$, and both arms of the diamond exhibit similar signal amplitudes in the charge detector at finite source drain bias.

On the other hand, Fig. 6.25c illustrates what happens when one tunnel barrier is less transparent than the other, similar to the data in Fig. 6.24 and the equivalent energy diagram is given in panel (d). Since the drain tunnel barrier is much thicker than the source barrier, it takes a longer time for a hole to tunnel out of the dot than it does to tunnel in, $\Gamma_S \gg \Gamma_D$ resulting in the dot spending more time in the higher occupancy state of the transition. This scenario is known as 'source resonance'. In the source-drain bias schematic shown in panel (c), for the case of the positive slope (open blue circle) rather than transitioning between $N \leftrightarrow N-1$ from the dot to the drain, the hole spends more time in state N, causing this arm to remain virtually invisible, resulting in a series of diagonal lines with a negative slope. The larger Γ_S also increases the capacitive coupling between the source to the dot, compared to the dot and the drain $C_S \gg C_D$, seen as a brighter negative slope in the Coulomb diamond compared to the positive slope in the quantum dot conductance Fig. 6.23.

In the charge sensing panel Fig. 6.24, at higher occupancy the areas where the excited states occur appear as broad, smeared out, dark lines. This could be caused by two factors; firstly although the dot is small there are still a fair number of holes in the dot which reduces the excited state spacing, make them harder to resolve, especially if the quantum dot potential is shallow and wider, rather than tall and deep (as in the case of the nanowire dots described in Chapter 6.2.2). The second is by uneven tunnel barriers. As the plunger gate couples to its neighbouring barrier gates RB and LB, increasing its bias slightly may help to define the dot confining potential and tunnel barriers further, as seen towards lower occupancies in both Fig. 6.23 and Fig. 6.24. The charge sensor map, like the quantum dot map, also reflects the increase in both the charging energy and excited state spacing towards lower dot occupancy, with better resolved excited states showing up in the charge sensor map parallel to the $N-1$ diamond.

Fig. 6.24 also exhibits a change in behaviour of the relative tunneling rates between

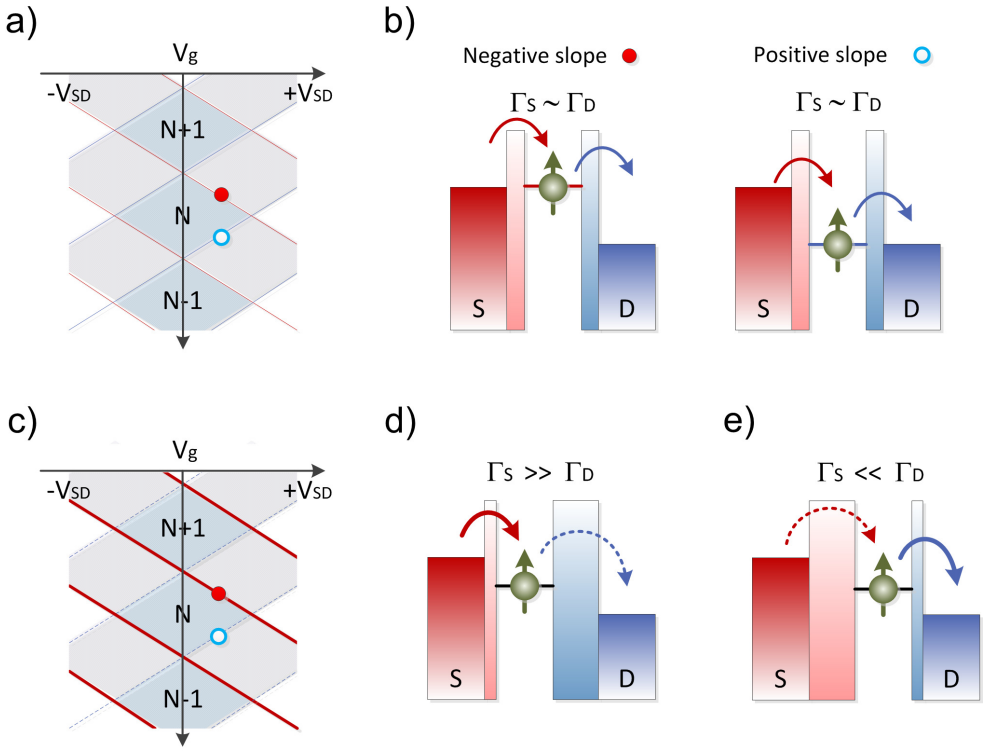

Figure 6.25: Effect of tunnel barriers upon the charge detector signal during source drain bias spectroscopy. (a) Hole-based source drain bias schematic of the charge sensor for even tunnel barrier rates $\Gamma_S \sim \Gamma_D$. The negative slope marked with a filled red circle corresponds to GS(N+1 $\leftrightarrow$ N) and the leftmost diagram of panel (b), where the dot energy level is aligned with the source electrochemical potential. The positive arm with an open blue circle corresponds to GS($N \leftrightarrow N-1$) and the rightmost diagram of panel (b) where the dot energy level is aligned with the drain. (c) Source drain bias schematic for the case of source resonance where $\Gamma_S \gg \Gamma_D$, characterized by a dominance in the negative slope of the diamond and undetectable positive arm. (d) The equivalent energy diagram schematic for source resonance in (c), where holes spend more time in the higher occupancy state of the transition. Panel (e) shows the energy diagram for the opposite scenario of drain resonance $\Gamma_S \ll \Gamma_D$, where holes spend more time in the lower energy state of the transition, leading to the source drain bias diamond exhibiting a dominant positively sloped arm and non-existent negative arm (not shown).

the source and drain reservoirs and the dot, for the transition $N{+}1 \rightarrow N$ compared to $N \rightarrow N{-}1$. For the $N{+}1 \rightarrow N$ diamond, once again source resonance is observed, characterized by a dominant negative slope and the absence of the positively sloped arm. On the other hand, between the N to $N{-}1$ diamonds, the opposite occurs i.e. the light colored positive slope is more dominant than its negative slope counterpart, despite the positive slope not showing up in the dot conductance map. In this case we have drain resonance as illustrated in Fig. 6.25e, where $\Gamma_S \ll \Gamma_D$ and the holes prefer to remain in the lower occupancy state of the transition. Here for the $N \leftrightarrow N{-}1$ transition in the positive arm, the hole tunnel out quickly to the drain and the dot spends more time in the $N{-}1$ state. For the $N \leftrightarrow N{-}1$ negative arm transition, holes take a longer time to tunnel from the source onto the dot and the dot once again spends more time in the $N{-}1$ state. In this region parts of the negative slope still remain visible in the charge sensor map, indicating more symmetric tunnel barriers compared to those with occupancies greater than $N{+}1$. Although the excited states running parallel to the negative slopes are still present, barely any excited states running parallel to the positive slopes can be observed.

Preliminary results in perpendicular field

After characterizing the dot at zero field, we now turn our attention to some preliminary measurements taken at a fixed perpendicular magnetic field of $B_z = 3\text{T}$.

The spin behaviour of the excited states in the hole dot, at $B_z = 3\text{T}$ was studied by repeating the source drain bias measurement over the last two diamonds $N{+}1$ and N, shown in Fig. 6.26. Here we observe a shift in the energy spectrum towards higher occupancy by $\Delta V_P = 0.013\text{V}$ compared to the zero field picture - only the tip of the $N{-}1$ state falls within a map over the same plunger gate voltage range, whilst at 3T the full $N{+}1$ diamond can be seen. This can be potentially be due to the magnetic field effect upon the orbital component of the holes, which increases the charging energy and energy spacing between holes in dot, shifting the Coulomb blockade peaks to more negative V_P values.

In Fig. 6.26 the signal through the dot is significantly diminished in field due to an

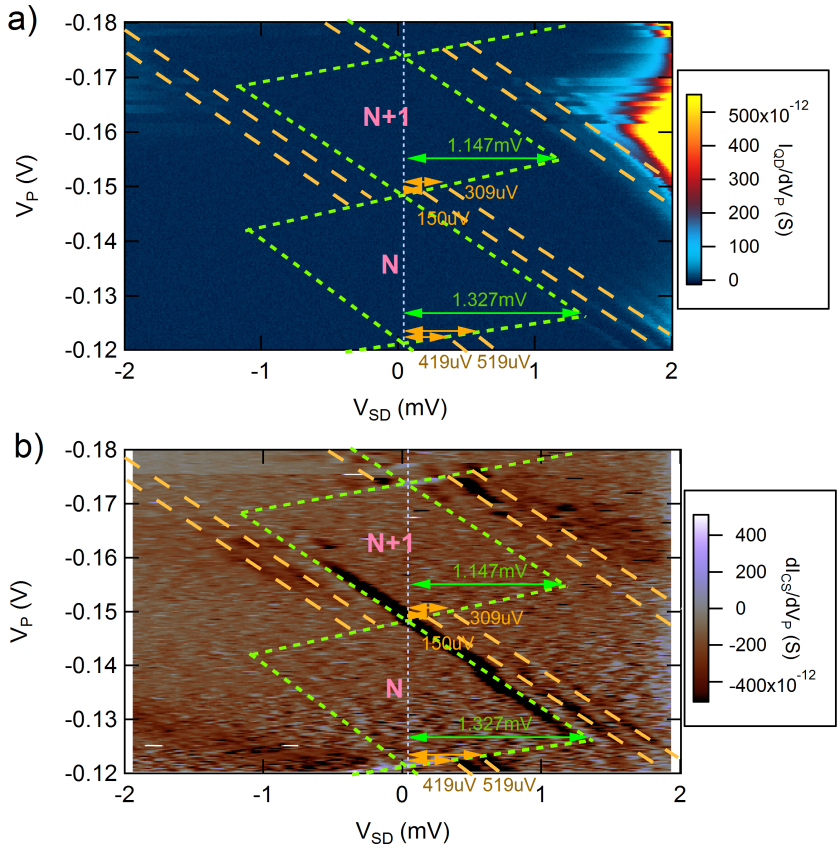

Figure 6.26: Source drain bias spectroscopy at 3T, over the same gate voltage range as Fig. 6.23. Panel (a) plots quantum dot differential conductance against plunger gate voltage (y-axis) and source drain bias (x-axis), and (b) maps the corresponding charge sensor derivative of the signal, taken with a moving average of 13 datapoints. Dashed green lines indicate ground states and orange lines the excited states.

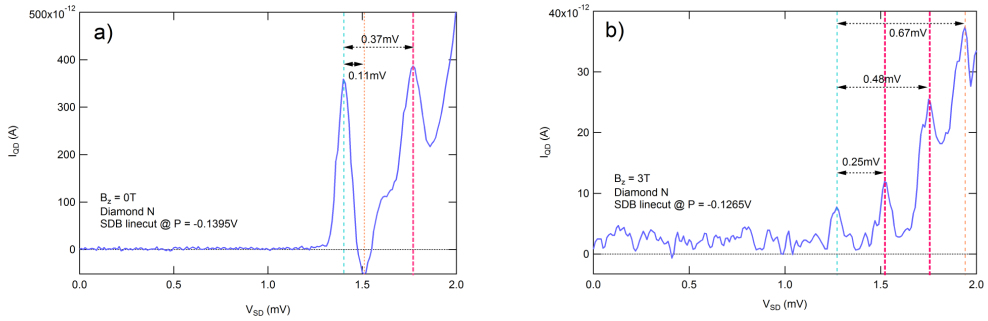

Figure 6.27: Source drain bias spectroscopy linecuts to compare movement of ES. Panel (a) taken at 0T is a linecut of raw quantum dot current along positive V_{SD} at the intersection of the 2 ground states, forming the rightmost corner of diamond N extracted from Fig. 6.23. Panel (b) is an equivalent linecut taken at 3T, of raw quantum dot current along positive V_{SD} at the rightmost corner of diamond N from Fig. 6.26a. In both plots, dashed green lines mark the position of the ground state features and orange lines the excited states.

increase in ohmic contact resistance, resulting in a much lower signal to noise ratio. As a result only the more dominant, source resonance negative slopes of the Coulomb diamond exhibit excited states. Fig. 6.27 shows the linecut along V_{SD} taken at the rightmost corner of diamond N, at the intersection of the two ground states (dashed green) for $B_z = 0$T and $B_z = 3$T respectively. The second excited state 0.37mV (dashed red) at $B = 0$T in panel (a) appears to split into two peaks in panel (b) shown in dashed pink at 0.25mV and 0.48mV. If we neglect orbital effects, this suggests that the two excited states have opposite spins. From the relation $\Delta E = \frac{1}{2} g \mu_B B$ we obtain a g factor of $g^*_{zz} = 2.7 \pm 0.52$. This value of the out-of-plane g^* is lower than the $g^*_{zz} = 7.2$ predicted by theory, but is consistent with optical measurements of hole g factors performed on confined excitons [88, 230, 271]. It would be interesting to conduct further studies into the g factor, such as introducing a parallel field by performing an situ rotation of the sample whilst sweeping the source-drain bias to determine how the split peaks and hence the g factor evolves with magnetic field orientation, as well as to investigate the separation of orbital and spin contributions. For this to be done, the setup and the quantum dot device needs to be optimized further. Since both the dot and charge sensing signal is significantly reduced in field, the increased electrical noise and thermal load incurred during rotation meant that it

was difficult to resolve the excited states from the background noise.

Going to the last hole

To determine the exact number of holes in the dot as opposed to a crude estimate based upon the dot energy spectrum, we squeeze the dot down to the last hole using a combination of gates to maintain the relative shape of the dot during the process. From the initial barrier maps in Fig. 6.21, we showed that if the bias on the plunger gate is too large the single dot fragments into a double dot. To prevent this from occurring, P was held fixed whilst the barrier gates LB and RB were swept simultaneously using the same increment (due to their similar α values), but with an offset of +0.12V in RB. To maintain the strength of the separating barrier confining potential, LT and RT were stepped simultaneously with increasing bias and the charge sensor Q was compensated after each increment in LT&RT. The resulting colour map is given in Fig. 6.28.

A series of straight lines starting from state N are observed in both the dot Fig. 6.28a, and charge sensor in panel (b). The quantum dot lines become unresolvable beyond $N-2$, however the features in the charge sensor signal continue until the last hole has been reached, beyond which there is no visible signal, which is the main goal of this chapter. The straightness of the charge sensing lines in panel (b) indicate that the single dot was maintained down to the last hole without fragmenting, where state N corresponds to hole number 8.

At $V_{LT\&RT} = +0.22$V, Q has been pulled back to its maximum operating value and beyond this the charge sensor signal diminishes as the increased bias on the separating barrier pinches-off the charge detector channel. Around $V_{LT\&RT} = +0.18$V we observe switching behaviour, followed by a small drift in the features of the colour map, probably due to fluctuations caused by a nearby charge trap or an additional parasitic dot.

We also observe that the transition between $0 \leftrightarrow 1$ exhibits greater jitter compared to the other transitions as the tunnelling time into (out of) the last hole state varies significantly and the spread of the jitter decreases with increasing bias on LT&RT.

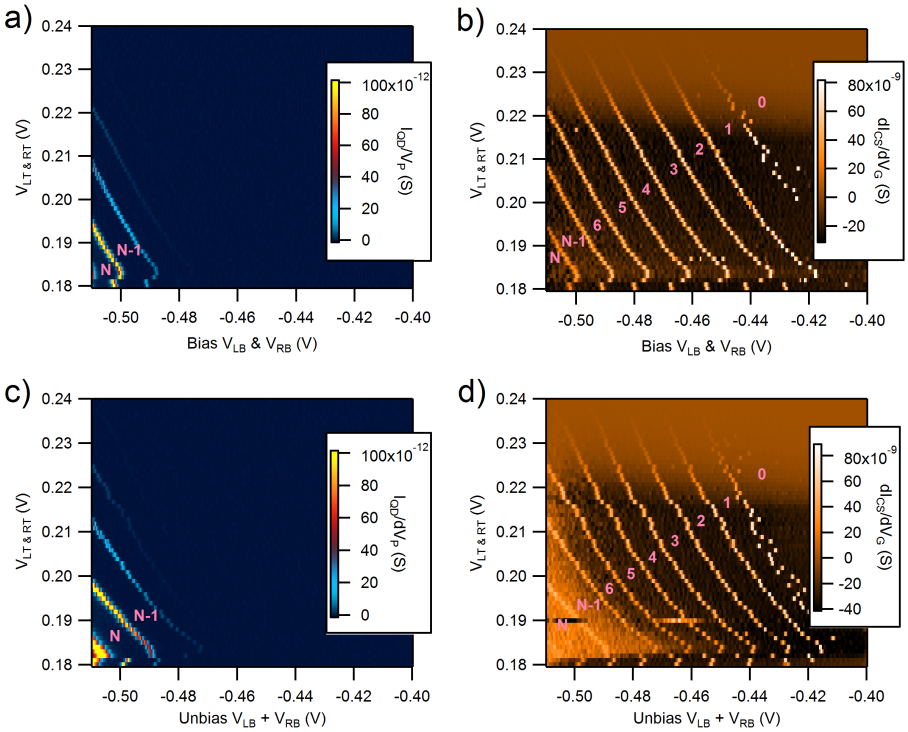

Figure 6.28: Colour maps of (a) conductance through the dot and (b) the corresponding conductance derivative through the charge sensor, as the dot is squeezed down to the last hole. LT and RT were biased simultaneously starting at $V_{LT} = V_{RT} = +0.18$V, whilst LB and RB were swept simultaneously starting at $V_{LB} = -0.51$V and $V_{RB} = -0.39$V. P was kept fixed to start from dot state N. The corresponding color maps for the unbias sweep direction for (a,b) are given by (c,d) respectively.

Such jitter and hysteresis behaviour that only appears towards the few-N regime has been associated with the presence of a secondary dot, whose occupancy affects the energy levels of the main dot under study and hence its tunnel rate [224, 294]. In this case of a single dot, a similar effect could be caused by the presence of a small, nearby unwanted charge trap or additional parasitic dot. We tried different combinations of biasing voltages on the gates in an attempt shift the quantum dot away from the area of charge, but were unable to completely remove the jitter in the $0 \leftrightarrow 1$ transition.

From Fig. 6.28a, the shell filling as a function of occupancy over the last 5 holes at a fixed $V_{LT\&RT} = 0.22$V is plotted in Fig. 6.29. Gate voltage was converted into an estimated addition energy by summing the alpha factors for gates being swept (LB and RB) from Table 6.2. Note, this conversion does not take into consideration the rapidly increasing charging energy towards the last hole and thus only provides a lower bound estimate on the actual charging energy of the dot at the last hole. From this picture, we observe the general trend of a decrease in addition energy towards higher occupancy, indicating a smoothly increasing capacitance as the dot area is increased with gate voltage. We do not observe any distinct enhancement in energy at certain values of N, that is indicative of a magic number sequence, such as that reported in electron dots (see Section 6.2.4).

The lack of a distinct magic number sequence, combined with the comparatively few, faint excited states suggests the shape of the dot is shallow and wide, with smaller orbital spacings, consistent with the larger effective mass of holes ($m^* \sim 0.2 - 0.5$) [169, 284] compared to electrons ($m^* = 0.067$). One possible route to obtaining orbital level spacings similar to those seen in electron systems, is to use shallower wafers with the 2DHG $<$ 100nm from the surface metal gates, which should help to decrease the size of the electrostatic confinement potential and reduce the thickness of the tunnel barriers for greater tunability.

Comparing the forward gate sweeps in Fig. 6.28(a,b) to the reverse sweeps Fig. 6.28(c,d), reveals a small hysteresis between sweep directions, which is most pronounced towards lower bias voltages on LT&RT ($V_{LT\&RT} = 0.18 - 0.19$V). This hysteresis also shows up as a small, constant offset ($\sim 24.8\mu$eV) in addition energy, in Fig. 6.29, when com-

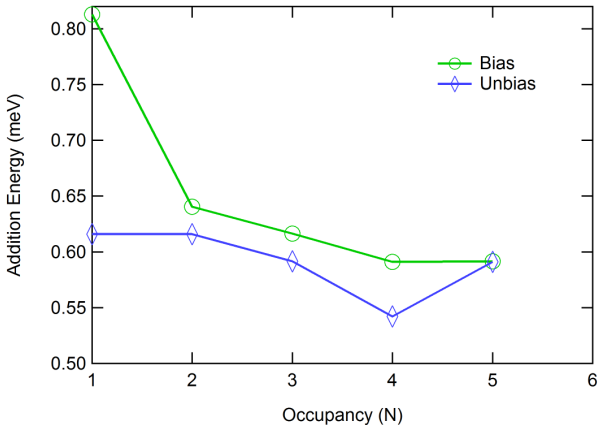

Figure 6.29: Shell filling sequence extracted from Fig. 6.28b for decreasing occupancy (green circles), and (d) for increasing occupancy (blue diamonds) at a fixed $V_{LT\&RT} = +0.22$V. The leftmost marker indicates the point where the first hole enters the dot and the number of holes N, increases by one for each increase in N. The y-axis marks the lower bound on the addition energy, calculated by converting gate voltage into energy from the alpha factors in Table 6.2, assuming the coupling remains the same all the way down to the last hole.

paring the forward gate sweep (green circles) to the reverse trace (blue diamond). One reason for this hysteresis could be due to the formation of a surface layer of charge between the GaAs surface and the AlOx dielectric as described in Chapter 3.4, which leads to a hysteresis in the 4-terminal conductance across a 2D hall bar. This hysteresis only appeared at a top gate of -1.6V and higher for wafer W0640. However, despite selecting a lower top gate voltage of -1.4V for this experiment, it may be possible that a very small layer of charge may have been induced at the surface, which is not enough to cause hysteresis in the large 4-terminal conductance, but enough to affect the Coulomb blockade peaks and charge sensing features in the few-hole regime.

To test this, we reduced the top gate bias (significantly) to -1.0V and retuned the dot. Over the last 5 holes, we found that there was virtually no hysteresis between the bias and unbias sweeps, except for the jitter in the $0 \leftrightarrow 1$ transition, which still remained. As the small dot pattern was designed to operate at a higher top gate voltage, it was difficult to obtain a set of operating voltages which allowed current to flow directly through the dot whilst maintaining well defined tunnel barriers. At this point it was decided that it was better to stop and re-design the quantum dot, for

operation at a lower top gate for the given dielectric type and thickness.

6.6 Conclusions and Future Work

In summary we have successfully fabricated and characterized an induced, few-hole single quantum dot, down to the last hole with QPC charge sensing. For the first time we have observed excited states through the charge sensor via source drain bias spectroscopy and showed that they split in perpendicular field. It would be interesting to perform further magnetic field experiments to characterize the spin filling of the last few holes, and study the influence of the magnetic field upon the orbital component of holes with a heavier effective mass and the spin response in a parallel field. In the process we discovered that the quantum dot geometry could be optimized further to operate with greater tunability at a lower density, to eliminate hysteresis stemming from a surface layer of charge.

To facilitate magnetospectroscopic studies of the last few holes using the charge detector where traditionally direct current through the dot was used, some modifications to the current quantum dot design to improve the tunnel barriers of future devices could include: (1) The use of heterostructures with shallower 2DHGs ($<$ 100nm from the wafer surface) combined with thinner metallic gates. This allows for the creation of a smaller but deeper dot with steeper and sharper tunnel barriers to improve the resolution of the finer featured excited states, increase the tunability of the tunnel barriers, as well as increase the orbital level spacings to compensate for the heavier effective mass of holes. (2) Potentially redesigning the dot pattern to run with the separating barrier LT&RT and two gates, such as LB and RB and remove the third gate to prevent the single dot fragmenting into two dots, or use an equivalent double-dot pattern instead. (3) Rather than using a single global top gate, one could consider breaking up the top gate into different segments, to allow for independent control of the dot density and the 2D source and drain reservoirs. Splitting the top gate into localized regions may also be done in such a way to reduce screening between the dot and charge sensor, as well as enable rf-measurements to be performed.

Chapter 7

Summary and Future Directions

7.1 Summary of thesis

In this thesis we have explored ballistic transport in GaAs low-dimensional systems, namely two-dimensional hole systems and quantum dots. We now present a general conclusion of the research conducted.

In Chapter 4 we observe the effect of an unusual non-collinear spin polarisation due to the presence of off-diagonal components in the gyromagnetic tensor, by applying an in-plane magnetic field and generating a net spin polarization perpendicular to the sample plane. Tilted-field measurements of magnetoresistivity oscillations were performed in a low-symmetry (311)A GaAs quantum well. We study the changes in spin splitting when the in-plane field is oriented along the high-symmetry $[01\bar{1}]$ crystal direction, compared to the low-symmetry $[\bar{2}33]$ direction. Along the high symmetry crystal axis, the SdH oscillations are symmetric with each other for both $+\theta$ and $-\theta$, desite a change in sign of the ratio $\pm B_x/B_z$. In contrast, when the in-plane field is applied along the low-symmetry direction, the SdH oscillations are distinctly asymmetric and appear out-of-phase between corresponding $+\theta$ and $-\theta$ traces at high in-plane fields. This unusual behaviour is due to a non-zero off-diagonal element g^*_{xz} which couples the in-plane field to the out-of-plane spin, and is present only along the low-symmetry crystal direction of a 2D hole system in a zinc blende crystal structure.

In Chapter 5 we further investigate the complex spin dynamics of 2D holes, show-

ing that the presence of such non-collinear behaviour observed in Chapter 4 can be explained by the non-abelian spin evolution of holes in tilted magnetic fields, due to mixing between the light hole and heavy hole subbands. The phase of the SdH oscillations were extracted as a function of tilt angle and compared to two theoretical models - the abelian Berry and the non-abelian gauge field. We demonstrate that the anisotropic phase evolution observed between $\pm\theta$ along the low-symmetry direction, is in good agreement with the paradigm of non-abelian gauge fields, even after significant variation of the fitting parameters.

Chapter 6 focuses upon the fabrication and characterization of lateral, gated, induced quantum dots, to create a device which can isolate single charge and spin states for transport studies. By replicating a standard few-N quantum dot pattern, with an integrated QPC charge sensor into an induced architecture with a 160nm deep heterojunction and Polyimide insulating layer, we begin by fabricating a small electron quantum dot. During characterization we discover that although we can form a dot with an estimated < 33 electrons, the electrostatics of a dot within an accumulation mode structure with a global top gate, are different to those in a modulation doped dot and the charge sensor lacked sensitivity due to strong coupling to the global top gate. After performing simulations in Nextnano++, we adapted the design to increase the sensitivity of the charge detector, including using a shallower 2D gas, thinner insulating layer with a stronger dielectric constant and spacing out the gates evenly to increase their tunability. We finally present preliminary results from a hole quantum dot with the adapted small dot design with an estimated length of $\sim$ 50nm down at the 2DHG. Using this pattern we are able to tune the dot down to the last hole, verified by an operational charge sensor with a step height of 12% versus its travel in gate voltage. We also present some initial source-drain bias measurements in a perpendicular magnetic field observed the splitting of an excited state.

7.2 Future work

In chapter 4 and 5 we have for the first time experimentally demonstrated non-collinear spin behaviour in a 2D hole system, and clarified the mechanism driving the asym-

metric spin-splitting of holes in a low-symmetry crystal axis. Despite this, much still remains unknown about the interplay between confinement and the crystal lattice symmetries and their influence upon the heavy hole, light hole spin dynamics.

It would be interesting to repeat the experiment with a 2D sample possessing both a front-gate and a back-gate, to allow us to control the density and keep it constant whilst independently tuning the confining potential and the Rashba SO. The experiment could also be repeated at different densities and different confining potential symmetries. Such an experiment would be best performed in a 3-axis vector magnet system which would allow for independent control over all 3 field components. On the theoretical front, further investigation is required to develop a practical model of the bandstructure of holes in tilted magnetic fields. Although we have presented measurements probing the off-diagonal g^*_{xz} component of the g tensor, much still remains unknown about its counterpart the g^*_{zx} term.

Another direction of curiosity would be to perform the same study over samples with different quantum well thicknesses and hence energy spacings between the light-hole and heavy hole subbands, which may lead to different LH-HH mixing probabilities and compare their spin behaviour to that seen in the 20nm quantum well.

In Chapter 6 we present preliminary results on induced small dots with charge sensing, operating within the few-N regime, with different gate geometries. Although we have been able to isolate and detect single holes, the geometry of the quantum dot design can still be optimized for greater tunability of the tunnel barriers. Additionally it would be interesting to try different dot geometries: including splitting the top gate into different regions to allow for independent tuning of the charge detector circuit and the quantum dot circuit. This will also enable rf and pulse-gate measurements to be performed and pave the way for further studies into the unusual spin behaviour of such 3/2 particles.

Appendix A

Low temperature experimental apparatus

A.1 Kelvinox 100 dilution refrigerator and magnet

All experiments reported in this thesis were performed in a Kelvinox 100 dilution refrigerator from Oxford Instruments, with a 15T superconducting magnet [123] and an *in situ* rotation system [2], which allows the sample to be configured in differing orientations with respect to the field, and rotated whilst maintaining temperatures below 100mK [299]. For full details on the design and specifications of the rotation system, its integration into the dilution refrigerator and preliminary test results, please refer to Ref. [297].

The K100 is a type of pumped 3He/4He wet dilution refrigerator and is the main apparatus used to obtain base temperatures as low as 20mK for studying semiconductor nano-structures. A photo of the K100 fridge insert, focusing upon its main operating components is shown in Fig A.1a together with the rotation stage at the end of the coldfinger. Part (b) is a corresponding general schematic drawing of the K100 fridge insert with the major stages of the fridge labelled. The schematic illustrates how the fridge insert sits within the cryostat housing the liquid Helium and the alignment of the sample holder within the bore of the superconducting magnet.

Once the sample is mounted in its holder on the rotation system at the end of the

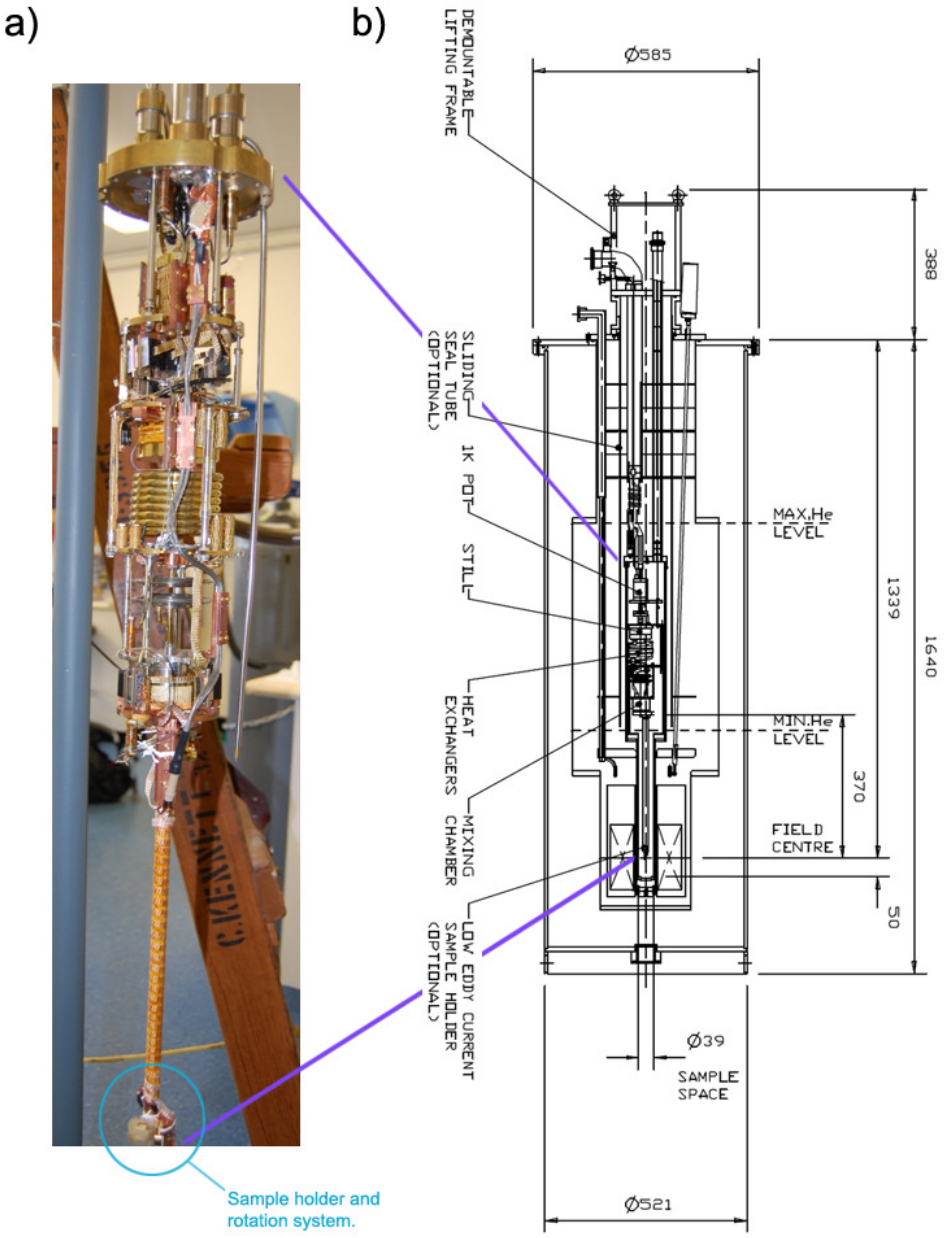

Figure A.1: K100 dilution refrigerator layout. (a) Photo of the main working components of the fridge with the rotation system attached to the end of the coldfinger, upon which the sample is mounted. (b) Corresponding K100 general fridge schematic sitting within the cryostat, with the major fridge components labelled, from Oxford Instruments [123]. Dimensions are given in millimeters.

coldfinger, the radiation shield followed by the outer vacuum can (OVC) are bolted in place over the insert and sample holder and the fridge is slowly lowered into the cryostat containing the liquid Helium. Once fully lowered, the sample sits at the field center of the superconducting magnet. Initially the sample equilibrates with the temperature of the liquid helium (4K), during which all the initial system checks such as rotation calibration and sample-to-field alignment are performed, see Appendix B. Once completed, the sample is cooled to base temperature ($\sim$ 20mK).

This cooling to base temperature is a process unique to dilution fridges and is achieved through the phase separation of 3He/4He mixture in the mixing chamber, illustrated in Fig. A.2. When a mixture of 3He and 4He is cooled below a critical temperature of 0.87K, it will separate into 2 phases; where the lighter 'concentrated' phase at the top of the mixing chamber is rich in 3He, whilst the heavier 'dilute' phase at the bottom is 4He rich. This results in the 3He from the concentrated phase 'evaporating' down into the dilute phase. Since the specific heat of 3He is larger in the dilute phase than it is in the concentrated phase, cooling is achieved at the phase boundary [123].

To maintain cooling power, the process must be continued/repeated. To achieve this, the 3He is extracted from the dilute phase and returned to the concentrated phase, thus maintaining dynamic equilibrium. This is done by sucking up and pumping on the surface of the dilute phase mixture (containing both 4He and 3He) in the still. The still is kept at a temperature of 0.6-0.7K so the vapour pressure of 3He is much greater than that of the 4He, causing the 3He to preferentially evaporate [123]. As result, pumping on the still reduces the concentration of 3He, creating an osmotic pressure difference between the mixing chamber and the still, driving the 3He flow across the rich-dilute phase boundary in the mixing chamber. The 3He vapour is pumped out of the still and into the condenser located within the 1K pot. The condenser is cooled by the 1Kpot and the 3He recondensed back into the mixing chamber, forming the 'concentrated' phase and the cycle repeats itself.

To cool the condenser, the 1K pot forms a part of a separate subsystem where the liquid 4He from an external reservoir (in this case, the main bath of the cryostat) is

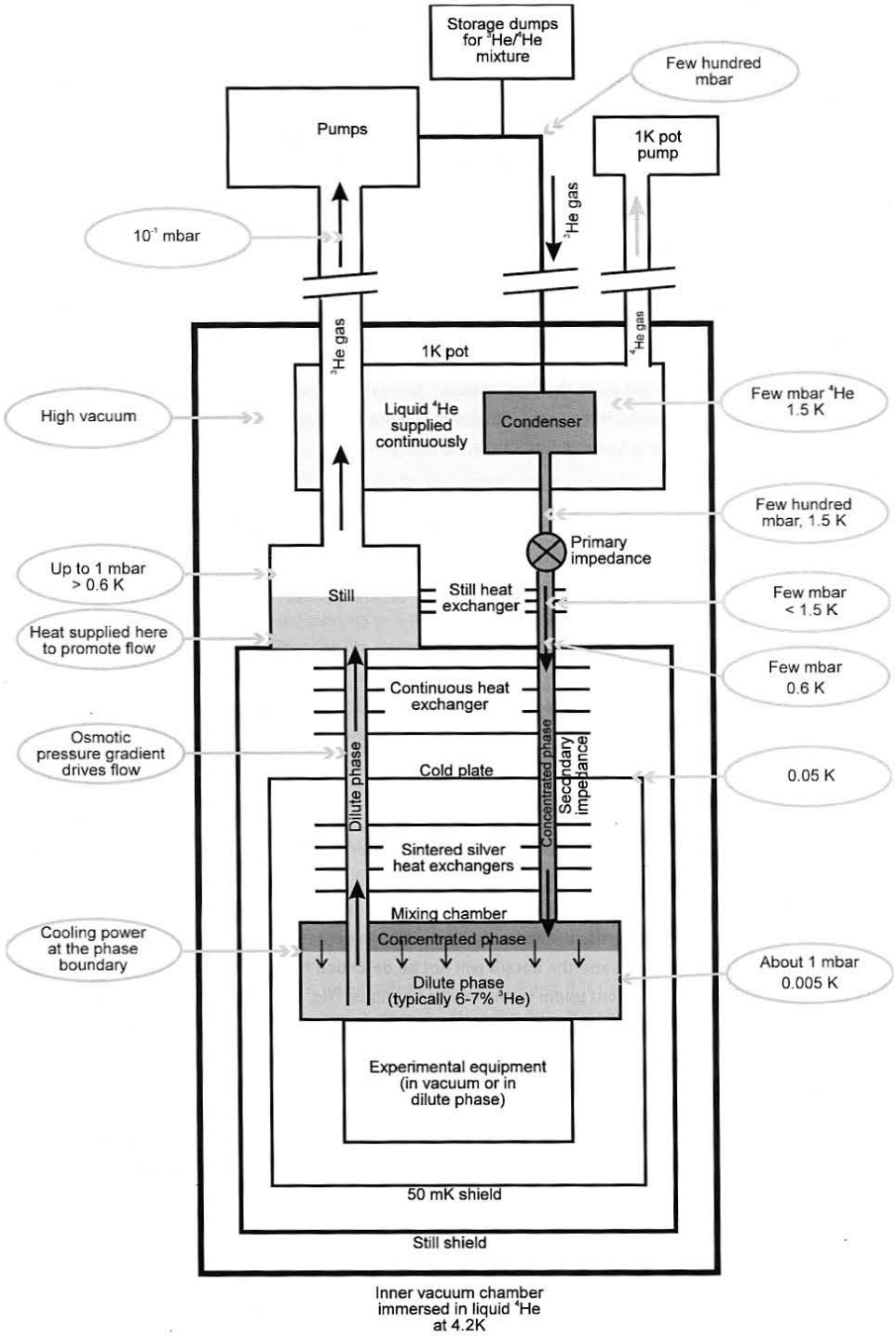

Figure A.2: Schematic illustrating the working principle of the Kelvinox 100 dilution refrigerator. Picture reproduced from Ref. [123].

drawn up into the 1K pot. By pumping on the 4He vapour, the temperature of the 1K pot is cooled to below 1.5K. This cools the condenser, allowing the 3He vapour inside it to condense and the cooling cycle to be maintained, such that the fridge eventually reaches temperatures as low as 20mK. As the fridge is a closed cycle system, this cooling power can be maintained indefinitely as long as there is a continuous supply of 4He from the main bath of the cryostat [123].

Appendix B

2D hole systems measurement setup

B.1 Sample and rotator angle calibration

The angle readout of the home built rotation system [299] was first calibrated against the magnetic field to ensure the accuracy of the sample's orientation with respect to the total magnetic field for any given tilt angle θ. For more details of the measurement apparatus see Appendix A.1. This was done by measuring the Hall voltage across the 2D device under study. Fig. B.1 plots the Hall voltage whilst the sample is rotated between the parallel and perpendicular orientations with respect to a total field of $B_{tot} = \pm 0.1$T. Fits were performed in the region where the Hall voltage changes sign and $\theta = 137.18°$ found to be the angle at which the sample is parallel to the field. The corresponding angle at which the Hall voltage reached its maximum value, indicating the sample was fully perpendicular to the total field was 227.18°. This preliminary calibration procedure was performed at 4K.

B.2 Magnet hysteresis characterization and correction

To check the 15T superconducting magnet in the K100 dilution refrigerator for hysteresis and characterize the hysteresis, the sample was rotated until the 2D plane was

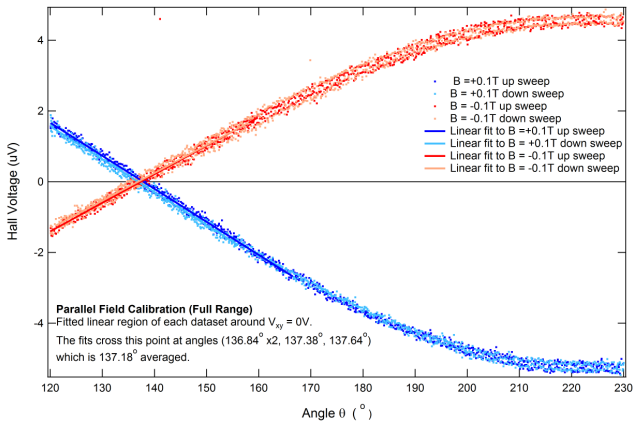

Figure B.1: Angle calibration: plot of Hall voltage at $B_{tot} = \pm 0.1$T as the sample is rotated between the two main positions (and a bit beyond each), perpendicular to the field and parallel to the field. Near the region where the Hall voltage changes sign, $\theta = 137.18°$ is the angle where sample plane is parallel to the field. The corresponding angle at which the sample was fully perpendicular to the total field was 227.18° (max V_h).

fully perpendicular to the total magnetic field. The Hall resistance was measured as a function of perpendicular magnetic field, sweeping through $B = 0$ and graphed in Fig. B.2. For more details of the measurement apparatus see Appendix A.1. This was done for a series of different sweep rates and different target total field values at a temperature of 4K. Panel (a) shows the full sweep range where the hysteresis is only noticeable in the low-field region. Panel (b) zooms into the area around $B = 0$, where the magnitude of the hysteresis is $\sim$ 35mT. We observe little variation in the hysteresis loop between different sweep rates and target values which are symmetric in $\pm B_{tot}$. Since this hysteresis encloses the same loop, upon each run, it is possible to do a correction to account for the hysteresis. The greatest corrections are required for transport measurements taken when the 2D hall bar sample is aligned perpendicular to the magnetic field (compared to parallel).

The hysteresis correction procedure involves averaging the up and down sweeps and mapping the measurement data onto the calibration data via interpolating the number of data points and spacings.

Example code in Igor Pro is given below. Note, these corrected field waves can then be used as is with the low field Rxx and Rxy data, or alternatively, the Rxx and

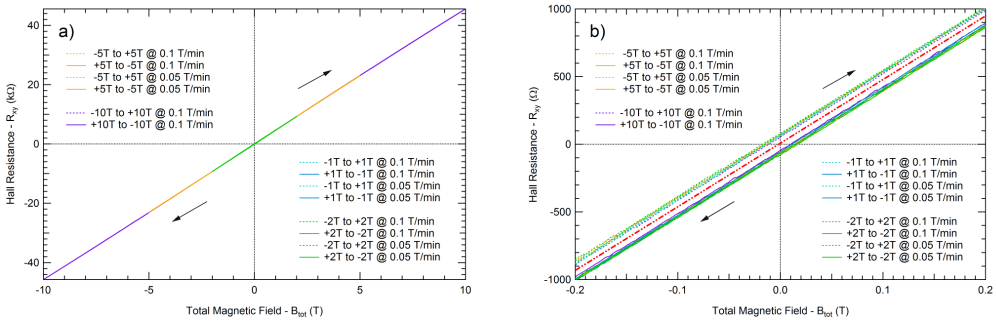

Figure B.2: Magnet hysteresis characterization. Measurements of Hall resistance versus total field, for a series of different field targets ±1T, ±2T, ±5T and ±10T and sweep rates 0.1T/min and 0.05T/min. (a) Shows the full sweep range tested, where the black arrows indicate the sweep direction. (b) Zooms into the center of the hysteresis data from panel (a) around $B = 0$, which exhibits a ±17.5mT hysteresis. The red dashed line marks the average value of the Hall traces.

Rxy data can be interpolated with the corrected B waves.

```
//Copy data waves to be used into a new folder
Duplicate::'2T': RxyUP RxyUP
Duplicate::'2T': RxyDOWN RxyDOWN
Duplicate::'2T': Bdata1 Bup
Duplicate::'2T': Bdata2 Bdown

Duplicate RxyUP interpUP
Duplicate RxyDOWN interpDOWN

//Set x-axis max/min limits of endpoints
setscale/I x -2,2, interpUP
setscale/I x -2,2, interpDOWN

//First create RxyUP data in even spaces of x
//(need Bup to get x-values for RxyUPdataset)
interpUP = interp(x, Bup, RxyUP)
interpDOWN = interp(x, Bdown, RxyDOWN)
```

```
Duplicate/O interpUP interpAvgUpDown
interpAvgUpDown = (interpUP + interpDOWN)/2

//Create waves to house corrected B values
Duplicate/O Bup BcorrUP
Duplicate/O Bdown BcorrDOWN

//Do actual interpolation/correction of B
BcorrUP = interp(RxyUP, interpAvgUpDown, Bup)
BcorrDOWN = interp(RxyDOWN interpAvgUpDown, Bdown)
```

Appendix C

Derivation of the spin-orbit interaction for heavy holes

$\rightarrow$ In a zinc blende semiconductor the hole wave function originates from atomic $p_{3/2}$ orbitals resulting in an angular momentum $J = 3/2$. In the long wavelength approximation, the effective Luttinger Hamiltonian for holes is second order in the hole momentum ($\boldsymbol{k}$) [172],

$$H = \frac{\hbar^2}{2m_e}\left[(\gamma_1 + \frac{5}{2}\gamma_2)k^2 - 2\gamma_2(\boldsymbol{k}\cdot\boldsymbol{J})^2\right] \ . \tag{C.1}$$

Here γ_1, γ_2 are the Luttinger-Kohn parameters; in GaAs $\gamma_1 \approx 6.8$, $\gamma_2 \approx 2.9$ [274]. Due to the confining potential $V(z)$, motion perpendicular to the 2D plane of the heterostructure is quantized, leading to the formation of 2D subbands, where only the lowest subband occupied in the low-temperature experimental regime. Assuming a square well confining potential of width d we have $\langle k_z^2\rangle = \frac{\pi^2}{d^2}$. Since $\langle k_z^2\rangle \gg k_F^2$, we may expand $-(\boldsymbol{k}\cdot\boldsymbol{J})^2 = -k_z^2 J_z^2 + \ldots$, with the leading term becoming diagonal in a basis of states with J_z. Due to the sign of the interaction, states with $J_z = \pm\frac{3}{2}$ (heavy hole) are lower in energy, and the splitting between these and states with $J_z = \pm\frac{1}{2}$ (light hole) at $k_x = k_y = 0$ becomes

$$\Delta_{hl} = \frac{2\pi^2\gamma_2\hbar^2}{m_e d^2} \approx 7.8\text{meV} \ . \tag{C.2}$$

Here we take $d = 20$nm and only the heavy-hole band is populated. We describe this band by the effective spin $s = 1/2$, $|J_z = +3/2\rangle \equiv |\uparrow\rangle$, $|J_z = -3/2\rangle \equiv |\downarrow\rangle$.

The off-diagonal part of $(\boldsymbol{k}\cdot\boldsymbol{J})^2$ in the Hamiltonian (C.1), $(\boldsymbol{k}\cdot\boldsymbol{J})^2 \to \frac{1}{4}\left(k_- J_+ + k_+ J_-\right)^2$, leads to heavy-light hole mixing.

$$\begin{aligned} |\boldsymbol{k},\uparrow\rangle &= \left[|+\frac{3}{2}\rangle + ak_+^2|-\frac{1}{2}\rangle\right] e^{i\boldsymbol{k}\cdot\boldsymbol{r}} \\ |\boldsymbol{k},\downarrow\rangle &= \left[|-\frac{3}{2}\rangle + ak_-^2|+\frac{1}{2}\rangle\right] e^{i\boldsymbol{k}\cdot\boldsymbol{r}} \\ a &= \frac{\sqrt{3}\gamma_2}{2m_e\Delta_{hl}}\frac{\sqrt{3}}{4\langle k_z^2\rangle} \ . \end{aligned} \tag{C.3}$$

Taking the square well width $d = 20$nm and the hole density $p = 10^{11}\text{cm}^{-2}$, we arrive at the following estimate for the mixing probability, $a^2k_F^4 = \frac{3}{4\pi^2}d^4p^2 \approx 1.2\times10^{-2}$. We will see below that the data is approximately consistent with this estimate for an effective well width of 20nm. This very small mixing, of order 1% in probability, is responsible for the SO interaction considered here.

The Zeeman interaction of a $J = 3/2$ hole with magnetic field $\boldsymbol{B}$ is [284],

$$\delta H = -\frac{g_0}{3}\mu_B \boldsymbol{B}\cdot\boldsymbol{J} \ . \tag{C.4}$$

Taking the matrix element of δH between states Eq. C.3 we find the effective matrix of H_{so}

$$\langle\downarrow|H_{so}|\uparrow\rangle \equiv \langle\downarrow|\delta H|\uparrow\rangle = -\frac{g_0\mu_B}{4\langle k_z^2\rangle}B_+k_+^2 \ . \tag{C.5}$$

Comparing this with H_{so} in Chapter 5 Eq. 5.23 we determine the coefficient α in this equation to be

$$\alpha = \frac{g_0\mu_B}{4\langle k_z^2\rangle} \ . \tag{C.6}$$

According to our fit of SdH data $|\lambda| = 2|\alpha|k_F^2/\mu_B \approx 1.1$. Hence we find that $k_F^2/k_z^2 \approx 0.3$ and the probability of the heavy-light hole mixing is $a^2k_F^4 = \frac{3}{16}\frac{k_F^4}{\langle k_z^2\rangle^2} \approx 1.7\times10^{-2}$. This estimate of the mixing magnitude is an approximate value, within the range of 1-2%, since there is a comparable contribution to α which is not accounted for by the calculations presented. So far, we have neglected the coupling to the vector potential created by $\boldsymbol{B}_\parallel$, $(\boldsymbol{k}\cdot\boldsymbol{J})^2 \to ((\boldsymbol{k}-e\boldsymbol{A})\cdot\boldsymbol{J})^2$. This coupling also gives a contribution to the coefficient α, see Refs. [148, 284]. This contribution is highly sensitive to the exact shape of the confining potential and therefore cannot be reliably calculated [148]. The kinematic form of H_{so} however remains unambigous and we can fit the value of α to the experimental data.

There is a small correction to H_{so} which has a form different from that in Eq. 5.23, and is third-order in δH, see Eq. C.4. From this, a degenerate perturbation theory calculation gives

$$H'_{so} = -\frac{1}{2}\alpha' \left[\sigma_+ B_-^3 + \sigma_- B_+^3\right]$$
$$\alpha' = \frac{(g_0\mu_B)^3}{36\Delta_{hl}^2} \,. \tag{C.7}$$

Generally H'_{so} is very small, $H'_{so} \ll H_{so}$. However, since $B_\parallel \propto 1/\tan\theta_{tilt}$, the effect of H'_{so} becomes more pronounced at smaller tilt angles. A simple estimate shows that in our experimental condition the ratio H'_{so}/H_{so} can reach 10% at $\theta_{tilt} = 5°$. Therefore, the small disagreement between the experimental data and the theoretical prediction in Chapter 5.4.3, Fig. 5.9 could be due to the unaccounted H'_{so}.

Appendix D

Berry phase concepts and derivations

D.1 The geometric Berry phase

In 1984 Berry [23] discovered that a phase difference can be acquired over the course of a cycle, when a system is subjected to cyclic adiabatic processes, resulting from the geometrical properties of the parameter space of the Hamiltonian. This additional phase factor is now known as the Berry phase. There are 3 key properties to the Berry phase which make the concept important [28, 240]. Firstly the Berry phase is gauge invariant, which makes it a physically meaningful and hence measurable quantity, with early experimental studies focused upon detecting it via interference phenomena. Secondly Berry phase is purely geometrical which makes the Berry phase extensible, in terms of local geometrical quantities within a parameter space e.g. the Berry phase can be expressed as the integral of an emergent field known as the 'Berry curvature', over a surface suspending the loop (Berry curvature). This enables Berry phase to describe a broad range of physical phenomena undergoing adiabatic evolution [135]. Thirdly, since the concept of Berry phase itself is very similar to a gauge field (with the Berry connection analogous to the vector potential and the Berry curvature corresponding to the electromagnetic field) [23], the Berry phase is a powerful, unifying approach. To use an analogy, one can liken the Berry phase to the Aharonov-Bohm phase of a

charged particle traversing a loop encircling a magnetic flux, whilst the Berry curvature is like the magnetic field itself [289].

Since the conception of Berry phase, many generalizations have been proposed to the original definition. In this chapter we shall focus on two main extensions: 1) the relation between Berry phase, Berry connection and Berry curvature; 2) the generalization from a single non-degenerate state to m degenerate states evolving together, resulting in a whole matrix rather than a single phase factor, giving rise to non-abelian behaviour [280]. Such a flexible theory can be used to explain the spin and charge transport of electrons/holes through a semiconductor crystal by taking the periodic lattice potential into consideration. Moreover the semiclassical formalism can be amended to include quantization effects such as Bloch oscillations and cyclotron orbits via the Bohr-Sommerfeld quantization rule [199]. The Berry phase enters naturally as a shift to the classical action, affecting the energies of the quantized Landau levels. More recent developments have shown that the Berry connection plays an explicit role in spin dynamics and is related to the spin-orbit interaction e.g. applications include the relativistic Dirac electron and the Kane model in semiconductors [91, 289].

D.1.1 Cyclic adiabatic evolution

Here we discuss how the Berry phase arises during the adiabatic evolution of a non-degenerate quantum state. We then introduce the local description of the Berry phase in terms of the Berry curvature.

Consider a quantum system in an eigenstate, of a Hamiltonian $\mathcal{H}$ with time varying parameters $\boldsymbol{R} = (R_1, R_2, ...)$, such that between time $t = 0$ to time $t = T$, $\boldsymbol{R}$ circulates around a closed path denoted $\mathcal{C}$ in the parameter space [23].

The state $|\psi(t)\rangle$ of the system evolves according to the time-dependent Schrödinger equation

$$i\hbar\frac{\partial}{\partial t}|\psi(t)\rangle = \mathcal{H}(\boldsymbol{R}(t))\,|\psi(t)\rangle \ . \tag{D.1}$$

For the rest of this chapter, we shall set $\hbar = 1$ for simplicity. At any instant in time, the natural orthonormal basis consists of the eigenstates $|n(\boldsymbol{R})\rangle$ of $\mathcal{H}(\boldsymbol{R})$ at each value

of the parameter $\boldsymbol{R} = \boldsymbol{R}(t)$, which satisfy

$$\mathcal{H}(\boldsymbol{R})\,|n(\boldsymbol{R})\rangle = E_n(\boldsymbol{R})\,|n(\boldsymbol{R})\rangle \ , \tag{D.2}$$

with discrete energies $E_n(\boldsymbol{R})$, where $n = (1, 2, ..., N)$ is the energy level index. Note, for simplicity we shall consider the case of a single non-degenerate energy level E_n. This eigenvalue equation alone does not completely determine the basis function $|n(\boldsymbol{R})\rangle$ - it still allows for an arbitrary $\boldsymbol{R}$-dependent phase factor of the eigenstates $|n(\boldsymbol{R})\rangle$. So any ('phase' or 'gauge') choice of basis function can be made, provided that the phase of the basis function is smooth and single-valued along path $\mathcal{C}$ within the parameter space [23].

If the environment and hence $\mathcal{H}$ is slowly altered (i.e. the characteristic frequency $2\pi/T$ is much smaller than the energy spacing between adjacent levels, $|\ E_n - E_{n'}\ |$), the effects of the slowly changing degrees of freedom upon faster moving degrees of freedom can be estimated using the adiabatic approximation. The adiabatic theorem [135, 186] predicts than a system starting off in one of its eigenstates $|n(\boldsymbol{R}(0))\rangle$ will remain as an instantaneous eigenstate $|n(\boldsymbol{R}(t))\rangle$ of the Hamiltonian $\mathcal{H}(\boldsymbol{R}(t))$ during the whole process, at any time t. So the only degree of freedom avaliable to change is the phase $\gamma_n(t)$ of the quantum state, whose wave-function can be expressed as

$$|\psi_n(t)\rangle = exp\left\{-i\int_0^t \mathrm{d}t'\, E_n(\boldsymbol{R}(t'))\right\} e^{i\gamma_n(t)}\,|n(\boldsymbol{R}(t))\rangle \ . \tag{D.3}$$

The first exponent is the dynamical phase factor, which describes the slowly varying time evolution of the stationary state. This dynamical phase is not geometrical, rather it depends only upon $\boldsymbol{R}(t)$ which parameterizes the path followed, and on the arbitrary gauge choice of a "zero phase" of the basis state at each point along the path.

The second exponent is the additional geometrical phase factor of interest, which is acquired by the quantum state during adiabatic evolution. Its phase $\gamma_n(t)$ cannot be written as a function of $\boldsymbol{R}$ only and is path dependent.

As the phase function $\gamma_n(t)$ requires $|\psi_n(t)\rangle$ to satisfy the Schrödinger equation, substituting D.3 into D.1 gives

$$\dot{\gamma}_n(t) = i\,\langle n(\boldsymbol{R}(t))\,|\,\boldsymbol{\nabla}_{\boldsymbol{R}}\,|\,n(\boldsymbol{R}(t))\rangle \cdot \dot{\boldsymbol{R}}(t) \quad . \tag{D.4}$$

The total phase change of state $|\psi\rangle_n$ round $\mathcal{C}$ is given by the evolution of the wavefunction between $t = 0$ and $t = T$,

$$|\psi_n(T)\rangle = exp\left\{-i\int_0^T \mathrm{d}tE_n(\boldsymbol{R}(t))\right\} e^{i\gamma_n(t)}\,|\psi_n(0)\rangle \ , \tag{D.5}$$

where the geometrical phase change is described by a path integral in parameter space and is independent of how the circuit is traversed in the adiabatic approximation [23]

$$\gamma_n(\mathcal{C}) = i\oint_{\mathcal{C}} \langle n(\boldsymbol{R})\,|\,\boldsymbol{\nabla}_{\boldsymbol{R}}\,|\,n(\boldsymbol{R})\rangle \cdot \mathrm{d}\boldsymbol{R} \quad . \tag{D.6}$$

The above equation can be simplified to

$$\gamma_n(\mathcal{C}) = \oint_{\mathcal{C}} \mathrm{d}\boldsymbol{R}\cdot\boldsymbol{A}_n(\boldsymbol{R}) \ , \tag{D.7}$$

where $\boldsymbol{A}_n(\boldsymbol{R})$ is a vector-valued function now known as the Berry connection (or Berry vector potential) [289]

$$\boldsymbol{A}_n(\boldsymbol{R}) = i\,\langle n(\boldsymbol{R})\,|\,\boldsymbol{\nabla}_{\boldsymbol{R}}\,|\,n(\boldsymbol{R})\rangle \ . \tag{D.8}$$

If we use a gauge transformation

$$|n(\boldsymbol{R})\rangle \ \rightarrow \ e^{i\zeta(\boldsymbol{R})}\,|n(\boldsymbol{R})\rangle \tag{D.9}$$

where $\zeta(\boldsymbol{R})$ is an arbitrary smooth function, the Berry connection $\boldsymbol{A}_n(\boldsymbol{R})$ transforms according to

$$\boldsymbol{A}_n(\boldsymbol{R}) \rightarrow \boldsymbol{A}_n(\boldsymbol{R}) - \boldsymbol{\nabla}_{\boldsymbol{R}}\zeta(\boldsymbol{R}) \ . \tag{D.10}$$

and the phase $\gamma_n(\mathcal{C})$ will be modified by $\zeta(\boldsymbol{R}(0)) - \zeta(\boldsymbol{R}(T))$ after the transformation, where $\boldsymbol{R}(0)$ and $\boldsymbol{R}(T)$ refer to the initial and final points of the path $\mathcal{C}$ respectively. Since $\zeta(\boldsymbol{R})$ is a single-valued function of $\boldsymbol{R}$, the phase factor $e^{i\zeta(\boldsymbol{R})}$ in the gauge transformation Eq. D.9 is unity. This implies that

$$e^{i\zeta(\boldsymbol{R}(0))-i\zeta(\boldsymbol{R}(T))} = e^{i2\pi\cdot\mathrm{integer}} = 1 \quad . \tag{D.11}$$

Thus $\gamma_n(\mathcal{C})$ is defined up to an integer multiple of 2π under the gauge transformation. For any closed path, $e^{i\gamma_n}$, the *geometric Berry phase* $\gamma_n(\mathcal{C})$ is gauge invariant and is given by

$$\gamma_n = \oint_{\mathcal{C}} \mathrm{d}\boldsymbol{R}\cdot\boldsymbol{A}_n(\boldsymbol{R}) \quad . \tag{D.12}$$

From this definition, the Berry phase only depends on the geometry of the closed path and is independent of the time variation of $\boldsymbol{R}(t)$ in the adiabatic limit. The Berry phase is a measurable quantitiy. Unlike the Berry phase, the local Berry connection $\boldsymbol{A}_n(\boldsymbol{R})$ is gauge dependent and hence can never be physically observable.

D.1.2 Berry curvature and gauge fields

Due to its universal description and elegance, it is useful to generalize Berry phase further. To do this we define a anti-symmetric second-rank, gauge invariant field (curvature) tensor, derived from the Berry vector potential $\boldsymbol{A}_n(\boldsymbol{R})$ in Eq. D.8 [289] via:

$$\begin{aligned} F^n_{\mu\nu}(\boldsymbol{R}) &= \frac{\partial}{\partial R^\mu}\mathrm{A}^n_\nu(\boldsymbol{R}) - \frac{\partial}{\partial R^\nu}\mathrm{A}^n_\mu(\boldsymbol{R}) \\ &= i\left[\left\langle \frac{\partial n(\boldsymbol{R})}{\partial R^\mu}\,\middle|\,\frac{\partial n(\boldsymbol{R})}{\partial R^\nu}\right\rangle - (\nu \leftrightarrow \mu)\right] . \end{aligned} \tag{D.13}$$

This field $F^n_{\mu\nu}(\boldsymbol{R})$ is called the *Berry curvature*. From Stoke's theorem, for a closed path $\mathcal{C}$ forming the boundary of a surface $\mathcal{S}$, the Berry phase can be expressed as a surface integral

$$\gamma_n = \int_{\mathcal{S}} \mathrm{d}R^\mu \wedge \mathrm{d}R^\nu \; \frac{1}{2}F^n_{\mu\nu}(\boldsymbol{R}) \; , \tag{D.14}$$

where $\mathcal{S}$ is the surface enclosed by the path $\mathcal{C}$. Unlike the Berry vector potential (Berry connection), the Berry curvature described by Eq. D.13 is gauge invariant and observable. In a 3D parameter space, we can recast the Berry curvature Eq. D.13 and the closed-loop Berry phase D.14 into pseudovector form

$$\begin{aligned} \boldsymbol{F}_n(\boldsymbol{R}) &= \boldsymbol{\nabla}_{\boldsymbol{R}} \times \boldsymbol{A}_n(\boldsymbol{R}) \; , \\ \gamma_n &= \int_{\mathcal{S}} \mathrm{d}\boldsymbol{S} \cdot \boldsymbol{F}_n(\boldsymbol{R}) \; . \end{aligned} \tag{D.15}$$

The Berry curvature tensor $F^n_{\mu\nu}$ is related to the vector $\boldsymbol{F}_n$ by the relation $F^n_{\mu\nu} = \epsilon_{\mu\nu\zeta}(\boldsymbol{F}_n)_\zeta$, where $\epsilon_{\mu\nu\zeta}$ is the Levi-Civita totally antisymmetric tensor [289]. In vector form, the Berry curvature can be thought of as a magnetic field in parameter space.

Another way to express Berry curvature from Eq. D.13 is as a summation over the

eigenstates, via the relation $\left\langle n \left| \boldsymbol{\nabla}_{\boldsymbol{R}} \right| n^{'} \right\rangle = \left\langle \boldsymbol{\nabla}_{\boldsymbol{R}} \left| n^{'} \right\rangle (E_n - E_{n^{'}})$ for $n^{'} \neq n$ [23, 289]:

$$F^n_{\mu\nu}(\boldsymbol{R}) = i \sum_{n^{'} \neq n} \frac{\left\langle n \left| \frac{\partial H}{\partial R^{\mu}} \right| n^{'} \right\rangle \left\langle n^{'} \left| \frac{\partial H}{\partial R^{\nu}} \right| n \right\rangle - (\nu \leftrightarrow \mu)}{(E_n - E_{n^{'}})^2} \,. \tag{D.16}$$

This summation equation is advantageous as no differentiation on the wave function is involved. Moreover it provides further insight into the origin of the Berry curvature itself.

One implication of the Berry curvature summation equation, is that $F^n_{\mu\nu}(\boldsymbol{R})$ becomes singular if two energy levels $E_n(\boldsymbol{R})$ and $E_{n^{'}}(\boldsymbol{R})$ are brought together at certain values of $\boldsymbol{R}$, resulting in a degeneracy point.

The abelian Berry paradigm covers the situation where a single energy level is separated out in the adiabatic evolution, but if the energy levels are degenerate, then the corresponding dynamics must be projected onto a subspace spanned by these degenerate eigenstates, naturally resulting in a non-abelian Berry curvature [280].

D.2 Non-abelian Berry paradigm

The Berry phase itself is geometric in character and so in systems where electrons/holes behave as ultrarelativistic particles, Berry phase directly reflects the shape of the spin trajectory. Measurements of the Shubnikov-de Haas oscillations in graphene [198, 305] and in topological insulators [227] have highlighted the contribution of this geometric phase arising from the internal degrees of freedom (pseudospin and spin respectively) of the systems under study.

In contrast the concept of Berry phase is not well defined in 2D semiconductors due to the existence of two coupled Fermi surfaces with opposing spins. The following section shows how the concept of Berry phase can be extended to such systems, comprising of degenerate (or nearly degenerate) energy bands. Since degenerate Bloch states possess multiple components, the Berry curvature becomes a matrix with a non-abelian gauge structure, ultimately resulting in a non-abelian Berry curvature (i.e. the non-abelian *field*).

D.2.1 Non-abelian Berry phase

Beginning with the adiabatic problem, Wilczek and Zee [280] derived the non-abelian Berry phase in a similar manner to that for the geometric Berry phase. Consider a family of Hamiltonians $\mathcal{H}(\boldsymbol{R})$ varying continuously with parameters $\boldsymbol{R}$, for a single energy level with M degenerate states. For simplicity we set these energy levels to E=0. Following the adiabatic theorem, if the parameters vary slowly from an initial value $\boldsymbol{R}_i$ to some final value $\boldsymbol{R}_f$ over time interval T, and assuming the given space of degenerate levels do not cross other levels, we can solve the time-dependent Schrödinger equation

$$i\frac{\partial\psi}{\partial t} = \mathcal{H}(\boldsymbol{R}(t))\psi \ , \tag{D.17}$$

with boundary conditions $\boldsymbol{R}(0) = \boldsymbol{R}_i$ and $\boldsymbol{R}(T) = \boldsymbol{R}_f$. Wilczek and Zee found that even for the closed path condition $\boldsymbol{R}_i = \boldsymbol{R}_f$, the dynamics of the wave function ψ become non-trivial and gauge fields are necessary [280]. Although for a single non-degenerate level M=1, the evolution of $\psi_i(\boldsymbol{R}) \rightarrow \psi_f(\boldsymbol{R})$ corresponds to a phase multiplication, i.e. a $U(1)$ gauge field similar to that used in the abelian Berry phase [23, 244].

Choosing an arbitrary set of bases $|n_a(\boldsymbol{R}(t))\rangle$ (where a and b are indices of the Mth degenerate state, analogous to spin $\uparrow,\downarrow$) we obtain

$$\mathcal{H}_{ab}(\boldsymbol{R}(t))\,|n_b(\boldsymbol{R}(t))\rangle = 0 \quad . \tag{D.18}$$

For solutions of the Schrödinger equation Eq. D.17 using the initial condition $|n_a(\boldsymbol{R}(0))\rangle$, and assuming the adiabatic limit [280] we obtain,

$$|n_a(\boldsymbol{R}(t))\rangle = \mathcal{U}_{ab}(t)\,|n_b(\boldsymbol{R}(t))\rangle \ , \tag{D.19}$$

where $\mathcal{U}_{ab}(t)$ is a unitary matrix. To determine $\mathcal{U}_{ab}(t)$ we first assume that $|n_a(\boldsymbol{R}(t))\rangle$ remains normalized so that

$$\begin{aligned} 0 &= \langle n_b \,|\, \dot{n}_a\rangle \\ &= \left\langle n_b \,\middle|\, \dot{\mathcal{U}}_{ac} n_c \right\rangle + \langle n_b \,|\, \mathcal{U}_{ac}\dot{n}_c\rangle \end{aligned} \tag{D.20}$$

which leads to,

$$i(\mathcal{U}^{-1}\dot{\mathcal{U}})_{ba} = i\,\langle n_b \,|\, \dot{n}_a\rangle \equiv \mathcal{A}_{ab}(\tau) \tag{D.21}$$

where $\mathcal{A}$ is an anti-Hermitian matrix playing the role of a gauge potential, and the $(\boldsymbol{R}(t))$ term of the basis states have been dropped for simplicity. Solving the above equation as a path-ordered integral yields,

$$\mathcal{U}(t) = \mathcal{P}\ exp\left\{ i \int_0^t \mathcal{A}(\tau) \mathrm{d}\tau \right\} \quad . \tag{D.22}$$

Note that $\mathcal{U}(t)$ and $\mathcal{A}(\tau)$ are now matrices, where $\mathcal{U}(t)$ and $\mathcal{A}(\tau)$ do not commute with $\mathcal{U}(t^{'})$ and $\mathcal{A}(\tau^{'})$ respectively. $\mathcal{A}$ is the non-abelian analog for the Berry connection defined in Eq. D.8 and can be expressed as [91]

$$\mathcal{A}^{\mu}_{ab} = i \left\langle n_a \,|\, \partial_\mu \,|\, n_b \right\rangle \quad . \tag{D.23}$$

The non-abelian Berry connection $\mathcal{A}^{\mu}_{ab}(\boldsymbol{R})$ is now a matrix-valued vector indexed by (a, b) for all indices of the degenerate subspace $(1, ..., M)$, where μ refers to a set of matrices $\mathcal{A}$ and ∂_μ is shortened notation for $\frac{\partial}{\partial \boldsymbol{R}_\mu}$. The specific form of $\mathcal{A}$ from Eq. D.21 depends upon the choice of basis states $|n_a(\boldsymbol{R}(t))\rangle$. For a different choice e.g.

$$n(\boldsymbol{R}(t)) = \Omega(t)\psi(t) \ , \tag{D.24}$$

the set of fields $\mathcal{A}^{\mu}$ then transform as full gauge potentials

$$\mathcal{A}^{\mu^{'}}_{ab}(t) = \partial^{\mu}\Omega\Omega^{-1} + \Omega\mathcal{A}^{\mu}\Omega^{-1} \ . \tag{D.25}$$

So the path ordered integral now becomes generalized to a $\mathcal{U}(M)$ matrix

$$\mathcal{U}(t) = \mathcal{P}\ exp\left\{ i \int_0^t \mathcal{A}_\mu(\boldsymbol{R}(t)) \mathrm{d}R^{\mu} \right\} \quad , \tag{D.26}$$

which depends only upon its path and not upon its parameterization. For a closed path we obtain the Wilson loop, which is a matrix analogy to the geometric Berry phase,

$$\mathcal{U} = \mathcal{P}\ exp\left\{ i \oint \mathcal{A}_\mu \mathrm{d}R^{\mu} \right\} \quad . \tag{D.27}$$

D.2.2 Deriving the non-abelian Berry curvature

To cover the case of degenerate bands where conventional adiabatic theorem fails, as done for the Berry phase, we can likewise extend the non-abelian Berry formalism to describe non-abelian Berry curvature. For the semiclassical framework, a correct

treatment of the system involves a wave packet constructed from the degenerate levels [52, 241]. Thus, the Berry curvature tensor $F^n_{\mu\nu}(\boldsymbol{R})$ from the abelian Eq. D.13 must be extended to a matrix definition $\mathcal{F}^{ab}_{\mu\nu}(\boldsymbol{R})$ in analogy to non-abelian gauge theories [280], by substituting the curl with the covariant derivative [91, 241]

$$\begin{aligned}
\mathcal{F}^{ab}_{\mu\nu}(\boldsymbol{R}) &= \partial_\mu \mathcal{A}^{ab}_\nu - \partial_\nu \mathcal{A}^{ab}_\mu + i\left[\mathcal{A}_\mu, \mathcal{A}_\nu\right]^{ab} \\
&= \{i\,\langle \partial_\mu n_a(\boldsymbol{R}) \,|\, \partial_\nu n_b(\boldsymbol{R})\rangle - i\,\langle \partial_\nu n_a(\boldsymbol{R}) \,|\, \partial_\mu n_b(\boldsymbol{R})\rangle\} \\
&\quad + i\left[\langle \partial_\nu n_a(\boldsymbol{R}) \,|\, n_c(\boldsymbol{R})\rangle \,\langle n_c(\boldsymbol{R}) \,|\, \partial_\mu n_b(\boldsymbol{R})\rangle\right] \\
&\quad - i\left[\langle \partial_\mu n_a(\boldsymbol{R}) \,|\, n_c(\boldsymbol{R})\rangle \,\langle n_c(\boldsymbol{R}) \,|\, \partial_\nu n_b(\boldsymbol{R})\rangle\right] \qquad \text{(D.28)}
\end{aligned}$$

Just as in the abelian scenario where the Berry connection (Berry curvature) have the same mathematical structures as the vector potential (magnetic field), this correspondence also holds for the non-abelian gauge theory e.g. $SU(2)$ gauge theory [280]. The subspace of degenerate eigenstates is subject to a $U(M)$ gauge freedom. The non-abelian Berry connection $\mathcal{A}^{\mu}_{ab}(\boldsymbol{R})$ under the gauge transformations, is transformed according to Eq. D.25 and the corresponding non-abelian Berry curvature $\mathcal{F}^{ab}_{\mu\nu}(\boldsymbol{R})$ to [91]

$$\mathcal{F}^{ab'}_{\mu\nu}(\boldsymbol{R}) = \mathcal{U}^\dagger(\boldsymbol{R})\; \mathcal{F}^{ab}_{\mu\nu}(\boldsymbol{R})\; \mathcal{U}(\boldsymbol{R}) \quad . \qquad \text{(D.29)}$$

Thus the non-abelian Berry curvature matrix $\mathcal{F}^{ab}_{\mu\nu}(\boldsymbol{R})$ is changing under a gauge rotation and therefore cannot be directly observed [36]. But we can derive gauge invariant quantities from it which are physically meaningful, such as the trace of the Berry curvature matrix, tr$\mathcal{F}$. This trace will play a crucial role in interpreting our experimental data which is discussed in Sections 5.3.2 and 5.4 of the main body of this thesis.

Appendix E

Electron Quantum Dot: 3-terminal setup considerations

E.1 Model of electrical setup

Here we shall discuss the effect of the 3-terminal measurement setup used to measure the electron quantum dot and address any anti-correlation effects due to Kirchoff's laws. A schematic of the single-source and dual-drain setup of the quantum dot (QD) and charge sensor (CS) is given in Fig E.1, which takes into account the line resistances of the fridge, ohmic contact resistances and other electronic components. A 10^4 voltage divider brings the 1Vac input down to 100μV at the source terminal. The fridge lines have a fixed resistance of $R_{line} = 161\Omega$ and the input impedance of the SRS830 lock-in amplifier is $R_{LIA} = 1000\Omega$.

Initially, the contact resistances (R_{SRC}, R_{QD-DRN}, R_{CS}) as well as the resistance of the quantum dot R_{QD} and charge sensor R_{CS} are unknown. As a 4-terminal measurement was not possible, to estimate the contact resistance, the were unbiased gates to 'remove' the presence of the CS and the dot, resulting in a 2D region so that $R_{QD} = R_{CS} \to 0$. From Fig. 6.9 in the main chapter, this happens around $V_G \sim 0$V when the gates are pulled back. Here the corresponding dot current is $i_{QD} = 15$nA and CS current is $i_{CS} = 22$nA.

Since both R_{SRC} and R_{QD-DRN} lie along the length of the hall bar and the current

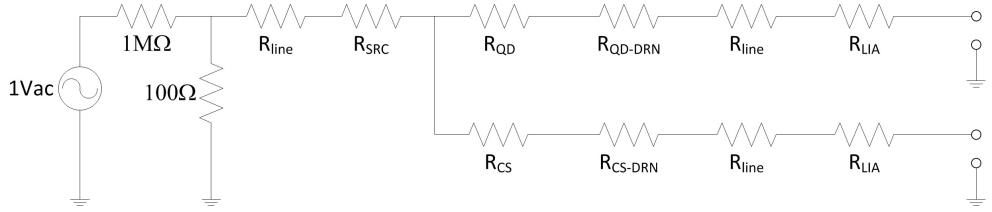

Figure E.1: Schematic of the 3-terminal electrical measurement setup which simultaneously measures current through both the quantum dot and the charge sensor. The configuration is that of a single source and two drains, taking into account other resistances such as the contact resistances, fridge line resistances and other electrical components.

through the dot circuit is smaller than the CS circuit, we can assume that $R_{SRC} \approx R_{QD-DRN} = R_C$. The current through the quantum dot arm in 2D can be expressed as:

$$\begin{aligned} 15nA &= \approx \frac{100\mu V}{(161 \times 2 + 1000) + 2R_C} \\ \therefore R_c &= 2672\Omega \quad . \end{aligned} \tag{E.1}$$

From this value of R_{SRC} and the current through the CS arm we obtain

$$\begin{aligned} 22nA &= \approx \frac{100\mu V}{(161 \times 2 + 1000 + 2672) + R_{CS-DRN}} \\ \therefore R_{CS-DRN} &= 551\Omega \quad . \end{aligned} \tag{E.2}$$

Thus we can modify the circuit diagram to that shown in Fig E.2. Once again, assuming the 2D limit where $R_{QD} = R_{CS} \to 0$, we can solve for the equivalent circuit and obtain a total resistance of $R_{tot} = 1,000,097.6\Omega$. Given our 1Vac source, the corresponding total current is $I_{tot} = 100\mu$A. The corresponding voltage output from the divider is $V_{div} = 97.6\mu V \approx 100\mu V$ as anticipated, where most of the current passes down the 100Ω leg of the voltage divider. So, for the rest of the analysis we shall focus upon a reduced region of the circuit starting from the V_{div} node onwards as depicted in Fig E.3.

The circuit can be modelled using a series of equations. From Kirchoff's current law we first obtain

$$i_{tot} = i_{CS} + i_{QD} \quad . \tag{E.3}$$

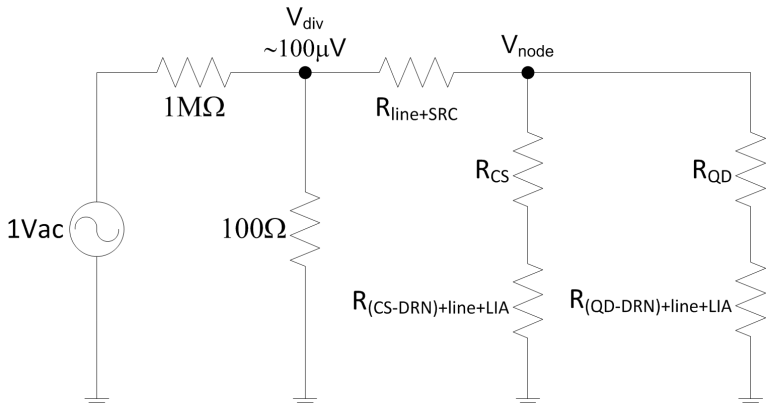

Figure E.2: Modified circuit diagram from Fig E.1 where the contact resistances, line resistances and instrument resistances remain fixed and can be summed into a single element.

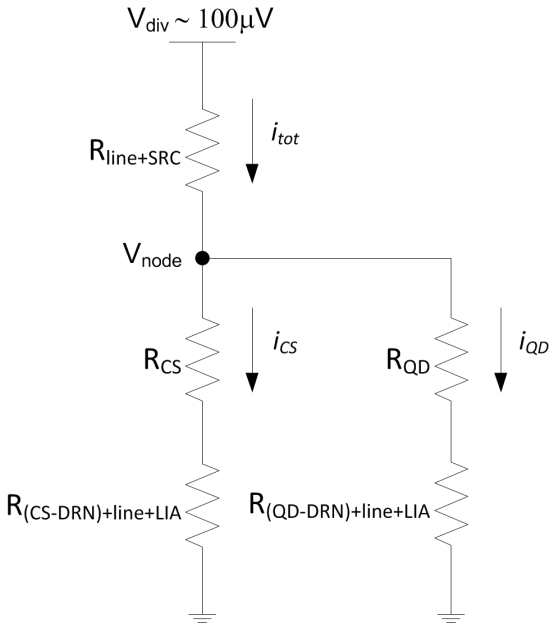

Figure E.3: Reduced circuit from Fig E.2, assuming a constant $V_{div} \sim 100\mu$V, such that $i_{tot} = i_{CS} + i_{QD}$ at the point V_{node}. The values of the fixed resistances are $R_{line+SRC} = 2833\Omega$, $R_{CS-DRN+line+LIA} = 1712\Omega$ and $R_{QD-DRN+line+LIA} = 3833\Omega$.

Performing a nodal analysis, we can break the circuit up into individual arms;

$$i_{tot} = \frac{100\mu V - V_{node}}{R_{line+SRC}} \quad , \tag{E.4}$$

$$V_{node} = i_{CS} \times (R_{CS} + R_{CS-DRN+line+LIA}) \quad , \tag{E.5}$$

$$V_{node} = i_{QD} \times (R_{QD} + R_{QD-DRN+line+LIA}) \quad . \tag{E.6}$$

The following lumped element resistances remain fixed at:

$$\begin{aligned} R_{line+SRC} &= 2833\Omega \\ R_{CS-DRN+line+LIA} &= 1712\Omega \\ R_{QD-DRN+line+LIA} &= 3833\Omega \end{aligned} \tag{E.7}$$

E.2 Comparision of model to experimental data: estimating 3-terminal setup contributions

We will now apply the model to our experimental data, namely Fig. 6.14 of the main text, to determine the impact of the 3-terminal setup upon the measurement and in particular to see if the anomalous oscillations seen in the charge sensor current Fig. 6.14c, is caused by the setup. To make this task easier, we re-plot the same dataset seen in Fig. 6.14 panels (c),(d) in terms of raw current, rather than conductance shown in Fig. E.4 panels (b),(d) for the charge sensor and quantum dot respectively.

From Fig. E.4, if we take the values of $i_{QD} \approx 100$pA and $i_{CS} \approx 3.5$nA (at $V_p = -1.1$V), substituting into Eq. E.3 gives

$$i_{tot} = i_{CS} + i_{QD} = 3.5nA + 100pA = 3.6nA$$

Subsequently V_{node} becomes:

$$\begin{aligned} \frac{100\mu V - V_{node}}{2833} &= 3.6nA \\ V_{node} &= 89.8\mu V \end{aligned} \tag{E.8}$$

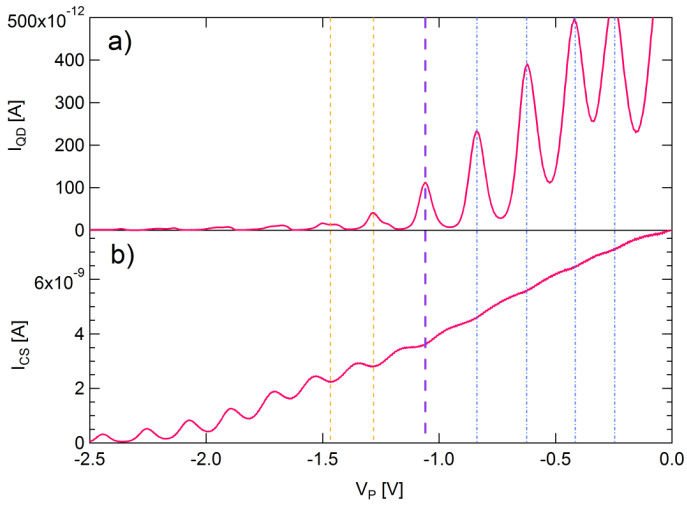

Figure E.4: Reproduced Fig. 6.14 in the main text, where current through the dot (a) corresponds to Fig. 6.14d; and the charge sensor (b) corresponds to Fig. 6.14c; are plotted as a function of plunger gate voltage which is swept to change the occupancy of the dot. Dashed vertical blue lines indicate points where the Coulomb blockade peaks in the dot correspond to dips in the charge sensor. Dashed orange lines mark the beginning points at which these features start to diverge as V_p is swept more negative. At $V_p = -1.1$V (purple dashed), $i_{QD} \approx 100$pA and $i_{CS} \approx 3.5$nA.

To roughly quantify the effect of the 3-terminal setup upon the measured signals when the quantum dot operates in the single-electron tunneling regime, a Coulomb blockade peak was singled out for study. Here we choose the point at $V_p = -1.1$V in Fig. E.4 where $i_{QD} \approx 100$pA and $i_{CS} = 3.5$nA (marked in longer dashed purple lines). As i_{QD} goes from ≈ 100pA to 0pA, between tunneling and blockaded regimes,

- How much will R_{QD} change by? (If we assume R_{CS} remains fixed at the value where $i_{CS} \approx 3.5$nA initially?)
- How will i_{CS} evolve?

Starting with the scenario where the dot configuration allows for tunneling to occur, i.e. $i_{QD} \approx 100$pA:

First obtain R_{QD} from Eq. E.6,

$$\begin{aligned} 89.8\mu V &= 100pA \times (R_{QD} + 3833) \\ R_{QD} &= 894,167\Omega \end{aligned} \tag{E.9}$$

Likewise we obtain a value of R_{CS} from Eq. E.5, which is about half G_0 i.e. $\sim 2 \times 12,909\Omega$,

$$\begin{aligned} 89.8\mu V &= 3.5nA \times (R_{CS} + 1712) \\ R_{CS} &= 23,945\Omega \\ &. \end{aligned} \tag{E.10}$$

When the quantum dot is blockaded and $i_{QD} \to 0$:

To determine i_{CS} we setup Eq. E.5 and Eq. E.3,

$$V_{node} = i_{CS} \times (23,945 + 1712)$$

$$\begin{aligned} i_{tot} &= i_{CS} + 0 \\ \frac{100\mu V - V_{node}}{2833} &= \frac{V_{node}}{23,945 + 1712} \end{aligned} \tag{E.11}$$

substituting for V_{node} gives,

$$\begin{aligned} \frac{100\mu V - V_{node}}{2833} &= \frac{V_{node}}{25,657} \\ \frac{100\mu V - (i_{CS} \cdot 25,657)}{2833} &= \frac{(i_{CS} \cdot 25,657)}{25,657} \\ 100\mu V &= i_{CS} \cdot 2833 + i_{CS} \cdot 25,657 \\ 100\mu V &= i_{CS} \cdot 28,490 \\ \therefore i_{CS} &= 3.51nA \end{aligned} \tag{E.12}$$

this 100pA drop in i_{QD} results in a slight increase in i_{CS} by 10pA. Recalculating a new value for V_{node} from Eq. E.5 gives,

$$\begin{aligned} V_{node} &= 3.51nA \times (23,945 + 1712) \\ V_{node} &= 90.1\mu V \end{aligned} \tag{E.13}$$

which is an increase in V_{node} of $\Delta V_{node} = 0.3\mu V$. The corresponding change (increase) in i_{CS} due to ΔV_{node} can be calculated from Eq. E.5,

$$\begin{aligned} \Delta V_{node} &= \Delta i_{CS} \times (23,945 + 1712) \\ \Delta i_{CS} &= \frac{0.3\mu V}{25,657} \\ \Delta i_{CS} &= 11.7pA \end{aligned} \tag{E.14}$$

From this brief analysis, we find that the 3-terminal measurement setup results in a small, inversely proportional relationship between the charge sensor and quantum dot currents. The variation in the charge sensor current of 11.7pA, as the quantum dot state alternates between tunnelling and blockaded and is quite small in comparison to the amplitude of the oscillations seen in i_{CS} in Fig. E.4 beyond $V_p = -1.2$V. These anomalous oscillations in the data appear to have an amplitude ranging between $1 - 0.5$nA, i.e. $\sim 50 - 100\times$ larger than Δi_{CS}, which is not consistent with a purely 3-terminal setup effect as seen from our model.

Appendix F

Nextnano++ simulation code snippets

F.1 Modelling the induced structure

The 3D nano device simulator nextnano++ Schrödinger-Poisson-current solver software package for simulating low dimensional structures [273]. The modelling was done with assistance from R. Li, by adapting an Si/SiO_2 template for our GaAs/AlGaAs heterostructure. A schematic illustrating a cross section of the modified heterostructure is given in Fig F.1, where the thickness of each layer is supplied in brackets. This was done by changing the parameters for the SiO_2 layer to match those of the polyimide or AlOx dielectric and thickness. Next is a layer of metal surface gates to model the gates forming the quantum dot. Below that, parameters for the straight silicon substrate were substituted with those of the AlGaAs dielectric. This was followed by a 2000nm thick layer of GaAs to model the substrate and form the heterojunction with the AlGaAs. Below this, two extra layers are added, a doping layer and a contact plane, which acts as the global ground point.

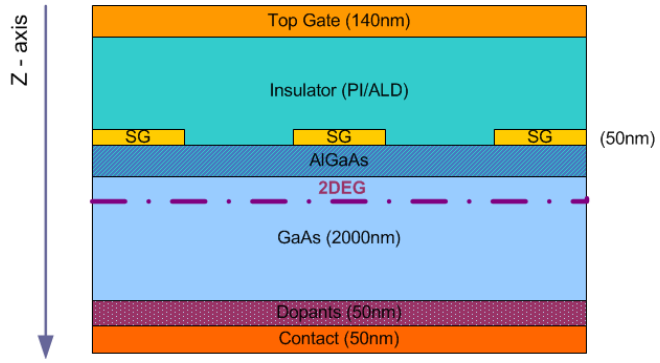

Figure F.1: Cross section of the GaAs/AlGaAs heterostructure setup for the Nextnano++ simulation. The thickness of each layer is given in brackets where appropriate.

The parameters used to model the electron quantum dot measured in Chapter 6.3 are:

```
#Begin NextnanoWizard parameter section
$SGb = -1.8          # QPC charge sensor gate bias (V)
$LGb = -0.48          # Left gate bias
$PGb = -0.1          # middle thin plunger gate bias
$RBGb = -0.8         # right bottom gate bias
$RTGb = -0.83         # right top gate bias
$TGb = 8             # overall top gate bias
$BCb = 0             # back contact bias
$SctBarHeight = 3.075   #Schottky barrier height (modelled as SiO2
to Si flat band condtn = 3.075)
$DOPING = 1.0e20  # doping concentration (cm^-3)
$XGRID = 10          # grid spacing in x-direction (nm)
$YGRID = 10          # grid spacing in y-direction (nm)
$ZGRID = 50          # grid spacing in z-direction (nm)
$QUANTUM = 0       # use either classical (0) or quantum (1) density
$NUMEV = 100       # number of electron states to be calculated
$ALPHA = 0.1       # underrelaxation parameter for current equation
```

```
$AVS = 1          # 2D output in AVS (1) or Origin (0) format


#Begin the parameter define
$GateWidth = 80   # Width of most gates (nm)
$PGWidth = 50     # Width of PG (nm)
$QPCWidth = 400   # Width of QPC channel
$QDBWidth = 350   # Width of the quantum dot barrier
$SGLeng = 500    # Length of the QPC charge sensor gate
$RBGLeng = 500   # Length of the right bottom gate (nm)
$RTGLeng = 500   # Length of the right top gate
$REmptS = 500    # Empty space on the right hand side
$PGSep = ($QDBWidth-$PGWidth)/2  # Separation of the PG to other gates
$TGt = 140        # Thickness of the overall top gate
$PIt = 600        # Thickness of the PI with Dielectric const = 3.5
$SGt = 50         # Thickness of surface gate
$GDt = 160        # Thickness of the gate dielectric (AlGaAs)
$GaAst = 2000     # Thicnkess of GaAs
$Dopet = 50       # Thickness of bottom doping
$Contactt = 50    # Thickness of the bottom contact
#End parameter define
```

The parameters used to model the 'Sunbeam' induced hole quantum dot measured in Chapter 6.5.1 are:

```
#Begin NextnanoWizard parameter section
$QGb = -1.8        # QPC charge sensor gate bias (V)
$LTGb = -0.9       # Left Top gate bias
$LBGb = -0.8       # Left Bottom gate bias
$PGb = -0.6       # middle Plunger gate bias
$RTGb = -0.9       # Right Top gate bias
```

```
$RBGb = -0.8       # Right Bottom gate bias
$TGb = 1.34           # global Top Gate bias
$BCb = 0           # back contact bias
$SctBarHeight = 3.075   #Schottky barrier height (modelled as SiO2
to Si flat band condtn = 3.075)
$DOPING = 1.0e20  # doping concentration (cm^-3)
$XGRID = 20        # grid spacing in x-direction (nm)
$YGRID = 20        # grid spacing in y-direction (nm)
$ZGRID = 50        # grid spacing in z-direction (nm)
$QUANTUM = 0      # use either classical (0) or quantum (1) density
$NUMEV = 100      # number of electron states to be calculated
$ALPHA = 0.1      # underrelaxation parameter for current equation
$AVS = 1          # 2D output in AVS (1) or Origin (0) format

#Begin the parameter define
$GateWidth = 80   # Width of most gates (nm)
$BGWidth = 40     # Width of building blocks of Bottom Right
and Left gates (nm)
$QPCWidth = 800   # Width of QPC channel
$QDWidth = 320   # Width of the quantum dot area
$GateLeng = 400    # Length of most gates
$LTRTGLeng = 500    # Length of top barrier gates (left and right)
$PGSep = ($QDWidth-$GateWidth)/2  # Seperation of the PG to other gates
$TGt = 140        # Thickness of the overall top gate
$PIt = 30         # Thickness of the ALD with Dielectric const = 8
$SGt = 50         # Thickness of surface gate
$GDt = 110        # Thickness of the gate dielectric (AlGaAs)
$GaAst = 2000     # Thicnkess of GaAs
$Dopet = 50       # Thickness of bottom doping
$Contactt = 50    # Thickness of the bottom contact
```

```
#End parameter define
```

Bibliography

[1] S. Adachi. GaAs, AlAs, and Al_x $Ga_{1-x}As$: Material parameters for use in research and device applications. *Journal of Applied Physics*, 58:R1–R29, 1958.

[2] Attocube Systems AG. User manual attocube systems' positioners v1.6, 2010.

[3] Y. Aharonov and D. Bohm. Significance of Electromagnetic Potentials in the Quantum Theory. *Physical Review*, 115(3):485, 1959.

[4] B. Altshuler, D. Khmel'nitzkii, A. Larkin, and P. Lee. Magnetoresistance and Hall effect in a disordered two-dimensional electron gas. *Physical Review B*, 22(11):5142, 1980.

[5] S. Amasha, K. MacLean, Iuliana Radu, D. Zumbühl, M. Kastner, M. Hanson, and A. Gossard. Electrical Control of Spin Relaxation in a Quantum Dot. *Physical Review Letters*, 100(4), 2008.

[6] J. G. Analytis, R. D. McDonald, S. C. Riggs, J-H. Chu, G. S. Boebinger, and I. R. Fisher. Two-dimensional surface state in the quantum limit of a topological insulator. *Nature Physics*, 6:960, 2010.

[7] J. Anandan. The geometric phase. *Nature*, 360:307, 1992.

[8] T. Ando. Self-consistent results for a $GaAs/Al_xGa_{1-x}As$ heterojunction. II. Low temperature mobility. *Journal of the Physical Society of Japan*, 51(12):3900, 1982.

[9] T. Ando, Y. Matsumoto, and Uemura Y. Theory of Hall effect in a 2D electron system. *Journal of the Physical Society of Japan*, 39(2):10, 1975.

[10] Tsuneya Ando. Electronic properties of two-dimensional systems. *Reviews of Modern Physics*, 54(2):437–672, 1982.

[11] S. J. Angus, A. J. Ferguson, A. S. Dzurak, and R. G. Clark. Gate-Defined Quantum Dots in Intrinsic Silicon. *Nano Lett*, 7(7):2051, 2007.

[12] N. Ares, V. Golovach, G. Katsaros, M. Stoffel, F. Fournel, L. Glazman, O. Schmidt, and S. De Franceschi. Nature of tunable hole g factors in quantum dots. *Physical Review Letters*, 110(4), 2013.

[13] D. P. Arovas and Y. Lyanda-Geller. Non-Abelian geometric phases and conductance of spin-3/2 holes. *Physical Review B*, 57(19):12302, 1998.

[14] R. Ashoori, H. Stormer, J. Weiner, L. Pfeiffer, K. Baldwin, and K. West. N-electron ground state energies of a quantum dot in magnetic field. *Physical Review Letters*, 71(4):613–616, 1993.

[15] R. Ashoori, H. Stormer, J. Weiner, L. Pfeiffer, S. Pearton, K. Baldwin, and K. West. Single-electron capacitance spectroscopy of discrete quantum levels. *Physical Review Letters*, 68(20):3088–3091, 1992.

[16] R. C. Ashoori. Electrons in artificial atoms. *Nature*, 379:7, 1996.

[17] D. Averin, A. Korotkov, and K. Likharev. Theory of single-electron charging of quantum wells and dots. *Physical Review B*, 44(12):6199, 1991.

[18] D. D. Awschalom and M. E. Flatté. Challenges for semiconductor spintronics. *Nature Physics*, 3:7, 2007.

[19] A. Balocchi, Q. H. Duong, P. Renucci, B. L. Liu, C. Fontaine, T. Amand, D. Lagarde, and X. Marie. Full Electrical Control of the Electron Spin Relaxation in GaAs Quantum Wells. *Physical Review Letters*, 107(13), 2011.

[20] C. W. J. Beenakker. Theory of Coulomb-blockade oscillations in the conductance of a quantum dot. *Physical Review B*, 44(4):1646, 1991.

[21] A. J. Bennett, M. A. Pooley, Y. Cao, N. Skold, I. Farrer, D. A. Ritchie, and A. J. Shields. Voltage tunability of single-spin states in a quantum dot. *Nature Communications*, 4:1522, 2013.

[22] K. Berggren and M. Pepper. New directions with fewer dimensions. *Physics World*, page 6, 2002.

[23] M. V. Berry. Quantal Phase Factors Accompanying Adiabatic Changes. *Proceedings of the Royal Society A: Mathematical, Physical and Engineering Sciences*, 392(1802):45, 1984.

[24] G. L. Bir, E. I. Butikov, and G. E. Pikus. Spin and combined resonance on acceptor centres in Ge and Si type crystals - I. *Journal of Physics and Chemistry of Solids*, 24:1475, 1963.

[25] G. L. Bir, E. I. Butikov, and G. E. Pikus. Spin and combined resonance on acceptor centres in Ge and Si type crystals - II. *Journal of Physics and Chemistry of Solids*, 24:1475, 1963.

[26] T. Bitter and D. Dubbers. Manifestation of Berrys topological phase in neutron spin rotation. *Physical Review Letters*, 59(3):251, 1987.

[27] J. Blokland, F. Wijnen, P. Christianen, U. Zeitler, J. Maan, P. Kailuweit, D. Reuter, and A. Wieck. Hole levels in InAs self-assembled quantum dots. *Physical Review B*, 75(23), 2007.

[28] A. Bohm, A. Mostafazadeh, H. Koizumi, Q. Niu, and J. Zwanziger. *The Geometric Phase in Quantum Systems: Foundations, Mathematical Concepts, and Applications in Molecular and Condensed Matter Physics*. Springer-Verlag, Berlin, 2003.

[29] M. G. Borselli, K. Eng, E. T. Croke, B. M. Maune, B. Huang, R. S. Ross, A. A. Kiselev, P. W. Deelman, I. Alvarado-Rodriguez, A. E. Schmitz, M. Sokolich, K. S. Holabird, T. M. Hazard, M. F. Gyure, and A. T. Hunter. Pauli spin blockade in undoped Si/SiGe two-electron double quantum dots. *Applied Physics Letters*, 99(6):063109, 2011.

[30] D. Brunner, B. D. Gerardot, P. A. Dalgarno, G. Wust, K. Karrai, N. G. Stoltz, P. M. Petroff, and R. J. Warburton. A coherent single-hole spin in a semiconductor. *Science*, 325(5936):70–2, 2009.

[31] Christo Buizert, Frank H. L. Koppens, Michel Pioro-Ladriére, Hans-Peter Tranitz, Ivo T. Vink, Seigo Tarucha, Werner Wegscheider, and Lieven M. K. Vandersypen. InSitu Reduction of Charge Noise in GaAs/AlGaAs Schottky-Gated Devices. *Physical Review Letters*, 101(22), 2008.

[32] E. Buks, M. Heiblum, Y. Levinson, and H. Shtrikman. Scattering of a two-dimensional electron gas by a correlated system of ionized donors. *Semiconductor Science and Technology*, 9:2031–2041, 1994.

[33] Denis Bulaev and Daniel Loss. Spin Relaxation and Decoherence of Holes in Quantum Dots. *Physical Review Letters*, 95(7), 2005.

[34] M. Büttiker. Quantized transmission of a saddle-point constriction. *Physical Review B*, 41(11):4, 1990.

[35] Yu. A. Bychkov and E. I. Rashba. Oscillatory effects and the magnetic susceptibility of carriers in inversion layers. *Journal of Physics C: Solid State Physics*, 17:8, 1984.

[36] Ming-Che Chang and Qian Niu. Berry curvature, orbital moment, and effective quantum theory of electrons in electromagnetic fields. *Journal of Physics: Condensed Matter*, 20(19):193202, 2008.

[37] James Chelikowsky and Marvin Cohen. Nonlocal pseudopotential calculations for the electronic structure of eleven diamond and zinc-blende semiconductors. *Physical Review B*, 14(2):556, 1976.

[38] J. C. H. Chen. *Electronic transport of low dimensional holes in induced p-type GaAs devices*. University of New South Wales, Thesis, 2012.

[39] J. C. H. Chen, O. Klochan, A. P. Micolich, A. R. Hamilton, T. P. Martin, L. H. Ho, U. Zülicke, D. Reuter, and A. D. Wieck. Observation of orientation-

and k-dependent Zeeman spin-splitting in hole quantum wires on (100)-oriented AlGaAs/GaAs heterostructures. *New Journal of Physics*, 12(3):033043, 2010.

[40] J. C. H. Chen, D. Q. Wang, O. Klochan, A. P. Micolich, K. Das Gupta, F. Sfigakis, D. A. Ritchie, D. Reuter, A. D. Wieck, and A. R. Hamilton. Fabrication and characterization of ambipolar devices on an undoped AlGaAs/GaAs heterostructure. *Applied Physics Letters*, 100(5):052101, 2012.

[41] YenTing Chiu, Medini Padmanabhan, T. Gokmen, J. Shabani, E. Tutuc, M. Shayegan, and R. Winkler. Effective mass and spin susceptibility of dilute two-dimensional holes in GaAs. *Physical Review B*, 84(15), 2011.

[42] T. Choi, T. Ihn, S. Schön, and K. Ensslin. Counting statistics in an InAs nanowire quantum dot with a vertically coupled charge detector. *Applied Physics Letters*, 100(7):072110, 2012.

[43] M. Ciorga, A. S. Sachrajda, P. Hawrylak, C. Gould, P. Zawadzki, S. Jullian, Y. Feng, and Z. Wasilewski. Addition spectrum of a lateral dot from Coulomb and spin-blockade spectroscopy. *Physical Review B*, 61(24):315, 2000.

[44] J. Climente, J. Planelles, M. Pi, and F. Malet. Magnetic-field dependence of hole levels in self-assembled InGaAs quantum dots. *Physical Review B*, 72(23):233305, 2005.

[45] J. I. Climente, C. Segarra, and J. Planelles. Spin-orbit-induced hole spin relaxation in InAs and GaAs quantum dots. *New Journal of Physics*, 15(9):093009, 2013.

[46] D. Cobden, N. Patel, M. Pepper, D. Ritchie, J. Frost, and G. Jones. Noise and reproducible structure in a GaAs/$Al_xGa_{1-x}As$ one-dimensional channel. *Physical Review B*, 44(4):1938, 1991.

[47] D. Cobden, A. Savchenko, M. Pepper, N. Patel, D. Ritchie, J. Frost, and G. Jones. Time-irreversible random telegraph signal due to current along a single hopping chain. *Physical Review Letters*, 69(3):502, 1992.

[48] B. E. Cole, J. M. Chamberlain, M. Henini, T. Cheng, W. Batty, A. Wittlin, J. A. A. J. Perenboom, A. Ardavan, A. Polisski, and J. Singleton. Cyclotron resonance in ultra-low-hole-density narrow p-type GaAs/(Al,Ga)As quantum wells. *Physical Review B*, 55(4):2503, 1997.

[49] P. Coleridge, R. Stoner, and R. Fletcher. Low-field transport coefficients in GaAs/$Ga_{1-x}Al_xAs$ heterostructures. *Physical Review B*, 39(2):1120, 1989.

[50] Dan Csontos and Ulrich Zülicke. Large variations in the hole spin splitting of quantum-wire subband edges. *Physical Review B*, 76(7):073313, 2007.

[51] Dimitrie Culcer, Xuedong Hu, and S. Das Sarma. Dephasing of Si spin qubits due to charge noise. *Applied Physics Letters*, 95(7):073102, 2009.

[52] Dimitrie Culcer, Yugui Yao, and Qian Niu. Coherent wave-packet evolution in coupled bands. *Physical Review B*, 72(8):085110, 2005.

[53] R. Danneau, O. Klochan, W. Clarke, L. Ho, A. Micolich, M. Simmons, A. Hamilton, M. Pepper, D. Ritchie, and U. Zülicke. Zeeman Splitting in Ballistic Hole Quantum Wires. *Physical Review Letters*, 97(2):026403, 2006.

[54] Robert Darling. Defect-state occupation, Fermi-level pinning, and illumination effects on free semiconductor surfaces. *Physical Review B*, 43(5):4071, 1991.

[55] B. Das, D. Miller, S. Datta, R. Reifenberger, W. Hong, P. Bhattacharya, J. Singh, and M. Jaffe. Evidence for spin splitting in $In_xGa_{1-x}As/In_{0.52}Al_{0.48}As$ heterostructures as $B \to 0$. *Physical Review B*, 39(2):1411, 1989.

[56] A. G. Davies, J. E. F. Frost, D. A. Ritchie, D. C Peacock *, R. Newbury, E. H. Linfield, M. Pepper, and G. A. C. Jones. The growth and physics of high mobility two-dimensional hole gases. *Journal of Crystal Growth*, 111:318, 1991.

[57] J. H. Davies. *The Physics of Low Dimensional Semiconductors: An Introduction*. University Press, Cambridge, 1998.

[58] E. de Andrada e Silva, G. La Rocca, and F. Bassani. Spin-split subbands and magneto-oscillations in III-V asymmetric heterostructures. *Physical Review B*, 50(12):8523, 1994.

[59] C. Dekker, A. Scholten, F. Liefrink, R. Eppenga, H. van Houten, and C. Foxon. Spontaneous resistance switching and low-frequency noise in quantum point contacts. *Physical Review Letters*, 66(16):2148, 1991.

[60] W. Desrat, F. Giazotto, V. Pellegrini, F. Beltram, F. Capotondi, G. Biasiol, L. Sorba, and D. Maude. Magnetotransport in high-g-factor low-density two-dimensional electron systems confined in In0.75Ga0.25As/In0.75Al0.25As quantum wells. *Physical Review B*, 69(24):245324, 2004.

[61] W. Desrat, F. Giazotto, V. Pellegrini, M. Governale, F. Beltram, F. Capotondi, G. Biasiol, and L. Sorba. Anticrossings of spin-split Landau levels in an InAs two-dimensional electron gas with spin-orbit coupling. *Physical Review B*, 71(15):153314, 2005.

[62] U. Dötsch, U. Gennser, C. David, G. Dehlinger, D. Grützmacher, T. Heinzel, S. Lüscher, and K. Ensslin. Single-hole transistor in a p-Si/SiGe quantum well. *Applied Physics Letters*, 78(3):341, 2001.

[63] G. Dresselhaus. Spin-Orbit Coupling Effects in Zinc Blende Structures. *Physical Review*, 100(2):580, 1955.

[64] Daniel Dufåker, K. F. Karlsson, L. O. Mereni, V. Dimastrodonato, G. Juska, E. Pelucchi, and P. O. Holtz. Quantum dot asymmetry and the nature of excited hole states probed by the doubly positively charged exciton X^{2+}. *Physical Review B*, 88(4):045321, 2013.

[65] P. Dutta and P. M. Horn. Low-frequency fluctuations in solids: $1/f$ noise. *Reviews of Modern Physics*, 53(3):497, 1981.

[66] A. Efros, F. Pikus, and G. Samsonidze. Maximum low-temperature mobility of two-dimensional electrons in heterojunctions with a thick spacer layer. *Physical Review B*, 41(12):8295, 1990.

[67] A. L. Efros and M. Rosen. Quantum size level structure of narrow-gap semiconductor nanocrystals: Effect of band coupling. *Physical Review B*, 58(11):7120, 1998.

[68] J. Eisenstein, H. Störmer, V. Narayanamurti, A. Gossard, and W. Wiegmann. Effect of Inversion Symmetry on the Band Structure of Semiconductor Heterostructures. *Physical Review Letters*, 53(27):2579, 1984.

[69] J. P. Eisenstein. High-precision torsional magnetometer: Application to two-dimensional electron systems. *Applied Physics Letters*, 46(7):695, 1985.

[70] J. Elzerman, R. Hanson, J. Greidanus, L. Willems van Beveren, S. De Franceschi, L. Vandersypen, S. Tarucha, and L. Kouwenhoven. Few-electron quantum dot circuit with integrated charge read out. *Physical Review B*, 67(16):161308(R), 2003.

[71] J. M. Elzerman, R. Hanson, L. H. Willems van Beveren, L. M. K. Vandersypen, and L. P. Kouwenhoven. Excited-state spectroscopy on a nearly closed quantum dot via charge detection. *Applied Physics Letters*, 84(23):4617, 2004.

[72] J. M. Elzerman, R. Hanson, L. H. Willems van Beveren, B. Witkamp, L. M. K. Vandersypen, and L. P. Kouwenhoven. Single-shot read-out of an individual electron spin in a quantum dot. *Nature*, 430:431, 2004.

[73] L. Engel, S. Hwang, T. Sajoto, D. Tsui, and M. Shayegan. Fractional quantum Hall effect at $\nu = 2/3$ and $3/5$ in tilted magnetic fields. *Physical Review B*, 45(7):3418, 1992.

[74] S. R. Eric Yang, D. Broido, and L. Sham. Holes at GaAs-$Al_xGa_{1-x}As$ heterojunctions in magnetic fields. *Physical Review B*, 32(10):6630, 1985.

[75] F. F. Fang and P. J. Stiles. Effects of a tilted magnetic field on a two-dimensional electron gas. *Physical Review*, 174(3):823, 1968.

[76] M. Field, C. Smith, M. Pepper, D. Ritchie, J. Frost, G. Jones, and D. Hasko.

Measurements of Coulomb blockade with a noninvasive voltage probe. *Physical Review Letters*, 70(9):1311, 1993.

[77] Jan Fischer, W. Coish, D. Bulaev, and Daniel Loss. Spin decoherence of a heavy hole coupled to nuclear spins in a quantum dot. *Physical Review B*, 78(15):155329, 2008.

[78] Jan Fischer and Daniel Loss. Hybridization and spin decoherence in heavy-hole quantum dots. *Physical Review Letters*, 105(26):266603, 2010.

[79] Liang Fu and C. Kane. Superconducting Proximity Effect and Majorana Fermions at the Surface of a Topological Insulator. *Physical Review Letters*, 100(9):096407, 2008.

[80] T. Fujisawa, T. Hayashi, Y. Hirayama, H. D. Cheong, and Y. H. Jeong. Electron counting of single-electron tunneling current. *Applied Physics Letters*, 84(13):2343, 2004.

[81] M. Fujiwara, M. Sasaki, and M. Akiba. Reduction method for low-frequency noise of GaAs junction field-effect transistor at a cryogenic temperature. *Applied Physics Letters*, 80(10):1844, 2002.

[82] Takahiro Fukui and Yasuhiro Hatsugai. Quantum Spin Hall Effect in Three Dimensional Materials: Lattice Computation of Z2Topological Invariants and Its Application to Bi and Sb. *Journal of the Physical Society of Japan*, 76(5):053702, 2007.

[83] Rayda Gammag and Cristine Villagonzalo. Two-dimensional electron gas tilt-induced Landau level crossings. *Solid State Communications*, 156:16, 2013.

[84] C. Garrett and W. Brattain. Physical Theory of Semiconductor Surfaces. *Physical Review*, 99(2):376, 1955.

[85] L. Gaudreau, G. Granger, A. Kam, G. C. Aers, S. A. Studenikin, P. Zawadzki, M. Pioro-Ladière, Z. R. Wasilewski, and A. S. Sachrajda. Coherent control of three-spin states in a triple quantum dot. *Nature Physics*, 8:54, 2011.

[86] M. Geller, C. Kapteyn, L. Müller-Kirsch, R. Heitz, and D. Bimberg. 450 meV hole localization in GaSb/GaAs quantum dots. *Applied Physics Letters*, 82(16):2706, 2003.

[87] Fabrice Gerbier, Nathan Goldman, Maciej Lewenstein, and Klaus Sengstock. Non-Abelian gauge fields. *Journal of Physics B: Atomic, Molecular and Optical Physics*, 46(13):130201, 2013.

[88] S. Glasberg, H. Shtrikman, and I. Bar-Joseph. Photoluminescence of a low-density two-dimensional hole gas in a GaAs quantum well: Observation of valence-band Landau levels. *Physical Review B*, 63(20):201308(R), 2001.

[89] S. L. Glashow. Partial-symmetries of weak interactions. *Nuclear Physics*, 22:579, 1961.

[90] B. Goss Levi. The geometric Berry phase. *Physics Today*, 46:17, 1993.

[91] M. Gradhand, D. V. Fedorov, F. Pientka, P. Zahn, I. Mertig, and B. L. Gyorffy. First-principle calculations of the Berry curvature of Bloch states for charge and spin transport of electrons. *J Phys Condens Matter*, 24(21):213202, 2012.

[92] G. Granger, D. Taubert, C. E. Young, L. Gaudreau, A. Kam, S. A. Studenikin, P. Zawadzki, D. Harbusch, D. Schuh, W. Wegscheider, Z. R. Wasilewski, A. A. Clerk, S. Ludwig, and A. S. Sachrajda. Quantum interference and phonon-mediated back-action in lateral quantum-dot circuits. *Nature Physics*, 8:522, 2012.

[93] Boris Grbić, Renaud Leturcq, Klaus Ensslin, Dirk Reuter, and Andreas D. Wieck. Single-hole transistor in *p*-type GaAs/AlGaAs heterostructures. *Applied Physics Letters*, 87(23):232108, 2005.

[94] Boris Grbic, Renaud Leturcq, Thomas Ihn, Klaus Ensslin, Dirk Reuter, and Andreas Wieck. Aharonov-Bohm Oscillations in the Presence of Strong Spin-Orbit Interactions. *Physical Review Letters*, 99(17):176803, 2007.

[95] S. Gustavsson, R. Leturcq, B. Simovič, R. Schleser, T. Ihn, P. Studerus, and K. Ensslin. Counting Statistics of Single Electron Transport in a Quantum Dot. *Physical Review Letters*, 96(7):076605, 2006.

[96] B. Habib, E. Tutuc, S. Melinte, M. Shayegan, D. Wasserman, S. Lyon, and R. Winkler. Spin splitting in GaAs (100) two-dimensional holes. *Physical Review B*, 69(11):113311, 2004.

[97] B. Habib, E. Tutuc, S. Melinte, M. Shayegan, D. Wasserman, S. A. Lyon, and R. Winkler. Negative differential Rashba effect in two-dimensional hole systems. *Applied Physics Letters*, 85(15):3151, 2004.

[98] F. Haldane and Yong-Shi Wu. Quantum dynamics and statistics of vortices in two-dimensional superfluids. *Physical Review Letters*, 55(26):2887, 1985.

[99] A. R. Hamilton, M. Y. Simmons, M. Pepper, and D. A. Ritchie. Influence of Inversion Symmetry on the Metallic Behaviour in a Dilute Two-dimensional Hole System. *Australian Journal of Physics*, 53:523, 2000.

[100] R. Hanson and D. D. Awschalom. Coherent manipulation of single spins in semiconductors. *Nature*, 453(7198):1043, 2008.

[101] R. Hanson, J. R. Petta, S. Tarucha, and L. M. K. Vandersypen. Spins in few-electron quantum dots. *Reviews of Modern Physics*, 79(4):1217, 2007.

[102] D. Harbusch, D. Taubert, H. P. Tranitz, W. Wegscheider, and S. Ludwig. Phonon-Mediated versus Coulombic Backaction in Quantum Dot Circuits. *Physical Review Letters*, 104(19):196801, 2010.

[103] R. H. Harrell. *Induced electron gases in undoped GaAs/AlGaAs heterostructures.* University of Cambridge, Thesis, 1998.

[104] R. H. Harrell, K. S. Pyshkin, M. Y. Simmons, D. A. Ritchie, C. J. B. Ford, G. A. C. Jones, and M. Pepper. Fabrication of high-quality one- and two-dimensional electron gases in undoped GaAs/AlGaAs heterostructures. *Applied Physics Letters*, 74(16):2328, 1999.

[105] John B. Hart. A simple geometric model for visualizing the motion of a Foucault pendulum. *American Journal of Physics*, 55(1):67, 1987.

[106] F. Hatami, N. N. Ledentsov, M. Grundmann, J. Böhrer, F. Heinrichsdorff, M. Beer, D. Bimberg, S. S. Ruvimov, P. Werner, U. Gösele, J. Heydenreich, U. Richter, S. V. Ivanov, B. Ya Meltser, P. S. Kopev, and Zh. I. Alferov. Radiative recombination in type-II GaSb/GaAs quantum dots. *Applied Physics Letters*, 67(5):656, 1995.

[107] T. Hayashi, T. Fujisawa, H. Cheong, Y. Jeong, and Y. Hirayama. Coherent manipulation of electronic states in a double quantum dot. *Physical Review Letters*, 91(22):226804, 2003.

[108] R. K. Hayden, L. Eaves, M. Henini, E. C. Valadares, O. Kuhn, D. K. Maude, J. C. Portal, T. Takamasu, N. Miura, and U. Ekenberg. Probing the anisotropic dispersion of hole states in (100) and (311)A AlAs/GaAs/AlAs quantum wells. *Semiconductor Science and Technology*, 9:298, 1994.

[109] Lixin He, Gabriel Bester, and Alex Zunger. Electronic Phase Diagrams of Carriers in Self-Assembled Quantum Dots: Violation of Hund's Rule and the Aufbau Principle for Holes. *Physical Review Letters*, 95(24):246804, 2005.

[110] Lixin He and Alex Zunger. Multiple charging of InAs/GaAs quantum dots by electrons or holes: Addition energies and ground-state configurations. *Physical Review B*, 73(11):115324, 2006.

[111] J. J. Heremans, M. B. Santos, K. Hirakawa, and M. Shayegan. Mobility anisotropy of 2D hole systems in (311)A GaAs-$Al_xGa_(1-x)As$ heterojunctions. *Journal of Applied Physics*, 76(3):1980, 1994.

[112] W. Heuring, E. Bangert, K. Grotsch, G. Landwehr, G. Weimann, W. Schlapp, J.-H. Reemtsma, and K. Heime. Influence of warping on quantum oscillations in p-type GaAs-(GaAl)As heterostructures. *Surface Science*, 229:76, 1990.

[113] Kenichi Hitachi, Takeshi Ota, and Koji Muraki. Intrinsic and extrinsic origins

of low-frequency noise in GaAs/AlGaAs Schottky-gated nanostructures. *Applied Physics Letters*, 102(19):192104, 2013.

[114] F. Hofmann, T. Heinzel, D. A. Wharam, J. P. Kotthaus, G. Böhm, W. Klein, G. Tränkle, and G. Weimann. Single electron switching in a parallel quantum dot. *Physical Review B*, 51(19):13872, 1995.

[115] F. N. Hooge, T. G. M. Kleinpenning, and L. K. J. Vandamme. Experimental studies on $1/f$ noise. *Reports on Progress in Physics*, 44:479, 1981.

[116] M. G. House, Ming Xiao, GuoPing Guo, HaiOu Li, Gang Cao, M. M. Rosenthal, and HongWen Jiang. Detection and Measurement of Spin-Dependent Dynamics in Random Telegraph Signals. *Physical Review Letters*, 111(12):126803, 2013.

[117] D. Hsieh, D. Qian, L. Wray, Y. Xia, Y. S. Hor, R. J. Cava, and M. Z. Hasan. A topological Dirac insulator in a quantum spin Hall phase. *Nature*, 452(7190):970, 2008.

[118] D. Hsieh, Y. Xia, L. Wray, D. Qian, A. Pal, J. H Dil, J. Osterwalder, F. Meier, G. Bihlmayer, C. L. Kane, Y. S. Hor, R. J. Cava, and M. Z. Hasan. Observation of Unconventional Quantum Spin Textures in Topological Insulators. *Science*, 323:919, 2009.

[119] Y. Hu, H. O. Churchill, D. J. Reilly, J. Xiang, C. M. Lieber, and C. M. Marcus. A Ge/Si heterostructure nanowire-based double quantum dot with integrated charge sensor. *Nat Nanotechnol*, 2(10):622, 2007.

[120] Y. Hu, F. Kuemmeth, C. M. Lieber, and C. M. Marcus. Hole spin relaxation in Ge-Si core-shell nanowire qubits. *Nature Nanotecnology*, 7:47, 2011.

[121] Chiao-Ti Huang, Jiun-Yun Li, Kevin S. Chou, and James C. Sturm. Screening of remote charge scattering sites from the oxide/silicon interface of strained Si two-dimensional electron gases by an intermediate tunable shielding electron layer. *Applied Physics Letters*, 104(24):243510, 2014.

[122] Thomas Ihn, Simon Gustavsson, Urszula Gasser, Bruno Küng, Thomas Müller, Roland Schleser, Martin Sigrist, Ivan Shorubalko, Renaud Leturcq, and Klaus Ensslin. Quantum dots investigated with charge detection techniques. *Solid State Communications*, 149(35-36):1419, 2009.

[123] Oxford Instruments. Kelvinox 100 dilution refrigerator manual, 2005.

[124] Toshifumi Itakura and Yasuhiro Tokura. Dephasing due to background charge fluctuations. *Physical Review B*, 67(19):195320, 2003.

[125] Y. Iye, E. Mendez, W. Wang, and L. Esaki. Magnetotransport properties and subband structure of the two-dimensional hole gas in GaAs-$Ga_{1-x}Al_xAs$ heterostructures. *Physical Review B*, 33(8):5854, 1986.

[126] A. Johnson, C. Marcus, M. Hanson, and A. Gossard. Charge sensing of excited states in an isolated double quantum dot. *Physical Review B*, 71(11):115333, 2005.

[127] A. C. Johnson, J. R. Petta, and C. M. Marcus. Singlet-triplet spin blockade and charge sensing in a few-electron double quantum dot. *Physical Review B*, 72(16):165308, 2005.

[128] A. C. Johnson, J. R. Petta, and C. M. Marcus. Singlet-triplet spin blockade and charge sensing in a few-electron double quantum dot. *Physical Review B*, 72(16):165308, 2005.

[129] K. Kandiah, M. O. Deighton, and F. B. Whiting. A physical model for random telegraph signal currents in semiconductor devices. *Journal of Applied Physics*, 66(2):937, 1989.

[130] B. E. Kane, L. N. Pfeiffer, K. W. West, and C. K. Harnett. Variable density high mobility two-dimensional electron and hole gases in a gated GaAs/$Al_xGa_{1-x}As$ heterostructure. *Applied Physics Letters*, 63(15):2132, 1993.

[131] E. O. Kane. The k . p method. *Semiconductors and Semimetals*, 1:75, 1966.

[132] Ning Kang, Kazuya Suzuki, Eisuke Abe, Yoshiaki Hashimoto, Yasuhiro Iye, and Shingo Katsumoto. Observation of spinorbit Berry phase in magnetoresistance of a two-dimensional hole antidot system. *Physica E: Low-dimensional Systems and Nanostructures*, 40(5):1051, 2008.

[133] M. A. Kastner. Artificial atoms. *Physics Today*, 46:24, 1993.

[134] M. A. Kastner. The single electron transistor and artificial atoms. *Annals of Physics*, 9(11-12):885, 2000.

[135] T. Kato. On the adiabatic theorem of quantum mechanics. *Journal of the Physical Society of Japan*, 5:435, 1950.

[136] G. Katsaros, P. Spathis, M. Stoffel, F. Fournel, M. Mongillo, V. Bouchiat, F. Lefloch, A. Rastelli, O. G. Schmidt, and S. De Franceschi. Hybrid superconductor-semiconductor devices made from self-assembled SiGe nanocrystals on silicon. *Nature Nanotechnology*, 5(6):458, 2010.

[137] O. Klochan, J. C. H. Chen, A. P. Micolich, A. R. Hamilton, K. Muraki, and Y. Hirayama. Fabrication and characterization of an induced GaAs single hole transistor. *Applied Physics Letters*, 96(9):092103, 2010.

[138] O. Klochan, W. R. Clarke, R. Danneau, A. P. Micolich, L. H. Ho, A. R. Hamilton, K. Muraki, and Y. Hirayama. Ballistic transport in induced one-dimensional hole systems. *Applied Physics Letters*, 89(9):092105, 2006.

[139] O. Klochan, A. P. Micolich, A. R. Hamilton, D. Reuter, A. D. Wieck, F. Reininghaus, M. Pletyukhov, and H. Schoeller. Scaling of the Kondo zero-bias peak in a hole quantum dot at finite temperatures. *Physical Review B*, 87(20):201104(R), 2013.

[140] O. Klochan, A. P. Micolich, A. R. Hamilton, K. Trunov, D. Reuter, and A. D. Wieck. Observation of the Kondo Effect in a Spin-3/2 Hole Quantum Dot. *Physical Review Letters*, 107(7):076805, 2011.

[141] O. Klochan, A. P. Micolich, L. H. Ho, A. R. Hamilton, K. Muraki, and Y. Hirayama. The interplay between one-dimensional confinement and two-dimensional crystallographic anisotropy effects in ballistic hole quantum wires. *New Journal of Physics*, 11(4):043018, 2009.

[142] O. V. Klochan. *Ballistic transport in one-dimensional p-type GaAs devices.* University of New South Wales, Thesis, 2007.

[143] R. Knobel, N. Samarth, J. Harris, and D. Awschalom. Measurements of Landau-level crossings and extended states in magnetic two-dimensional electron gases. *Physical Review B*, 65(23):235327, 2002.

[144] S. Koduvayur, L. Rokhinson, D. Tsui, L. Pfeiffer, and K. West. Anisotropic Modification of the Effective Hole g Factor by Electrostatic Confinement. *Physical Review Letters*, 100(12):126401, 2008.

[145] M. Kohmoto. Topological invariant and the quantization of the Hall conductance. *Annals of Physics*, 160:343, 1985.

[146] Y. Komijani, T. Choi, F. Nichele, K. Ensslin, T. Ihn, D. Reuter, and A. D. Wieck. Counting statistics of hole transfer in a p-type GaAs quantum dot with dense excitation spectrum. *Physical Review B*, 88(3):035417, 2013.

[147] Y. Komijani, M. Csontos, T. Ihn, K. Ensslin, D. Reuter, and A. D. Wieck. Observation of excited states in a p-type GaAs quantum dot. *Europhysics Letters*, 84(5):57004, 2008.

[148] Y. Komijani, M. Csontos, I. Shorubalko, U. Zülicke, T. Ihn, K. Ensslin, D. Reuter, and A. D. Wieck. Anisotropic Zeeman shift in p-type GaAs quantum point contacts. *EPL (Europhysics Letters)*, 102(3):37002, 2013.

[149] A. Kopf and K. Lassmann. Linear Stark and nonlinear Zeeman coupling to the ground state of effective mass acceptors in silicon. *Physical Review Letters*, 69(10):1580, 1992.

[150] L. P. Kouwenhoven, D. G. Austing, and S. Tarucha. Few-electron quantum dots. *Reports on Progress in Physics*, 64:701, 2001.

[151] B. Kramer and A. MacKinnon. Localization: Theory and experiment. *Rep. Prog. Phys.*, 56:1469, 1993.

[152] M. Kugler, T. Andlauer, T. Korn, A. Wagner, S. Fehringer, R. Schulz, M. Kubová, C. Gerl, D. Schuh, W. Wegscheider, P. Vogl, and C. Schller. Gate control of low-temperature spin dynamics in two-dimensional hole systems. *Physical Review B*, 80(3):035325, 2009.

[153] C. Kurdak, C-J. Chen, D. C. Tsui, S. Parihar, S. Lyon, and G. W. Weimann. Resistance fluctuations in GaAs/$Al_xGa_{1-x}As$ quantum point contact and Hall bar structures. *Physical Review B*, 56(5):9813, 1997.

[154] R. Lassnig. $k \cdot p$ theory, effective-mass approach, and spin splitting for two-dimensional electrons in GaAs-GaAlAs heterostructures. *Physical Review B*, 31(12):8076, 1985.

[155] Patrick A. Lee. Disordered electronic systems. *Reviews of Modern Physics*, 57(2):287, 1985.

[156] Patrick A. Lee and Xiao-Gang Wen. Doping a Mott insulator: Physics of high-temperature superconductivity. *Reviews of Modern Physics*, 78(1):17, 2006.

[157] E. Leobandung, L. Guo, and S. Y. Choua. Single hole quantum dot transistors in silicon. *Applied Physics Letters*, 67(16):2338, 1995.

[158] HaiOu Li, Ming Xiao, Gang Cao, Cheng Zhou, RuNan Shang, Tao Tu, Guang-Can Guo, HongWen Jiang, and GuoPing Guo. Back-action-induced non-equilibrium effect in electron charge counting statistics. *Applied Physics Letters*, 100(9):092112, 2012.

[159] Qiuzi Li, Łukasz Cywiński, Dimitrie Culcer, Xuedong Hu, and S. Das Sarma. Exchange coupling in silicon quantum dots : Theoretical considerations for quantum computation. *Physical Review B*, 81(8):085313, 2010.

[160] R. Li, F. E. Hudson, A. S. Dzurak, and A. R. Hamilton. Single hole transport in a silicon metal-oxide-semiconductor quantum dot. *Applied Physics Letters*, 103(16):163508, 2013.

[161] Yongqing Li, Cong Ren, Peng Xiong, Stephan von Molnár, Yuzo Ohno, and Hideo Ohno. Modulation of Noise in Submicron GaAs/AlGaAs Hall Devices by Gating. *Physical Review Letters*, 93(24):246602, 2004.

[162] Y. X. Liang, Q. Dong, M. C. Cheng, U. Gennser, A. Cavanna, and Y. Jin. Insight into low frequency noise induced by gate leakage current in AlGaAs/GaAs high electron mobility transistors at 4.2 K. *Applied Physics Letters*, 99(11):113505, 2011.

[163] E. M. Lifshits and A. M. Kosevich. Theory of the Shubnikov-de Haas effect. *Journal of Physics and Chemistry of Solids*, 4:1, 1958.

[164] W. H. Lim, H. Huebl, L. H. Willems van Beveren, S. Rubanov, P. G. Spizzirri, S. J. Angus, R. G. Clark, and A. S. Dzurak. Electrostatically defined few-electron double quantum dot in silicon. *Applied Physics Letters*, 94(17):173502, 2009.

[165] Y. J. Lin, R. L. Compton, K. Jimenez-Garcia, J. V. Porto, and I. B. Spielman. Synthetic magnetic fields for ultracold neutral atoms. *Nature*, 462(7273):628, 2009.

[166] D. Loss and D. P. DiVincenzo. Quantum computation with quantum dots. *Physical Review A*, 57(1):120, 1998.

[167] D. Loss, H. Schoeller, and Paul Goldbart. Observing the Berry phase in diffusive conductors: Necessary conditions for adiabaticity. *Physical Review B*, 59(20):13328, 1999.

[168] J. P. Lu, J. B. Yau, S. P. Shukla, M. Shayegan, L. Wissinger, U. Rössler, and R. Winkler. Tunable Spin-Splitting and Spin-Resolved Ballistic Transport in GaA/AlGaAs Two-Dimensional Holes. *Physical Review Letters*, 81(6):1282, 1998.

[169] T. M. Lu, Z. F. Li, D. C. Tsui, M. J. Manfra, L. N. Pfeiffer, and K. W. West. Cyclotron mass of two-dimensional holes in (100) oriented GaAs/AlGaAs heterostructures. *Applied Physics Letters*, 92(1):012109, 2008.

[170] W. Lu, Z-Q. Ji, L. Pfeiffer, K. W. West, and A. J. Rimberg. Real-time detection of electron tunnelling in a quantum dot. *Nature*, 423:422, 2003.

[171] W. Lu, J. Xiang, B. P. Timko, Y. Wu, and C. M. Lieber. One-dimensional hole gas in germanium/silicon nanowire heterostructures. *Proc Natl Acad Sci U S A*, 102(29):10046, 2005.

[172] J. Luttinger and W. Kohn. Motion of Electrons and Holes in Perturbed Periodic Fields. *Physical Review*, 97(4):869, 1955.

[173] J. M. Luttinger. Quantum Theory of Cyclotron Resonance in Semiconductors: General Theory. *Physical Review*, 102(4):1030, 1956.

[174] W. Y. Mak, K. Das Gupta, H. E. Beere, I. Farrer, F. Sfigakis, and D. A. Ritchie. Distinguishing impurity concentrations in GaAs and AlGaAs using very shallow undoped heterostructures. *Applied Physics Letters*, 97(24):242107, 2010.

[175] W. Y. Mak, F. Sfigakis, K. Das Gupta, O. Klochan, H. E. Beere, I. Farrer, J. P. Griffiths, G. A. C. Jones, A. R. Hamilton, and D. A. Ritchie. Ultrashallow quantum dots in an undoped GaAs/AlGaAs two-dimensional electron gas. *Applied Physics Letters*, 102(10):103507, 2013.

[176] A. Manaselyan and T. Chakraborty. Enhanced Rashba effect for hole states in a quantum dot. *Europhysics Letters*, 88(1):17003, 2009.

[177] R. W. Martin, R. J. Nicholas, G. J. Rees, S. K. Haywood, N. J. Mason, and P. J. Walker. Two-dimensional spin confinement in strained-layer quantum wells. *Physical Review B*, 42(14):9237, 1990.

[178] T. P. Martin, A. Szorkovszky, A. P. Micolich, A. R. Hamilton, C. A. Marlow, R. P. Taylor, H. Linke, and H. Q. Xu. Field-orientation dependence of the

Zeeman spin splitting in (In,Ga)As quantum point contacts. *Physical Review B*, 81(4):041303(R), 2010.

[179] L. Martin-Moreno, J. T. Nicholls, N. K. Patel, and M. Pepper. Non-linear conductance of a saddle-point constriction. *J Phys Condens Matter*, 4(1323):1323, 1992.

[180] Harsh Mathur. Thomas precession, spin-orbit interaction, and Berrys phase. *Physical Review Letters*, 67(24):3325, 1991.

[181] B. M. Maune, M. G. Borselli, B. Huang, T. D. Ladd, P. W. Deelman, K. S. Holabird, A. A. Kiselev, I. Alvarado-Rodriguez, R. S. Ross, A. E. Schmitz, M. Sokolich, C. A. Watson, M. F. Gyure, and A. T. Hunter. Coherent singlet-triplet oscillations in a silicon-based double quantum dot. *Nature*, 481(7381):344, 2012.

[182] Ines Meinel, Dirk Grundler, Silke Bargstädt-Franke, Christian Heyn, Detlef Heitmann, and Bernd David. High-sensitive superconducting magnetometry on a two-dimensional electron gas up to 10 Tesla. *Applied Physics Letters*, 70(24):3305, 1997.

[183] Yigal Meir, Ned Wingreen, and Patrick Lee. Transport through a strongly interacting electron system: Theory of periodic conductance oscillations. *Physical Review Letters*, 66(23):3048, 1991.

[184] U. Meirav, M. Kastner, and S. Wind. Single-electron charging and periodic conductance resonances in GaAs nanostructures. *Physical Review Letters*, 65(6):771, 1990.

[185] F. Merlet, B. Pajot, Ph Arcas, and A. Jean-Louis. Experimental study of the Zeeman splitting of boron levels in silicon. *Physical Review B*, 12(8):3297, 1975.

[186] A. Messiah. *Quantum mechanics*, volume 2. North-Holland Pub. Co, Amsterdam, 1962.

[187] G. Moore and N. Read. Nonabelions in the fractional quantum Hall effect. *Nuclear Physics B*, 360:362, 1991.

[188] A. F. Morpurgo, J. P. Heida, T. M. Klapwijk, and B. J. van Wees. Ensemble-Average Spectrum of Aharonov-Bohm Conductance Oscillations: Evidence for Spin-Orbit-Induced Berry's Phase. *Physical Review Letters*, 80(5):1050, 1998.

[189] S. Murakami, N. Nagaosa, and S-C. Zhang. Dissipationless Quantum Spin Current at Room Temperature. *Science*, 301:1348, 2003.

[190] S. S. Murzin, S. I. Dorozhkin, G. Landwehr, and A. C. Gossard. Effect of hole-hole scattering on the conductivity of the two-component 2D hole gas in GaAs/(AlGa)As heterostructures. *JETP Letters*, 62(2):113, 1998.

[191] G. Nenciu. Dynamics of band electrons in electric and magnetic fields: rigorous justification of the effective Hamiltonians. *Reviews of Modern Physics*, 63(1):91, 1991.

[192] Fabrizio Nichele, Stefano Chesi, Szymon Hennel, Angela Wittmann, Christian Gerl, Werner Wegscheider, Daniel Loss, Thomas Ihn, and Klaus Ensslin. Characterization of Spin-Orbit Interactions of GaAs Heavy Holes Using a Quantum Point Contact. *Physical Review Letters*, 113(4):046801, 2014.

[193] R. Nicholas, R. Haug, K. Klitzing, and G. Weimann. Exchange enhancement of the spin splitting in a GaAs-$Ga_xAl_{1-x}As$ heterojunction. *Physical Review B*, 37(3):1294, 1988.

[194] J. Nitta, T. Akazaki, H. Takayanagi, and T. Enoki. Gate Control of Spin-Orbit Interaction in an Inverted $In_{0.53}Ga_{0.47}As/In_{0.52}Al_{0.48}As$ Heterostructure. *Physical Review Letters*, 78(7):4, 1997.

[195] J. Nitta, H. Takayanagi, and S. Cavlet. Magnetoresistance oscillations in an Aharonov-Bohm ring using two-dimensional electron gas InAs. *Microelectronic Engineering*, 47:85, 1999.

[196] E. Nordberg, G. Eyck, H. Stalford, R. Muller, R. Young, K. Eng, L. Tracy, K. Childs, J. Wendt, R. Grubbs, J. Stevens, M. Lilly, M. Eriksson, and M. Carroll. Enhancement-mode double-top-gated metal-oxide-semiconductor nanostructures with tunable lateral geometry. *Physical Review B*, 80(11):115331, 2009.

[197] S. M. North, P. R. Briddon, M. A. Cusack, and M. Jaros. Electronic structure of GaSb/GaAs quantum domes. *Physical Review B*, 58(19):12601, 1998.

[198] K. S. Novoselov, A. K. Geim, S. V. Morozov, D. Jiang, M. I. Katsnelson, I. V. Grigorieva, S. V. Dubonos, and A. A. Firsov. Two-dimensional gas of massless Dirac fermions in graphene. *Nature*, 438(7065):197, 2005.

[199] L. Onsager. Interpretation of the de Haas-van Alphen effect. *Philosophical Magazine*, 43:1006, 1952.

[200] W. Pan, K. Lai, S. P. Bayrakci, N. P. Ong, D. C. Tsui, L. N. Pfeiffer, and K. W. West. Cyclotron resonance at microwave frequencies in two-dimensional hole system in AlGaAs/GaAs quantum wells. *Applied Physics Letters*, 83(17):3519, 2003.

[201] S. Papadakis, E. De Poortere, and M. Shayegan. Anisotropic Magnetoresistance of Two-Dimensional Holes in GaAs. *Physical Review Letters*, 84(24):5592, 2000.

[202] S. Papadakis, E. De Poortere, and M. Shayegan. Confinement symmetry, mobility anisotropy, and metallic behavior in (311)A GaAs two-dimensional holes. *Physical Review B*, 62(23):15375, 2000.

[203] S. Papadakis, E. P. De Poortere, and M. Shayegan. Anomalous spin splitting of two-dimensional electrons in an AlAs quantum well. *Physical Review B*, 59(20):R12743, 1999.

[204] S. J. Papadakis. The Effect of Spin Splitting on the Metallic Behavior of a Two-Dimensional System. *Science*, 283(5410):2056, 1999.

[205] K. D. Petersson, J. R. Petta, H. Lu, and A. C. Gossard. Quantum Coher-

ence in a One-Electron Semiconductor Charge Qubit. *Physical Review Letters*, 105(24):246804, 2010.

[206] J. Petta, A. Johnson, C. Marcus, M. Hanson, and A. Gossard. Manipulation of a Single Charge in a Double Quantum Dot. *Physical Review Letters*, 93(18):186802, 2004.

[207] J. Petta, A. Johnson, A. Yacoby, C. Marcus, M. Hanson, and A. Gossard. Pulsed-gate measurements of the singlet-triplet relaxation time in a two-electron double quantum dot. *Physical Review B*, 72(16):161301, 2005.

[208] J. R. Petta, A. C. Johnson, J. M. Taylor, E. A. Laird, A. Yacoby, M. D. Lukin, C. M. Marcus, M. P. Hanson, and A. C. Gossard. Coherent manipulation of coupled electron spins in semiconductor quantum dots. *Science*, 309(5744):2180, 2005.

[209] Loren Pfeiffer, K. W. West, H. L. Stormer, and K. W. Baldwin. Electron mobilities exceeding $10^7 \mathrm{cm}^2/\mathrm{V}$ s in modulation-doped GaAs. *Applied Physics Letters*, 55(18):1888, 1989.

[210] J. R. Pilbrow and M. R. Lowrey. Low-symmetry effects in electron paramagnetic resonance. *Rep. Prog. Phys.*, 43:433, 1980.

[211] M. Pioro-Ladrière, M. Abolfath, P. Zawadzki, J. Lapointe, S. Studenikin, A. Sachrajda, and P. Hawrylak. Charge sensing of an artificial H2+ molecule in lateral quantum dots. *Physical Review B*, 72(12):125307, 2005.

[212] M. Pioro-Ladriére, John Davies, A. Long, A. Sachrajda, Louis Gaudreau, P. Zawadzki, J. Lapointe, J. Gupta, Z. Wasilewski, and S. Studenikin. Origin of switching noise in GaAs/$\mathrm{Al}_x\mathrm{Ga}_{1-x}$As lateral gated devices. *Physical Review B*, 72(11):115331, 2005.

[213] V. S. Pribiag, S. Nadj-Perge, S. M. Frolov, J. W. G. van den Berg, I. van Weperen, S. R. Plissard, E. P. A. M. Bakkers, and L. P. Kouwenhoven. Electrical control of single hole spins in nanowire quantum dots. *Nature Nanotechnology*, 8:170, 2013.

[214] Xiao-Liang Qi and Shou-Cheng Zhang. Topological insulators and superconductors. *Reviews of Modern Physics*, 83(4):1057, 2011.

[215] C. Qu, Z. Zheng, M. Gong, Y. Xu, L. Mao, X. Zou, G. Guo, and C. Zhang. Topological superfluids with finite-momentum pairing and Majorana fermions. *Nat Commun*, 4:2710, 2013.

[216] Clarke. W. R. *Quantum interaction phenomena in p-GaAs microelectronic devices.* University of New South Wales, Thesis, 2005.

[217] K. Rachor, T. Raab, D. Heitmann, C. Gerl, and W. Wegscheider. Cyclotron resonance of carbon-doped two-dimensional hole systems: From the magnetic quantum limit to low magnetic fields. *Physical Review B*, 79(12):125417, 2009.

[218] Maryam Rahimi, M. Sakr, S. Kravchenko, S. Dultz, and H. Jiang. Compressibility of a two-dimensional hole gas in a tilted magnetic field. *Physical Review B*, 67(8):081302, 2003.

[219] Raffaele Resta. Macroscopic polarization in crystalline dielectrics: the geometric phase approach. *Reviews of Modern Physics*, 66(3):899, 1994.

[220] Raffaele Resta. Manifestations of Berry's phase in molecules and condensed matter. *Journal of Physics: Condensed Matter*, 12(9):R107, 2000.

[221] D. Reuter, P. Kailuweit, A. Wieck, U. Zeitler, O. Wibbelhoff, C. Meier, A. Lorke, and J. Maan. Coulomb-Interaction-Induced Incomplete Shell Filling in the Hole System of InAs Quantum Dots. *Physical Review Letters*, 94(2):026808, 2005.

[222] D. Reuter, P. Schafmeister, P. Kailuweit, and A. D. Wieck. Frequency-dependent C(V) spectroscopy of the hole system in InAs quantum dots. *Physica E: Low-dimensional Systems and Nanostructures*, 21(2-4):445, 2004.

[223] S. Roddaro, A. Fuhrer, P. Brusheim, C. Fasth, H. Xu, L. Samuelson, J. Xiang, and C. Lieber. Spin States of Holes in Ge/Si Nanowire Quantum Dots. *Physical Review Letters*, 101(18):186802, 2008.

[224] A. Rossi, T. Ferrus, G. J. Podd, and D. A. Williams. Charge detection in phosphorus-doped silicon double quantum dots. *Applied Physics Letters*, 97(22):223506, 2010.

[225] C. Rössler, T. Krähenmann, S. Baer, T. Ihn, K. Ensslin, C. Reichl, and W. Wegscheider. Tunable charge detectors for semiconductor quantum circuits. *New Journal of Physics*, 15(3):033011, 2013.

[226] C. Rössler, B. Küng, S. Dröcher, T. Choi, T. Ihn, K. Ensslin, and M. Beck. Highly tunable hybrid quantum dots with charge detection. *Applied Physics Letters*, 97(15):152109, 2010.

[227] B. Sacepe, J. B. Oostinga, J. Li, A. Ubaldini, N. J. Couto, E. Giannini, and A. F. Morpurgo. Gate-tuned normal and superconducting transport at the surface of a topological insulator. *Nat Commun*, 2:575, 2011.

[228] T. Sakamoto and K. Nakamura. Carrier traps in a GaAs/Al_xGa_{1-x}As single electron transistor. *Applied Physics Letters*, 68(20):2861, 1996.

[229] T. Sakamoto, Y. Nakamura, and K. Nakamura. Distributions of single-carrier traps in GaAs/Al_xGa_{1-x}As heterostructures. *Applied Physics Letters*, 67(15):2220, 1995.

[230] V. Sapega, M. Cardona, K. Ploog, E. Ivchenko, and D. Mirlin. Spin-flip Raman scattering in GaAs/Al_xGa_{1-x}As multiple quantum wells. *Physical Review B*, 45(8):4320, 1992.

[231] S. Sarkozy. *Mesoscopic transport in undopd heterostructures*. University of Cambridge, Thesis, 2008.

[232] S. Sarkozy, K. Das Gupta, C. Siegert, A. Ghosh, M. Pepper, I. Farrer, H. E. Beere, D. A. Ritchie, and G. A. C. Jones. Low temperature transport in undoped mesoscopic structures. *Applied Physics Letters*, 94(17):172105, 2009.

[233] J. R. Schrieffer. *Mobility in inversion layers: theory and experiment*. University of Pennysylvania Press, Philadelphia, 1957.

[234] D. Schröer, A. Greentree, L. Gaudreau, K. Eberl, L. Hollenberg, J. Kotthaus, and S. Ludwig. Electrostatically defined serial triple quantum dot charged with few electrons. *Physical Review B*, 76(7):075306, 2007.

[235] A. Schwan, B. M. Meiners, A. Greilich, D. R. Yakovlev, M. Bayer, A. D. B. Maia, A. A. Quivy, and A. B. Henriques. Anisotropy of electron and hole g-factors in (In,Ga)As quantum dots. *Applied Physics Letters*, 99(22):221914, 2011.

[236] J. Scott-Thomas, Stuart Field, M. Kastner, Henry Smith, and D. Antoniadis. Conductance Oscillations Periodic in the Density of a One-Dimensional Electron Gas. *Physical Review Letters*, 62(5):583, 1989.

[237] A. M. See. *Undoped AlGaAs/GaAs Quantum Dots with Thermally Robust Quantum Properties*. University of New South Wales, Thesis, 2012.

[238] A. M. See, O. Klochan, A. R. Hamilton, A. P. Micolich, M. Aagesen, and P. E. Lindelof. AlGaAs/GaAs single electron transistor fabricated without modulation doping. *Applied Physics Letters*, 96(11):112104, 2010.

[239] A. M. See, I. Pilgrim, B. C. Scannell, R. D. Montgomery, O. Klochan, A. M. Burke, M. Aagesen, P. E. Lindelof, I. Farrer, D. A. Ritchie, R. P. Taylor, A. R. Hamilton, and A. P. Micolich. Impact of Small-Angle Scattering on Ballistic Transport in Quantum Dots. *Physical Review Letters*, 108(19):196807, 2012.

[240] A. Shapere and F. Wilczek. *Geometric phases in physics*, volume 5 of *Advanced Series in Mathematical Physics*. World Scientific, 1989.

[241] Ryuichi Shindou and Ken-Ichiro Imura. Noncommutative geometry and non-Abelian Berry phase in the wave-packet dynamics of Bloch electrons. *Nuclear Physics B*, 720(3):399, 2005.

[242] C. B. Simmons, J. R. Prance, B. J. Van Bael, Teck Seng Koh, Zhan Shi, D. E. Savage, M. G. Lagally, R. Joynt, Mark Friesen, S. N. Coppersmith, and M. A. Eriksson. Tunable Spin Loading and T_1 of a Silicon Spin Qubit Measured by Single-Shot Readout. *Physical Review Letters*, 106(15):156804, 2011.

[243] M. Y. Simmons. Fabrication of high mobility in situ back-gated (311)A hole gas heterojunctions. *Applied Physics Letters*, 70(20):2750, 1997.

[244] Barry Simon. Holonomy, the Quantum Adiabatic Theorem, and Berry's Phase. *Physical Review Letters*, 51(24):2167, 1983.

[245] C. G. Smith, M. Pepper, H. Ahmed, J. E. F. Frost, D. G. Hasko, D. C. Peacock, D. A. Ritchie, and G. A. C. Jones. The transition from one- to zero-dimensional ballistic transport. *Journal of Physics C: Solid State Physics*, 21:L893, 1988.

[246] T. Smith Iii and F. Fang. g factor of electrons in an InAs quantum well. *Physical Review B*, 35(14):7729, 1987.

[247] P. M. Solomon, C. M. Knoedler, and S. L. Wright. A GaAs gate heterojunction FET. *IEEE electron device letters*, 5(9):379, 1984.

[248] D. Sprinzak, Yang Ji, M. Heiblum, D. Mahalu, and Hadas Shtrikman. Charge Distribution in a Kondo-Correlated Quantum Dot. *Physical Review Letters*, 88(17):176805, 2002.

[249] Paul C. Spruijtenburg, Joost Ridderbos, Filipp Mueller, Anne W. Leenstra, Matthias Brauns, Antonius A. I. Aarnink, Wilfred G. van der Wiel, and Floris A. Zwanenburg. Single-hole tunneling through a two-dimensional hole gas in intrinsic silicon. *Applied Physics Letters*, 102(19):192105, 2013.

[250] A. Srinivasan, L. A. Yeoh, O. Klochan, T. P. Martin, J. C. Chen, A. P. Micolich, A. R. Hamilton, D. Reuter, and A. D. Wieck. Using a tunable quantum wire to measure the large out-of-plane spin splitting of quasi two-dimensional holes in a GaAs nanostructure. *Nano Lett*, 13(1):148, 2013.

[251] A. Srinivasan, L. A. Yeoh, O. Klochan, T. P. Martin, J. C. Chen, A. P. Micolich, A. R. Hamilton, D. Reuter, and A. D. Wieck. Using a tunable quantum wire to measure the large out-of-plane spin splitting of quasi two-dimensional holes in a GaAs nanostructure. *Nano Lett*, 13(1):148, 2013.

[252] H. Stormer, Z. Schlesinger, A. Chang, D. Tsui, A. Gossard, and W. Wiegmann. Energy Structure and Quantized Hall Effect of Two-Dimensional Holes. *Physical Review Letters*, 51(2):126, 1983.

[253] Hui Sun, Xun-Li Feng, Chunfeng Wu, Jin-Ming Liu, Shangqing Gong, and C. H. Oh. Optical rotation of heavy hole spins by non-Abelian geometrical means. *Physical Review B*, 80(23):235404, 2009.

[254] Dieter Suter, Gerard C. Chingas, Robert A. Harris, and Alexander Pines. Berry's phase in magnetic resonance. *Molecular Physics*, 61(6):1327, 1987.

[255] M. Syperek, D. Yakovlev, A. Greilich, J. Misiewicz, M. Bayer, D. Reuter, and A. Wieck. Spin Coherence of Holes in GaAs/(Al,Ga)As Quantum Wells. *Physical Review Letters*, 99(18):187401, 2007.

[256] S. Takahashi, R. Deacon, A. Oiwa, K. Shibata, K. Hirakawa, and S. Tarucha. Electrically tunable three-dimensional g-factor anisotropy in single InAs self-assembled quantum dots. *Physical Review B*, 87(16):161302, 2013.

[257] S. Takahashi, R. S. Deacon, K. Yoshida, A. Oiwa, K. Shibata, K. Hirakawa, Y. Tokura, and S. Tarucha. Large Anisotropy of the Spin-Orbit Interaction in a Single InAs Self-Assembled Quantum Dot. *Physical Review Letters*, 104(24):246801, 2010.

[258] S. Tarucha, D. G. Austing, T. Honda, R. J. van der Hage, and L. P. Kouwenhoven. Shell Filling and Spin Effects in a Few Electron Quantum Dot. *Physical Review Letters*, 77(17):3613, 1996.

[259] H. Tezuka, A. R. Stegner, A. M. Tyryshkin, S. Shankar, M. L. W. Thewalt, S. A. Lyon, K. M. Itoh, and M. S. Brandt. Electron paramagnetic resonance of boron acceptors in isotopically purified silicon. *Physical Review B*, 81(16):161203, 2010.

[260] L. H. Thomas. The motion of the spinning electron. *Nature*, 117(2945):514, 1926.

[261] T. Thornton, M. Pepper, H. Ahmed, D. Andrews, and G. Davies. One-Dimensional Conduction in the 2D Electron Gas of a GaAs-AlGaAs Heterojunction. *Physical Review Letters*, 56(11):1198, 1986.

[262] D. Thouless, M. Kohmoto, M. Nightingale, and M. den Nijs. Quantized Hall Conductance in a Two-Dimensional Periodic Potential. *Physical Review Letters*, 49(6):405, 1982.

[263] G. Timp, R. Behringer, and J. Cunningham. Suppression of impurity scattering in a one-dimensional wire. *Physical Review B*, 42(14):9259, 1990.

[264] I. Toft and R. Phillips. Hole g factors in GaAs quantum dots from the angular dependence of the spin fine structure. *Physical Review B*, 76(3):033301, 2007.

[265] Akira Tomita and Raymond Chiao. Observation of Berry's Topological Phase by Use of an Optical Fiber. *Physical Review Letters*, 57(8):937, 1986.

[266] L. A. Tracy, T. W. Hargett, and J. L. Reno. Few-hole double quantum dot in an undoped GaAs/AlGaAs heterostructure. *Applied Physics Letters*, 104(12):123101, 2014.

[267] A. Tsukazaki, A. Ohtomo, M. Kawasaki, S. Akasaka, H. Yuji, K. Tamura, K. Nakahara, T. Tanabe, A. Kamisawa, T. Gokmen, J. Shabani, and M. Shayegan. Spin susceptibility and effective mass of two-dimensional electrons in $Mg_xZn_{1-x}O$/ZnO heterostructures. *Physical Review B*, 78(23):233308, 2008.

[268] E. Tutuc, S. Melinte, E. De Poortere, M. Shayegan, and R. Winkler. Role of finite layer thickness in spin polarization of GaAs two-dimensional electrons in strong parallel magnetic fields. *Physical Review B*, 67(24):241309, 2003.

[269] E. Valadares. Strong anisotropy of hole subbands in (311) GaAs-AlAs quantum wells. *Physical Review B*, 46(7):3935, 1992.

[270] J. van der Heijden, J. Salfi, J. A. Mol, J. Verduijn, G. C. Tettamanzi, A. R.

Hamilton, N. Collaert, and S. Rogge. Probing the spin states of a single acceptor atom. *Nano Lett*, 14(3):1492, 2014.

[271] H. W. van Kesteren, E. C. Cosman, W. A. J. A. van der Poel, and C. T. Foxon. Fine structure of excitons in type-II GaAslAlAs quantum wells. *Physical Review B*, 41(8):5283, 1990.

[272] B. J. van Wees, H. van Houten, C. W. J. Beenakker, J. G. Williamson, L. P. Kouwenhoven, D. van der Marel, and C. T. Foxon. Quantized conductance of point contacts in a Two-dimensional electron gas. *physical Review Letters*, 60(9):848, 1988.

[273] P. Vogl, T. Andlauer, A. Trellakis, T. Zibold, P. Greck, T. Eissfeller, and S. Birner. nextnano GmbH, Germany, http://www.nextnano.com/nextnanoplus/ [Last accessed: 13 March 2015], 2012.

[274] I. Vurgaftman, J. R. Meyer, and L. R. Ram-Mohan. Band parameters for IIIV compound semiconductors and their alloys. *Journal of Applied Physics*, 89(11):5815, 2001.

[275] W. I. Wang, E. E. Mendez, Y. Iye, B. Lee, M. H. Kim, and G. E. Stillman. High mobility two-dimensional hole gas in an $Al_{0.26}Ga_{0.74}As$/GaAs heterojunction. *Journal of Applied Physics*, 60(5):1834, 1986.

[276] M. B. Weissman. $1/f$ noise and other slow, nonexponential kinetics in condensed matter. *Reviews of Modern Physics*, 60(2):537, 1988.

[277] D. A. Wharam, T. J. Thornton, R. Newbury, M. Pepper, H. Ahmed, J. E. F. Frost, D. G. Hasko, D. C. Peacock, D. A. Ritchie, and G. A. C. Jones. One-dimensional transport and the quantisation of the ballistic resistance. *Journal of Physics C: Solid State Physics*, 21:L209, 1988.

[278] A. Wieck, E. Batke, D. Heitmann, J. Kotthaus, and E. Bangert. Lifting of the Spin Degeneracy of Hole Subbands in a Surface Electric Field on Silicon. *Physical Review Letters*, 53(5):493, 1984.

[279] S. A. J. Wiegers, A. S. van Steenbergen, M. E. Jeuken, M. Bravin, P. E. Wolf, G. Remenyi, J. A. A. J. Perenboom, and J. C. Maan. A sensitive and versatile torque magnetometer for use in high magnetic fields. *Review of Scientific Instruments*, 69(6):2369, 1998.

[280] Frank Wilczek and A. Zee. Appearance of Gauge Structure in Simple Dynamical Systems. *Physical Review Letters*, 52(24):2111, 1984.

[281] A. Wild, J. Sailer, J. Nützel, G. Abstreiter, S. Ludwig, and D. Bougeard. Electrostatically defined quantum dots in a Si/SiGe heterostructure. *New Journal of Physics*, 12(11):113019, 2010.

[282] R. Winkler. Highly Anisotropic g-Factor of Two-Dimensional Hole Systems. *Physical Review Letters*, 85(21):4574, 2000.

[283] R. Winkler. Rashba spin splitting in two-dimensional electron and hole systems. *Physical Review B*, 62(7):4245, 2000.

[284] R. Winkler. *Spin-Orbit Coupling Effects in Two-Dimensional Electron and Hole Systems*, volume 191 of *Springer Tracts in Modern Physics*. Springer, 2003.

[285] R. Winkler. Spin polarization of quasi-two-dimensional hole systems. *Physical Review B*, 71(11):113307, 2005.

[286] R. Winkler, Dimitrie Culcer, S. J. Papadakis, B. Habib, and M. Shayegan. Spin orientation of holes in quantum wells. *Semiconductor Science and Technology*, 23(11):114017, 2008.

[287] R. Winkler and U. Züelicke. Private communications, 2014.

[288] S. A. Wolf, D. D. Awschalom, R. A. Buhrman, J. M. Daughton, S. von Molnar, M. L. Roukes, A. Y. Chtchelkanova, and D. M. Treger. Spintronics - A spin-based electronics vision of the future. *Science*, 294:1488, 2001.

[289] Di Xiao, Ming-Che Chang, and Qian Niu. Berry phase effects on electronic properties. *Reviews of Modern Physics*, 82(3):1959, 2010.

[290] Di Xiao, Yugui Yao, Wanxiang Feng, Jun Wen, Wenguang Zhu, Xing-Qiu Chen, G. Malcolm Stocks, and Zhenyu Zhang. Half-Heusler Compounds as a New Class of Three-Dimensional Topological Insulators. *Physical Review Letters*, 105(9):096404, 2010.

[291] M. Xiao, M. G. House, and H. W. Jiang. Measurement of the Spin Relaxation Time of Single Electrons in a Silicon Metal-Oxide-Semiconductor-Based Quantum Dot. *Physical Review Letters*, 104(9):096801, 2010.

[292] M. V. Yakunin, A. V. Suslov, S. M. Podgornykh, S. A. Dvoretsky, and N. N. Mikhailov. Effects of spin polarization in the HgTe quantum well. *Physical Review B*, 85(24):245321, 2012.

[293] C. Yang and R. Mills. Conservation of Isotopic Spin and Isotopic Gauge Invariance. *Physical Review*, 96(1):191, 1954.

[294] C. H. Yang, A. Rossi, N. S. Lai, R. Leon, W. H. Lim, and A. S. Dzurak. Charge state hysteresis in semiconductor quantum dots. *Applied Physics Letters*, 105(18):183505, 2014.

[295] J. B. Yau, E. P. De Poortere, and M. Shayegan. Manifestation of Berry's phase in AharonovBohm oscillations in a 2D system with spinorbit interaction. *Microelectronic Engineering*, 63:211, 2002.

[296] Jeng-Bang Yau, E. De Poortere, and M. Shayegan. Aharonov-Bohm Oscillations with Spin: Evidence for Berrys Phase. *Physical Review Letters*, 88(14):146801, 2002.

[297] L. A. Yeoh. *A rotation system for the characterization of spin-polarization in hole one-dimensional quantum wires.* University of Technology Sydney, Thesis, 2009.

[298] L. A. Yeoh, A. Srinivasan, O. Klochan, R. Winkler, U. Zülicke, M. Y. Simmons, D. A. Ritchie, M. Pepper, and A. R Hamilton. Noncollinear Paramagnetism of a GaAs Two-Dimensional Hole System. *Physical Review Letters*, 113(23):236401, 2014.

[299] L. A. Yeoh, A. Srinivasan, T. P. Martin, O. Klochan, A. P. Micolich, and A. R. Hamilton. Piezoelectric rotator for studying quantum effects in semiconductor nanostructures at high magnetic fields and low temperatures. *Rev Sci Instrum*, 81(11):113905, 2010.

[300] Z. Q. Yuan, R. R. Du, M. J. Manfra, L. N. Pfeiffer, and K. W. West. Landau level spectrum in a two-dimensional hole gas in C-doped (100) GaAs/$Al_{0.4}Ga_{0.6}As$ square quantum well. *Applied Physics Letters*, 94(5):052103, 2009.

[301] P. Zeeman. The effect of magnetisation on the nature of light emitted by a substance. *Nature*, 55(1424):347, 1987.

[302] L. X. Zhang, J. P. Leburton, R. Hanson, and L. P. Kouwenhoven. Engineering the quantum point contact response to single-electron charging in a few-electron quantum-dot circuit. *Applied Physics Letters*, 85(13):2628, 2004.

[303] L. X. Zhang, P. Matagne, J. Leburton, R. Hanson, and L. Kouwenhoven. Single-electron charging and detection in a laterally coupled quantum-dot circuit in the few-electron regime. *Physical Review B*, 69(24):245301, 2004.

[304] Y. Zhang, Z. Jiang, J. P. Small, M. S. Purewal, Y. W. Tan, M. Fazlollahi, J. D. Chudow, J. A. Jaszczak, H. L. Stormer, and P. Kim. Landau-Level Splitting in Graphene in High Magnetic Fields. *Physical Review Letters*, 96(13):136806, 2006.

[305] Y. Zhang, Y. W. Tan, H. L. Stormer, and P. Kim. Experimental observation of the quantum Hall effect and Berry's phase in graphene. *Nature*, 438(7065):201, 2005.

[306] Z. Zhong, Y. Fang, W. Lu, and C. M. Lieber. Coherent single charge transport in molecular-scale Si nanowires. *Nano Lett*, 5(6):1143, 2005.

[307] J. Zhu, H. Stormer, L. Pfeiffer, K. Baldwin, and K. West. Spin Susceptibility of an Ultra-Low-Density Two-Dimensional Electron System. *Physical Review Letters*, 90(5):056805, 2003.

[308] M. Zieliński. Fine structure of light-hole excitons in nanowire quantum dots. *Physical Review B*, 88(11):115424, 2013.

[309] I. Zutic, J. Fabian, and S. Das Sarma. Spintronics: Fundamentals and applications. *Reviews of Modern Physics*, 76(2):323, 2004.

[310] F. A. Zwanenburg, C. E. W. M. van Rijmenam, Y. Fang, C. M. Lieber, and L. P. Kouwenhoven. Spin States of the First Four Holes in a Silicon Nanowire Quantum Dot. *Nano Letters*, 9(3):1071, 2009.

[311] J. Zwanziger, M. Koenig, and A. Pines. Non-Abelian effects in a quadrupole system rotating around two axes. *Physical Review A*, 42(5):3107, 1990.